Dissertation zur Erlangung des Doktorgrades
der Fakultät für Chemie und Pharmazie
der Ludwig–Maximilians–Universität München

Cryo-EM studies of tubular membrane shaping by the N-BAR protein amphiphysin

Julia Adam
aus
Neuburg an der Donau, Deutschland

2016

Erklärung

Diese Dissertation wurde im Sinne von § 7 der Promotionsordnung vom 28. November 2011 von Frau Prof. Elena Conti, PhD betreut.

Eidesstattliche Versicherung

Diese Dissertation wurde eigenständig und ohne unerlaubte Hilfe erarbeitet.

München,.....

.....

Julia Adam

Dissertation eingereicht am

Erstgutachter:	Prof. Elena Conti, PhD
Zweitgutachter:	Dr. Daniel Wilson

Mündliche Prüfung am 12.04.2016

Preface

Parts of this thesis have been published in:

Adam, J., Basnet, N., Mizuno, N., Structural insights into the cooperative remodeling of membranes by amphiphysin/BIN1, Scientific Reports 5, 15452 (2015)

Contents

Summary

Membrane remodelling is important in cellular processes like vesicle trafficking, organelle shaping, movement or division. In *Drosophila* the membrane-shaping N-BAR protein amphiphysin is involved in the biogenesis and stabilization of deep invaginations of the sarcolemma, the T-tubules, crucial for the excitation-contraction coupling machinery in striated muscles. *Drosophila* amphiphysin mutants are viable but flightless due to an disorganized T-tubule network. However, details of the amphiphysin membrane interaction, the underlying molecular mechanism how amphiphysin is remodelling and maintaining tubular membrane shapes and the three dimensional structure of the amphiphysin assembly are unknown. In this study I structurally characterized the helical arrangement of *Drosophila* amphiphysin on membrane tubes by using cryo-EM. I found that the BAR domain cooperatively self-assembles to a helical arrangement on the membrane surface. The cryo-EM 3D reconstruction of amphiphysin N-BAR-mediated tubes provided first structural insights into the unique and well-connected helical amphiphysin BAR assembly. One tip of the crescent-shaped BAR dimer is immersed into the membrane whereas the other tip is protruding outwards from the tube surface. In addition, it seems that the regulatory domains with a SH3 domain of amphiphysin are not involved in the membrane remodelling process. The helical BAR lattice is well-connected by laterally locking BAR domains in adjacent lattice rows via the H0 helix and by tip-to-center interactions of neighbouring BAR domains in one lattice row. The H0 helix is insignificant for the membrane remodelling activity but essential for the fast initiation of the helical BAR polymerization and for the formation of a rigidly organized BAR arrangement on the tube surface. Mutations at the tip region or ΔH0 helix mutants showed impaired tube remodelling activity and an disorganized helical BAR arrangement. This suggests that the H0 helix as well as the BAR tips are crucial for an efficient and organized BAR assembly on the tube surface. I observed that amphiphysin N-BAR-mediated tubes are more rigid and uniform as endophilin N-BAR-mediated tubes, contributing to the dynamic membrane scission process in endocytosis. The cooperative BAR self-assembly and the unique and well-connected BAR arrangement on membranes give insights into the molecular mechanism of membrane shaping by amphiphysin and its ability to maintain the shape of T-tubules.

1 Introduction

1.1 Membranes

1.1.1 Biological membranes

The separation of the inside of a cell to the outside environment was a crucial event to create life on earth. With the help of curved, flexible, self-sealing and semipermeable barriers, also known as membranes, cells and intracellular compartments could be formed and shaped, allowing the cell to perform complex and coordinated intracellular biochemical processes. Membranes are needed for the uptake of nutrients, excretion of cellular waste, sensing of external signals and for communicating information. Furthermore, membranes have to be modulated during membrane trafficking events like endocytosis, exocytosis, tubulation, cell migration, cell division and organelle development. All this various cell operations are possible because of the dynamic and flexible membrane morphology, making it possible to remodel the membrane into various shapes in a specific three-dimensional and temporal way.

1.1.2 Mechanisms of membrane curvature formation

Biological membranes reveal a general structural organization of an approximately 4 - 5 nm thick flexible lipid bilayer, being formed out of amphipathic phospholipids (hydrophilic headgroups and hydrophobic acyl chains) [1]. The plasma membrane (PM) and membranes of the various compartments are composed with different lipid compositions, being more or less asymmetrical ordered. Flat membranes can be formed into different degrees of curvature (from weak to shallow to high) by changes in the lipid composition and various proteins. The intracellular remodelled membrane can be divided into different shapes (Fig. 1.1, B): flat, tubular, spherical and saddle-like. For instance the non-invaginated plasma membrane shows a rather flat membrane shape. Tubular shapes can be found at t-tubules in muscle cells or at the neck of endocytotic vesicles before scission by connecting the vesicle to the membrane. All budded transport vesicles reveal a spherical shape. The saddle-like deformation is observed when the invaginated vesicle, emerging from the membrane, is not completely developed. Here no vesicle neck is generated to link the vesicle to the membrane. Moreover, the induced curvature will be distinguished between positive and negative bending (Fig. 1.1, A). Positive curvature means that the membrane bends inwards to the cytoplasm side. In negative curvature events the membrane is

curved the opposite way. Figure 1.1 illustrates the types of generated curvature.

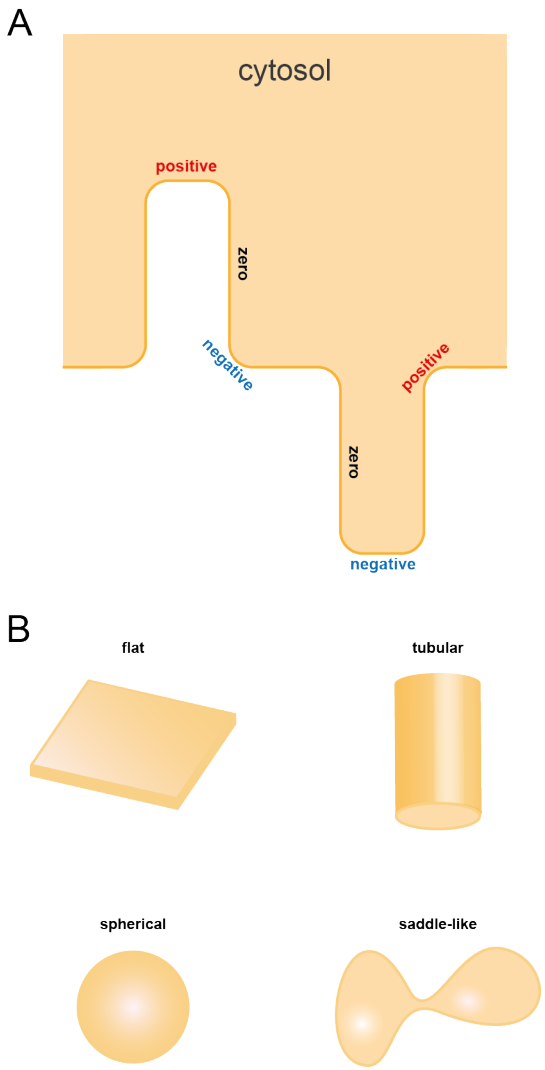

Figure 1.1 – Types of remodelled curvatures | (A) Induced curvature can be defined as positive or negative curvature. Positive curvature shows an inward to the cytosol bended membrane. Negative curvature means that the membrane is curved outwards. No membrane bending means zero curvature induction. (B) Membrane deformation can be divided into four types of remodelled membrane shapes: flat, tubular, spherical and saddle-like.

1.1.2.1 Influence of lipid compositions

Phospholipids have specific shapes because of their head group and acyl chain compounds (Fig. 1.3, B). The intrinsic shape of the lipids, being arranged next to each other, is influencing how the membrane is bend. Clusters of related lipid shapes could lead to a spontaneous membrane curvature formation of the monolayer.

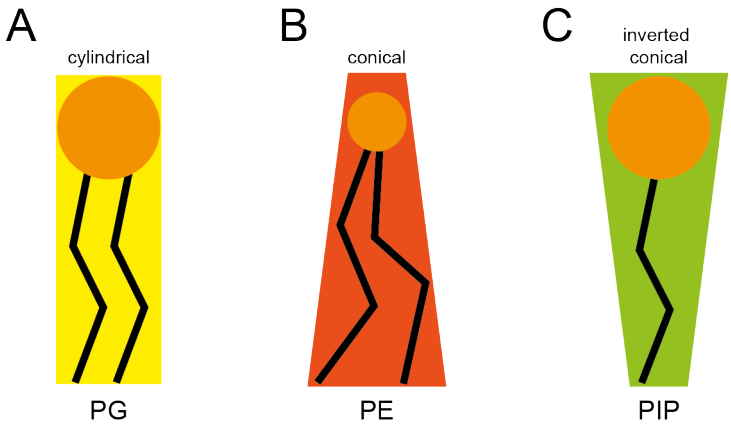

Figure 1.2 – Lipids and their shape | (A) Cylindrical shape: headgroup and acyl chain tail have the same size. (B) conical shape: headgroup is smaller than the acyl chain tail. (C) Inverted conical shape: headgroup is larger than the acyl chain tail. PG = phosphatidylglycerole, PE = phosphatidylethanolamine, PIP = phosphatidylinositol phosphate

Phosphatidylcholine (PC), phosphatidylglycerole (PG) and phosphatidylserine (PS) have a cylindrical shape where the headgroup and the fatty tail have the same size, leading to a flat monolayer formation (Fig. 1.2, A). Phosphatidylethanolamine (PE) and phosphatic acid (PA) are conical lipids, showing a smaller headgroup than the fatty acyl chain tail and therefore leading to a negative membrane because the small headgroups are moving closer together (Fig. 1.2, B). Another class are the inverted conical (inverted cone) lipids (Fig. 1.2, C) like phosphatidylinositol (PI) and the phosphatidylinositol phosphates (PIPs) like phosphatidylinositol-3-phosphate (PI3P), phosphatidylinositol-3,4-bisphosphate (PI(3,4)P_2) or phosphatidylinositol-4,5-bisphosphate (PI(4,5)P_2), generating a positively curved membrane due to that the headgroups act like a wedge in the lipid monolayer [2–4]. In addition, double bonds (i.e. oleic acid) in the acyl chain can occupy more space in the membrane. It can influence the headgroup to tail size ratio and defines the lipid geometry [5]. Variation in the lipid compositions (and their shapes) and the different sum of lipids in the outer and inner bilayer leaflet are defining the membrane asymmetry [6], influencing the bilayer curvature. Phospholipids can be also translocated from the outer extracellular to the inner cytosolic membrane side (or the opposite way) by various membrane proteins like the lipid flippase type IV P-type ATPases [7,8], leading to altered lipid distribution and membrane curvature [9].
Depending on the lipid composition and charge (Table 1.1 proteins can recognize and interact with the membrane in various ways (Fig. 1.3, A). They can recognize charged membranes without insertion of a specific domain ether with an poly-cationic motif, using a nonspecific electrostatic interaction with lipids [10,11], or via a structural protein pocket, binding to specific lipids like PS, PI or PIPs [12,13].

Lipid	Charge
PS	negative
PG	negative
PIPs	negative
PE	neutral
PC	neutral

Table 1.1 – Lipids and their charge | PS = phosphatidylserine, PG = phosphatidylglycerole, PIP = phosphatidylinositol phosphate, PE = phosphatidylethanolamine, PC = phosphatidylcholine

1.1.2.2 Effect of transmembrane proteins

Inserted transmembrane proteins like receptors, ion channels and transporters can also lead to bending of the membrane (Fig. 1.3, C). The shape of transmembrane domains could be ether conical or inverted conical [14], showing a similar bending mechanism like phospholipids of an identical shape class. Furthermore, crowding of transmembrane proteins induces a stronger local curvature formation [15]. For example the nicotinic acetylcholin receptor at the K+ channels [16] or neuromuscular junctions [17] has a conical shape, forcing the membrane leaflet to bend towards it [14,18]. With the help of attachment proteins this receptor and other transmembrane proteins are able to oligomerize to from clusters. Crowding of transmembrane proteins induces a stronger local curvature formation [19,20]. Clustering of transmembrane receptors plays also a role in vesicle cargo loading at the clathrin-coated pits (CCPs). Clustered receptors add and stabilize the membrane curvature at the CCPs [21]. Moreover, large extra-membrane domains of receptors or conformational changes in the membrane-bending domain could lead to membrane deformation [15,18].

1.1.2.3 Hydrophobic motif insertion

Nanoscopic curvature generation is also enabled by inserting a specific amphipathic or hydrophobic protein motif into the membrane (Fig. 1.3, D). Amphipathic helices are inducing local membrane curvature by embedding their hydrophobic side into the membrane monolayer [22,23]. The hydrophilic side is facing the cytoplasm and its positively charged residues could interact with anionic phospholipid headgroups. Thus, the helix center is on the height of the glycerol backbone of the lipids [24–26], making it possible that the amphipathic helix can recognize the surrounding charge of the lipid headgroups and package of the lipid acyl chains [27,28]. Epsin with an epsin N-terminal homology (ENTH) domain was one of the first characterized proteins with this kind of motif [29]. Moreover, BAR (Bin/Amphiphysin/Rvs) domain proteins like endophilin, amphiphysin, BIN1 (bridging integrator 1 or MYC box-dependent interacting protein 1) and nadrin or the endosomal sorting complex required for transport (ESCRT)-III protein CHMP4B (Charged Multivesicular Body Protein 4B) are carrying an amphipathic helix. All amphipathic helices are not identical due to a variation in the helix length or the residue

composition of the hydrophobic and polar face[27,28,30]. These properties plus the size and charge of the residues could influence how the amphipathic helix is sensing membrane curvature, interacting with the membrane and remodeling the membrane[23].
Next to amphipathic helices hydrophobic motifs within a protein could insert into the lipid bilayer by loop formation, which is generating membrane curvature. For example caveolins at caveolae or reticulons at the ER oligomerize to remodel the membrane after they embedded their motif into the membrane[31,32]. The self-assembly of these loop motif proteins could lead to various membrane shapes. Another way to induce membrane deformation is by the insertion of a C2 domain of various proteins like DOC2 (double-C2 domain) proteins or synaptotagmin-1, being involved in Ca^{2+} dependent membrane fusion[33–36].

1.1.2.4 Scaffolding of membrane proteins

Several distinguished protein types can deform the membrane by acting like a scaffold on the membrane (Fig. 1.3, E). Coat proteins like clathrin, being involved in clathrin-mediated endocytosis (CME)[37,38], and coat protein complex I and II (COPI/II), taking part in vesicle transport between endoplasmic reticulum (ER) and Golgi apparatus[39,40], induce and stabilize membrane curvature by assembling into rigid curved "cage" structures, transferring its shape to the membrane. These proteins can not interact with the membrane directly and therefore need membrane bound adapter or cargo proteins to form a linkage to the membrane (indirect scaffolding mechanism)[18].
Dynamin GTPase family proteins are interacting with and helical polymerize around membranes, generating tube-like deformations. For a correct self-assembly of dynamin the membrane has to be already curved and should be under tension. For example dynamin is involved in CME and is polymerizing around the vesicle neck and is using GTP hydrolysis to perform vesicle fission.
BAR domains are also act like a scaffold to remodel membranes (direct scaffolding mechanism). They can induce various degrees of membrane curvature, which is depending on the intrinsic curvature of the BAR dimer unit[41,42]. The dimeric BAR domain is interacting with the membrane by electrostatic interaction between negatively charged phospholipids like PS or PIPs and positively charged amino acid patches on the concave surface[43,44]. Oligomerization of several BAR proteins is increasing the local protein concentration on the membrane surface, generating stronger membrane curvature formation[44]. Several BAR proteins contain one or more amphipathic helices, which is increasing their membrane remodeling ability[43,45,46]. Furthermore, some BAR proteins are able to helical polymerize around the membrane, forcing the membrane to remodel itself into a tubular shape[43,47–49]. BAR proteins are involved in various cellular processes like CME, T-tubule and organelle biogenesis, formation of filopodia or lamellipodia and so on. Section 1.2 will provide profound insights into BAR proteins and their role in membrane remodeling.

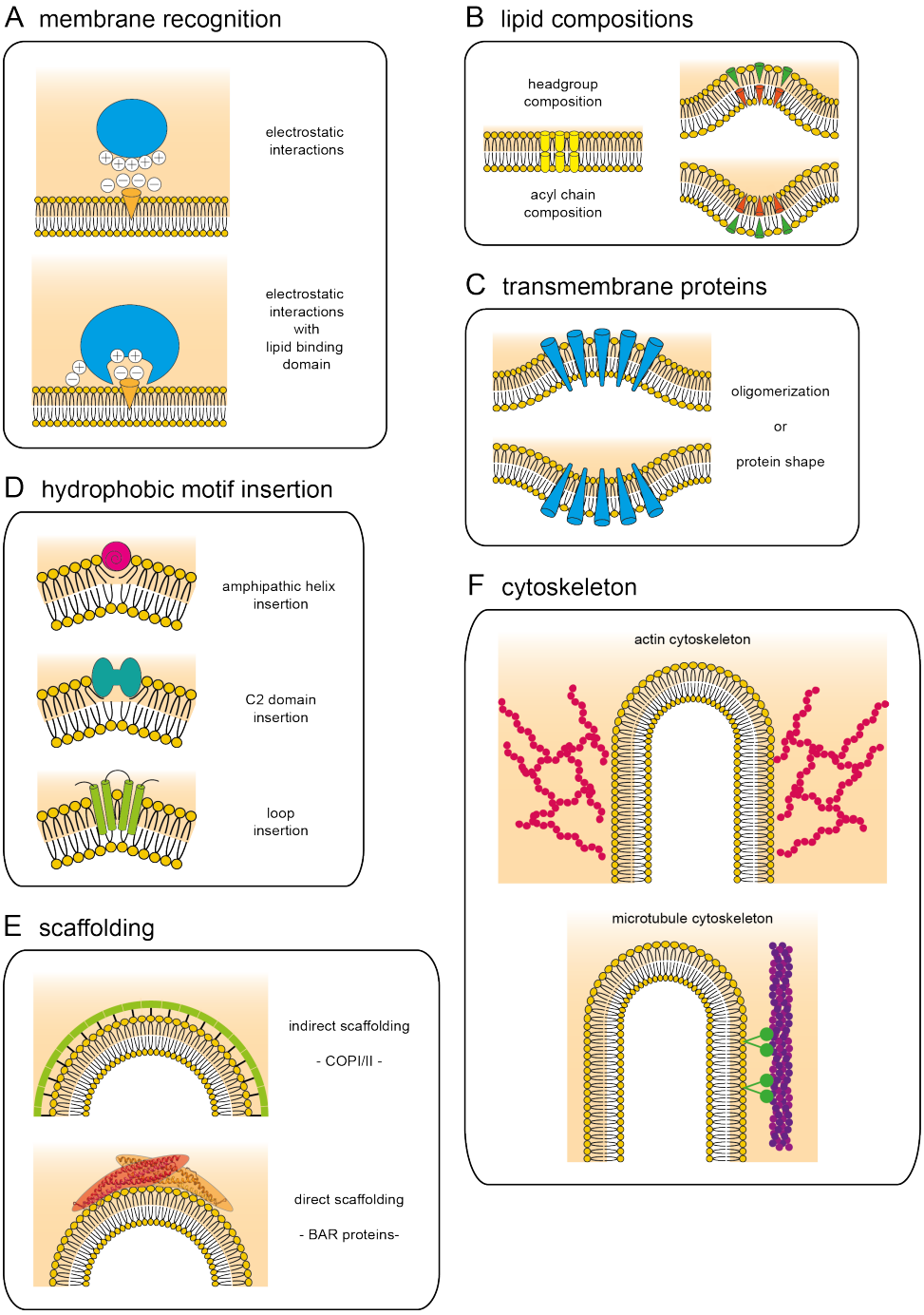

Figure 1.3 – Mechanism of membrane curvature formation | Several mechanism of membrane bending are known. (A) Membranes can be recognized by proteins either by electrostatic interactions or electrostatic interactions with additional specific lipid binding domain. (B) To induce local curvature, various lipid compositions are embedded into the membrane. The lipid shape is defined by the headgroup or acyl chain composition. (C) Transmembrane proteins can induce curvature either by oligomerization or because of their protein shape. (D) Local curvature can be generated by the insertion of hydrophobic motifs: amphipathic helix, C2 domain or loop insertion. (E) Proteins can act like a scaffold to remodel membranes. The scaffolding mechanism uses either indirect scaffolding such as COPI/II, being connected to the membrane via adapter proteins, or direct scaffolding like seen with BAR proteins, which bind to membranes and induce curvature due to polymerization. (F) The actin or microtubule cytoskeleton is connected to the membrane it can also help to bend membranes.

1.1.2.5 Influence of the cytoskeleton and motor activity

Plasma membrane and organelle remodeling can be also induced by the cytoskeleton (Fig. 1.3, F)[50]. Macroscopic membrane shaping by assembly, disassembly, branching or bundling of the cytoskeleton could be found in filopodia, lamellipodia, membrane arrangements during phagocytosis and organelles like the ER and Golgi. Microtubule (MT), actin and intermediate filaments are involved in maintaining the membrane tension because they are intermittently linked to the membrane bilayer and they are shaping the membrane by supplying a underlying scaffold[51–53]. Moreover, myosin, dynein and kinesin motors are attached to the membrane and could actively induce a pulling and pushing force to the membrane, which is generating membrane deformation. Therefore the cytoskeleton is able to influence the cell mobility[54], formation of tubular shapes[55] or vesicles[56] and to remodel and support the morphology of several organelles like ER or Golgi. Moreover, the cytoskeleton can interact with various membrane binding and/or remodeling proteins like BAR domain proteins, which could have an impact on protein driven membrane curvature formation[43,57].

1.1.3 Coupling of biological membrane shaping to function

To obtain different membrane morphologies numerous membrane shaping mechanism are combined in the cell. In various membrane shaping processes a interplay between membrane deforming proteins, membrane interacting proteins, lipids and physical forces is taking place, making it possible to sense, generate and stabilize membrane curvature. The regulation of membrane shaping is required for cellular life because it is coupled to essential functions within the cell. Every generated cellular shape has a particular physiological reason. This section will give a short overview about membrane bending and its involvement in organelle shaping, transport vesicle formation and membrane fusion.

1.1.3.1 Compartment morphology

Every intracellular organelle has its own specific membrane shape. The shape is defined by the degree and position of the membrane curvature. The ER, Golgi, endosome, autophagosome, mitochondria or transport carriers and further organelles have their own characteristic dynamic form, which is remodeling itself during necessary cellular events e.g. maturation, fission, fusion or formation of transport carriers and endocytic vesicles etc[31,58]. For example the Golgi apparatus and the ER reveal a very complex and dynamic structural setup, having interwoven connections of cylinders, tubular shapes, disks like cisternae[59]. These two organelles evolved particular structural features to do their specified functions in the cell. The Golgi is a stack of semi-circular membrane cisternae, being interconnected, more saccular and fenestrated[60] with enzymes so that the traveling through proteins can be modified. In contrast the ER has a tubular network

with smaller flattened cisternae[61], containing enzyme storage, because of the production of proteins, lipids, carbohydrates and steroid hormones and the quality control of protein folding. Despite their different shapes both organelle morphologies develop a maximized surface with a lower inner volume, making it possible to have a fast molecule turnover[4].

1.1.3.2 Creating transport vesicles

Every organelle in the cell has a particular function, requiring specific different factors like proteins or phospholipids for its specific tasks. Small membrane vesicles allow cargo exchange between the compartments and thus transport specific molecules such as proteins as cargo from the originated to the destined compartment[62]. Coat proteins use the indirect scaffolding mechanism to deform the membrane (Fig. 1.3, E) so that small vesicles can emerge from the membrane and take up the cargo. During the vesicle budding process several proteins cooperate with each other to stimulate membrane remodeling[63]. Most of the coat proteins are interacting with the membrane via specific adaptor proteins that are strictly required for the cage formation[64]. In the CME several key players are involved to invaginate clathirn-coated pits to vesicles. The coat protein clathrin, which is not directly binding to the membrane, is binding to several adapter proteins to form CCPs. One of these adapter proteins is epsin, containing an amphipathic helix motif (ENTH motif) and a clathrin binding side[65–68]. Epsin can induce local membrane curvature by binding to PI(4,5)P_2 and localizes clathrin to the membrane, which is promoting CCP formation because it goes along with clathrin polymerization[68,69]. During the clathrin polymerization process a cage is formed using the scaffolding mechanism to shape the vesicle[37,38]. The vesicle body, being surrounded by the clathrin cage, is attached to the membrane by a neck. The transition from the vesicle body and to the neck shows a negative curvature. For this reason clathrin can not continue to polymerize along the neck because it can only induce positive membrane curvature. Several neck forming proteins like the N-BAR domain proteins endophilin and amphiphysin are needed to form the neck where the vesicle scission is taking place[43]. The neck is formed because of the BAR dimer scaffold and the insertion of amphipathic helix motifs[43,70]. Dynamin, being recruited by amphiphysin, is polymerizing around the neck and subsequently vesicle scission occurs by GTP hydrolysis. High local concentrations of amphipathic helices like in the case of amphiphysin or endophilin induce mechanical stress in the membrane bilayer, facilitating scission of the vesicle from the membrane.
Proteins with an amphipathic helix like epsin or amphiphysin play also a role in the COPI and COPII vesicle formation. Secretion-associated Ras-related protein 1 (Sar1) for COPII and ADP-ribosylation factor 1 (Arf1) for COPI are small GTPases, containing a amphipathic helix[71–74]. In their GTP bound active state Sar1 and Arf1 are exposing their amphipathic helix, which is inserted into the membrane leaflet[75–77] In their membrane-bound state they act like an anchor for the corresponding COPI/II components[77,78]. The arriving coat proteins assemble to a cage and form a coated vesicle[40,79,80]. The

formed vesicle is detached from the membrane by GTPase independent scission [75,76,81].

1.1.3.3 Membrane fusion

The formed transport vesicles are carried to their destined compartment where membrane bending proteins are involved in vesicle tethering and fusion [82]. Golgin GMAP-210 is localized at the cis-Golgi and could tether small transport vesicles to the Golgi by an amphipathic lipid-packing sensor (ALPS) motif. This motif can notably sense curved membranes and is only folded in the presence of strong curvature, existing in small vesicles. After the vesicles are trapped at the membrane they can fuse with the Golgi via soluble N-ethylmaleimide-sensitive fusion protein-attachment protein receptors (SNARES) [29,83]. The SNARE complex plays a role in the fusion of one vesicle with its target membrane by bringing both membranes closer together [84]. Next to SNARE complex several more proteins are necessary for the fusion process. For example some of these proteins belong to the curvature inducing synaptotagmin and DOC2 protein family [36,85]. Synaptotagmin family proteins are involved in the calcium dependent synaptic vesicle fusion and located at the arriving vesicle by a transmembrane domain. Under an increased calcium level the two cytoplasmic C2 domains of synaptotagmin-1 are embedded into the target membrane and generate high curvature in proximity to the SNARE complex. The high curvature at the membrane is necessary to enable the fusion process between vesicle and target membrane [34,35]. DOC2 proteins are cytosolic soluble and acting in a similar way like synaptotagmin-1 by bending the membrane next to the SNARE complex, leading to the capability to induce fusion [33]. This suggest that membrane fusion by the SNARE complex is attended by high curvature formation at the target membrane.

1.2 Membrane remodeling by BAR domain proteins

Members of the Bin-Amphiphysin-Rvs domain protein superfamily are key regulators of membrane remodeling in the cell. The BAR domain was firstly identified as conserved (from yeast to human) N-terminal protein domain in BIN1, amphiphysin and Rvs161/167, giving the domain its name. Numerous proteins of these superfamily have been found since then. They play a major role in sensing, inducing, binding and stabilizing membrane curvature during cell development and cellular processes.

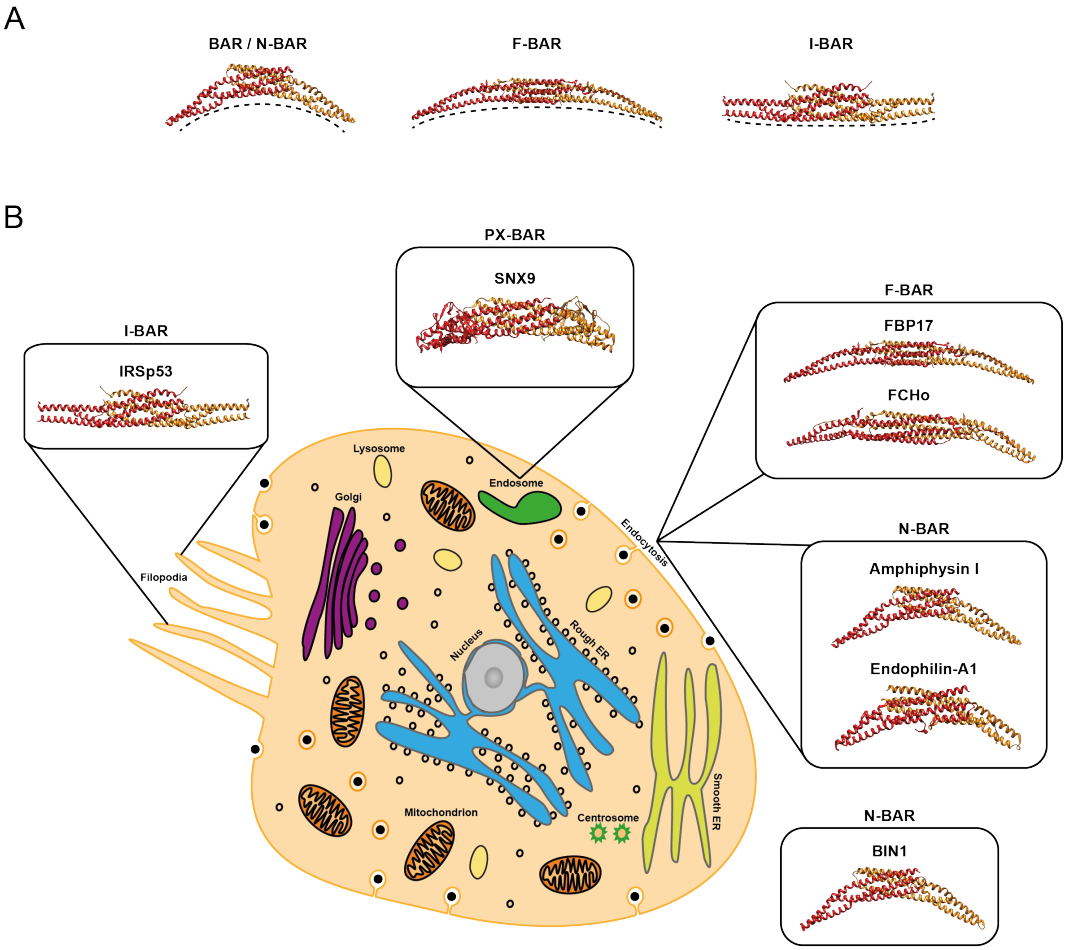

Figure 1.4 – Membrane remodeling in the cell by BAR proteins | (A) BAR proteins can be classified into three types. (Left) BAR/N-BAR proteins induce the strongest positive membrane curvature. (Middle) F-BAR proteins are more elongated and generate a more shallow positive curvature. (Right) I-BAR proteins induce negative curvature. (B) BAR proteins have different roles in the cell. The I-BAR proteins like IRSp53 (corresponding PDB code: 2YKT)[86] are participate in the formation of lamellipodia and filopodia. The PX-BAR protein SNX9 (2RAI)[87] is involved in tubular-based endosomal sorting. The F-BAR proteins FBP17 (2EFL)[88] and FCHO2 (2V0O)[89] and the N-BAR proteins amphiphysin I (3SOG) and endophilin-A1 (2C08)[26] play are role in endocytosis, being a dynamic membrane remodeling process. The N-BAR protein BIN1 (2FIC)[90] is involved in the formation and stabilization of T-tubules in muscles.

1.2.1 Structural architecture and members of the BAR domain superfamily

In 2004, ten years after the first identification of BAR proteins, the crystal structure of the *Drosophila* amphiphysin BAR domain was solved[43]. The crystal structure revealed that BAR domains form a dimer where the dimer core shows a bundle of six helices, being formed by three long kinked helices of each monomer. The kinked monomers dimerize in a specific angle, making the dimer look like a banana or boomerang (Fig. 1.4).

The positively charged loop between helix 2 and 3 at each tip of the dimer is poorly ordered and flexible. The BAR domain dimer has positively charged residue patches on its concave surface. Therefore it can interact with negatively charged phospholipids in the membrane[43]. It was shown that amphiphysin can deform membranes into tubes because of the intrinsic BAR dimer shape, acting like a scaffold on the membrane[43,47,49]. In the last couple of years more and more BAR proteins were structurally investigated, showing similarity in the BAR domain structural architecture. Moreover, all BAR proteins contain at least one additional domain next to the BAR domain. For protein-protein interaction, BAR proteins can have a src-homology 3 (SH3) domain, binding to prolin-rich domain (PRD) proteins such as dynamin I. Several BAR proteins are also containing an additional lipid interaction motif like one or more amphipathic helices, a pleckstrin homology (PH) or phox homology (PX) domain[45,91]. It is assumed that some of these domains could be integrated into the membrane bending helical arrangement of BAR domains, which was for example seen for the SH3 domain of endophilin[70] and arfaptin-2 forming a complex with the GTPase Arl1[92]. Besides, there are some BAR proteins known, which are conjunct with a guanine nucleotide exchange factor (GEF) or GTP hydrolysis activating protein (GAP), which enables regulation of small GTPases[45,93]. Depending on their sequence homology, BAR superfamily members can be classified into BAR domain types (Fig. 1.4, A): classical BAR, FCH-BAR (F-BAR) or IMD/Inverse BAR (I-BAR). Between the classes the sequence homology is rather modest. All of these BAR domain proteins are able to sense and induce various degrees of membrane curvatures corresponding to the intrinsic curved shape of the BAR dimer (Fig. 1.4). In this thesis the BAR dimer will be also referred as BAR and BAR domain and the BAR monomer as BAR monomer or BAR unit 1/2.

A closer look at the first identified classical BAR domain proteins (Fig. 1.4, B) revealed that they can be further divided into subgroups according to additional membrane binding motifs or domains. Arfaptin, being involved at the vesicle budding at the Golgi, is an BAR domain protein without any additional membrane insertion motif. In addition, classical BAR domain proteins can contain a N-terminal amphipathic helix, recalled H0 helix, and hence are termed as N-BAR domain proteins. Amphiphysin and endophilin, which are both key players in the CME, are members of this subgroup. Besides, endophilin carries an additional amphipathic helix within its BAR domain. Furthermore, BAR domain proteins can also have an additional membrane binding domain. APPL1 (Adaptor Protein, Phosphotyrosine Interaction, PH Domain And Leucine Zipper Containing 1), taking part in the regulation of cell proliferation, contains a PH domain next to the BAR domain. Furthermore, BAR domain proteins like sorting nexin (SNX) proteins, participating in tubular-based endosomal sorting, contain a PX domain. PH and PX domains are special phosphoinositide binding motifs, enabling interaction with specific membranes in the cell[45]. In comparison to other BAR types, all classical BAR domain proteins can induce the highest positive curvatures due to their strong intrinsic curved

shape.
F-BAR domain proteins are another type of the BAR superfamily (Fig. 1.4). F-BAR domains contain an N-terminal Fes/CIP4 homology (FCH) domain belonging to a larger BAR-like domain [57]. In contrast to classical BAR proteins the crescent BAR shape of F-BAR proteins is elongated and the intrinsic curvature is more shallow [44]. The intrinsic crescent shape of F-BAR proteins can be from almost planar like in FCHO (Fes/CIP4 homology domain) to rather high curved (syndapins) [94]. Hence, this family can generate a broader range of positive membrane curvatures. They are the largest and most versatile BAR family and can be further divided into six subfamilies [95]. Like other BAR proteins, F-BAR proteins can contain an additional domain like a SH3 domain being seen in the CME involved proteins CIP4 (cdc42-interacting protein 4), FBP17 (formin binding protein 17) or Toca-1/FNBP1L (formin binding protein 1-like) [57,88].
I-BAR (Inverse-BAR or IM (IRSp53/MIM homology) BAR) proteins have a convex curved curvature (Fig. 1.4), being in contrast to the concave membrane binding surface of classical BAR or F-BAR proteins [96]. Therefore I-BAR proteins like IRSp53 (insulin receptor tyrosine kinase substrate p53) and MIM (metastasis suppressor protein 1) induce negative curvature within the cell and play a role in membrane protrusion and formation of lamellipodia and filopodia [97]. A special form of I-BAR domain proteins is the Pinkbar domain, which has no intrinsic curvature. Thus, Pinkbar is not able to induce membrane curvature but instead generates planar membrane sheets [98].

1.2.2 Mechanism of membrane bending by BAR domain proteins

The crystal structure of all resolved BAR proteins (except of Pinkbar) revealed the intrinsic crescent shape of the BAR domain dimer. The form of this curved shape makes it possible that BAR proteins sense, induce and stabilize membrane curvature by using the membrane bending mechanism of scaffolding and hydrophobic insertion [4,41].
The BAR domains have the basic requirements, which are needed to remodel membranes by the scaffolding mechanism. BAR domains are able to recognize membranes via electrostatic interactions between its positively charged curved surface and the negatively charged headgroups of the membrane lipids [26,43]. First of all this membrane-binding interface makes it possible to interact with the membrane. Next, the BAR domains can apply the scaffolding mechanism to induce membrane curvature. The BAR domain dimers are stable and have an intrinsic rigid crescent shape, which is forcing the membrane to mold according to its profile [4,46]. In addition, the membrane-binding interface area should be large enough to force its shape to the membrane [41]. It was calculated that the energy release of one BAR domain binding to the membrane is not enough for the deformation of the bilayer. More than one BAR domain has to assemble on the membrane surface to induce membrane remodeling [41,99]. For many BAR proteins like endophilin, SNXs, APPL, CIP4, FBP17 it was shown by biochemical or cryo-electron microscopy (cryo-EM) analysis that BAR proteins self-assemble on the membrane surface to generate

deformation.[70,88,100–104]. Moreover, the cryo-EM structure analyses proposed that the neighbouring BAR proteins of the self-assembly are connected with each other, leading to a organized BAR lattice[70,88,103,105]. Next to the BAR "scaffolding", the hydrophobic insertion mechanism, being also called "wedging", can bend membranes by inserting a amphipathic domain into the membrane[26,27,31,106]. The amphipathic motifs can sense already positive curved membranes due to easy embedding between the displaced lipid headgroups[46]. Due to biophysical experiments it was shown that the H0 helix is only ordered in the presence of lipids[43,107,108]. Computational and biochemical experiments displayed that the amphipathic motif of amphiphysin and endophilin, being N-BAR proteins with an H0 helix, seems to be inserted during membrane remodeling[26,46,89,109]. The insertion of the amphipathic wedge into the membrane is strengthening the membrane protein interaction. Moreover, the anchoring of the BAR domain to the membrane by the amphipathic motif contributes to the interaction of further BAR proteins and the formation of an BAR self-assembly on the membrane surface.

1.2.3 Examples of BAR scaffolding on membranes by cryo-EM

For the tubulation of membranes, BAR domain proteins use the scaffolding mechanism by polymerizing into a helical protein assembly around the tube membrane surface. Studies of the F-BAR domain proteins CIP4 and FBP17 demonstrated that the molded F-BAR-mediated tubes were generated and stabilized by a helical F-BAR assembly, where adjacent F-BAR dimers are connected by extensive lateral and tip-to-tip interactions[88,103]. Moreover, different degrees of membrane curvature and consequently, various tube diameters via the helical F-BAR domain packing can be achieved by a rotation of the F-BAR dimer along its longitudinal axis.
The ACAP1 (Arfgap with Coil coil, Ankyrin repeat, and PH domain protein 1) BAR-PH domain deforms membranes in its very particular way[110]. The BAR domain alone cannot interact with membranes and thus, cannot induce membrane curvature due to a relatively weak electrostatic interaction. For membrane binding and molding the neighboring PH domain is needed. To form a tubular shape, ACAP1 BAR-PH uses three main interaction interfaces within the lattice. First, two BAR dimers form a tetramer with a 2-fold symmetry, looking like a elongated banana-like shape (arch) and each end is interacting with the membrane by one PH domain. Of the tetramer two PH domains are membrane bound and the other two are not. For the helical assembly of ACAP1 BAR-PH on the membrane surface, the ACAP1 BAR-PH tetramer interacts laterally with another tetramer by an end-to-arch interaction. One tetramer end is embedded in the membrane blow the neighbouring tetramer arch. Moreover, the free PH domain of one tetramer binds to the arch of the adjacent tetramer. All three interfaces are necessary to induce curvature and stabilize the remodelled tubes.
The helical assembly of endophilin N-BAR on the tube surface shows another BAR protein packing[70,100]. The N-BAR lattice displays no lateral interactions between the

neighbouring BAR domain dimers. Due to this the BAR assembly is rather lose and membrane areas without protein covering are exposed. The N-BAR lattice stabilize itself likely by the membrane embedded N-terminal amphipathic helix, anchoring the BAR domain to the tube membrane. To stabilize the helical lattice, two amphipathic helices of BAR dimers of neighbouring lattice rows are forming anti-parallel, non-specific interactions. In contrast to F-BAR proteins, which are only scaffolding on the tube surface, N-BAR proteins seem to disturb the membrane integrity by remodeling small vesicles out of the formed tubes. So far, it was not known how the helical packing of amphiphysin N-BAR, having a similar N-BAR crystal structure like endophilin [26,43], is organized and if the N-BAR domains of endophilin and amphiphysin show a similar packing within the same BAR class like observed with the F-BAR proteins CIP4/FBP17.

1.3 Amphiphysin

1.3.1 Biological overview

Amphiphysin is a N-BAR domain protein containing a N-terminal amphipathic helix H0, a BAR domain, following central region domains and an C-terminal SH3 domain. The amphiphysin N-BAR domain monomer is a kinked three α-helical coiled-coil, forming a crescent shaped dimer. The positively charged concave dimer surface interacts with the negatively charged lipids in the membrane by electrostatic interactions. The N-terminal amphipathic helix is predicted to be ordered when interacting with the membrane by acting like a wedge [43]. Amphiphysin is involved in membrane remodeling processes *in vivo* such as endocytosis or T-tubule formation in myocytes and can induce high-curvatures of 20 to 50 nm , corresponding to the banana-shape of its N-BAR domain.
In the case of endocytosis, being a dynamic process where vesicles are formed, amphiphysin isoforms form the neck connecting the formed vesicle to the membrane. In T-tubule formation another amphiphysin isoform is remodeling membranes into stable tubular structures. For the N-BAR domain proteins amphiphysin and endophilin it was observed that they are able to form bilayer tubes with a variety in their diameter, micellar tubular structures as well as small highly curved vesicles *in vitro* [43,47,70,100,109]. Amphiphysin is able to mold tubes from liposomes *in vitro* [47]. The process of forming tubes from membranes is called "tubulation". The amphiphysin N-BAR protein is using the scaffolding and hydrophobic insertion mechanism to remodel membranes into different grades of positive curvature. Moreover, it was observed that N-BAR domains are polymerizing into a helical protomer around the membrane surface to form tubes [47,70,100].
Characteristic for the amphiphysin protein family is the N-terminal N-BAR domain, being conserved from yeast, *Drosophila* to human. In addition, the C-terminal SH3 domain is conserved in most isoforms of the amphiphysin family. Mammalian amphiphysin I and amphiphysin II/BIN1 isoforms are expressed in the brain and nervous system [111–113].

They are involved in pre-synaptic endocytosis by interacting with other key players of the CME such as clathrin and AP-2 (adapter protein complex 2) by the central CLAP domain (clathrin and adaptor binding domain) or synaptojanin and dynamin by the SH3 domain [47,90,114]. A special isoform of mammalian amphiphysin II BIN1 is expressed in the skeletal muscles where it takes part in T-tubule formation. *Drosophila* amphiphysin resembles rather an orthologue of the muscle BIN1 isoform as it is essential for the T-tubule formation and redundant for the synaptic vesicle endocytosis [49,115,116].

1.3.2 Mammalian amphiphysin I and amphiphysin II/BIN1 isoforms

1.3.2.1 Amphiphysin I

Human amphiphysin 1, being a homologue to the first identified chicken amphiphysin 1, was discovered as a 128-kDa synaptic vesicle associated protein and as auto-antigen in breast cancer with stiff-man syndrome [117–119]. Human amphiphysin 1 is highly enriched in brain tissue and nervous system and localizes to punctate presynaptic termini [117,120,121]. In addition, several amphiphysin I transcripts were also found in specific other tissues such as testis, ovary, pancreas, adrenal gland and pituitary [118,121,122]. 6 isoforms are known for amphiphysin I, which are the brain amphiphysin I (695 residues), one non-neuronal expressed amphiphysin I (653 residues with deletion of residues 425-466) and 4 retina specific amphiphysin Irs (amphiphysin Irs-1 is 179 residues, Irs-2 is 276 residues, Irs-3 is 580 residues and Irs-4 is 174 residues) [123,124].
It was shown that amphiphysin I plays a role in CME by colocalizing and consequently interacting with dynamin I. Dynamin I is a GTPase, being involved in synaptic vesicle endocytosis, with a PRD, which is interacting with the SH3 domain of amphiphysin [47,120]. In addition, the SH3 domain of amphiphysin I binds N-WASP (neuronal WiskottâĂŞAldrich Syndrome protein) to facilitate an actin linkage and synaptojanin, being also key players in CME [125–127]. Moreover, the CLAP domain of amphiphysin interacts with clathrin and AP-2, which are involved in formation of CCPs and the clathrin cage [111,128]. During CME, amphiphysin I plays a role for the dynamic curvature formation at the neck of the budding vesicle, connecting it to the plasma membrane, before the dynamin I scission process. The PRD of amphiphysin I is interacting with the SH3 domain of the other neck forming N-BAR protein endophilin [129]. It was observed that at the formed neck, endophilin is closely located to the vesicle and amphiphysin is occupying the elongated neck between vesicle and plasma membrane [130]. There are several hints that amphiphysin I plays a role in the fission process of the CME. It is located at the neck where it helps to localize the scission protein dynamin I so that the fission can take place [128,131,132]. Amphiphysin I is coordinating the membrane remodeling with other endocytosis proteins like clathrin, endophilin and dynamin [42,133]. Due to the relevance of amphiphysin I at the neck and in the fission process it is predicted that it attends the CME at the late stage [133].

In addition, amphiphysin I is also contributing to other cellular processes next to endocytosis. Some of these processes are connected to the cytoskeleton network where it was shown that amphiphysin proteins are able to modulate the actin and microtubulin network[134–136]. It is suggested that amphiphysin I is necessary for cellular phagocytosis by playing a role in the actin polymerization. It was shown that during phagocytosis actin-rich structures like ruffles, phagocytic cups and phagosomes are formed where amphiphysin I accumulates, too. Amphiphysin I can interact with the actin regulator N-WASP by its SH3 domain and thus, it can regulate the dynamics of the actin polymerization. It was also observed that in amphiphysin 1 (-/-) Sertoli cells phagocytosis was noticeable diminished[134].

1.3.2.2 Amphiphysin II/BIN1

Next to amphiphysin I, amphiphysin II/BIN1 is expressed in mammals. Amphiphysin II, also known as BIN1, was first identified to interact with the c-Myc transcription factor due to its Myc-binding domain (MBD)[137–139]. Amphiphysin II contains several alternative spliced isoforms contributing to a complexer expression and to more functions as amphiphysin I[140]. Some amphiphysin II isoforms are either expressed in specific tissues or ubiquitously expressed. The amphiphysin II isoforms, which are expressed in brain and nervous system, are similar to amphiphysin I and thus, localize and play a role in endocytosis, too. Other amphiphysin II/BIN1 isoforms, which are expressed in other tissues, are lacking brain specific domains and therefore, they are not involved in endocytosis[112,113,137,141–143]. It was shown that via the N-terminal BAR domain, amphiphysin I and amphiphysin II form a heterodimer, whose predominantly form is found in the brain[122,144]. In amphiphysin I knocked out mice, amphiphysin II is almost missing although the amphiphysin II mRNA level is normal[122]. Amphiphysin I is necessary to stabilizes the brain expressed amphiphysin II. In addition, electrophysiological studies showed that endocytosis was only slightly reduced because less clathrin, AP-2 and dynamin was located to the membrane. This gave a hint that amphiphysin plays an important role in the recruitment and orchestration of several endocytic components.[145]. BIN1 isoform 8 is highly expressed in skeletal muscles and is involved in the formation of T-tubules[112,146]. The muscle sarcolemma membrane of skeletal and cardiac muscles cells is invaginated to form ion channel enriched T-tubules, which are required in the excitation-contraction coupling machinery (Fig. 1.5, 1)[147]. BIN1 homozygous knocked out mice show a disorganization in severe cardiac muscles due to loss of the maintenance of the T-tubule system[148]. Moreover, in muscle BIN1 the interaction site of clathrin and AP-2 is absent but instead it contains a polybasic sequence (exon 11, NCBI nomenclature), which interacts with PIPs on the plasma membrane and improves the membrane binding due to a stronger electrostatic interaction[112,113,149]. It was shown that the SH3 domain of BIN1 autoinhibits BIN1 by interacting with the exon 11 sliced PI binding motif[150,151]. $PI(4,5)P_2$, being enriched in the membrane, is interrupting the autoinhibition by binding

to the PI binding motif, making it possible for the SH3 domain to interact with a PRD binding partner like dynamin 2 [151].

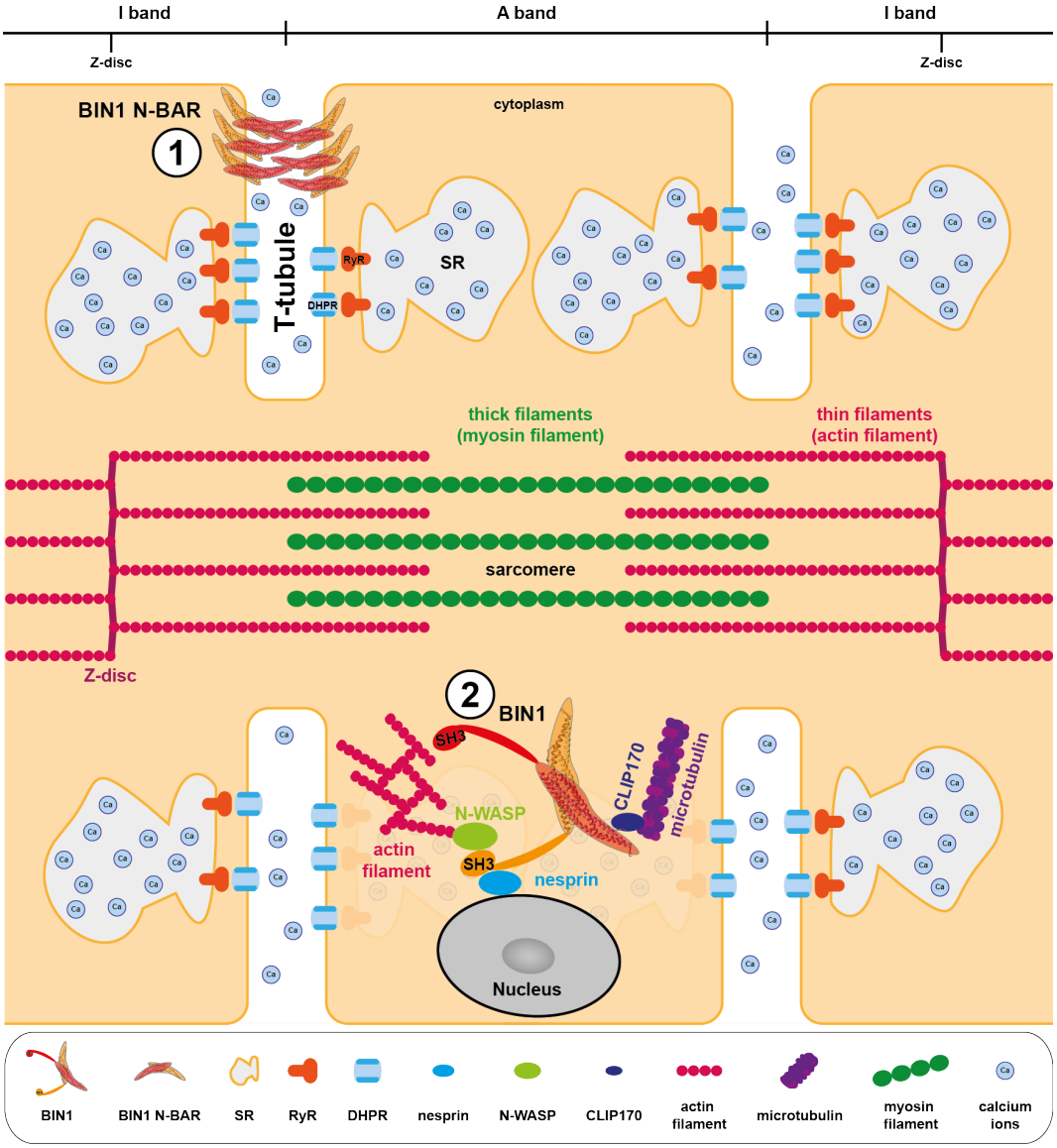

Figure 1.5 – BIN1 in skeletal muscles | (1) BIN1 plays a role in the biogenesis and stabilization of T-tubules. (2) BIN1 regulates the nucleus positioning and shape by linking the nuclear envelope via nesprin to the microtubule and actin cytoskeleton by CLIP-170 and N-WASP, respectively. SR = sarcoplasmic reticulum, RyR = ryanodine receptors, DHPR = dihydropyridine receptor

Furthermore, for muscle BIN1 it is proposed that it modulates the nucleus positioning and shape by annexing the nuclear envelope (NE) to the microtubule and actin cytoskeleton (Fig. 1.5, 2) [136]. An altered nucleus position was found in the muscular disorder centronuclear myopathy (CNM) where mutated muscle BIN1 is involved [149,152,153]. It is suggested that BIN1 binds nesprin, being an NE protein, and orchestrates the positioning of the nucleus by linking nesprin with the MT plus ends [136]. BIN1 interacts with

microtubules by binding to the coiled-coil region of CLIP-170, which is stabilizing the plus-end of MT, via its BAR domain [135,136]. In addition, by binding actin BIN1 possibly fine tunes the linkage between the actin cytoskeleton to the nuclear envelope. Actin is bound to the SH3 domain of BIN1 [136].
Furthermore, isoforms of BIN1 are involved in apoptosis and DNA repair. The BIN1 Myc-binding domain of some isoforms binds to the MB1 domain of c-Myc. C-Myc is a transcription factor, having a basic helix-loop-helix-leucine zipper structure, and is essential in apoptosis, cell growth and malignancy [137]. Apoptosis can only be activated by BIN1 isoforms such as isoform 9 if they are located in the nucleus [113,138,143,154]. BIN1 inhibits the nuclear function of c-Myc, which in some cases leads to apoptosis [137,155]. It was observed that overexpression of BIN1 only induces programmed cell death in malignant cells [156,157]. In tumor cells a decreased level of BIN1 is found [137,154,156,158,159]. C-Myc in transformed cells can suppress BIN1, promoting easier cell transformation [160]. In addition, BIN1 is contributing to DNA repair by inhibiting poly (ADP-ribose) polymerase 1 (PARP1) [160,161]. PARP1 is a key player in the base excision repair pathway [161]. BIN1 interacts with PARP1 via its BAR domain [160,161]. Reduced level of BIN1 in cells with cisplatin, being a DNA-damaging chemotherapeutic agent, activates c-Myc and PARP1, induces DNA repair and hence, suppresses cell death [160]. Amphiphysin I and II/BIN1 are involved in several cellular processes. Hence, they have a medical relevance as they are linked to several diseases connected to cancer, myopathies, heart failure or late-onset Alzheimer's disease [162,163]. For the muscle BIN1 isoform 8 an orthologue is found in *Drosophila* which is also involved in T-tubule formation.

1.3.3 Amphiphysin in *Drosophila*

In *Drosophila* only one gene encoding amphiphysin is found. Three *Drosophila* amphiphysin isoforms are expressed and found throughout the body like in muscles, being involved at the T-tubule network, neuronal cells, the postsynaptic membrane of the neuromuscular junction (NMJ), photoreceptor cells and in epithelial cells [49,115,116]. Amphiphysin contains the N-BAR domain, some central region domains without CLAP or PRD domain and the C-terminal SH3 domain. It is suggested that postsynaptic NMJ expressed amphiphysin is necessary for the orchestration of several postsynaptic proteins but not for endocytosis by recycling synaptic vesicles [116]. As *Drosophila* amphiphysin misses the CLAP and PRD domain it can not interact with endocytotic relevant proteins such as clathrin, AP-2 or endophilin. Moreover, it was shown that the SH3 domain is binding to vertebrate but not to *Drosophila* dynamin. This is probably due to the lack of the specific amphiphysin SH3 binding motif (PxRPxR) in the PRD of *Drosophila* dynamin. In addition, amphiphysin is enriched at postsynaptic and not presynaptic membranes [49,115,116]. Amphiphysin mutations have a phenotype of viable and fertile flies but they show a locomotive defect by being sluggish and flightless. These flies do not show any defects in endocytosis. Even though *Drosophila* amphiphysin is expressed in

neurons it seems not to be involved in synaptic vesicle endocytosis [49,115,116]. It is likely that other *Drosophila* proteins such as DAP-160, which orchestrates several endocytic proteins and recruits dynamin, are involved in invertebrate endocytosis [164].
It was proposed that *Drosophila* amphiphysin, being found at glutamatergic larval NMJ, plays a role in the postsynaptic exocytosis by being involved in SNARE-dependent postsynaptic Fasciclin II (FasII) membrane cycling [165]. Amphiphysin mutants showed a lower level of postsynaptic external FasII at the NMJ although the total FasII concentration stayed constant. This suggests that invertebrate amphiphysin may have a function in exocytosis and vertebrate amphiphysin in endocytosis [165]. In the cases of endocytosis as well as exocytosis, which use distinguish subsets of involved proteins, membrane deformation is needed to perform ether fusion or fission. This may explain why amphiphysin could play a role in exocytosis, too.
One of the main functions of amphiphysin in *Drosophila* is its involvement in T-tubule formation and consequently the organisation of the excitation-contraction coupling machinery in muscles (Fig. 1.5, 1). Amphiphysin mutant flies are viable and fertile and have no significant defect in neurotransmission but they show a slowed down locomotion in their larvae state and as adults they are not able to fly [49,115]. These flightless flies have a disorganized T-tubule and sarcoplasmic reticulum system (T-SR) with a reduced, mislocalized and altered T-tubule and T-SR junction formation. In the mutant the developed T-tubules and T-SR junctions had a larger sizes than the wild type. The T-tubules and consequently, the ability to fly could be rescued by expressing wild type amphiphysin in their muscles [49]. This showed that the changed locomotion behavior in the mutants flies is caused by the altered T-tubule network resulting in a loss of the muscle excitation-contraction machinery. Expression of the human orthologue muscle BIN1 in myoblastic C2C12 cells resulted in a generation of T-tubule like invaginated structures of the plasma membrane within the cell [146]. Moreover, it was seen that the human orthologue is not colocalizing with clathrin [166]. This all indicates that the membrane deforming protein *Drosophila* amphiphysin is playing a role in the tubulogensis of T-tubules.
In a recent study it was proposed that during cellularization in *Drosophila* embryos amphiphysin is needed for the formation of tip-tubules at cleavage furrows on schedule [167]. For the formation of new columnar epithelial cells each nucleus has to be surrounded by a ingression of plasma membrane cleavage furrows [168]. During this process cleavage furrow ingression is taking place with contribution of the endocytic and possible the exocytic pathway [167,169]. Cleavage furrow tips (CFT-tubules) are formed at the end of the ingressed cleavage furrows. One type of CFT-tubule remodeling requires the BAR domain of amphiphysin. Loss of amphiphysin resulted in an higher rate of furrow ingression. Even with the prevention of CFT-tubule remodeling ingression of the cleavage furrow occurred, meaning that amphiphysin is not necessary for the membrane molding to form ingression. Amphiphysin is located at the tip end of the cleavage furrows and

it is possible that it acts like a negative regulator for membrane ingression. Variantly, without CFT-tubule formation more plasma membrane is accessible to form furrow ingression, fitting to the higher rate of ingression in amphiphysin mutant flies. This results goes in hand with the observation that the membrane regression rate is reduced when CFT-tubules become longer due to *Drosophila* dynamin depletion. This means that the CFT-tubules and consequently amphiphysin is regulating the accessible plasma membrane for efficient cleavage furrow ingression. It is still not clear yet if these CFT-tubules are specifically remodelled tubular structures like T-tubules or if they are a result of a specific endocytotic process [167].

1.3.4 Domain organization and protein organization of mammalian BIN1 and *Drosophila* amphiphysin

Amphiphysin 1 and amphiphysin 2/BIN1 have a sequence homology of 49% [170,171]. The gene of amphiphysin II/BIN1 has 20 exons, resulting into various isoforms due to alternative splicing. Exon 1 - 10 encodes the N-terminal N-BAR domain with its known crescent BAR banana-shape [43,45]. The N-BAR domain is found in all isoforms [112,137,140,170]. Afterwards the exon 11 encodes a polybasic sequence, being a PI-binding motif, and it is only spliced in muscle BIN1 [112,113,146,149]. The expressed exon 11 enhances the capability of BIN1 to bind to PI(4,5)P_2 enriched membranes and to remodel T-tubules [146,153]. The CLAP domain is defined by the neuronal spliced exon 13 - 16 [112,142,154,172]. Only brain enriched amphiphysin 2 is having this domain to bind to the endocytic proteins clathrin and AP-2 [173]. Exon 17 and 18 encodes the Myc-binding domain and is found in all isoforms [112,137,142,154,170,173]. Alternative splicing of exon 17 leads to the loss of binding to c-Myc [113,143]. In all isoforms the C-terminal SH3 domain is spliced by exon 19 and 20. The SH3 domain interacts with the cytoskeleton and other possible binding proteins with a PRD domain like dynamin I and II [122,174,175]. The SH3 domain of amphiphysin I and II is rather special because it has a large patch of negative electrostatic potential and an exceptional n-Src loop [171]. Miss splicing of exon 13 is often connected with cancer such as melanoma due to a missing binding of c-Myc to BIN1 [154]. It has been shown that defected splicing of exon 7 and 11 is associated with myotonic dystrophy [153,166]. In addition, several mutations in the BAR or SH3 domain are found in myopathies and myotonic dystrophy (DM) [149,176]. CNM related mutations in the SH3 domain of BIN1 can influence the confirmation of BIN1 and consequently the binding to dynamin [149,150]. The function of BIN1, and in which tissue it is expressed, is modulated by the splicing of specific exons. Moreover, a differed exon splicing could lead to a changed protein-protein interaction. An altered splicing of exon 7 in the BAR domain may affect the protein-protein binding with dynamin [172]. In addition, muscle enriched BIN1 is also regulated by autoinhibition. The BAR domain with the exon 11 encoded PI-binding motif binds intramolecular to the SH3 domain [150,151,177]. In the "closed" state the SH3 domain of

BIN1 can not interact with its interaction partners. Binding of PI(4,5)P_2, being enriched in specific membranes, to the PI-binding motif leads to an "open" conformation so that the BAR domain can bind and remodel the membrane and the SH3 domain can interact with its interaction partners such as dynamin[151]. Furthermore, amphiphysin I and consequential, amphiphysin II/BIN1 are regulated by phosphorylation[178–181].
Around 30% of *Drosophila* amphiphysin is identical with rat amphiphysin I and II. The N-BAR domain of *Drosophila* with the N-BAR domain of vertebrate amphiphysin I and II shows an identity of ~38% and a similarity of ~60%[115]. *Drosophila* amphiphysin is encoded by 10 exons. The N-BAR domain, being encoded by exon 1 - 6, is shaped like a banana and could interact with membranes via electrostatic interactions. The central region is spliced by exon 7 and 8 and is poorly conserved between vertebrates and invertebrates[115]. The CLAP domain of amphiphysin I and some amphiphysin II isoforms is missing in *Drosophila*[49,115]. This shows that *Drosophila* amphiphysin is rather an orthologue of the mammalian muscle BIN1[90]. Moreover, in the central region a new conserved sequence between *Drosophila* and mammalian amphiphysin 2 was identified. But on the contrary this specific conserved sequence was not found in the BIN1 splice variants. This region between residues 363 to 398 is spliced by non-variable part of exon 8[115]. The C-terminal SH3 domain is encoded by exon 9 an 10 and is to ~60% identical with the SH3 domain of vertebrate amphiphysin 1 and 2[115]. The *Drosophila* amphiphysin SH3 domain contains the specific large patch of negative electrostatic potential and the exceptional n-Src loop just like the SH3 domain of mammalian amphiphysin I and II/BIN1[115,116,171]. In *Drosophila* five isoforms were identified[115]. One is the full-length amphiphysin with 602 residues. The other isoforms are different because of alternative splicing within exon 8 before or after residues 363 to 398. In addition, the shortest isoforms have a shorter 3' UTR because of polyadenylation at a cryptic side, being 120 bp after the stop codon. The following amphiphysin isoforms of 502 residues (amphiphysin-B1), 502 residues with a shorted 3' UTR (amphiphysin-B2), 522 residues (amphiphysin-C1) and 522 with a shorted 3' UTR (amphiphysin-C2) are expressed. The expression of *Drosophila* amphiphysin is regulated by alternative splicing. Several phosphorylation sites are found in *Drosophila* amphiphysin[182], which may be phosphorylated like mammalian amphiphysin or BIN1[178,180,181,183,184].

1.3.5 Mammalian BIN1 and *Drosophila* amphiphysin in T-tubules

1.3.5.1 T-tubules

Transverse tubules are only found in striated muscle types like skeletal and cardiac muscles and they are essential for the excitation-contraction (EC) coupling machinery[185]. To trigger synchronous contraction of the striated muscles, the incoming action potential by a nerve has to be transmitted to the muscle contraction force of the myocytes. This is mediated by the EC coupling machinery by translating the incoming neural action

potential signal into intracellular calcium release, leading to muscle contraction due to the actin/myosin force apparatus in muscle fibers. The action potential triggers the calcium channels in the T-tubules to facilitate the initial calcium entry into the muscle cells[185]. Inside the myocytes the T-tubules are associated with sarcoplasmic reticulum (SR), containing closed ryanodine receptors (RyR)[186–188]. An intracellular local increase of calcium by T-tubules activates the RyR and a large amount of calcium, being stored in SR storage, is released into the myocyte cytoplasm[189]. Afterwards, the cytosolic calcium binds to Troponin C of the actin filaments, resulting in cellular contraction[190–192].
T-tubules are highly branched invagination of the sarcolemma, which is the plasma membrane of myocytes, and they have an enrichment of calcium channels on the surface[193,194]. In skeletal and cardiac muscles these voltage gated channels are known as Dihydhrophyridine Receptors (DHPR) and L-type calcium channels (LTCC), respectively[185,195,196]. T-tubules are basically transverse to the longitudinal axis of the myocyte and wrap around and between myofibrils[194]. In addition, as T-tubule are a branched network they also show longitudinal extension, which could compromise around 40% of the whole T-tubule volume.[194,197,198]. The T-tubule system in cardiac muscles has a large membrane surface, which is corresponding to up to ~20 to 60% of the sarcolemma[194,199,200]. The T-tubule diameter in skeletal muscles is ~20 to 50 nm , being less heterogeneous than the cardiac muscle T-tubules with an overall diameter average of ~100 to 300 nm (range 20 to 450 nm)[194,201–203]. T-tubules are linked to the SR via an area called terminal cisternae or junctional SR. In skeletal myocytes several T-tubule are associated to two surrounding terminal cisterna (Fig. 1.5), named triad, and they are located at the junctional overlap between the A and I band (at each side of the Z-line) of the sarcomere[204,205]. In contrast T-tubules of cardiac muscle cells are affiliated with only one terminal cisterna of the SR, named dyad, and they are found at ~1.8 µm-intervals along the longitudinal axis of the cell and hence, locate approximately at every Z-line of the sarcomeres[194,206]. Along the Z-line, the distance intervals of the T-tubules is ~1.2 µm[206]. T-tubules have the important function to bridge calcium transients into the interior of myocytes for effective EC coupling[196].
During the T-tubule biogenesis and triad/dyad (skeletal and cardiac, respectively) formation and maintenance several proteins like muscle BIN1[146,207,208], caveolin-3 (CAV3)[147,209], junctophilin-1/2 (JPH1/2)[210] and dysferlin (DYSF)[211,212] are involved to remodel and stabilize the T-tubule network. BIN1, CAV3 and DYSF are contributing to the T-tubule biogenesis. Junctophilin-2 is playing a role in the triad/dyad formation. Caveolin-3 is associated with the sarcolemma of striated muscles cells and forms flask-like shaped invagination, called caveolae, being involved in the regulation of signal transduction events, by interacting with C2 domain membrane deforming protein dystrophin and its belonging glycoproteins[213–215]. CAV3 knocked down mice lead to disorganization of T-tubules due to dilated tubules and loss of their transverse orientation[209,215]. This suggest that CAV3 is involved in the biogenesis of T-tubules by temporary associating to

the developing T-tubules and additionally, it is also likely that CAV3 contributes to the early development of T-tubules [215–217].
Dysferin, containing several C2 membrane remodeling domains, is localized to the sarcolemma and contributes to membrane fusion and repair [218,219]. It was observed that DYSF colocalizes to the T-tubule membrane where it is involved in the maintenance of Ca2+ homeostasis during mechanical stress to protect T-tubules from damage [220–222]. DYSF is associated to DHPR/LTCC channels in the T-tubules and localizes to the T-tubule associated triad/dyad [222,223]. Depletion of DYSF results in a similar T-tubule disorganization as seen in CAV3-deficient muscles [218]. This shows that dysferin plays a role in the development and maintenance of T-tubules [218,221,223,224].
Junctophilin-2 is linking the T-tubule membrane to the SR by its N-terminal domain and C-terminal transmembrane domain, respectively, to form the triad/dyad. The N-terminal T-tubule binding domain can interact with the membrane phospholipids such as sphingomyelin and phosphatidylcholine [210,225]. Depletion of skeletal muscle JPH1 in mice leads to a quick death because of jaw muscle defect, leading to the inability to drink milk [226]. Moreover, morphological abnormalities of the triads are found and consequently, defects in the muscle contraction occur [226,227]. JPH2 is also found in cardiac muscles, being implicated in hypertrophic cardiomyopathies [225,228]. JPH1/2 are not directly involved in the maintenance and biogenesis of T-tubules structures [210].

1.3.5.2 Mammalian BIN1 in T-tubules

BIN1 isoform 8 is specifically expressed in skeletal muscles and is involved in the biogenesis of T-tubules [146,173]. In the cardiac muscles specific BIN1 isoforms as BIN1 + 13 and BIN + 13 + 17 are found. The BIN1 + 13 + 17 isoform, containing exon 13 and 17, is the main cardiac BIN1 isoform and involved in the biogenesis of T-tubules [207]. The cardiac as well as the skeletal BIN1 are also referred as BIN1 or muscle BIN1. The polybasic sequence (encoded by Exon 11), binding to the PIPs such as $PI(4,5)P_2$, is crucial to locate BIN1 to the T-tubule membranes [146,173]. During C2C12 myotubes differentiation it was observed that the concentration of $PI(4,5)P_2$ increases simultaneously with the level of BIN1 [143,146]. The binding to $PI(4,5)P_2$ enriched membranes leads to a conformational change of BIN1 so that the BAR domain binds to the membrane and the SH3 domain to its interaction partners like dynamin 2 [151,177]. BIN1 mutants with a depletion of the PI-binding sequence show no tubular network formation in myotubes [177]. Mutations of BIN1 in skeletal muscle can lead to several different diseases such as CNM with non-progressive muscle weakness (onset at birth or infancy) [149,176,229] and myotonic dystrophy with progressive muscle wasting, heart conduction defects, myotonia and cataracts. BIN1 mutations or decreased BIN1 expression in the cardiac muscle can lead to cardiovascular disorder such as ventricular arrhythmia [207,230,231], heart failure [208,230,232].
BIN1 plays several roles in the maintenance and biogenesis of T-tubules. First of all it is a N-BAR domain membrane remodeling protein and hence, the N-BAR domain of BIN1

remodels the sarcolemma to form T-tubules[146]. Next to the membrane remodeling, BIN1 is also involved in several more task at the T-tubules. For BIN1, being localized at the cardiac T-tubules, it is suggested that it is localizing the $Ca_v1.2$ channels (subunits of LTCC channel) to the T-tubules where they are clustered in a close distance to the SR and the RyRs[233]. Moreover, it was observed that BIN1 also helps to target the calcium channels to the T-tubules by regulating the LTCC trafficking via microtubule binding. $Ca_v1.2$ vesicles are transported by MT, which are tethered to the T-tubule membrane by BIN1, from the trans-Golgi to the T-tubules[230,233]. BIN1 knocked down mice show a lower level of T-tubule membrane integrated $Ca_v1.2$ channels, leading to reduces concentration of transient calcium, being important for the EC coupling and the mammalian cardiac contractility[208,230,233]. This revealed that BIN1 is not only able to induce membrane curvature in T-tubules but in addition is involved in the trafficking of membrane proteins, being transported by microtubules. Vesicles of $Ca_v1.2$ channels a specifically delivered to the T-tubule membrane by BIN1 and not by the T-tubule overall structure.
In addition, in cardiac T-tubules, showing a highly restricted ion diffusion near the T-tubule sarcolemma ("fuzzy space")[234–237], BIN1 (cardiac BIN1 + 13 + 17 isoform) forms T-tubules with actin-organized dense protective inner membranes microfolds[207], also seen as torturous frequent hairpin bends or membrane infolds[238,239]. BIN1 promotes actin polymerization via N-WASP binding and activation, which anchors and connects those microfolds to the alpha-actin of the myofilament. Inside the T-tubule system microfolds generate an ion diffusion barrier by caputuring extracellular ions. This slow diffusion areas, being formed by the microfolds and close to the SR, are one of the characteristics of cardiac T-tubules. BIN1 depletion in mice results in smooth T-tubule without torturous tubule structure, resulting in a free calcium and potassium ions diffusion, and consequently, in an extended action potential duration, which could lead to arrhythmia. The microfolds are physical diffusion barriers to shield from high concentrations of extracellular ions. This observation could clarify why the ion level within T-tubules can be different to the extracellular surrounding so that the electrical stability can be maintained[207]. In skeletal muscles of zebrafish ultrastructures within T-tubules were found[240]. This could lead to the assumption that skeletal BIN1 is also able to form microfolds at T-tubules.

1.3.5.3 *Drosophila* amphiphysin in T-tubules

In *Drosophila* amphiphysin is a mammalian BIN1 orthologue and is found at the post-synaptic membranes of neuromuscular junctions where it is localized at the T-tubules of skeletal muscles such as larval body wall muscles and adult flight muscles[49,115,116]. Deletion of amphiphysin in *Drosophila* results in viable and fertile but flightless flies with a general sluggish locomotion[49]. As the flies are flightless the most detailed study by Razzaq[49] was done in the indirect flight muscles (IFM) of *Drosophila*, which can

contract up to 300 Hz. In the IFM, T-tubule develop a large branched T-tubule network which is located midway between the myosin anchored M and the actin anchored Z line of the sarcomere and forms dyadic and occasionally triadic junctions to the SR. In Drosophila the dyads are located alongside the sarcomere and midway between the M and Z line. From the longitudinal axis of the myofibril it was observed that the branches of the T-tubule network are transverse and longitudinal extended from the dyads. This observations are compatible with the BIN1 studies in mammalian skeletal muscles[112,193,204].

Null amphiphysin mutant flies, being flightless, show a disorganization, mislocalization and reduction of dyads and T-tubules[49]. The remaining dyads were larger than in normal flies. *Drosophila* amphiphysin plays an important role in the organization and correct formation of the T-tubule system. In the mutant flies the less formed T-tubules showed a reduction in transverse elements, which suggest that amphiphysin is involved in T-tubule branching either alone or cooperation with other T-tubule remodeling proteins. Moreover, amphiphysin seems to be involved in anchoring the T-tubules to the myofibrils, in fact, midways between the M and Z line of the sarcomeres with the help of the cytoskeleton. Depletion of amphiphysin and consequently, the loss of the myofibril anchoring by the cytoskeleton results in misplaced T-tubules and dyads. Amphiphysin plays a role in the organization of T-tubules by interacting with several proteins, being involved in the formation of T-tubules. The protein discs-large, which localizes channels and cell adhesion proteins to synapses, is found in domains in T-tubules, which partially colocalize with amphiphysin. DLG could have a similar role in T-tubules as in synapses. Moreover, for the transmission of calcium transients into the muscle cell ion channels are located into the membrane of T-tubules. In vertebrates it is known that T-tubules contain several proteins next to BIN1 such as cell adhesion, ion channels and cytoskeletal proteins[241,242]. *In vitro* tubulation of *Drosophila* amphiphysin alone shows thinner tubes as observed in *in vivo*. This supports the suggestion that several proteins and not only amphiphysin are involved in the formation of T-tubules in *Drosophila*. Without an organized T-tubule system in the flight muscles the excitation-contraction coupling is affected by an altered calcium flux into the cytosol, leading to flightless flies. Disturbed calcium dynamics in the IFMs decrease the speed, rate and synchronization of the muscle contraction. For flying a fast coordinated cycles of contraction and relaxation is needed. This revealed that *Drosophila* amphiphysin just like mammalian BIN1 plays a role in maintenance and biogenesis of the T-tubule network and that it is an important part of the EC coupling machinery.

1.3.6 BIN1 in diseases

It was observed that down-regulated or altered BIN1 expression can lead to several cancer diseases such as colon, melanoma, breast, lung and prostate cancer, neuroblastoma and hepatocarcinoma[243–246]. Miss-splicing or loss of heterozygosity of BIN1 can also

influence the development of metastasis and the cancer prognosis[154,158,159,243]. Amphiphysin2/BIN1 is contributing to the MYC and Raf pathway in the nucleus, being involved in senescence and apoptosis. BIN1 regulates the nuclear function of some MYC oncogene members and DNA repair proteins. BIN1 plays a role in the balance of proliferation and programmed cell death by apoptosis. One BIN1 isoform operates as a tumor suppressor inhibiting c-Myc[137,155]. A normal BIN1 expression level inhibits MYC-dependent cell transformation and tumor growth[137,247]. It is suggested that the loss of BIN1 in human tumors eludes the cell death, being associated with c-Myc activation, and is related to overall organ tissue inflammation and lung and liver cancer in mosaic mice[155]. Ectopic re-expression enforces the process of programmed cell death[137,154,156,158,159]. In addition, decreased level of BIN1 correlates also with cisplatin resistance in cancer cells by increasing c-Myc and PARP1 (poly-(ADP-ribose) polymerase 1) activities, which is up-regulating the DNA repair[160]. In addition, BIN1 is also involved in the regulation of N-Myc, being another oncogene of the MYC family[248]. Overexpression of N-Myc, which is usually highly expressed in neurons, is found in neuroblastoma[248–251]. In neuroblastoma cell lines it was observed that overexpression of N-Myc leads to downregulation of BIN1. If BIN1 is overexpressed the cells starts apotosis[252].

Neuronal amphiphysin II/BIN1 is a one of the most important risk loci of late onset Alzeiheimer's disease (LOAD). In LOAD BIN1 seems to be contributing to the modulation of the tau pathology as it is interacting with the microtubule-assocciated protein tau[253,254]. Depletion of amphiphysin resulted in a suppression of tau-induced neurotoxiticy[255]. Tau seems to modulate the stability of neuronal microtubules. Misfolded or altered modified tau disassociates from the MT resulting in dysfunctional neuronal MT and intracellular neurofibrillary tangles containing tau[254,256,257]. How exactly BIN1 is contributing to Alzheimer's disease (AD) is not fully understood. Maybe an interplay of different functions of BIN1 in modulating of tau pathology, endocytosis, trafficking, inflammation, apoptosis and calcium homestasis could account for AD pathogenesis[254]. Future studies will help to understand the involvement of brain enriched BIN1 in Alzheimer's diseases.

In muscles BIN1 plays a role in T-tubule formation and maintenance. *Drosophila* amphiphysin and mammalian muscles BIN1 play a role in T-tubule formation and maintenance. T-tubules are long transverse plasma membrane invagination into the muscles. Amphiphysin knock out leads to viable but flightless flies[49]. The mammalian BIN1 isoform 8 is also involved in T-tubule formation in skeletal muscles. In human BIN1 the following missense mutation K35N, D151N, R154Q in the N-BAR domain[149,229], nonsense mutations Q434X and K436X and stop mutations Q573stop and K575stop in the SH3 domain[149,258,259] and a exon 11 mutation, leading to the PI binding motif skipping[176], are involved in the autosomal rezessive neuromuscular disorder CNM, displaying in muscle weakness. The histological report reveals heightened centralized nuclei and fiber atrophy without linkage to exceeding muscle generation[176,260]. The

known mutations are not influencing the expression level of BIN1. For the mutations in the N-BAR domain and the skipping of the PI binding motif a disrupted tube formation ability of BIN1 was observed. The mutations and truncations in the SH3 domain lead to an affected intramolecular binding between the SH3 domain to the PI binding motif and binding to dynamin 2. The GTPase dynamin 2 is contributing to cytoskeleton and membrane molding and mutation in dynamin 2 are implicated in autosomal dominant CNM[261].

Misregulated alternative splicing of BIN1 is also implicated in myotonic dystrophies, being a RNA-mediated multisystemic disease with progressive muscle weakness, heart conduction defects, cataracts and myotonia[153]. DM shows similar histological features like centralized nuclei and muscle weakness. Myotonic dystrophies can be divided into congenital myotonic dystrophy (CDM1) and myotonic dystrophy of type 1 (DM1) or of typII (DM2) The cause for DM is the expression of RNAs with expanded CUG (in CDM1 and DM1) or CCUG (in DM2) repeats, which sequestrate the splicing regulator Muscleblind-like-1 (MBNL1), leading to specific altered splicing of other pre-mRNAs such as the pre-mRNA of BIN1 in skeletal muscles (found in CDM1, DM1 and DM2). MBNL1 is a splicing factor, which regulates the alternative splicing of BIN1. Misregulation of the alternative splicing of the pre-RNA of BIN1 results in an BIN1 form with altered spliced exon 11 and consequently, without PI binding motif. This BIN1 form shows a declined membrane remodeling activity of T-tubules in muscles due to the lacking of the PI(5)P binding.

Decreased levels of BIN1 in cardiac muscles result in heart and cardiac diseases such as ventricular arrhythmia and heart failure[175,210,230]. Down regulated BIN1 results in misregulation of the T-tubule functions with an altered mediation of calcium transient, which leads to an electrical instability and a changed regulation of the muscle contractility and heart rate[230]. BIN1 is responsible for the T-tubule remodeling, microtubule-trafficking of calcium channels to the T-tubules[208,230,233] and actin-dependent shaping of microdomains[207], which influence the ion flux and clustering of calcium channels. Reduced levels of BIN1 lead to a decreased distribution and clustering of the calcium channels LTCC on the T-tubules, resulting in a delay of calcium influx and an altered EC coupling[233].

1.4 Aim of thesis

In muscles T-tubules are rigidly formed tubular invaginations of the plasma membrane, being formed and maintained by the N-BAR domain protein *Drosophila* amphiphysin[49]. The crystal structure of amphiphysin BAR was solved in 2004[43] but since then no further structural information about the helical amphiphysin assembly, leading to tubular membrane remodeling, have been available. Therefore until now no specific details about the amphiphysin membrane interaction, the underlying molecular mechanism how

amphiphysin is remodeling and maintaining tubular membrane shapes and the three dimensional structure of the amphiphysin assembly were known. The aim of this thesis was to understand the protein lattice organization and the protein-membrane interaction of amphiphysin by solving the 3D structure of amphiphysin-mediated membrane tubes. First, before the role of the amphipathic helix, the BAR domain and the regulatory domains in the helical BAR arrangement could be explored several recombinant amphiphysin fragments were cloned, expressed and purified. Second, the amphiphysin membrane interaction was analyzed by performing *in vitro* liposome tubulation assays with various lipid mixtures. Third, to investigate the amphiphysin lattice formation on membranes and to understand the role of the H0 helix, BAR domain and the regulatory domains in the membrane remodeling process, biochemical, biophysical and structural approaches were used. This included *in vitro* tubulation assays, light scattering, mass per length, fluorescence light microscopy, negative stain EM and cryo-EM. At last, to get structural insights into the organization of the helical amphiphysin assembly, amphiphysin-mediated tubes were analyzed by negative stain EM and cryo-EM. The cryo-EM 3D reconstructions were verified by comparing the reprojections with corresponding power spectra to the original 2D cryo-EM averages and by fitting in the crystal structure of amphiphysin BAR. In addition, CNM and tip mutant analysis were performed, being analyzed by *in vitro* tubulation assays, fluorescence light microscopy and negative stain EM.

On the basis of the structural characterization of amphiphysin-mediated tubes several essential questions were answered: what role plays the H0 helix, the BAR domain and the regulatory domains in the membrane remodeling process? What is the mechanism behind the amphiphysin BAR assembly on the membrane surface? Is there a difference in the helical BAR lattice packing of *Drosophila* amphiphysin in comparison to other BAR proteins, being involved in dynamic remodeling events such as endocytosis? How is the helical BAR lattice organized that the sculpted tubular membrane shape is maintained? Finally, the results and conclusions were discussed in relation to the role of amphiphysin in the biogenesis and maintenance of T-tubules, in striated muscles and in the neuromuscular disorder CNM.

2 Results

2.1 *Drosophila* amphiphysin constructs

Drosophila amphiphysin, being involved in T-tubules formation in muscle cells, comprises a N-terminal membrane deforming BAR domain with an amphipathic helix (H0 helix), a weakly conserved and structural unknown central region and a C-terminal SH3 domain. *In vitro* and *in vivo* membrane tubulation by amphiphysin can be used to gain structural insights into muscle t-tubule remodeling. To understand the role of the H0 helix, the BAR domain and the regulatory domains in membrane interaction and tube formation, four truncated amphiphysin fragments were designed and analyzed for this. Various constructs with or without H0 helix were cloned, expressed and purified (Fig. 2.1): *Drosophila* amphiphysin N-BAR with H0 (N-BAR, residues 1-244) or without H0 helix (N-BAR-deltaH0, residues 27-247), full-length amphiphysin with H0 (FL, residues 1-602) or without H0 helix (deltaH0, residues 27-602). These constructs were used for the following analyses in this thesis.

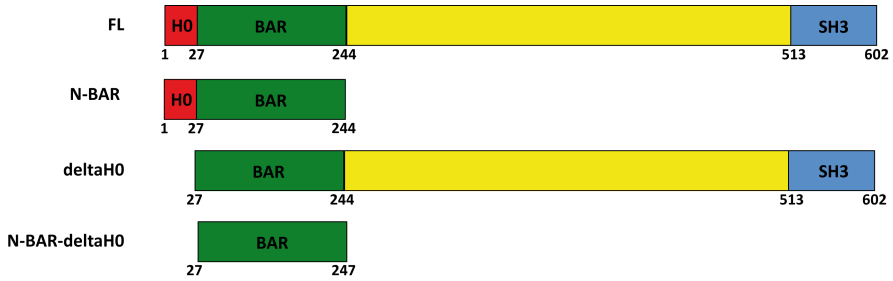

Figure 2.1 – *Drosophila* amphiphysin constructs with or without H0 helix | Schematic representation of the used amphiphysin fragments with or without the amphipathic helix H0. Full-length amphiphysin (FL), residues 1 to 602, contains a N-terminal N-BAR domain, a central region and the C-terminal SH3 domain. N-BAR domain alone consist of the N-terminal H0 helix and BAR domain,residues 1 to 244. deltaH0, residues 27 to 602, comprises the BAR domain, the central regions and the C-terminal SH3 domain. The fragment N-BAR-deltaH0 contains only the BAR domain from residues 27 to 247.

All amphiphysin constructs were expressed in *E.coli* (BL21 gold), using either a N-terminal His-sumo-tag or N-terminal His-tag. Afterwards the proteins were purified via Ni-NTA column, ion exchange chromatography (IEX) and size exclusion chromatography (SEC). For further details about the purification see section 4.2.3 in methods. The last purification step by SEC revealed that all amphiphysin fragments form a dimer as expected [43]. Appendix A1 shows all SEC profiles with corresponding SDS-PAGE of the

purified amphiphysin constructs.

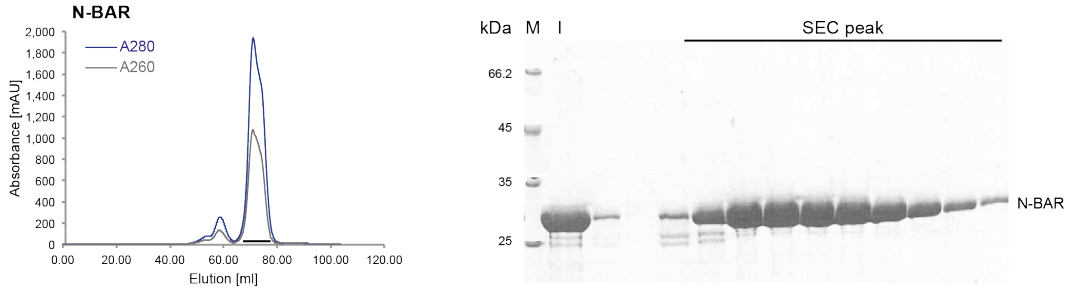

Figure 2.2 – SEC analysis of N-BAR using a Superdex 200 16/60 column | (Left) Size exclusion chromatogram of purified N-BAR (30.4 kDa), showing a peak at ~75 ml (~58 kDa) by UV absorbance at 280 nm (blue) and 260 nm (grey). N-BAR formed a dimer. (Right) SDS-PAGE shows the peak fractions of N-BAR, which is marked by a line. M = protein marker in kDa, I = injected protein sample, SEC = Size exclusion chromatography

2.2 Lipid composition dependent membrane remodeling by amphiphysin

The N-BAR domain is known to tubulate liposomes by helical polymerization around the membrane *in vitro* and *in vivo*[47,49,70,100]. During the helical assembly of amphiphysin the positively charged concave surface of the BAR domains is interacting with the negatively charged membrane[43]. Thus, I assume that the charge of the membrane should play a role in how amphiphysin is remodeling the membrane. Mammalian muscle BIN1, containing a PI-binding motif (exon 11), needs to bind to the PI(4,5)P_2 enriched sarcolemma so that T-tubules could be formed[146,151,173]. This polybasic sequence (RKKSKLFSRLRRKKN), which binds specifically to PI(4,5)P_2, is missing in *Drosophila* amphiphysin, being an orthologue to the mammalian muscle BIN1. Alignment of *Drosophila* amphiphysin with the exon 11 PI-binding motif of human muscle BIN1 showed shorter consensus polybasic sequences within the N-terminal amphipathic helix and the concave surface of the BAR domain in helix 2 of one monomer (see Appendix A2). It is predicted that in *in vitro* *Drosophila* amphiphysin shows only membrane tubulation in the presence of PI(4,5)P_2 in the membrane[262].

To understand the effect of different lipid compositions, affecting the charge of the membrane, on membrane-protein interactions and the lattice formation, various large unilamellar vesicles (LUVs) were incubated with amphiphysin N-BAR *in vitro*. It was observed that the *in vitro* amphiphysin-mediated tubes have similar size as T-tubules in myocytes[49]. The formed tubes were observed by negative stain EM and some tube conditions were confirmed by cryo-EM (Fig. 2.3).

Single particle EM by negative stain EM as well as cryo-EM is an useful technique in structural biology. Negative stain EM, being a easy, quick and qualitative EM technique, uses a simple specimen preparation method where protein samples are embedded into

a thin layer of heavy metal salt solution, which enhances the sample contrast [263]. For cryo-EM the specimen is quickly frozen by liquid ethane so that the hydrated protein is embedded in a thin layer of vitreous ice [264]. Cryo-EM has several advantages in comparison to negative stain EM. First the specimen is in its native condition because it is flush frozen leading to vitreous ice and not negatively stained with heavy metal atoms. Negative staining can lead to staining artefacts because of dehydration, which could lead to flattening of the 3D structure. Structural analysis by cryo-EM can gain higher resolution (>10 Å) of the specimen because there is no movement of the stain or stain granularity. For helical assemblies, cryo-EM can also help to observe the diversity in macromolecules and conformational differences. However, negative stain EM is still an important technique to study biological structures. Because of the increased image contrast in negative stain EM, relatively smaller biological samples can be examine and visualized. Moreover, due to the fast and easy sample preparation negative staining can be used to have a quick look at purified protein samples or *in vitro* protein reconstitution. Negative stain EM helps to gain information about the quality of the protein preparation, the formation of protein complexes or large biological assemblies, or the homogeneity or heterogeneity of the sample. Therefore, negative stain EM is a straight forward method to screen and optimize specimen for cryo-EM.

The *in vitro* tubulation ability of amphiphysin under different liposome conditions is observed and screened by negative stain EM (see 4.2.6 in Methods). For the analysis, 5 µM of protein was mixed with 180 µM LUVs. In the case of LUVs made of 100% POPC, being an uncharged phospholipid, no tubes were generated (Fig. 2.3, A, POPC). Liposomes made of 2POPG:1POPE have an overall membrane charge of 66%. This lipid mixtures showed bilayer membrane tubes formation, looking uniform and rigid (Fig. 2.3, A, 2POPG:1POPE). This shows that amphiphysin N-BAR is able to remodel membranes without PI(4,5)P_2 *in vitro*. The membrane bilayer tubes with the 2POPG:1POPE lipid mixture were additionally verified by cryo-EM (Fig. 2.3, B, 2POPG:1POPE, C). When the liposome is becoming very negatively charged, which is in the case of LUVs with 100% POPG, the N-BAR domain starts to make stable micellar tubes (Fig. 2.3, A, POPG), which was additionally confirmed by cryo-EM (Fig. 2.3, B, POPC, and D). This is likely due to stronger binding of the positively charged concave BAR surface with the negatively charged membrane. To know the protein-lipid interaction in the close-to-physiological conditions bovine lipid brain extract (Folch Fraction I), containing PIPs, PS and other brain lipids, was used as a control, showing bilayer and micellar tube remodeling under negative stain EM and cryo-EM observations (Fig. 2.3, A and B, Folch fraction I). However, when bilayer tube formation by N-BAR is observed (Fig. 2.3, C), the diameters of the tubes appear to be consistent (240 to 350 Å) regardless of the charged membrane compositions with or without PI(4,5)P_2. In addition, a certain amount of negatively charged phospholipids in the membrane is necessary to form bilayer tubes. If the percentage of the negatively charged compositions is getting too high

amphiphysin N-BAR seems to bind very strong to the membrane, leading to micellar tube molding (Fig. 2.3, D). Among the tested conditions, 2POPG:1POPE was the lipid composition that gave the most consistent and rigid tube formation, which is useful for further biophysical and structural investigations. Moreover, more or less uniform tubes should facilitate the improvement of the structural analysis, raising the resolution of the 3D reconstructions. Before I moved to the structural analyses I wanted get an insight how amphiphysin is remodeling lipsomes into tubes. To get an idea about the helical assembly of amphiphysin on the tube surface the role of its domains in the membrane remodeling process has to be understood. Therefore, several *in vitro* tubulation assays with N-BAR, N-BAR-deltaH0, H0 and FL were performed (see 2.3).

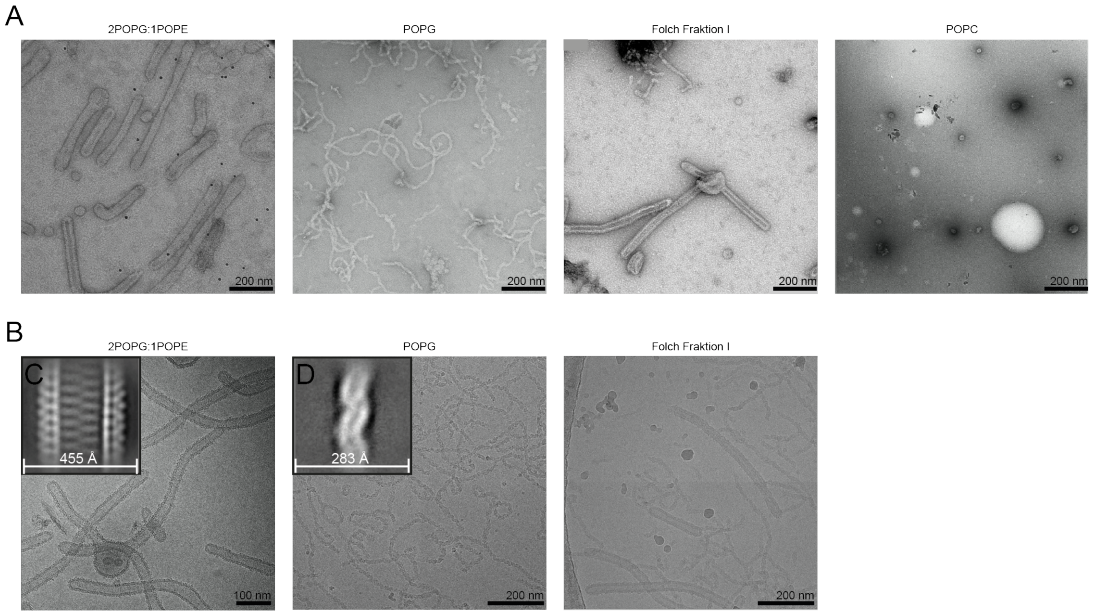

Figure 2.3 – Negative stain EM observation of *in vitro* membrane tubulation by N-BAR with various lipid compositions | (A) Negative stain EM of the tested liposome mixtures remodelled by amphiphysin N-BAR. 2POPG:1POPE showed rigid uniform bilayer tube formation. For POPG micellar tubes are formed. In the physiological lipid mixture Folch fraction I micellar and rigid uniform tubes were observed. With POPC no tubes were remodelled. (B) Cryo-EM of N-BAR with 2POPG:1POPE, POPG and Folch fraction showed the same tube morphologies as observed with negative stain EM results. (C) 2D class average of the remodelled bilayer 2POPG:1POPE tubes by N-BAR. (D) 2D class average of the micellar tubes formed by N-BAR with 100% POPG

2.3 *In vitro* liposome tubulation with various amphiphysin fragments

N-BAR domain proteins remodel liposomes into tubes *in vitro* by an helical assembly around the membrane surface[47,49,70,100]. During this process a helical lattice is formed because of membrane-protein interactions and protein-protein interactions[70,100]. To elucidate the roles of the H0 helix, the BAR domain and the regulatory domains of

amphiphysin in membrane tubulation several amphiphysin fragments with H0 (N-BAR, FL) and without H0 helix (N-BAR-deltaH0, deltaH0) were analyzed by tubulation assays with EM or light scattering.

2.3.1 The role of the H0 helix in *in vitro* liposome tubulation

For the N-BAR domain containing protein endophilin, it was proposed that the amphipathic helix H0 is relevant for rigid lattice formations [70,262]. Thus, I wanted to test if the H0 helix of the N-BAR domain protein amphiphysin is relevant for the tube formation as well.
At first, membrane remodeling of amphiphysin N-BAR, FL, N-BAR-deltaH0 and deltaH0 with multi-lamellar vesicles (MLVs) of 2POPG:1POPE was studied by negative stain EM (Fig. 2.4).

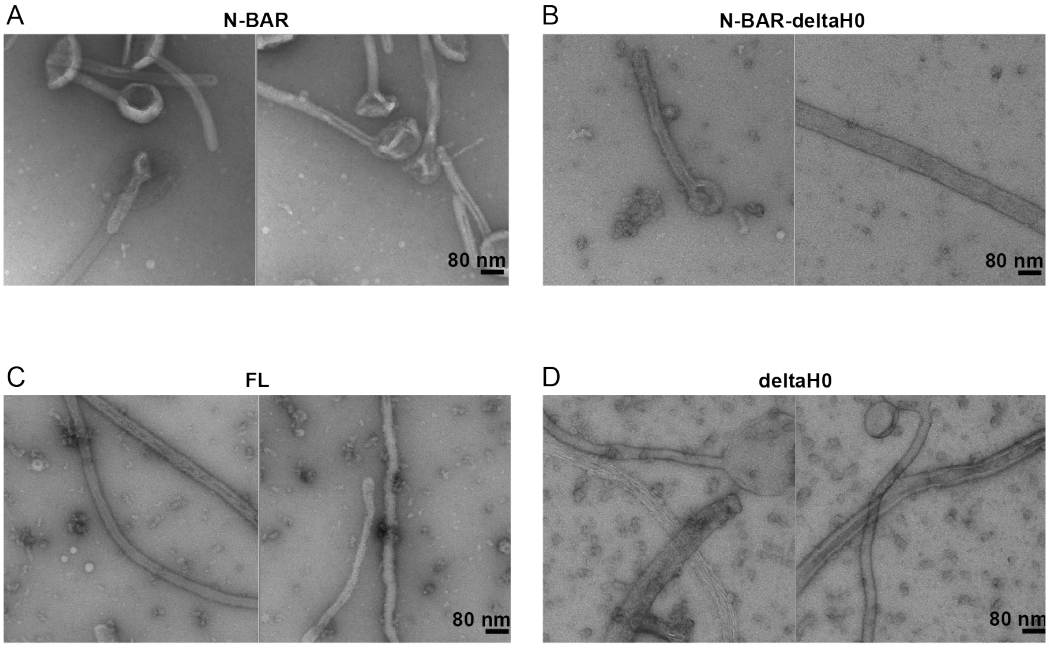

Figure 2.4 – ***In vitro* tubulation by several amphiphysin fragments** | Negative stain EM of *in vitro* tubulation performed with 180 µM MLVs (2POPG:1POPE) and 150 µg/ml of (A) N-BAR, (B) N-BAR-deltaH0, (C) FL and (D) deltaH0. N-BAR and FL showed the same rigid uniform tube formation with a similar tube diameter of around 240 to 360 Å. For N-BAR-deltaH0 and deltaH0 thicker tubes up to 850 Å were additionally observed.

N-BAR and FL showed tubes with a diameter range of 200 to 350 Å (Fig. 2.4 A and C). The resulting tubes of N-BAR-deltaH0 and deltaH0 showed mostly a similar shape as N-BAR constructs, but in addition, significant populations of thicker tubes with a width of up to 85 nm were observed (Fig. 2.4 B and D). To observe the remodelled tubes in its native state, several fragments were analyzed by cryo-EM (Fig. 2.7). The constructs N-BAR and FL with H0 helix showed tubes with a diameter of approximately 300 Å with a distinct stripped pattern. Similar to the negative staining EM analysis

N-BAR-deltaH0 showed 45% thicker tubes without any prominent patterns in contrast to the thinner tubes with 300 Å. This observations reveal that the N-terminal amphipathic helix H0 is not necessary for the tube formation. It rather suggests that the H0 helix is likely influencing the BAR organization. Hence, to understand the role of the H0 helix in the dynamic membrane remodeling process amphiphysin with or without H0 helix was analysed with time-dependent tubulation assays by light scattering and EM (2.3.2).

2.3.2 The initiation of the tube formation by the H0 helix

In cellular processes membrane curvature is taking place in a spatial and temporal manner[126,133,265]. To find out if there is a tubulation behavior change between FL, deltaH0, N-BAR and N-BAR-deltaH0, the membrane remodeling was monitored by light scattering as a function of time. For the tubulation assay I used MLVs because they show a strong scattering signal. To quantify the membrane molding by light scattering, the absorption of the tube formation by various amphiphysin fragments was recorded at 400 nm (Fig. 2.5). Liposomes scatter light optimally at a wavelength of approximately 400 to 500 nm. After I added 6 µM of each amphiphysin fragment to 180 µM (corresponding to 150 µg/ml) liposomes tubes were formed and therefore the scattering got weaker.
All constructs showed an increase of the scattering after the protein was added to the liposomes. This rise of the scattering signal is related to the formation of tubes. This observation was confirmed by negative stain EM (Fig. 2.6). N-BAR (Fig. 2.5, blue) showed the strongest boost of the scattering in comparison to FL (Fig. 2.5, violet), N-BAR-deltaH0 (Fig. 2.5, light green) and deltaH0 (Fig. 2.5, green). Directly after the rise of the scattering signal N-BAR and FL showed a proceeding decrease in the signal, being in contrast to the amphiphysin fragments without H0 helix. The scattering signal of N-BAR-deltaH0 and deltaH0 increased relatively slowly and afterwards no decay followed as it stayed steady.

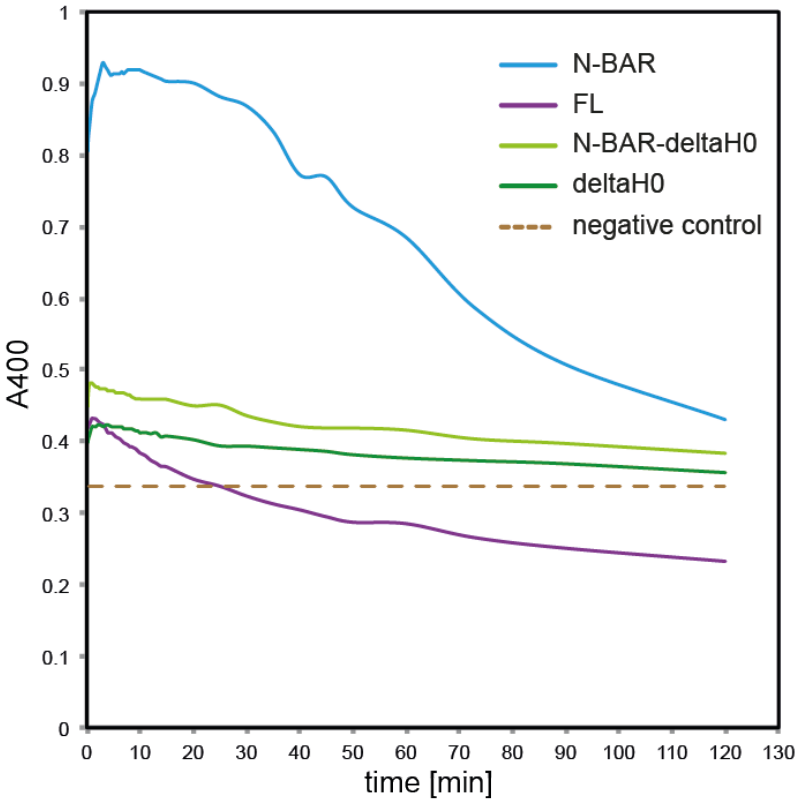

Figure 2.5 – Light scattering of liposome tubulation by various amphiphysin fragments | 180 µM 2POPG:1POPE lipid vesicles were mixed with 6 µM of N-BAR (blue), FL (violet), N-BAR-deltaH0 (light green) and deltaH0 (green) and observed by absorbance measurements at 400 nm for up to 120 min. As negative control (brown) only liposomes were used. Increase of the scattering signal corresponded to tube formation. In the beginning N-BAR showed the strongest rise of the signal in contrast to the other amphiphysin fragments. Afterwards a decrease of the N-BAR and FL signal was observed. After adding the protein to the lipsomes the absorbance of N-BAR-deltaH0 and deltaH0 slightly increased before it stayed stable without signal dropping. Adopted from [266].

Different time points of the *in vitro* tubulation assay of 15 µM N-BAR and N-BAR-deltaH0 were observed under negative stain EM. Negative stain EM revealed that tubes were immediately remodelled after the proteins were added to the liposomes (Fig. 2.6). In contrast to N-BAR, N-BAR-deltaH0 (Fig. 2.6, B, + N-BAR-deltaH0) was forming tubes with a thicker tube diameter. Moreover, N-BAR (Fig. 2.6, B, + N-BAR) showed already rigid uniform tubes right from the start.

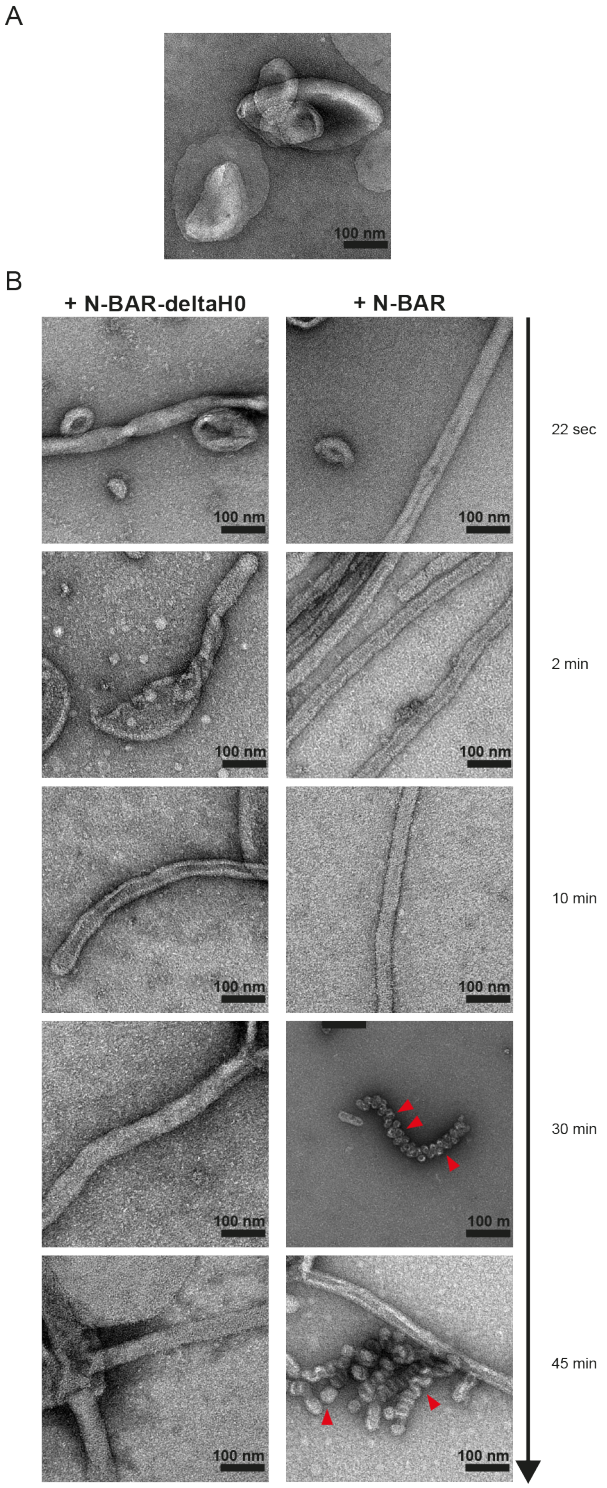

Figure 2.6 – Negative stain EM of liposome tubulation by N-BAR and N-BAR-deltaH0 | 180 µM 2POPG:1POPE lipid vesicles were mixed with 15 µM N-BAR and N-BAR-deltaH0 and and observed by negative stain EM. (A) As negative control only liposomes were used. (B) Tube formation of N-BAR (left) and N-BAR-deltaH0 (right) was recorded for both fragments. The tubes were displayed after mixing (22 sec) and at various time points (2 min, 10 min, 30 min and 45 min) up to 45 min. N-BAR showed rigid uniform bilayer tubes from the beginning. After around 30 min, small vesicles of 300 Å (red arrowhead) emerged from the remodelled tubes transformed into small vesicles. For N-BAR-deltaH0 thicker bilayer tubes were observed from the start and throughout the whole measurement. Adopted from [266].

After approximately 30 min the remodelled tubes with N-BAR-deltaH0 stayed stable (Fig. 2.6, B, + N-BAR-deltaH0, 30 min), corresponding to a stable light scattering signal. At the same time, in the presence of the N-BAR domain some of the tubes are squeezed into small vesicles with a diameter of 300 Å (Fig. 2.6, B, + N-BAR, 30 min, red arrowhead), fitting to the strong decrease of the light scattering signal. Furthermore, the moment was recorded when small vesicles emerged from the tubes (Fig. 2.6, B, + N-BAR, 45 min, red arrowhead).
Taken together the tubulation assays showed that the amphipathic helix H0 is influencing how amphiphysin is remodeling membranes into tubes. I observed that the H0 helix seems to induce faster tube remodeling by helping to form the rigid uniform BAR lattice. Furthermore, the N-BAR domain with H0 helix is squeezing out small vesicles from the remodelled tubes probably because of a strong wedging effect of the membrane embedded H0 helix, which likely disrupts the integrity of the membrane (see Introduction, 1.2.2). In the subsequent cryo-EM analysis I wanted to have closer look on the morphology of amphiphysin N-BAR, BAR an FL-mediated tubes (see 2.3.3).

2.3.3 Influence of the H0 helix on the tube diameter

In the previous tubulation assays by negative stain EM (see Fig. 2.4) it was observed that the formed tubes had a variation in their diameter size. Moreover, it was seen that the remodelled tubes in the presence of N-BAR-deltaH0 and deltaH0 had a dominant population of thicker tubes (Fig. 2.4, B and D). But negative stain EM did not resolve if there was a difference in the tube width distribution between membrane remodeling by N-BAR and FL (Fig. 2.4, A and C), containing additional regulatory domains. To determine the tube diameter populations, tube remodeling by N-BAR, N-BAR-H0 and FL was analyzed via cryo-EM (Fig. 2.7).
Figure 2.7 (A - C) shows the tube morphology under negative stain EM in the presence of the three fragments. In the condition of N-BAR (Fig. 2.7, A) and FL (Fig. 2.7, C) rigid uniform tube were observed with similar tube diameter. In contrast, for N-BAR-deltaH0 (Fig. 2.7, B) a population of thicker tubes and thinner tubes like N-BAR and FL were found. With the following cryo-EM image analysis the tube width distribution should be analysed in native state without negative stain artifact effects. At a magnification of 80000x micrographs of N-BAR (Fig. 2.7, D), N-BAR-deltaH0 (Fig. 2.7, E) and FL (Fig. 2.7, F) were collected, using a F20 and FEI Eagle CCD (charged couple device) camera, and the containing tubes were segmented (13455, 2921 and 1699 segmented particles, respectively). Only in the case of N-BAR-deltaH0 thicker tubes were additionally observed and were segmented with a bigger box size (Fig. 2.7, H, right). Therefore the N-BAR-deltaH0 segmented tubes were divided into two data sets "N-BAR-deltaH0" and "N-BAR-deltaH0 thick". Afterwards a 2D classification of the particles was done to visualize the BAR packing on the surface of the tubes and to determine the tube width (see 2D classification procedure in section 2.5.1).

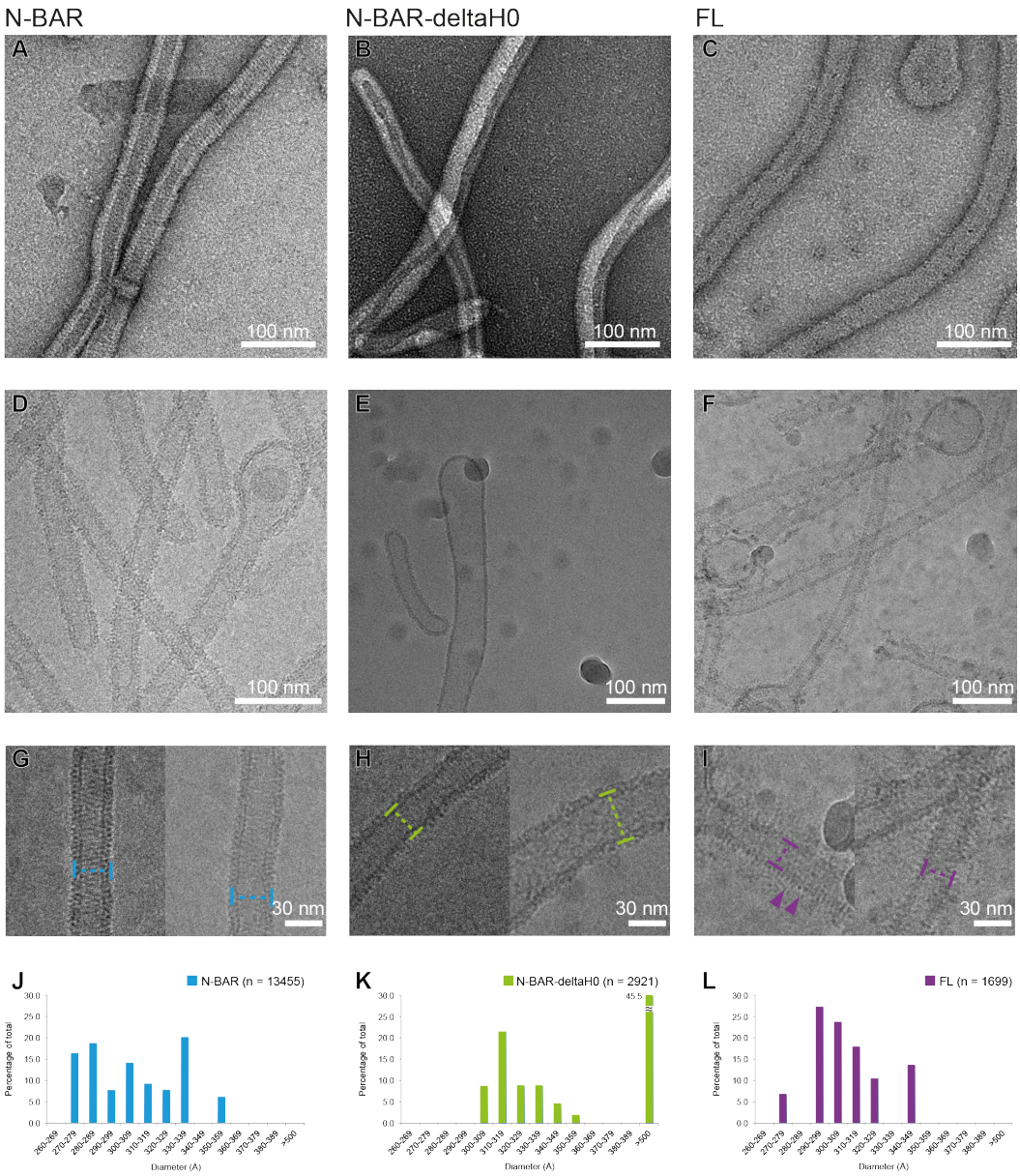

Figure 2.7 – Tube width determination of the formed tubes by N-BAR, N-BAR-deltaH0 and FL | Tube formation recorded by negative stain EM for N-BAR (A), N-BAR-deltaH0 (B) and FL (C). Cryo-EM observations(D to I) of N-BAR (D and G) showed tubes with an visible BAR assembly pattern on the surface (G). N-BAR-deltaH0 showed thicker and thinner tubes (E and H). The thicker tubes did not reveal any obvious BAR lattice on the membrane surface (H, right). For FL (F and I) similar tubes like N-BAR were observed. A closer look revealed protruding out densities on the tube surface (I, purple arrowheads). The measured tube width of N-BAR (J), N-BAR-deltaH0 (K) and FL (L) were displayed via a histogram. For all amphiphysin fragments tubes with a width of 270 to 350 Å were observed. Only N-BAR-deltaH0 showed a population with ~45% of tubes with an tube diameter >500 Å. Adopted from [266].

A range of different tube diameter populations was observed for each construct (Fig. 2.7, G for N-BAR, H for N-BAR-deltaH0 and I for FL). N-BAR-delta H0 thick tubes did not reveal any dominant BAR assembly on the tube surface (Fig. 2.7, H, right). In contrast

to this, an organized BAR assembly was observed on N-BAR remodelled tubes (Fig. 2.7, G). To get the profile of the tube width, remodelled tubes were plotted across the tube axis so that the tube width can be determined and calculated. N-BAR mediated tubes showed diameters between 270 to 360 Å (Fig. 2.7, J). FL revealed a similar width distribution of 270 to 350 Å (Fig. 2.7, K). Tubes formed by N-BAR-deltaH0 had a width population of 300 to 360 Å and 650 to 850 Å, which was corresponding to ~45% of the segmented particles (Fig. 2.7, L). Without H0 the formed tubes have thicker tube morphologies. This demonstrates that the tube morphology is likely determined by the arrangement of the helical BAR lattice on the membrane. The helical assemblies of BAR domains with or without N-terminal H0 helices, wrapping around the tube surface, were investigated by 2D class average analyses with corresponding power spectrum (see 2.3.4).

2.3.4 Organization of the assembled BAR arrangement by the H0 helix and BAR

To understand the BAR arrangement of amphiphysin-mediated tubes, we attempted to reconstitute morphologically uniform tubes for further structural analysis by cryo-EM. The conditions of N-BAR and FL showed that the tubes have a diameter distribution of ~270 to 340 Å. One population of N-BAR-deltaH0 remodelled tubes show a width distribution of ~300 to 360 Å. In addition, it was observed that >45% of the remodelled tubes have a width of 650 - 850 Å. To get a first insight into the BAR assembly during the tube remodeling, the 2D class averages, including corresponding power spectra, of the segmented N-BAR (see 2.5.3), N-BAR-deltaH0 and FL (see 2.3.3) tubes were analyzed (Fig. 2.8).

The class averages of the segmented particles were produced by using the 2D classification option in Relion[267]. They show in real space a high signal-to-noise ratio in contrast to the raw images. 2D class averages with their corresponding power spectra reveal information about the lattice packing, the tube width, dimension and heterogeneity of the specimen. The 2D classes and power spectra reveal the first insight into the helical lattice organization before the structural analyses can follow by helical 3D reconstruction (see 2.4.1 and 2.4.2. The corresponding class averages of N-BAR and FL revealed a discrete lattice packing for N-BAR (Fig. 2.8, averages, first row) and FL (Fig. 2.8, averages, second row), looking like an interwoven pattern. This stripped pattern represents the superposition of the near and far side (Moiré pattern) of the protein-coated tube in an EM image. The lattices are organized by several but distinct protein positions in the helical array around the tube. Moreover, a range of different tube diameters were observed for each construct. The thicker tubes of N-BAR-deltaH0 (Fig. 2.8, averages, fourth row) lacked any distinctive BAR packing. In contrast, N-BAR-deltaH0 tubes (Fig. 2.8, averages, third row) showed an arranged BAR assembly but it was less organized, in comparison to N-BAR and FL. The class averages, containing the BAR assembly, showed

that a weakly arranged helical BAR polymer is wrapping around the tube surface. To get more information about the helical lattice organization, I calculated the 2D power spectra of the class averages. In a helical arrangement helical structures are repeated in a periodical manner (Fig. 2.15). The power spectra had a characteristic pattern of layer lines, corresponding to the structural repeats. The layer line separation is reciprocal to the spacing of the periodicity.

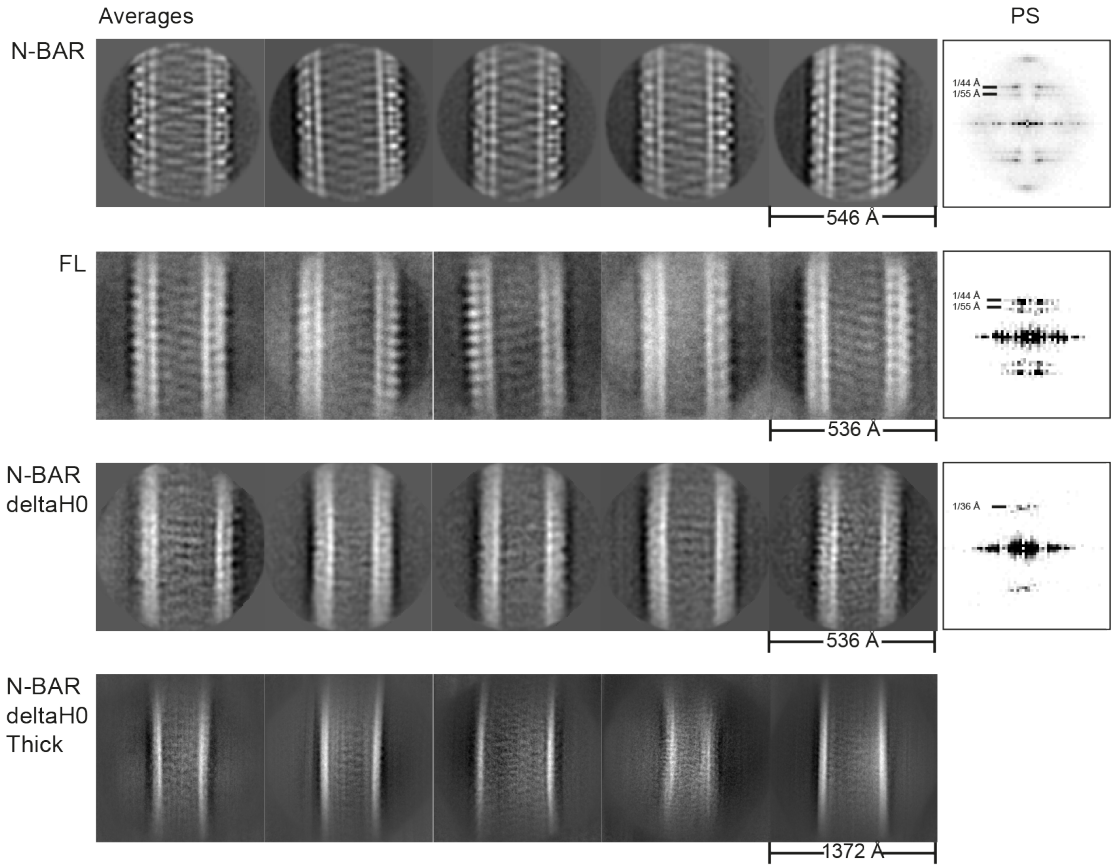

Figure 2.8 – 2D class averages and power spectra of N-BAR, FL and N-BAR-deltaH0 | The class averages of N-BAR (first row left to right) contain 1365, 1392, 1173, 692 and 1372 segmented particles, respectively. For the FL classification (second row, left to right) 398, 293, 284, 459 and 466 particles were used. The 2D classes of N-BAR-deltaH0 (third row, left to right) had 234, 312, 165, 185 and 132 particles and and the thick tubes class averages (fourth row, left to right) contain 159, 403, 118, 282 and 447 particles. Right: Power spectra of the most left 2D class averages. The class averages of N-BAR (first row) and FL (second row) showed interwoven pattern, corresponding to the organized BAR protein assembly. The corresponding power spectra display a periodical signal pattern of the striped pattern within the tube of 44 Å and 55 Å. N-BAR-deltaH0 (third row) displayed a spacing of ~36 Å in the power spectrum and the 2D class showed no interwoven protein packing. This indicated that the protein arrangement is not so rigid as in N-BAR remodelled tubes and thus, the protein assembly is changed. For the thicker tubes remodelled by N-BAR-deltaH0 (fourth row) no periodical pattern could be observed in the power spectra, fitting to the not observed BAR lattice on the membrane surface. Adopted from [266].

For the class averages of the N-BAR remodelled tubes with interwoven pattern a typical

diagonal patter of layer lines was observed, which confirms the helical assembly like in other BAR proteins. Two dominant layer lines were displayed, correlating to a structural spacing of 44 and 55 Å (Fig. 2.8, PS, first row). A similar observation was made for tubes in the presence of FL, containing the N-BAR domain (Fig. 2.8, PS, second row). The signal-to-noise ratio is lower than for N-BAR because the regulatory domains are interfering with the averaging of the segmented particles. For the thicker tubes derived from the N-BAR-deltaH0 no periodical pattern was determined indicating an disordered assembly of BAR domains. But even with disorganized BAR packing on the tube surface membrane remodeling was induced. A closer look at the the power spectra of the N-BAR-deltaH0 remodelled tubes (Fig. 2.8, PS, third row) showed that there was an existing periodical structural pattern on the tube surface but it was different to N-BAR and FL. Only one layer line with a periodical spacing of 36 Å was revealed. A second layer line, determining the lattice, like observed in N-BAR or FL-mediated tubes is missing. This indicates that the helical lattice of N-BAR-deltaH0 is disorganized. However, N-BAR-deltaH0 is still able to assemble itself on the membrane surface to remodel tubes but not as firm organized as the N-BAR arrangement.
This suggests that H0 helix is necessary for a correct organisation of the BAR assembly on the tube surface. The H0 helix determines the spacing of the BAR domains within the helical BAR lattice. Furthermore, in connection with the tubulation assay observations (Fig. 2.6) this result indicates that H0 initiates the fast tube formation by quickly organizing the self-assembly of the BAR domains. Without the H0 helix the tubes show an irregular and thicker morphology in the beginning before some of the BAR domains are able to arrange themselves on the membrane surface to form tubes with a diameter of approximately 320 Å. It seems that the H0 helix facilitates the organization of the helical BAR lattice. The H0 helix has a defined length, which may define the spacing between the helical lattice rows and consequently the BAR packing on the tube surface. To get further insights into the lattice formation, the H0 helix was extended to see if the BAR packing changes (see 2.3.5).

2.3.5 The role of the H0 length in N-BAR membrane remodeling

The amphipathic helix H0 is involved in the initiation of the organized N-BAR assembly and plays a role in how the BAR domain arranges itself in the helical lattice (Fig. 2.8). The 2D class averages with corresponding PS showed that without H0 helix the BAR lattice seems to be disorganized (see 2.3.4). Moreover, the H0 helix plays a role in the periodical spacing of the BAR domains in the lattice arrangement in real space. Therefore, artificial N-BAR constructs with additional H0 helix sequences were designed, expressed and purified (Fig. 2.9 and Appendix A3). With help of the helix wheel projection (Fig. 2.9, A) the H0 residues 1 - 18 and 1 - 7 were inserted in front of N-terminal amphipathic helix of amphiphysin N-BAR (M1-G18-N-BAR and M1-I7-N-BAR, respectively) (Fig. 2.9, B). The amphiphysin N-BAR fragments with extended H0 helix were purified like

N-BAR. Following the membrane remodeling was analysed by negative stain EM.

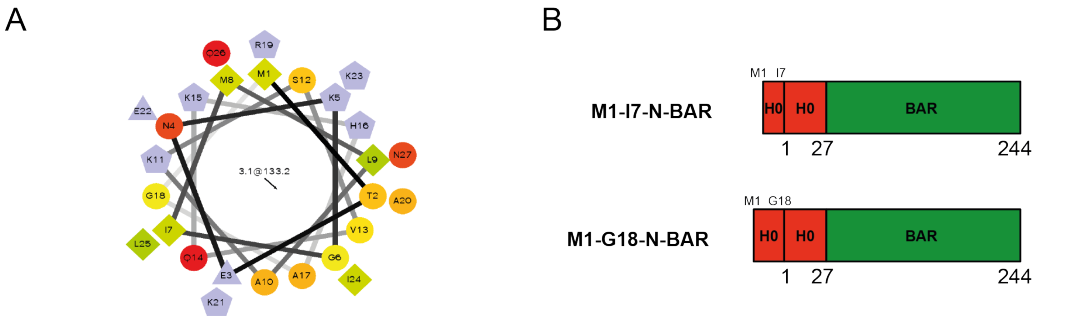

Figure 2.9 – N-BAR constructs with extended H0 helix | (A) H0 helix of amphiphysin displayed by helix wheel projection, demonstrating amphipathic potential. Residue numbering starts from the N-terminus. The shape of the residues represents the following: triangle = potentially negatively charged aa, pentagon = potentially positive charged aa, circle = hydrophilic aa, diamond = hydrophobic aa. The color code is: green = the most hydrophobic aa, the decreasing amount of the color green is proportional to the hydrophobicity, yellow = no hydrophobicity, red = most hydrophilic (uncharged) aa, the decreasing amount of the color green is proportional to the hydrophilicity. blue = potentially charged aa. (B) The following amphiphysin N-BAR constructs with extended H0 helix were used: M1-I7-N-BAR (top) and M1-G18-N-BAR (bottom). aa = amino acid

For native N-BAR it was observed that uniform rigid tubes are remodelled out of liposomes (Fig. 2.6, + N-BAR) as expected. After approximately 30 min, small vesicles (~30 nm) were emerging from the formed tubes. Surprisingly, with the double helix construct M1-G18-N-BAR the small vesicle formation was already observed from the beginning (Fig. 2.10, B, 1 min) and almost all tubes were remodelled into small vesicles after around 10 min (Fig. 2.10, B, 10 min and 45 min, E). A closer look on the few remaining tubes, being more or less rigid and uniform bilayer tubes, revealed that no helical lattice arrangement was visible.

In contrast, M1-I7-N-BAR displayed normal tube formation without early small vesicle formation (Fig. 2.10, A). This construct was rather behaving like N-BAR but much less tubes were remodelled and observed (Fig. 2.10, A, right). Most of the few formed tubes were rigid and uniform bilayer tubes (Fig. 2.10, A, left, 1 min and 45 min). But in addition, some tubes showed irregular tube morphologies (Fig. 2.10, A, left, 10 min). With an elongated amphipathic helix an increased wedging effect is taking place leading to a stronger membrane curvature generation. It also suggests that a longer H0 disrupts the spacing between the helical BAR lattice rows and thus, no organized BAR assembly was observed.

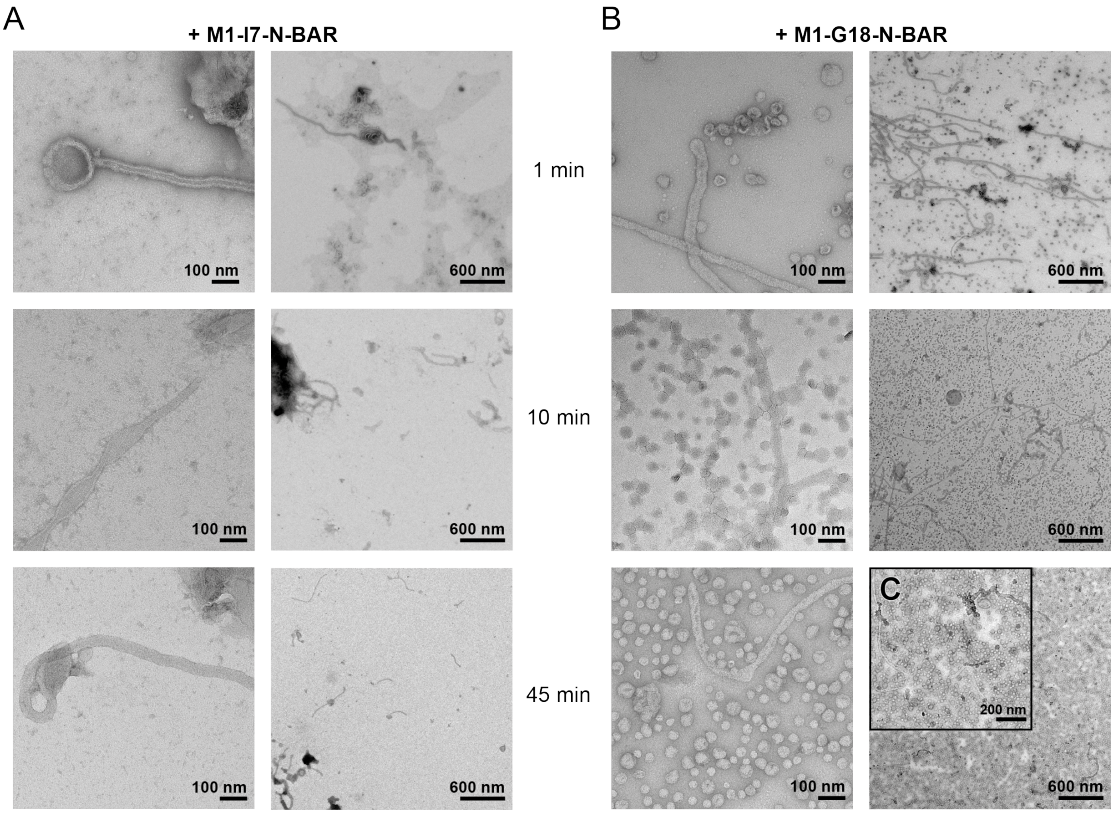

Figure 2.10 – Membrane tubulation of N-BAR with extended H0 helix | *In vitro* tubulation of M1-I7-N-BAR (A) and M1-G18-N-BAR (B) was observed by negative stain EM with several magnifications and incubation times. (A) M1-I7-N-BAR showed less tubulation as N-BAR and rigid uniform (left, 1 min and 45 min) and irregular remodelled (left, 10 min) tube formation without visible BAR lattice on the membrane surface. In contrast M1-G18-N-BAR (B) squeezes small vesicles out of tubes from the start and almost all tubes were remodelled into small vesicles after 10 min (10 min, 45 min and C). The few formed tubes look rigid and uniform without obvious BAR assembly on the tube surface (left).

This highlights the importance of the amphipathic helix and its involvement in the lattice arrangement. To further understand the role of the N-terminal H0 helix and the regulatory domains during membrane remodeling, the degree of tubulation was analysed as a function of the protein concentration (see 2.3.6).

2.3.6 Influence of the the protein concentration and H0 helix on the degree of tubulation

The critical tubulation concentration (CC) was determined to reveal the required protein concentration, which is needed for tube remodeling. To measure the degree of tubulation as a function of the protein concentration we used fluorescence light microscopy and light scattering at 490 nm .

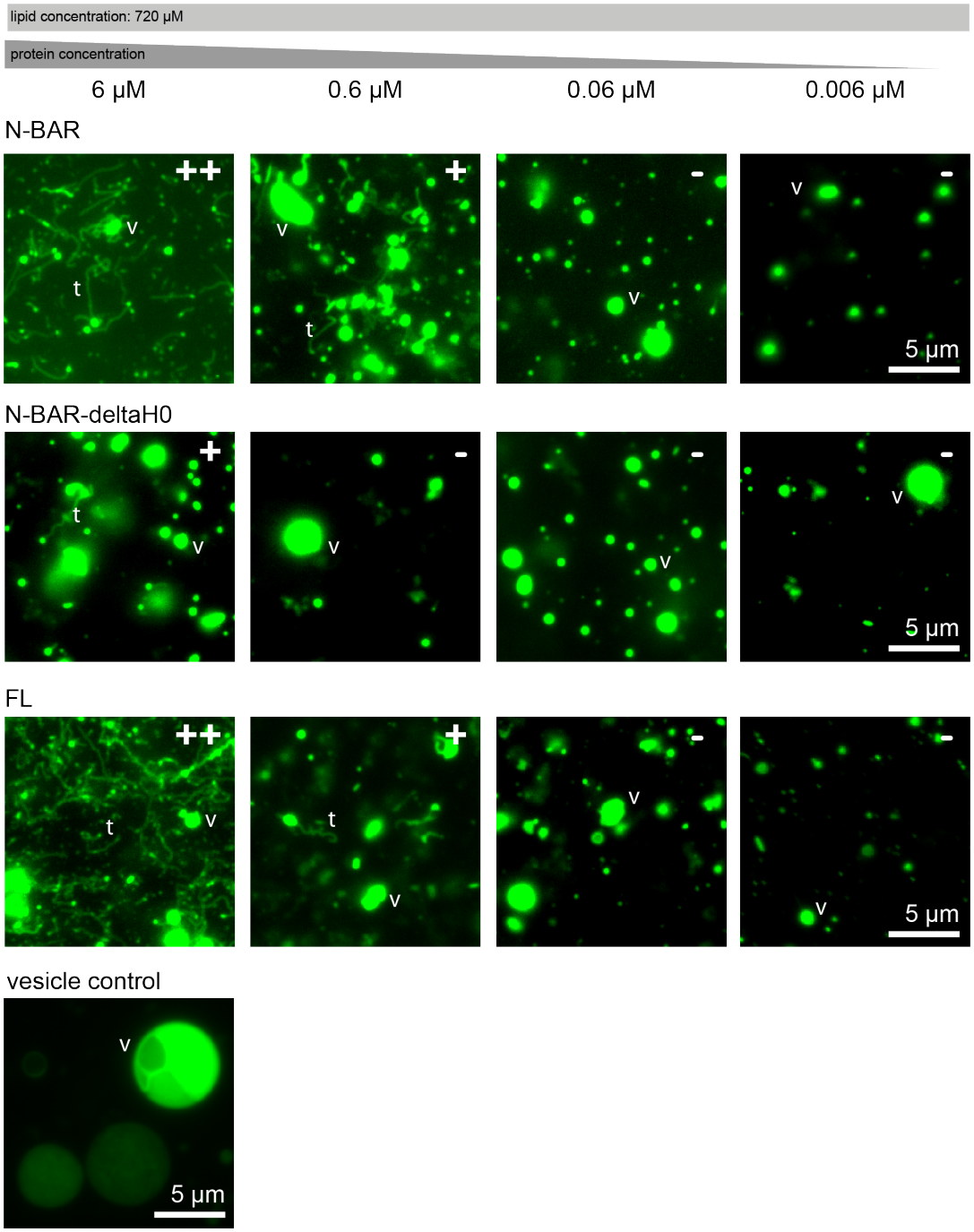

Figure 2.11 – Tubulation of N-BAR, N-BAR-deltaH0 and FL with various protein concentrations observed by fluorescence light microscopy | Various protein dilutions (6 µM, 0.6 µM, 0.06 µM and 0.006 µM) of N-BAR (first row), N-BAR-deltaH0 (second row) and FL (third row) were mixed with 720 µM (600 µg/ml) fluorescently labeled liposomes. N-BAR and FL showed tube remodeling up to concentration of 0.6 µM. N-BAR-deltaH0 formed tubes only with the concentration of 6 µM. Lower concentrations showed only small vesicles, being smaller as the liposomes of the vesicle control (fourth row). The tubulation degree is labeled like ++ (strong tubulation behavior > + > +/- (tubulation almost not occurring) > - (no tubulation). v corresponds to example of vesicles and t to example of tubes. Adopted from [266].

The fluorescence light microscopy analyses visualized the liposome tubulation, depending on the various protein concentrations. At a protein concentration of 6 µM all three constructs showed tube formation (Fig. 2.11, N,BAR, N-BAR-deltaH0 and FL in the first, second and third row, respectively). Whereas N-BAR and FL had a similar strong tubulation activity. In contrast, N-BAR-deltaH0-mediated tubes were rarely observed. In the condition of 0.6 µM some tube remodeling was only detected for N-BAR and FL. For N-BAR-deltaH0 the observed liposome vesicles were smaller as the vesicles of the negative control. Below 0.06 µM protein concentration solely vesicles and no tubulation was detected.

For a more precise determination of the CC light scattering measurements with protein dilutions (6, 3, 2, 1, 0.6. 0.3, 0.1, 0.06 µM) and 720 µM (corresponding to 150 µg/ml) MLVs were recorded (Fig. 2.12). The scattered light signal increases during tube formation and stays almost constantly stable when no membrane molding is taking place. The CC was attained at a protein concentration of ~0.4 µM for N-BAR (Fig. 2.12, A) and FL (Fig. 2.12, B) and of ~1.6 µM for N-BAR-deltaH0 (Fig. 2.12, C). A higher protein concentration of amphiphysin fragments without H0 was needed to generate tubes. Because of the missing organized self-assembly, which is initiated by the H0 helices, more BAR domains are necessary to arrange themselves around the membrane surface to induce tube remodeling. These results indicate that without the amphipathic helix H0, the capability of amphiphysin to interact with the membrane is less efficient. As the protein concentration plays a role in the membrane remodeling the following negative stain EM analysis should give insights how the amphiphysin N-BAR self-assembly is taking place at high and low protein concentrations (see 2.3.7).

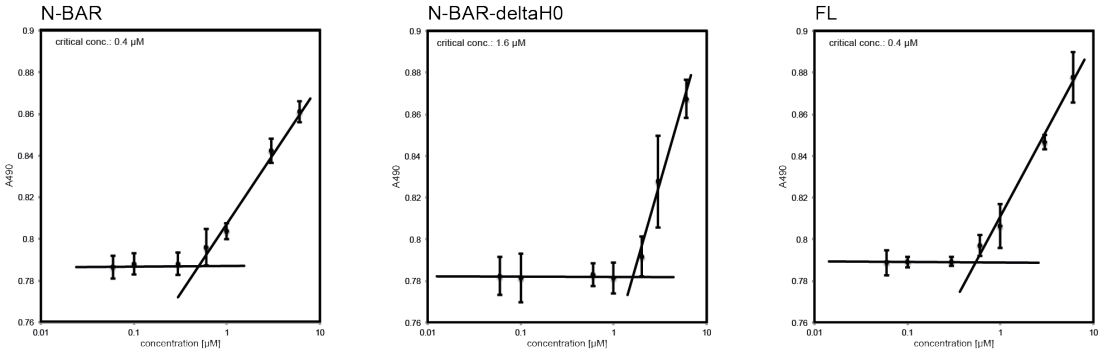

Figure 2.12 – Critical tubulation concentration determination by light scattering measurements | 720 µM liposomes were mixed with several concentrations of N-BAR (left), N-BAR-deltaH0 (middle) and FL (right) to determine the critical concentration where no tubulation is happening. The graphs display the light scattering measurements at 490 nm . The horizontal flat lines resemble the absence of tube formation. The critical tubulation concentrations of 0.4 µM for N-BAR and FL and 1.6 µM for N-BAR-deltaH0 were determined. CC = critical concentration. Adopted from [266].

2.3.7 N-BAR remodels tubes by a cooperative self-assembly on the membrane surface

The membrane tubulation depends on the concentration of amphiphysin (see 2.3.6). Therefore a closer inspection of the tubulation was monitored with different amounts of N-BAR by negative stain EM. Various N-BAR concentrations were mixed with MLVs (Table 2.1). Here it was again observed that at concentrations below the CC of 0.4 µM no tubulation occurred.

	tubulation	protein concentration	lipid concentration	protein/lipid ratio
experiment 1	yes	5.2 µM	180 µM	1 to35
	yes	0.52 µM	180 µM	1 to 346
	no	0.052 µM	180 µM	1 to 3462
	no	0.005 µM	180 µM	1 to 36000
experiment 2	yes	20.8 µM	720 µM	1 to 35
	yes	2.8 µM	720 µM	1 to 257
	no	0.28 µM	720 µM	1 to 2571
	no	0.028 µM	720 µM	1 to 25714

Table 2.1 – N-BAR concentration dependent liposome tubulation

Thus, further experiments were performed to see how the tubulation behaves at concentrations much higher and close to the critical tubulation concentration (Fig. 2.13). Therefore, 20 µM and 0.2 µM amphiphysin N-BAR were added to 720 µM 200 nm extruded LUVs and analyzed by negative stain EM (Fig. 2.13).
The concentration dependent tubulation of N-BAR revealed that at a protein concentration of 20 µM, almost all vesicles were remodelled to tubes (Fig. 2.13, A). Intact vesicles were only detected with 0.2 µM N-BAR (Fig. 2.13, C), confirming the determined CC of N-BAR of ~0.4 µM. Subsequently the length of the remodelled tubes were measured by quantifying 460 and 108 tubes for the N-BAR concentrations 20 µM (Fig. 2.13, C) and 0.2 µM (Fig. 2.13, D), respectively.
In both cases the tube length mostly ranged between 100 to 900 nm . A closer look at the distribution of length revealed that the major populations were found between 200 to 500 nm for both protein concentrations. This indicates that the N-BAR mediated tubulation occurs through a cooperative self-assembly of N-BAR domains, being induced by the lipid surface. If the helical N-BAR assembly was non-cooperative the analysis of the lower protein concentration would have shown a higher number of shorter molded tubes or slightly deformed vesicles. The H0 helix contributes to the cooperative self-assembly and lattice organization. As the H0 helix next to the BAR domain plays an important role in the amphiphysin packing the involvement of the regulatory domains in the lattice formation has to be analysed (see 2.3.8).

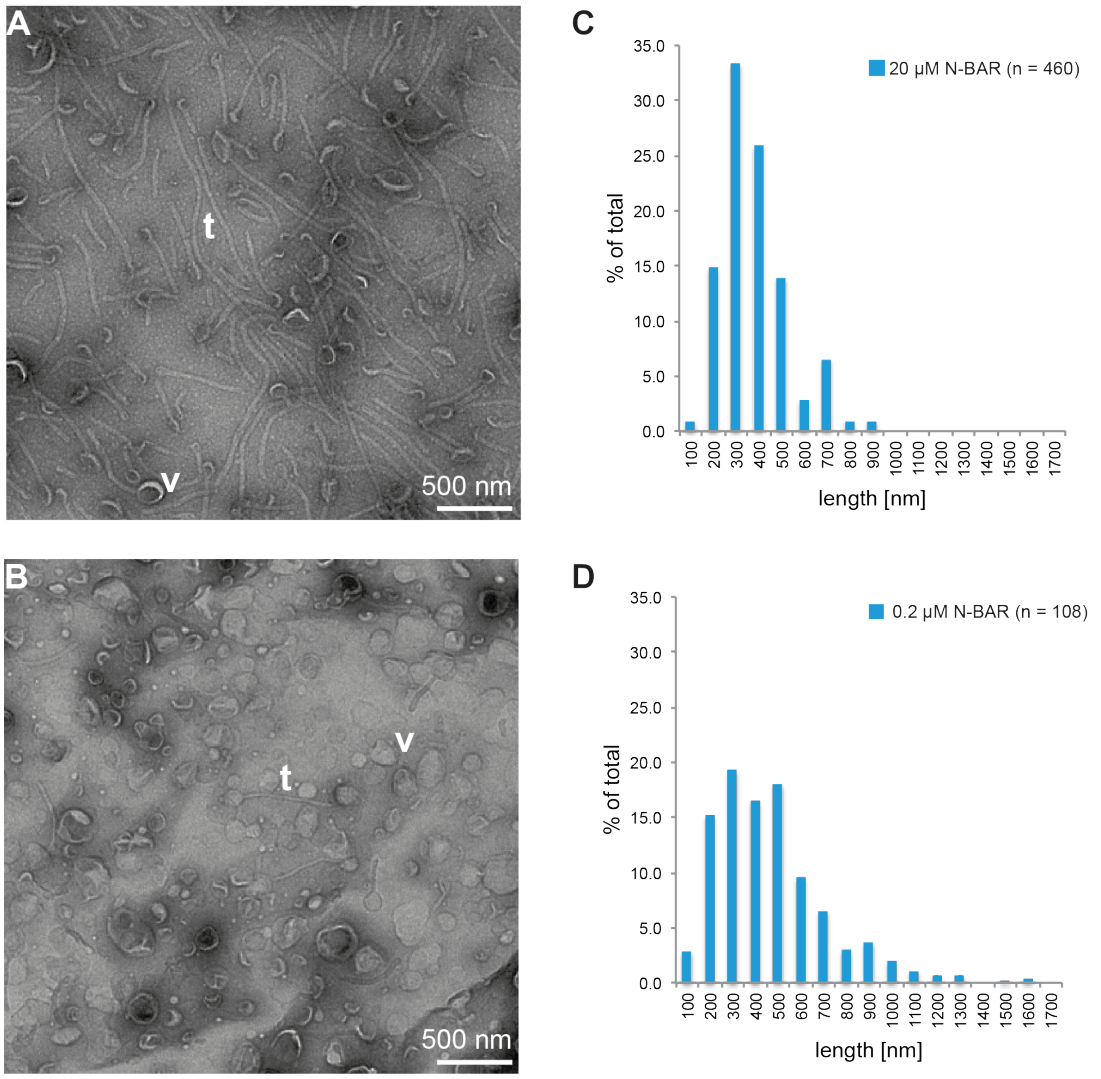

Figure 2.13 – Length measurements of N-BAR formed tubes by negative stain EM | 20 µM (A) and 0.2 µM (B) of N-BAR were mixed with 720 µM of 200 nm extruded liposomes and after 10 min negative stained for EM observations. Most of the vesicles are remodelled into tubes (A). With 0.2 µM N-BAR most of the vesicles were formed to tubes (B). The tube length is shown in a histogram (C and D). The tube length of 460 tubes of 20 µM N-BAR (A) is displayed in (C) and of 108 tubes of 0.2 µM N-BAR (B) in (D). Both N-BAR concentration show a similar length distribution of the formed tubes. t corresponds to an example of formed tubes. v corresponds to an example of vesicles. Adopted from [266].

2.3.8 No apparent involvement of the regulatory domains in the BAR lattice

It was proposed that the 8 kDa dynamin-binding SH3 domain, being the only regulatory domain, of the N-BAR protein endophilin is partly integrated into the organized packing on the tube surface [70]. Amphiphysin contains several central region domains next to its SH3 domain and therefore the whole regulatory domains would occupy more space than the SH3 domain of endophilin. In case of *Drosophila* amphiphysin the regulatory domains

have ~358 residues corresponding to ~37.9 kDA. To get insights into the involvement of the amphiphysin regulatory domains into the N-BAR lattice and membrane remodeling an extended analysis of the FL-mediated tubes was carried out (Fig. 2.14).

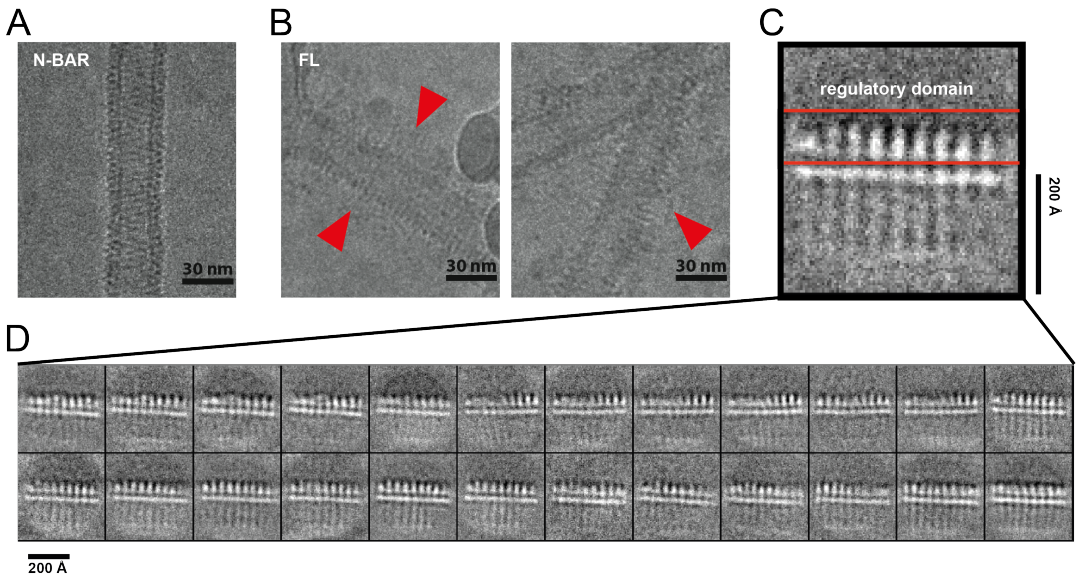

Figure 2.14 – Regulatory domain of amphiphysin analysed by cryo-EM | (A) Cryo-EM observation of N-BAR revealed visible BAR arrangement on the tube surface. (B) For FL protruding out densities on the membrane surface were observed in the cryo-EM images (red arrowheads). (C and D) 2D class average of bisected (a long the tube axis) tube segments showed stronger sticking out densities on the tube sides (C, red box) likely belonging to the amphiphysin regulatory domains.

In former sections (2.3, 2.3.3 and 2.3.4) I showed that FL was remodeling membranes into tubes looking like N-BAR (Fig. 2.7). The tubes were rigid and uniform and had a similar tube width distribution. But in contrast to N-BAR (Fig. 2.14, A), FL tubes had some needle-like density protruding out from the membrane surface (Fig. 2.14, B). The 2D class averages of the segmented tube particles revealed an interwoven stripped pattern, which was not as well-defined as in the case of N-BAR (Fig. 2.8, averages, first and second row, corresponding to N-BAR and FL, respectively). Probably this could be due to overlapping of the needle-like densities on the membrane surface, which was overlaying the density of the N-BAR domain forming the lattice on the tubes and hence was disturbing the averaging process. Furthermore, for the attempt to visualize the protruding out density on the tube surface the segmented tubes were centered and rotated into the same orientation and divided into half along the tube axis (image data collection by a Polara G2 F30, 300 kV, Gatan K2 direct detector). Afterwards the tube sides were classified (see 2D classification procedure in section 2.5.1). The 2D averages (Fig. 2.14, D) of the split tube revealed a slightly elongated density on the outside of the tube surface in comparison to the N-BAR tubes (Fig. 2.14, C). This may indicate that the regulatory domain is rather flexible on the tube surface because no dominant

averaged protein density was seen on the tube sides in the 2D classes.
The power spectrum of the 2D averages of the tube showed two periodical signals, corresponding to 44 and 55 Å in real space (Fig. 2.8, PS, second row). N-BAR-mediated tubes revealed the same layer lines in their power spectrum (Fig. 2.8, PS, first row). Thus, FL and N-BAR share the same BAR arrangement on the tube surface. The power spectrum indicated that most likely the regulatory domains are not incorporated into the helical protein packing. If the regulatory domain would be incorporated a change in the lattice arrangement would be observed by altered layer lines in the power spectrum. This implies that the sticking out extra needle-like density likely belongs to the regulatory domains. The results suggest that only N-BAR domain alone is involved in remodeling the membranes into tubes. I decided to use the N-BAR domain as smallest remodeling unit for the following structural analysis (see 2.4 and 2.5).

2.4 Structure prediction of N-BAR lattice by negative staining

As seen in section 2.3, amphiphysin N-BAR is arranging in a helical packing around the tubulated lipid vesicle *in vitro*. To determine the helical parameters of the lattice, I used the negative stained images of amphiphysin N-BAR tube and calculated the diffraction patterns and determined the likely helical lattice. Furthermore, I computationally simulated the N-BAR lattice using the known crystal structure of amphiphysin BAR domain.

2.4.1 2D Image analysis and averaging of N-BAR-mediated tubes

Before moving to cryo-EM, negative stain EM was used to get the first insights of the helical N-BAR arrangement on the membrane surface. Moreover, it was supposed to help to understand how helical lattices are formed and how to calculate them. N-BAR remodelled tubes with uniform diameter were chosen for image analysis. Those tubes were computationally segmented into boxes for image analysis. The collected segments were classified using k-means reference free classification and then 2D class averaged (Fig. 2.15, A, top, left). As the helical lattice should be arranged in a periodical manner, it could be treated like a tubular crystal. Therefore, the diffraction pattern was obtained from the averaged image (Fig. 2.15, A, top, right). Two dominant layer lines corresponding to the spacings of 45 $Å^{-1}$ and 33 $Å^{-1}$ were observed (Fig. 2.15).

2.4.2 Determination of helical parameters and helical simulation

In order to determine the helical structure, the lattice has to be drawn on the surface of the helical object (Fig. 2.15). The helical lattice can be seen as a 2D lattice, being rolled up like a cylinder (Fig. 2.15, B). The lattice arrangement can be predicted using

the diffraction patterns, by measuring the layer lines of the signals from the equator (Fig. 2.15, A, top, right). To calculate it, I used either manual angler measurement or the selection rule giving the |n| of fourier-bessel function [268]. For the determination of the helical parameters a basic helix (|n|=1 bessel order) is drawn on the helical lattice and the height between the proteins in the row (Δz) of the basic helix and the azimuthal angle ($\Delta\phi$) between the proteins in the row were determined according to the radius (r), being determined from the real-space image (Fig. 2.15, A, bottom).

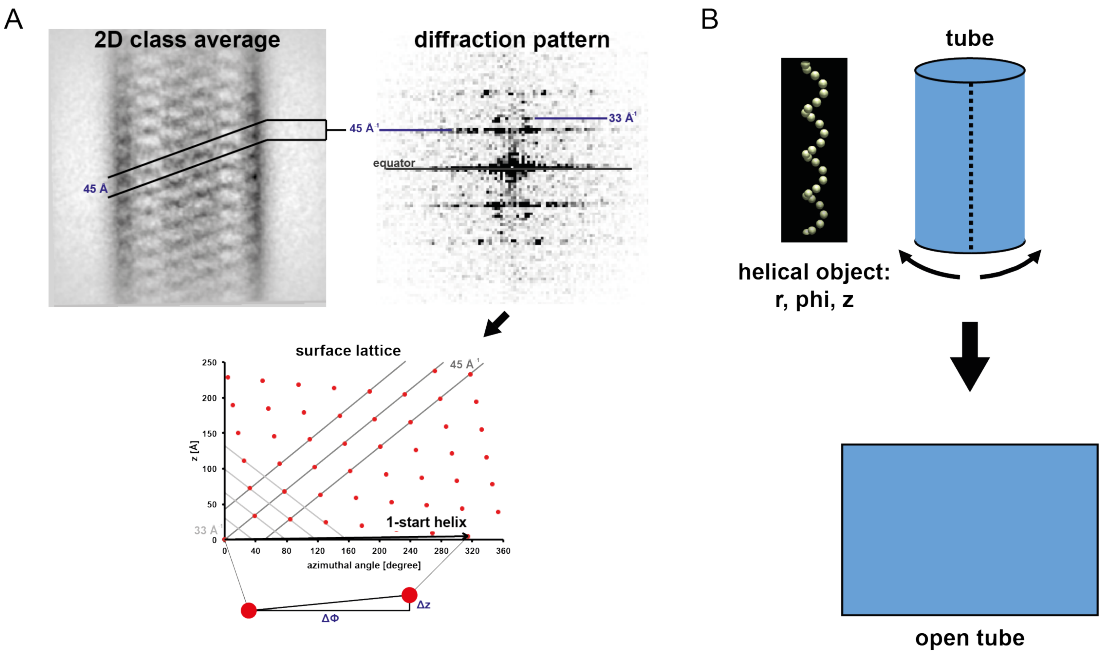

Figure 2.15 – Negative stain EM 2D class average with power spectrum and helical parameter determination | (A, top) Negative stain EM 2D average of amphiphysin N-BAR and its displayed helical array on the tube surface with corresponding calculated diffraction pattern (power spectrum). Two dominant layer lines corresponding to the spacings of 45 $Å^{-1}$ (13.5 pixel of power spectrum) and 33 $Å^{-1}$ (18 pixel of power spectrum) were observed. 13.5 pixel and 18 pixel correspond to the x-displacement of the signal from the equator in the diffraction pattern. The pixel size is 2.37 Å/pixel. Afterwards the helical parameter were determined. (B) The helical lattice can be seen as a 2D lattice, being rolled up like a cylinder. Then the cylinder was cut and unrolled so that a 2D helical array could be used for the calculation. (A, bottom) For the determination of the helical parameters the basic helix (|n|=1 bessel function) is drawn on the helical lattice and then Δz (height between the proteins in the row (basic helix)) and $\Delta\phi$ (azimuthal angle between the proteins in the row) together with r (radius, determined from the real-space image) on the helix are determined. Several helical parameters could be determined and used for further testing and computational simulating.

The diffraction of the 2D class average showed two dominant layer lines of 13.5 pixel and 18 pixel, which belong to the pattern with a periodicity in real space of 45 Å and 33 Å, respectively. Within the negative stain 2D class average I measured a dominant pattern with a periodicity of 45 Å and an angle of ~21° but no visible pattern with 33 Å (Fig. 2.15, A, top, left, black lines). Therefore I assumed that the 45 Å periodicity likely

belongs to the BAR domain which is tilted with an angle of ~21° whereas the origin of the pattern with 33 Å was not determined from the 2D class average. Subsequently, with help of the two periodicity and the tube circumference the helical lattice of the N-BAR domain was predicted.

The helical lattice can be described as a convolution of infinite numbers of helices. In my case two helices were determining the helical lattice. The helices of the 45 Å and 33 Å pattern correspond to a n=7 (7-start helix, family of lattice lines) and n=9 (9-start helix) helix, respectively (Fig. 2.15, A, bottom). But it is mathematically known that a basic helix (|n|=1 bessel order) (r, z, $\Delta\phi$) can be derived, which describes the entire helical lattice by going through all points in the helical lattice with equally spaced parallel lines[268]. Then several helical parameters were determined with Δz (height between the proteins in the row (basic helix) and $\Delta\phi$ (azimuthal angle between the proteins in the row) and tested by using helical symmetrization (Fig. 2.16).

In the simulation the atomic structure of the *Drosophila* amphiphysin BAR (pdb code 1URU)[43] was trimmed to 20 Å or 8 Å and then helically symmetrized to visualize the helical N-BAR assembly by using the helical parameters and the software bhelix of the bsoft package[269] (Fig. 2.16). Afterwards the helical simulation was reprojected into 2D for the comparison with the averaged negative stained image. The diffraction patterns of the simulated lattice were calculated and compared with the original averaged image.

In the beginning only the 45 Å periodical signal was taken into account because it was likely belonging to the BAR domain assembly. Hence, it was calculated that 6 BAR domains are arranged in one helix turn of 360°. Therefore, for the first trial the following helical parameters of Δz 7.5 Å and $\Delta\phi$ 60° were used for helical symmetrization (Appendix, Fig. A4, A). I observed that the 45 Å periodical signal belongs to the BAR domain (Appendix, Fig. A4, B). Next, it was tested if the 33 Å pattern corresponds to BAR dimer interactions such as shoulder-to-shoulder or tip-to-tip, or to the H0 helix (Appendix, Fig. A5, A and B). The BAR dimer interactions could be excluded as source for the periodicity of 33 Å because it was not determined in the power spectrum (Appendix, Fig. A5, C). For the helical symmetrization of the N-BAR domain, a modified amphiphysin BAR PDB with H0 helix and BAR domain was used (Appendix, Fig. A6). The diffraction pattern of the symmetrized N-BAR domain showed a signal at 45 $Å^{-1}$ and 33 $Å^{-1}$ and therefore, I suggested that the 33 Å pattern likely belongs to the H0 helix (Appendix, Fig. A5, A and D). Thus, new helical parameters of Δz 4.85 Å and $\Delta\phi$ 314.12° were determined because the 33 Å had to be included into the calculations (Fig. 2.17, A, right).

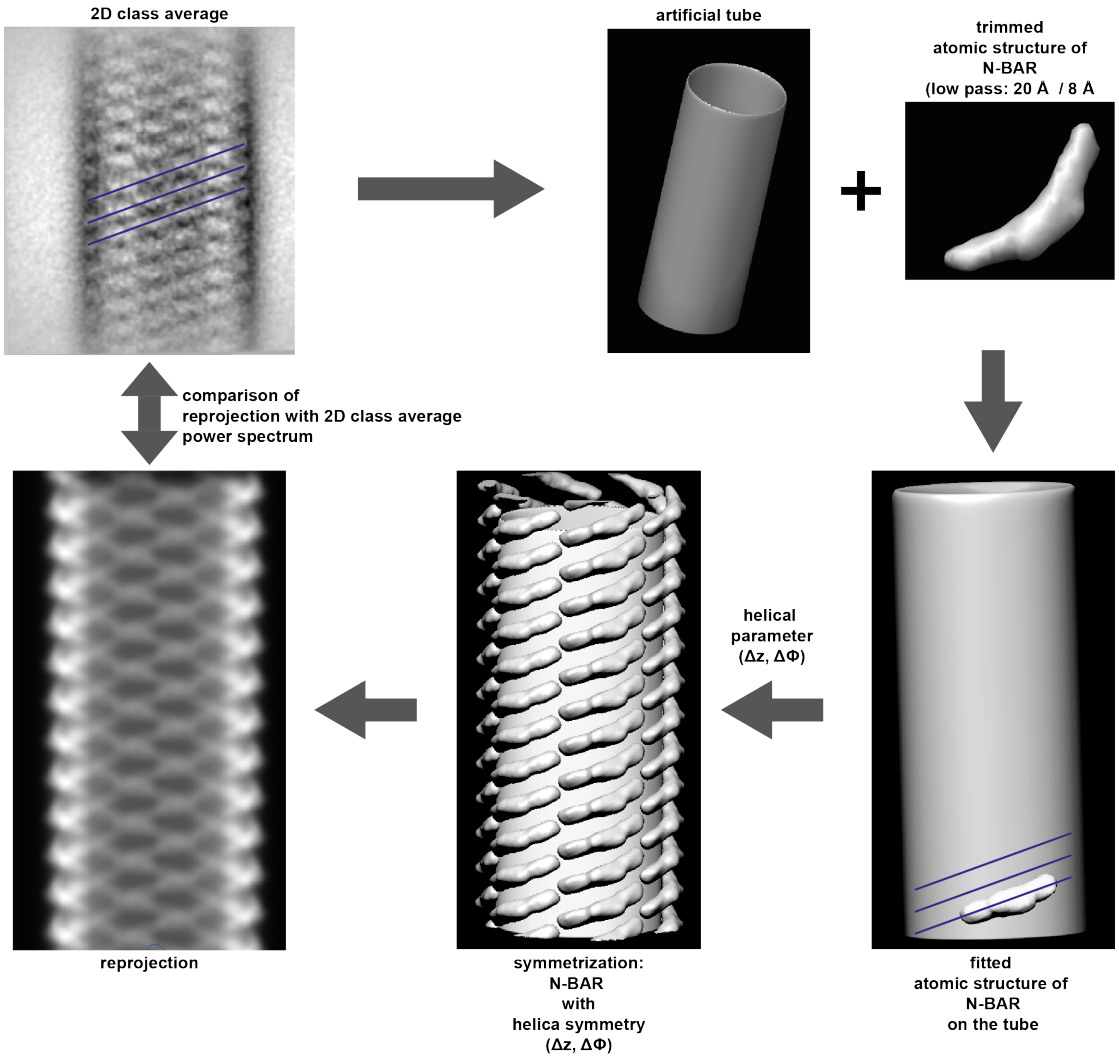

Figure 2.16 – Helical symmetrization | The helical parameters and hence, the model lattice were calculated with help of the power spectrum of the 2D class average of the segmented N-BAR mediated tubes. An artificial tube was computational created. The atomic structure of amphiphysin N-BAR (pdb code: 1URU) [43] was trimmed and low pass filtered to 20 or 8 Å. Then the low passed atomic structure was fitted to the artificial tube accordingly to the determined lattice. Then a helical simulation was conducted with the fitted atomic structure of N-BAR by using the helical parameters and the bsoft software bhelix [269]. Afterwards the symmetrized helical assembly was added on the artificial tube surface. At last a 2D projection and power spectrum of the calculated helical simulation was determined and compared with the negative stain EM 2D class averages and its power spectrum.

In addition, in the modified PDB of amphiphysin N-BAR the H0 helix was moved and rotated to get the most likely H0 helix orientation, showing the correct diffraction of 33 $Å^{-1}$ between two H0 helices (Appendix, Fig. A7, A). After several trials, one N-BAR symmetrization with a rotated H0 helix (Fig. 2.17, A, left) showed a similar 2D reprojection and diffraction pattern as the negative stain 2D class averages (Fig. 2.17, B). In the power spectrum the periodicity of 45 Å and 33 Å was observed. But in addition,

two more diffraction signals of 37 Å^{-1} and 32 Å^{-1} were found, which were not observed in the 2D class average.

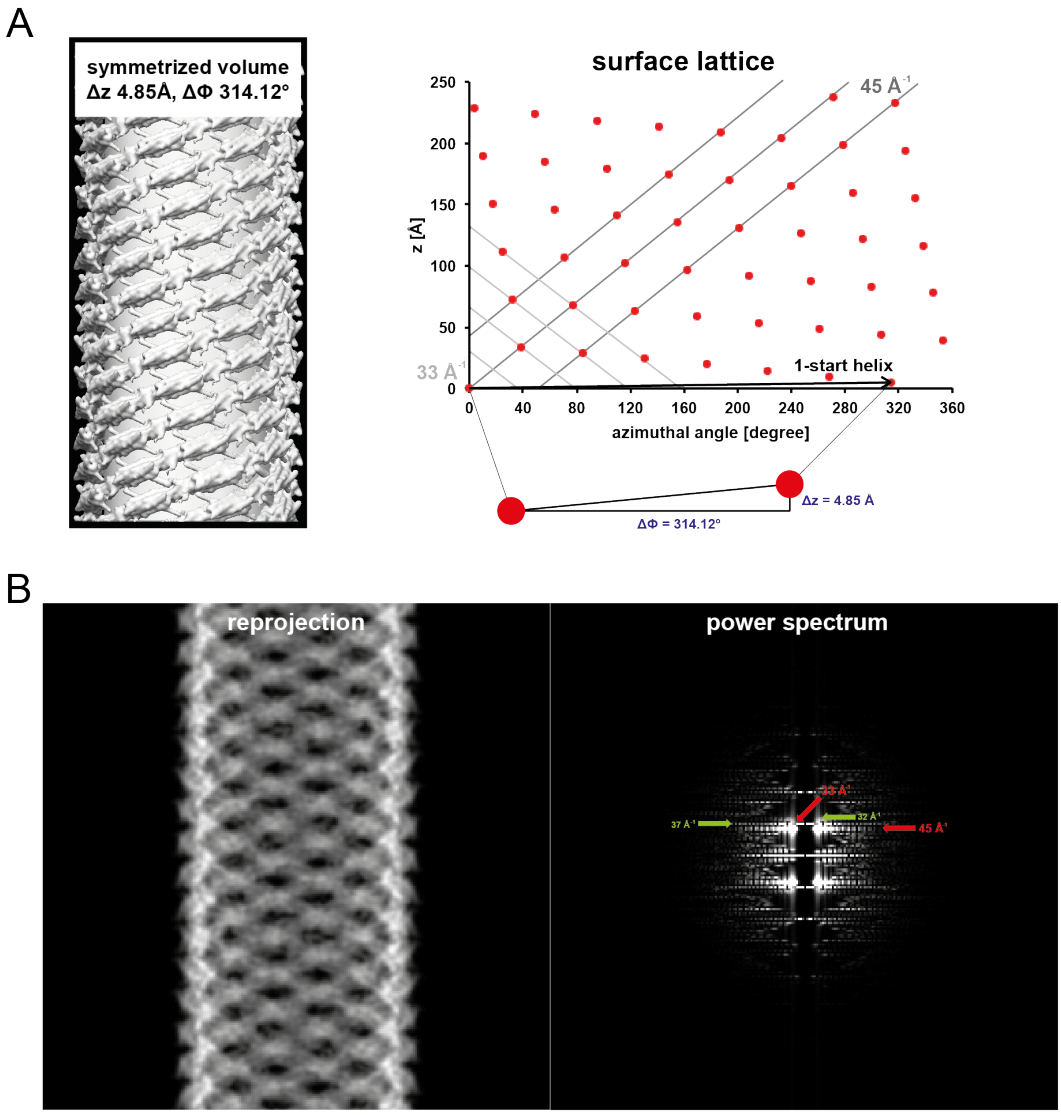

Figure 2.17 – Result of helical symmetrization of N-BAR | (A, left) Helical symmetrization of the modified N-BAR domain with rotated H0 helix with the helical parameters of Δz 4.85 Å and $\Delta\phi$ 314.12°. (A, right) Corresponding helical 2D lattice with the 1-start helix is displayed. The 1-start helix is derived from the two helices of the 45 Å and 33 Å pattern, corresponding to a n=7 (7-start helix, family of lattice lines) and n=9 (9-start helix) helix, respectively. (B, left) Reprojection of the symmetrized volume. (B, right) The calculated power spectrum of the reprojection showed diffraction signals of 45 Å^{-1}, 37 Å^{-1}, 33 Å^{-1} and 32 Å^{-1}

.

A quality control was performed to find the source of these two diffraction signals. The BAR domain and the H0 helix alone were symmetrized to "deconvolute" the diffraction signals (Fig. 2.18). The power spectrum of the near and far side of the symmetrized BAR domain showed periodicity of 45 Å, 37 Å, 33 Å and 32 Å (Fig. 2.18, A, top row). But

the diffraction of only one side was lacking the diffraction signals of 33 $Å^{-1}$ and 32 $Å^{-1}$ (Fig. 2.18, A, bottom row). To get an idea about the particular diffraction signals of the symmetrized BAR domain, several band pass filters were used (Appendix, Fig. A8). The band pass filter of 36 - 39 Å, 43 - 47 Å and 36 - 39 Å plus 43 - 47 Å showed a periodical pattern, which was similar to the BAR domain arrangement. In the band pass filter of 32 - 35 A a different periodical pattern was observed, which did not match to the BAR symmetrization. Then the same procedure was used for the H0 helix symmetrization (Fig. 2.18, B). After the symmetrization of the H0 helix the power spectrum showed similar diffraction signals as the symmetrized N-BAR (Fig. 2.17).
All power spectra before were determined without adding an additional tube, representing the lipid membrane, to the symmetrization. Therefore, to see if some of diffraction signals disappear, an artificial tube was added to the symmetrized H0 helix density (Appendix, Fig. A9, A). The diffraction pattern became much weaker and the signal at 37 $Å^{-1}$ got lost. Moreover, a band pass filter was done to see from where the signals of 33 Å and 37 Å came. The band pass of Å 32 - 35 Å likely showed a pattern of the arranged H0 helices and the band pass of 36 - 39 Å undefined pattern with a slightly larger spacing was observed. An additional artificial tube was also added to the symmetrized N-BAR domain were the diffraction signal of 37 $Å^{-1}$ became significantly weaker and the 32 $Å^{-1}$ signal got lost (Appendix, Fig. A9, B).
Furthermore, I analyzed how the power spectrum alters if the distance between the BAR domains in one lattice row became larger. The further apart the BAR domains were from each other the more significantly the diffraction pattern changed (Appendix, Fig. A10). Only when the BAR domains were close to each other the power spectrum was comparable to the 2D class average.
After systematical searches, I determined that the spacing of 45 $Å^{-1}$ is due to the BAR domain arrangement and the spacing of 33 $Å^{-1}$, which is roughly perpendicular to the arrangement of the BAR, is likely from the N-terminal amphipathic helix. The 2D reprojection of the helically symmetrized volume and the diffraction pattern look comparable to the averaged negative stained image. The simulated images showed additional diffraction signals of 32 $Å^{-1}$ and 37 $Å^{-1}$, which likely belong to the H0 helix and the BAR domain, respectively. It could be concluded that both signals of the symmetrization would vanish by adding background noise and lipid densities, which is the native situation. Moreover, it could be proposed that the adjacent BAR domains in one lattice row are closely arranged to each other. After the first trial to understand the N-BAR arrangement and how to calculate the helical parameters, cryo-EM image data sets were collected, showing the formed N-BAR tubes and the N-BAR arrangement on the membrane surface in its native state (see 2.5).

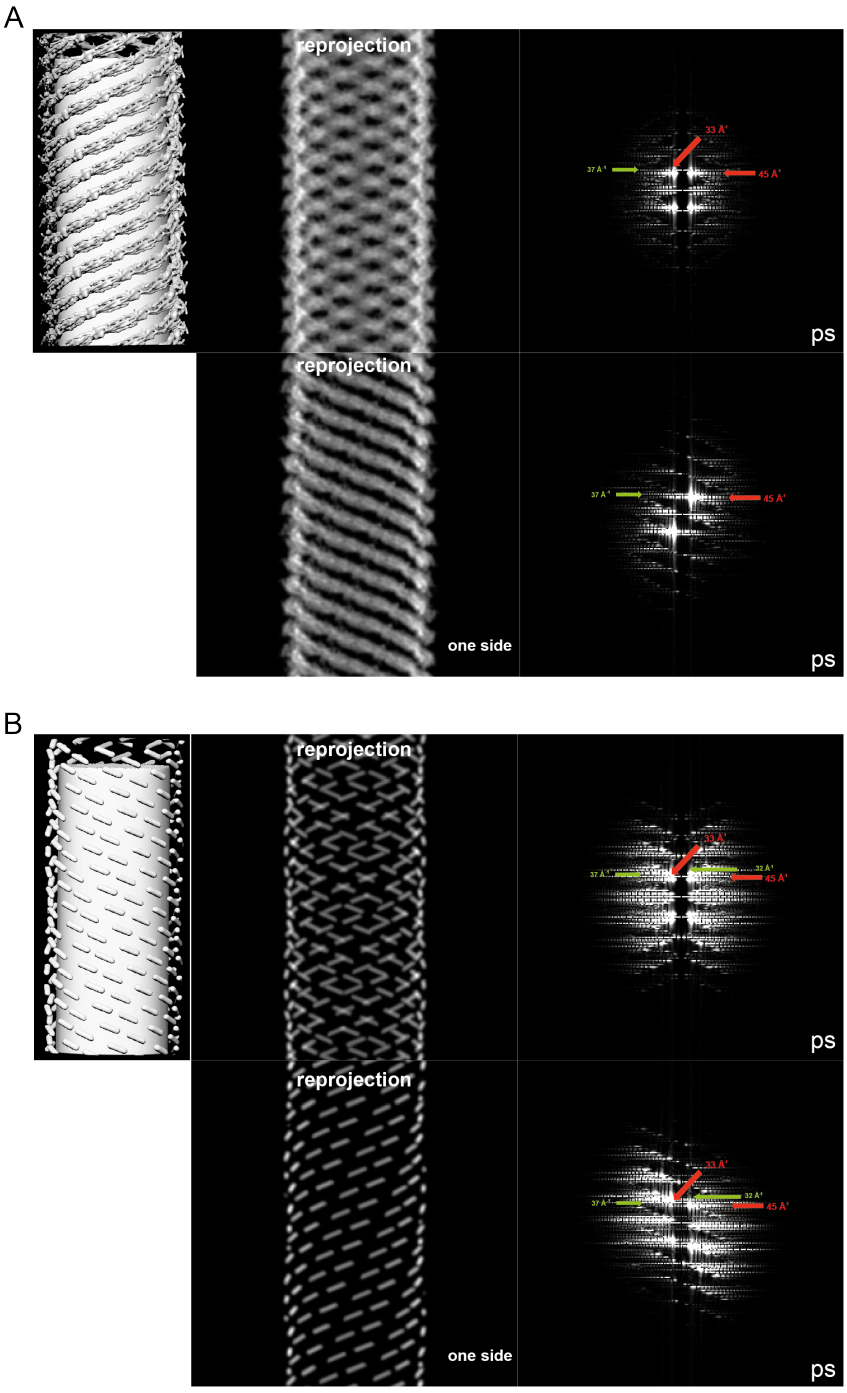

Figure 2.18 – **Helical symmetrization of the BAR domain and the H0 helix** | (A) The BAR domain was helically symmetrized with the helical parameters of Δz 4.85 Å and $\Delta\phi$ 314.12°. (A, top) From the power spectrum of the reprojection (near and far side of the helical volume), periodical pattern of 45 Å, 37 Å and 33 Å were determined. (A, bottom) The power spectrum of only one side of the reprojection showed periodical pattern of 45 Å, 37 Å, resembling the helical BAR arrangement. (B) The H0 helix was helically symmetrized with the helical parameters of Δz 4.85 Å and $\Delta\phi$ 314.12°. (B, top) From the power spectrum of the reprojection (near and far side of the helical volume), diffraction pattern of 45 $Å^{-1}$, 37 $Å^{-1}$ and 33 $Å^{-1}$ and 32 $Å^{-1}$ were calculated. (A, bottom) The power spectrum of only one side of the reprojection showed weaker periodical pattern of 45 Å and 37 Å and stronger signals of 37 Å and 33 Å, likely corresponding to the H0 helix. PS = power spectrum

2.5 3D helical reconstruction of the N-BAR scaffolding on membrane tubes by cryo-EM

2.5.1 First structural insights into the N-BAR lattice formation

Morphology studies in section 2.3.4 and 2.3.8 revealed that amphiphysin N-BAR with N-terminal amphipathic H0 helix and its BAR domain is the minimal functional domain to remodel membranes into tubes for structural investigation by cryo-EM. To get a first structural insight into the helical N-BAR packing on the tube surface, cryo-EM data sets of N-BAR was taken by a F20 electron microscope with a CCD camera. For imaging 5 µM N-BAR were added to 180 µM LUVs (200 nm , 2POPG:1POPE) and then vitrified. ~300 cryo-EM images (F20, 200 kV, magnifications 62000x) were taken and the tube densities were segmented into boxes (32772 boxes). The CTF (contrast transfer function) of the images was corrected by flipping phases using CTFFIND3 [270] and bctf of the Bsoft software package [269]. These particle segments were classified using reference-free alignment by eman [271], multivariate statistic analysis (MSA) and then averaged into 2D classes by hierarchical ascendant classification (HAC), being implemented into SPIDER (Fig. 2.19) [272,273].

At first, the collected particles were aligned and classified by the k-means reference-free procedure, being implemented into eman [271], and initial averages were obtained. The initial averages gave an overview of the potential helical N-BAR arrangements on the tube surface (Fig. 2.19, A). The segmented particles were 2D classified by using a MSA and HAC approach in SPIDER [273,274] and the initial averages as reference. The processes were iterated several times and the final averages were used for the helical parameter determination (Fig. 2.19, B). The class-averages showed rigid uniform tubes with a discrete lattice arrangement, suggesting that the helical packages are made of several, but distinct protein positions in the helical array around the tubes. The remodelled tubes showed a distribution in their width, which may give the indication for several protein-membrane interactions. This is in contrast to endophilin where the tubes differ in their width and straightness a long the tube axis [100]. The class averages were sorted into subclasses, according to their diameter and surface pattern. Afterwards they were used for helical 3D reconstructions to understand how the protein-protein interactions are changing in relation to the tube diameter. The structural approach will give insights into how the assembly is made and what BAR arrangement change could lead to the formation of the emerging small vesicles from the tubes.

In the beginning, class 8 (3427 particles), which showed a dominant BAR arrangement in the 2D class average, was selected for further calculations (Fig. 2.19, C). For this, the diffraction pattern of the averaged image was obtained and two spacings at 43Å^{-1} and 57Å^{-1} could be observed. The helical parameters were estimated by determining the Fourier-Bessel function from the layer lines of the power spectrum [275]. They showed a

helical rise per subunit (Δz) of 3.81 Å and an azimuthal rotation per subunit ($\Delta\phi$) of 55.99°.

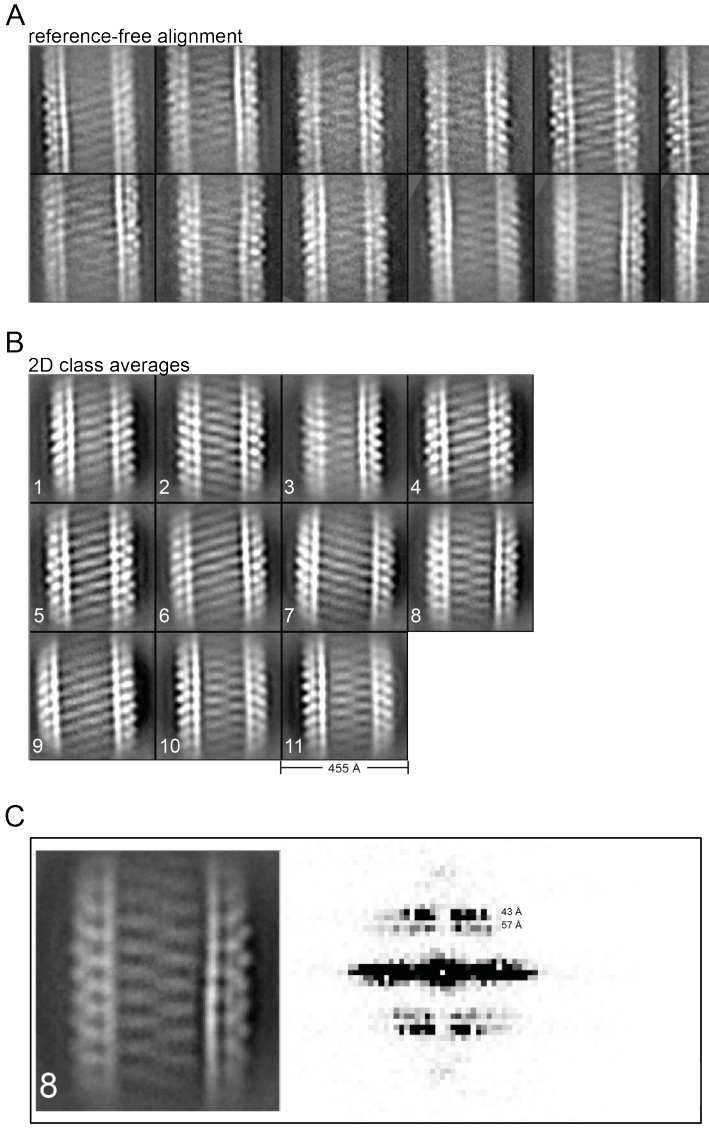

Figure 2.19 – Classification and 2D class averages of a F20 cryo-EM data set with CCD camera and a magnification of 62000x | (A) The alignment and classification of the collected segmented particles (box size of 455 x 455 Å) of the N-BAR remodelled tubes by k-means reference-free approach was performed and an interwoven pattern of the BAR assembly on the tube surface was observed. (B) After multi-reference alignment with MSA 2D class averages were obtained. The 11 class-averages show discrete lattice packages of amphiphysin N-BAR on the tubulated membranes. The tubes revealed various populations of tube diameters. (C) Class 8 (3427 segmented particles) was selected as example for the calculation of the power spectrum. For this, the diffraction pattern of the averaged image was calculated and two spacings at 43Å^{-1} and 57Å^{-1} could be observed. With the help of the power spectra, the following helical parameters of Δz of 3.81 Å $\Delta\phi$ of 55.99°were determined.

The IHRSR (iterative helical real-space reconstruction) [276] method, being implemented into SPIDER, was used to perform the 3D helical reconstruction. IHRSR utilize algorithms

of the single particle analysis in combination with real-space helical averaging and imposition of helical symmetry. In this method the segmented particles are aligned and orientated to the reprojections of an initial reference model volume by projection matching being a single particle technique[277]. The segmented particles in the aligned subclasses are back-projected to generate an initial asymmetric 3D volume. A search for correct helical parameter is processed on the created 3D volume to empirically determine the helical symmetry, which is afterwards imposed onto the 3D volume. The helical symmetric 3D volume is employed as the new "reference" model and several iterations of the cycle are following. After many iterations a helical reconstruction without density changes is calculated (Fig. 2.20).

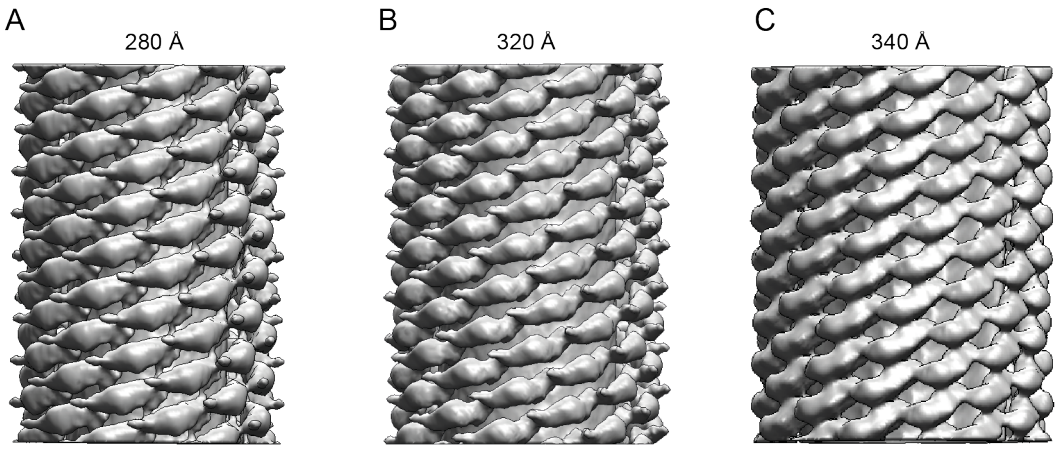

Figure 2.20 – Helical 3D reconstruction of N-BAR remodelled tubes (cryo-EM, F20, magnification of 62000x, CCD camera) | For all helical reconstructions of the N-BAR formed tubes with a diameter of 280 Å(A), 320 Å (B) and 340 Å (C) the BAR domain could be clearly observed as a lattice around the tube. The here displayed helical reconstructions by IHRSR without refinement were performed by using 2x binned particles.

In the helical 3D reconstruction of class 8 the helical polymer of BAR domains, having their banana-like shape, could be reconstructed on the tube surface, confirming the chosen helical parameters (Fig. 2.20, B). If the parameters are wrongly determined no helical BAR arrangement would be visible on the tube surface. The power spectrum of projections of the 3D volume revealed that the periodical pattern of 43 Å in real space likely belongs to the BAR domain. The spacing of 57Å is less obvious, but could be from the H0 helix. A dominant H0 helix density was not visualized in the reconstruction due to low resolution. It seems that the calculated helical parameters are correct for class 8 and the BAR domain could be clearly observed as a lattice around the tube (Fig. 2.20, B).

Classes 8, 10 and 11 (10763 particles) have the same observed tube diameter and helical parameter. Thus, the particles of these classes were combined and IHRSR was performed, showing the similar reconstruction like class 8. Furthermore, for class 1 (3477 particles), having the periodical pattern like class 8 but smaller tube width, the helical parameters

of Δz 25.18 Å and Δϕ 86.47°were determined, implying the existence of a 6-start helix (Fig. 2.20, A). The 3D reconstruction showed a BAR domain arrangement on the tube surface (Fig. 2.20, A). Moreover, for class 6, 7 and 9 (10217 particles) the thickest tube diameter was measured and a 2-start helix with the helical parameters of Δz 7.06 Å and Δϕ of 50.50°was calculated (Fig. 2.20, C). The reconstruction showed a thicker tube, being helical surrounded by BAR domains (Fig. 2.20, C). The first structural analysis of N-BAR revealed 3 types of tubes with 340 Å, 320 Å, and 280 Å in width with distinctive lattice formations. In addition, to get insights into the helical packing, including the helical parameters, the density of N-BAR on the tubes surface was analyzed by mass-per-length (MPL) measurements (see 2.5.2). As the width variable mediated tubes show a similar protein-protein and protein-membrane interaction the diversity in the calculated helical parameters has to be verified by MPL.
In all cases the amphipathic helices were not revealed in the reconstructions. Thus, it would be optimal to achieve higher resolution to visualize the N-terminal H0 helix. To gain a higher resolution, I moved to a higher magnification and a lower acceleration voltage, giving better contrast and being suitable for the FEI Eagle CCD camera at the F20 microscope. With a magnification of 80000x (120 kV), corresponding to a pixel size of 1.34 Å/pixel, around 200 images by a F20 with a FEI Eagle CCD camera, corresponding to 12197 segmented boxes, were collected. Then the the segmented tubes were 2D classified (Fig. 2.21). The classification showed similar looking 2D class averages like observed in the lower magnification (Fig. 2.19).

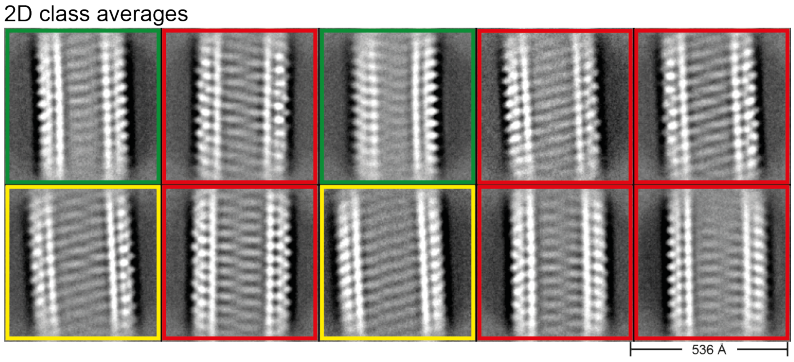

Figure 2.21 – 2D class averages of a F20 (120 kV) cryo-EM data set with CCD camera and a magnification of 80000x | After the alignment and classification of the collected segmented particles of the N-BAR remodelled tubes (box size of 536 x 536 Å) by multi-reference alignment with MSA, 2D class averages were obtained. The 10 class-averages show discrete lattice packages of amphiphysin N-BAR on the tube surface. The 2D class averages revealed various populations of tube diameters of "thin" with ~270 Å (green), "medium" with ~290 Å (red) and thick" with ~300 Å (yellow).

The N-BAR mediated tubes showed a similar diameter distribution. As before several classes could be combined and the 3D helical reconstructions by IHRSR were performed (Fig. 2.22). The 3D reconstructions revealed the characteristic banana-like shape of the BAR units, making array-like arrangements. Again 3 tubes types phrased like "thick"

300 Å (yellow), "medium" 290 Å (red), and "thin" 270 Å (green) in width with distinctive BAR arrangement were observed.

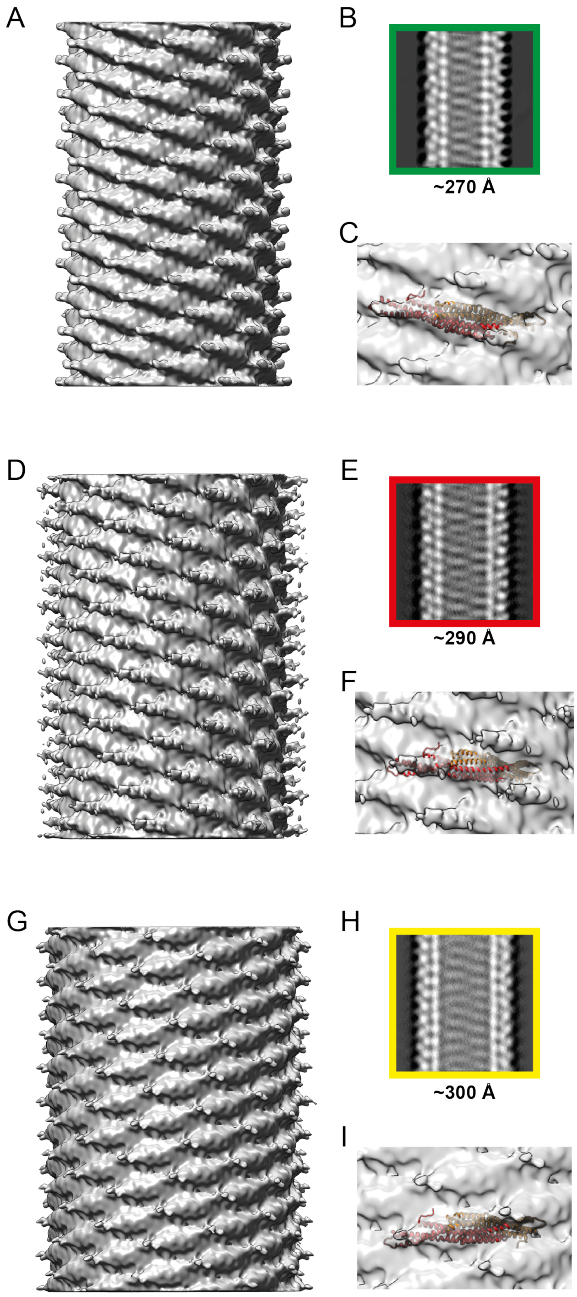

Figure 2.22 – Helical 3D reconstruction of N-BAR remodelled tubes (F20, magnification of 80000x) with fitting of the atomic structure of N-BAR | For all helical reconstructions of the N-BAR-mediated tubes (cryo-EM with a F20, magnification of 8000x, CCD camera) with a diameter of ~270 Å (A to C, green), ~290 Å (D to F, red) and ~300 Å (G to I, yellow), the BAR domain could be clearly seen as a helical arrangement around the tube. The helical reconstructions by IHRSR were performed by using the corresponding particles of the 2D class averages with refinement. (A, D and G) shows the helical reconstruction, (B, E, H) the helical reconstruction projection and (C, F and I) the fitted atomic structure of amphiphysin N-BAR (pdb code: 1URU). The helical 3D volumes were low-pass filtered to 9 Å.

The 3D reconstruction of these different types of the amphiphysin N-BAR tubes were carried out by applying the helical parameters, which were calculated before. The thin (2386 particles, Fig. 2.22 A to C), medium (4370 particles, Fig. 2.22 D to F) and thick (1738 particles, Fig. 2.22 G to I) tube types had the same helical parameters like class 1, class 8, 10, 11 and class 6, 9, respectively, in the data analysis at lower magnifications. Unfortunately, the resolution was only slightly improved to approximately 13 to 14 Å. In addition, the atomic structure of *Drosophila* amphiphysin N-BAR (pdb code: 1URU) [43] was docked into the helical reconstructions (Fig. 2.22, C, F and I). The atomic structure was fitting very well into the banana-shape density corresponding to the BAR dimer.
For the next image data acquisition a Polara G2 F30 electron microscope (300 kV) with a Gatan K2 direct detector was used to gain high resolution and thereby get more insight into the helical assembly of N-BAR (see 2.5.3).

2.5.2 N-BAR polymers and their packed assembly

To gain insights into N-BAR density on the tube surface mass per length measurements were carried out by scanning transmission electron microscopy (STEM) (Fig. 2.23). The image collection was performed by the Brookehaven STEM Facility. The MPL data were quantified by measuring the intensities in the images being detected via STEM in the dark-field mode. STEM image intensities are proportional to the mass densities (per unit area) of the unstained sample, which means that the background shows low intensities (weak electron (e^-)-scattering) and the membrane tubes, being surrounded by proteins, have high intensities (strong e^--scattering). To quantify the determined intensity values, a comparison of the tube intensities with the intensities of reference objects with a known mass densities was done by co-deposition of the control reference next to the tubes on the grid.
I observed that the N-BAR tubes were more or less consistent but showed a range in the diameter (Fig. 2.23, A, blue). For the analysis relatively straight tubes were used. As control the rigidly organized helical polymer of tobacco mosaic virus (TMV) was used (Fig. 2.23, A, yellow). N-BAR revealed a broader distribution of the MPL as TMV (13 ±0.7 kDa/Å (Fig. 2.23, B, yellow) and an average of 28 ±3 kDa/Å was determined (Fig. 2.23, B, blue). This shows that the tubes are not having a uniform package. The measured density is the sum of lipids and proteins. The next step was to figure out how the proteins contributed to the mass. The lipid density is approximated to be ~50Å^2/lipid. For a 300 Å width tube it was determined that ~18 lipids locate on the tube per Å, which is relating to a mass of ~14 kDa. Thus, the mass of N-BAR is ~14 kDa/Å. The density of the 56 kDa amphiphysin N-BAR dimer allocates 4 Å of the axial space along the tube axis. This fits to the calculated helical parameters of the medium tube with a helical rise of 3.81 Å. Consequently, for the following helical reconstructions the main focus was upon the helical parameter with Δz of 3.81 Å and $\Delta\phi$ of 55.99°(see 2.5.3.

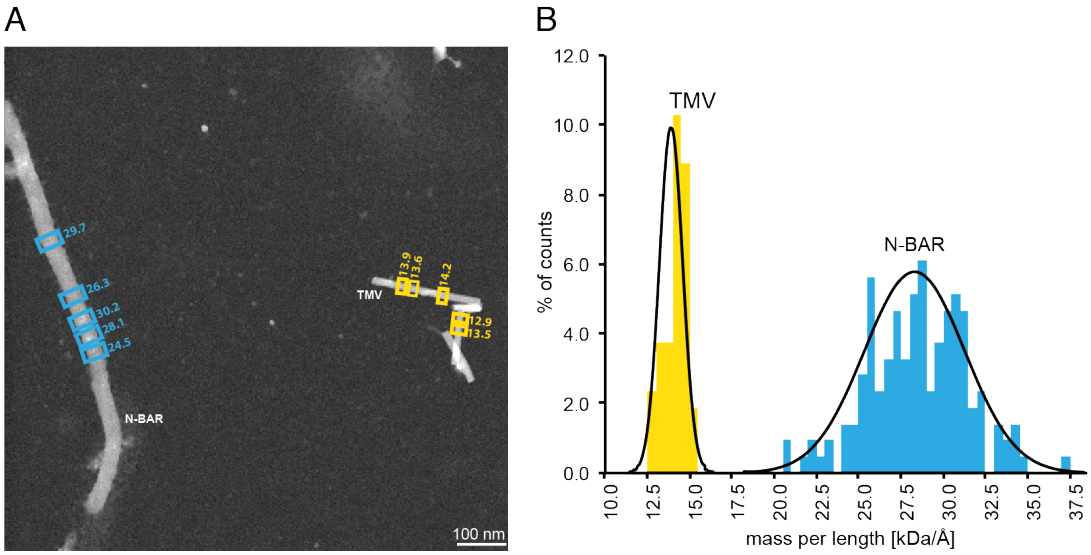

Figure 2.23 – Mass per length measurements of amphiphysin N-BAR on the membrane surface by STEM | (A) STEM image showed N-BAR remodelled tubes with co-deposited internal control of tobacco mosaic virus. 20 µM N-BAR were added to 720 µM of liposomes and immediately used for STEM measurements. The boxes show the mass per length (MPL) measurements with corresponding MPL values (blue: N-BAR, yellow: TMV). (B) The histogram displays the distribution of the measured MPL for N-BAR (blue) with an average of 28 ±3 and TMV (yellow) with 13 ±0.7. N-BAR revealed a broader distribution showing that the N-BAR tubes were not uniform packed due to the range of tube diameters. Adopted from [266].

2.5.3 Helical 3D reconstruction of N-BAR-mediated tubes with a tight N-BAR packing

To achieve higher resolution the micrographs were taken by a Polara G2 F30 microscope (300 kV) with a Gatan K2 summit direct detector. In contrast to a CCD camera, converting the incoming electrons into photons via scintillator before signal detection, the electrons are directly detected and converted into a signal. For the image data acquisition several frames can be taken during the exposure times, which is in contrast to the CCD where only one frame (image) is taken over the whole exposure time. Hence, direct detectors contain the movie mode option, which is removing sample movement during the exposure by aligning the collected frames. All of these new improvements in image detection are helping to gain higher resolution.

For the sample preparation 20 µM N-BAR were added to 720 µM LUVs (2POPG:1POPE) of 200 nm and afterwards the specimen was vitrified (see 4.2.6, Grid preparation for cryo-EM in Methods). Around 280 micrographs were taken recorded by a K2 direct detector, frame aligned (frames 10 to 40) and CTF corrected by phase flipping with CTFFIND3 [270] and bctf [269]. The collected tubes were segmented into 26754 segmented particles. Then the particles were classified by using the reference free 2D classification option in Relion [267] (Fig. 2.24). To gain better signal-to-noise ratios in the class averages, 7331 segments with bad quality were removed during several classification iterations. In

the end, 19423 boxed segments were classified and 50 class averages were obtained (Fig. 2.24, A).

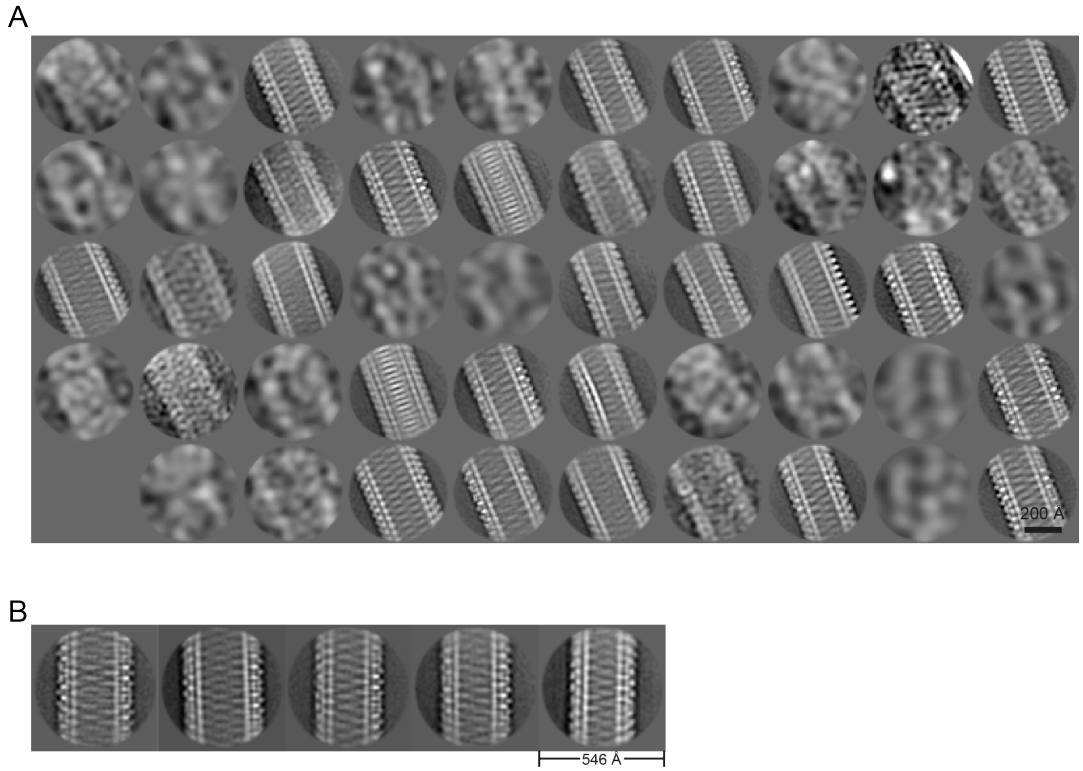

Figure 2.24 – 2D averages of N-BAR remodelled tubes (Polara, 300 kV, magnification of 61000x, K2 direct detector) | After CTF (phase-flipping) of the cryo-EM micrographs the N-BAR remodelled tubes were boxed into 26754 segmented particles (300 x 300 pixel corresponding to 546 x 546 Å). The segmented particles were classified via reference-free classification implemented into Relion software. To gain higher signal-to-noise ratios of the class averages, 7331 segments with bad quality were removed and afterwards 19423 boxed particles were used to get 50 2D class averages (A). (B) Five 2D classes with the most distinct features were used for the following helical reconstructions by IHRSR. Adopted from [266].

For the amphiphysin N-BAR structure analysis five classes with various diameters, showing the most distinct features, were selected (Fig. 2.24, B). The tube diameter of the classes were 280, 312, 262, 250 and 242 Å with 1948, 1392, 692, 1173 and 1372 segmented particles, respectively. The helical 3D reconstructions of each class were performed by IHRSR with the starting helical parameters of Δz of 3.81 Å and $\Delta\phi$ of 55.92°. During the refinement the "hsearch" option was switched on to get the local conversing point. Moreover, the azimuthal increment was set to 1 degre and the out-of-plane tilt to 1 degree increment up to $\pm$ 10 degree. Because of this 72000 reprojection images from the 3D volume were received being used for the projection matching.

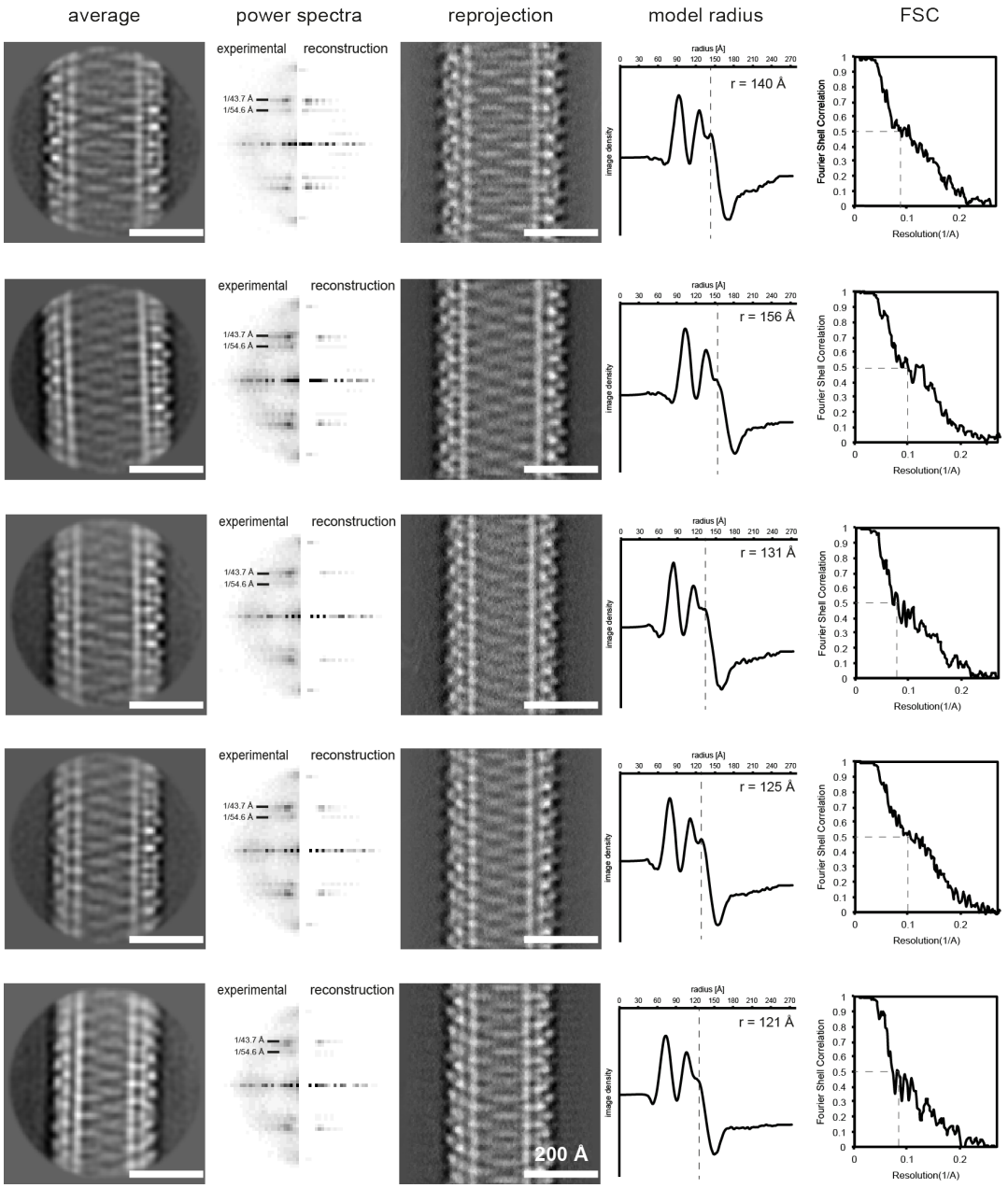

Figure 2.25 – Quality control data of the five chosen 2D classes of N-BAR mediated tubes | First column (average) shows the 2D class averages. Second column (power spectra) displays the averaged power spectra of the 2D class averages (left) and reprojections of the helical reconstructions (right), which are fitting to each other by showing the same layer lines of ~44 $Å^{-1}$ and ~55 $Å^{-1}$. The third column (reprojection) shows the projections of the helical reconstructions by IHRSR. In the fourth column (model radius) the density profiles (line-scan) of the reconstruction reprojections, revealing the tube radius. The line-scan shows three peaks from the tube center, belonging to inner leaflet, outer leaflet and the BAR protein density on the membrane surface. The fifth column (FSC) displays the fourier shell correlation (FSC) profile with the calculated resolution at the FSC=0.5 cutoff criteria. The first, second, third, fourth and fifth row belong to the tubes with a radius of 140 Å with a resolution of 10.3 Å, 156 Å with a resolution of 11.2 Å, 131 Å with a resolution of 10.9 Å, 125 Å with a resolution of 10.9 and 121 Å with a resolution of 12.1 Å. Adopted from [266].

Due to the possibility of some heterogeneity different helical parameter were calculated and used for helical 3D reconstructions. At the end the final helical parameter approximate to a rise per subunit of 3.81 Å, an azimuthal rotation of 55.92° for the main class with a diameter of 280 Å shown in Figure 2.26. For the other four classes related helical parameters (Δz, $\Delta\phi$) were determined as 3.83 Å, 55.96°, 3.84 Å, 56.01°, 3.82 Å, 55.93° and 3.85 Å, 55.99° for the tubes with a diameter of 312 Å (Fig. 2.27, A), 262 Å (Fig. 2.27B), 250 Å (Fig. 2.27, C) and 242 Å (Fig. 2.27, D), respectively.
I evaluated the 3D helical reconstructions by analyzing the density map and by comparing the resulting reprojections with the 2D class averages and the corresponding power spectra (Fig. 2.25). These 3D reconstructions of the Polara data set were used as the final reconstructions for the structural study of amphiphysin N-BAR.
All reconstruction showed the helical N-BAR assembly on the tube surface. It was observed that the banana-like shape of the N-BAR was winding around the membrane in a protomer arrangement, revealing a tight packing. As there is a distribution in the tube width and heterogeneity in the lattice assembly the resolution was limited to medium range from 10.3 to 12.1 Å by a FSC cut off of 0.5 (see Table 2.2).

Tube width	Resolution
280 Å	10.3 Å
312 Å	11.2 Å
262 Å	10.9 Å
250 Å	10.9 Å
242 Å	12.1 Å

Table 2.2 – Resolution of the helical reconstruction of the N-BAR mediated tubes

With this cryo-EM data set the helical rise was calculated to be ~3.8 Å, fitting to the MPL analysis of 4 Å/N-BAR (Fig. 2.23). In all reconstructions the translation of the BAR assembly along the tube axis corresponds to a 1-start helix.
To have a closer look at the tube width, a line-scan of the reprojections across the tube axis was performed, revealing three peaks from the center of the tube (Fig. 2.25, fourth column). The first peak from the center belongs to the inner leaflet of the membrane bilayer. The outer membrane was displayed as the second peak. The third and last peak belonged to the N-BAR protein density in the reprojections. The distance between the inner and outer of the lipid bilayer membrane was determined to be ~33 Å (Fig. 2.26, B and Fig. 2.25, first row).

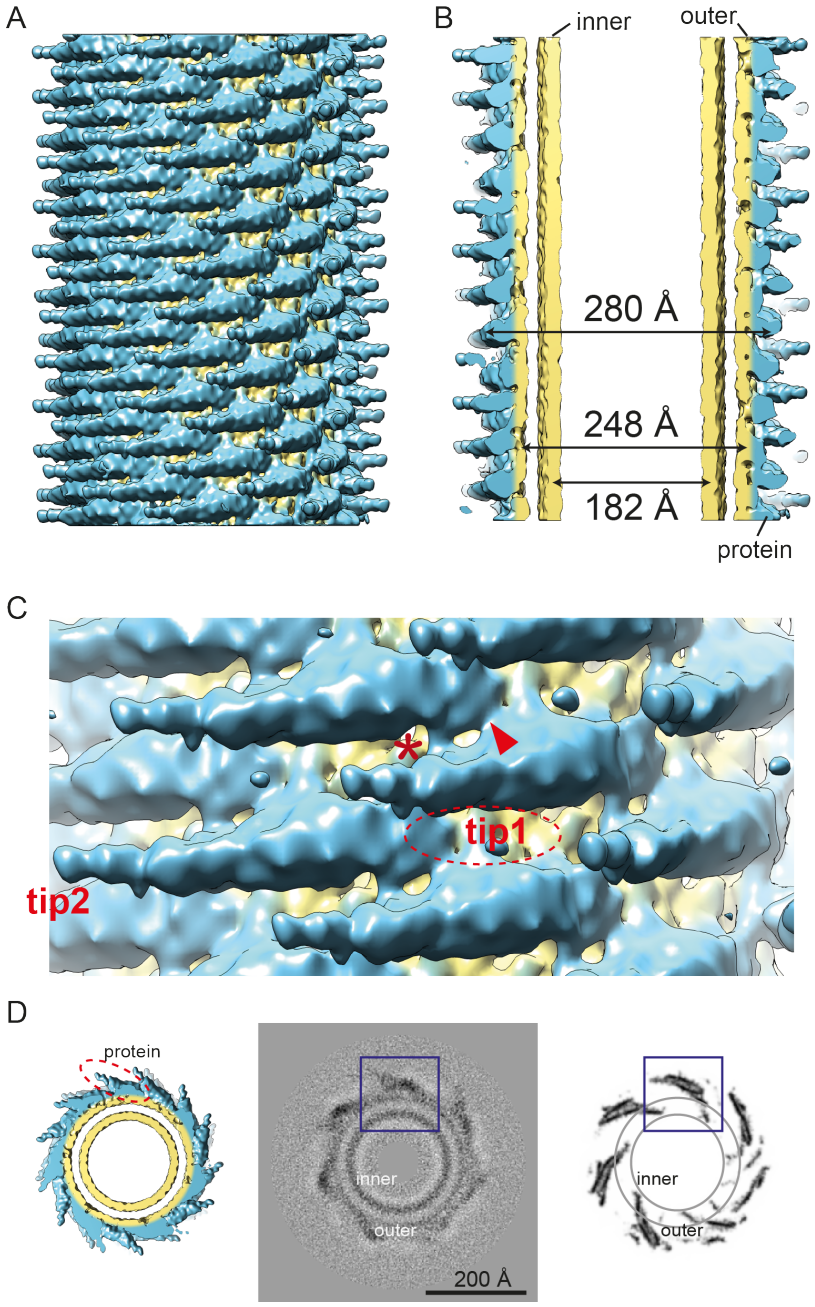

Figure 2.26 – 3D reconstruction of amphiphysin N-BAR remodelled tubes with a tube width of 280 Å | The density of the BAR domain is colored in blue and the lipid tube in yellow. The side view of the helical reconstruction by IHRSR is shown in (A). (B) Cross-section through the tube along the tube axis reveals an inner leaflet diameter of 182 Å, outer leaflet of 248 Å, colored in yellow. The tube diameter with protein density is 280 Å. The distance between inner and outer leaflet is 33 Å. (C) Zoom in of (A) displays that one tip of the BAR domain is immersed into in the tube membrane (tip1) and the other tip protrudes out of the membrane (tip2). An additional density is visible, which is connecting the neighbouring BAR domains (*). A further possible connection between the adjacent BAR domains was observed (red arrowhead). End view of the tube (D) shows that the protein density is protruding out of the tube surface (left). In the projection of the end view the sticking out protein density was observed (middle). The end view of a corresponding helical simulation (right) displays the BAR domain, which protrudes out. After the amplitude correction the 3D density volume was low-pass filtered to 11 Å. Adopted from [266].

Like in the F20 cryo-EM data sets before, a distribution of thin, medium and thick tubes was found (Fig. 2.26; Fig. 2.27). One of the major classes with a diameter of 280 Å (Fig. 2.26) showed the most distinctive features and the highest resolution of all reconstructions with 10.3 Å (Fig. 2.25). The helical reconstruction exhibited a tight BAR arrangement on the membrane surface.

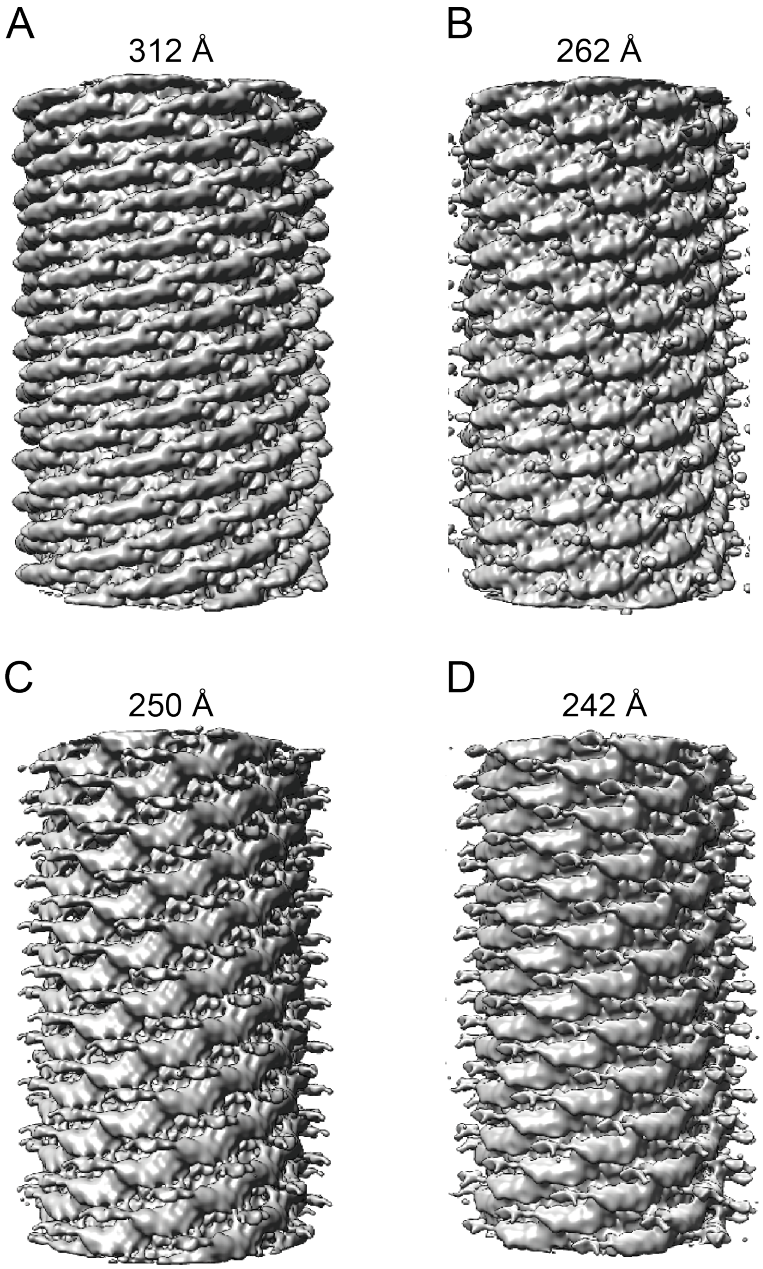

Figure 2.27 – 3D reconstruction of amphiphysin N-BAR remodelled tubes with a tube diameter of 312 Å, 262 Å, 250 Å and 242 Å | The helical reconstructions of the wider tube with a tube width of (A) 312 Å and the thinner tubes with a tube width of (B) 262 Å, (C) 250 Å and (D) 242 Å reveal the helical BAR domain assembly on the membrane surface. After the amplitude correction the 3D density volumes were low-pass filtered to (A) 11 Å, (B) 11 Å, (C) 12 Å and (D) 12 Å. Adopted from [266].

One of the other classes had a wider tube width of 312 Å, revealing a less tight packing of N-BAR (Fig. 2.27, A). The rest of the classes showed smaller tube diameters of 240 to 260 Å (Fig. 2.27, B - D). Here it appears that the BAR domains are fluctuating on the membrane surface. All reprojections of the reconstructions were looking similar to their corresponding class average (Fig. 2.25, column 1 and 3). Moreover, the layer line diffraction patterns of all reconstructions revealed the periodical spacing of ~44 $Å^{-1}$ and ~55 $Å^{-1}$, matching with the power spectra of the respective class averages of the segmented tube particles (Fig. 2.25, column 2). The spacing of 44 Å in real space corresponded to the BAR domain. The 55 $Å^{-1}$ layer line was likely belonging to the H0 helix.
The tight protein packing was also depicted by the membrane surface area, which was occupied by N-BAR. The concave surface area of the 56 kDa amphiphysin N-BAR dimer, interacting with the membrane, has a size of 10000 $Å^2$. Depending on the tube width, approximately 3000 - 4000 $Å^2$ of the membrane surface area was occupied by N-BAR. In contrast, endophilin is interacting with the membrane via a surface area of 18000 $Å^2$, being determined from the reconstruction of the remodeled tubes in presence of endophilin BAR[70]. With endophilin N-BAR, having a related crystal structure to amphiphysin N-BAR, a much looser helical assembly on the tube surface was observe[70,100]. The tight packing of amphiphysin N-BAR was achieved because one tip of the dimer was emerged into the membrane bilayer and the other one was protruding out (Fig. 2.26, C and D). Hence, much more proteins can get accommodated on the membrane surface when the helical lattice formation is taking place. Endophilin N-BAR and CIP4 F-BAR dimer show a tip-to-tip lattice organization because of their more loose packing. In the case of amphiphysin N-BAR this dimer-dimer interaction was not observed. It rather looks like the outwards protruding tip of one dimer, being not inserted into the membrane, was interacting with the center of the other dimer in the helical arrangement (Fig. 2.26, C). The tips, which are sticking out, were observed as the "jaggy" features on tube's side in the 2D class averages and helical 3D reconstructions. The reconstructions revealed that in contrast to endophilin, amphiphysin N-BAR arranges itself in a much tighter packing which likely lead to higher degree of rigidity of the remodelled tubes. Furthermore, the neighbouring N-BAR dimers seem to be well-connected to each other. To understand the protein-to-protein or protein-to-membrane interactions the resolved crystal structure of *Drosophila* amphiphysin BAR domain[43] was fitted into the density maps of the 3D reconstructions (Fig. 2.28, 2.29, 2.30).

2.5.4 Well-connected BAR units by multiple interfaces

The crystal structure of *Drosophila* amphiphysin N-BAR was already resolved in 2004[43]. The crystal structure of the amphiphysin N-BAR dimer consists of two monomers with three long kinked alpha helices, which are forming a six helix bundle at the dimer center (Fig. 2.28, A). The H0 helix was not resolved because it is disordered without membrane interaction. The fitting of the crystal structure disclosed the organization of the N-BAR

domain assembly on the remodelled tube surface and showed how the tight lattice packing was attained (Fig. 2.28, B). Rigid body fitting was the efficient and robust method of choice to dock the atomic model into the medium resolution density map of the helical reconstructions. The fitting was performed in the molecular graphics software Chimera [278].

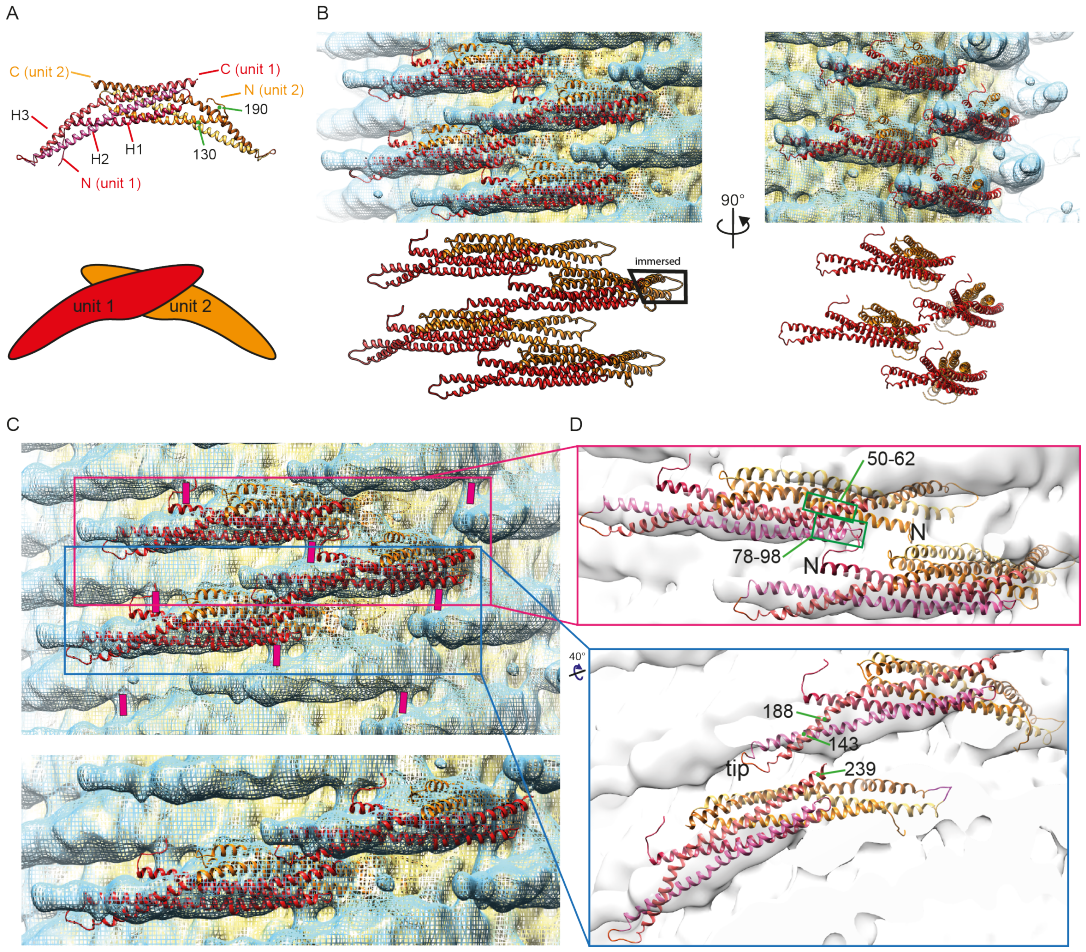

Figure 2.28 – Fitting of the *Drosophila* amphiphysin N-BAR atomic structure into the main class (280 Å) | (A) Atomic structure of the crescent shaped *Drosophila* amphiphysin N-BAR (PDB code: 1URU) (top), being made of monomer BAR unit 1 (red) and 2 (orange) (bottom). (B) For the docking of the atomic structure of N-BAR into the BAR density of the main class, rigid body fitting was used. The black box (bottom) highlights the immersed BAR tip, which was not visualized and resolved by the reconstruction due to the surrounding lipids. (D) An additional rod-like density, connecting the neighbouring BAR domains, was observed (top, pink bar). This density likely belonged to the amphipathic helix, which is not resolved in the atomic structure (bottom without pink bar). (E) Representation of the interaction sides between the neighbouring BAR domains is displayed, showing the BAR arrangement in the helical lattice. Adopted from [266].

First the main focus was laid on the reconstruction of the main class with a tube width of 280 Å. Here it was observed that one fourth of BAR domain dimer was directly interacting with the membrane surface (occupied membrane area ~3300 Å^2) (Fig. 2.28,

B), which is in contrast to endophilin N-BAR where the whole dimer seems to interact with the membrane. The membrane interaction was taking place at one dimer tip likely at the residues 130 to 190 of helix 2 and 3, including the loop at the tip end. A closer look revealed that the tip was not only interacting with the membrane; it was rather deeply immersed likely up to 9 Å into the lipid bilayer (Fig. 2.26, D). This is consistent with a published EPR study where it was shown that the residues 144, 147 and 151 were deeply embedded into the lipid leaflet, in fact up to the height of the lipid acyl chains[108]. The other tip side was protruding out from the membrane surface without any membrane contact. I was not able to accurately fit the tip region of atomic model into the protruding out tip density of the BAR dimer (Fig. 2.28 C, 2.29 B, 2.30 D to F). As this was the case for all helical reconstructed class averages (Fig. 2.30, D to F), probably the tip is locally fluctuating. This may be an indication that tip is newly orienting itself due to the assembly of the tightly packed BAR lattice or the interaction with the membrane.

Between the neighbouring N-BAR dimers an inter-connection was appearing (Fig. 2.26, C, red star). The fitted crystal structure without H0 was not occupying this additional density. Therefore, it is likely that this inter-dimer connection belongs to one of the H0 helices (Fig. 2.28, C, pink bar). The H0 helix of one N-BAR dimer is likely to interact with the residues 78 to 98 of the linked helix 1 and helix 2 of one monomer unit and/or the residues 50 to 62 of helix 1 of the other monomer unit of the dimer in the adjacent lattice row (Fig. 2.28, D, top). It was not possible to define the exact interaction sides due to the limitation of resolution. The second H0 helix of the N-BAR dimer was not resolved in the EM density map. The embedded tip of the dimer complicated the visualisation of the H0 helix. On closer examination of the helical reconstruction, an additional density (Fig. 2.26, C, red arrowhead) between the area of the immersed tip of one N-BAR and the neighbouring dimer occurred. I speculate that this density may belong to a second H0 helix, connecting the dimers.

Furthermore, it it possible that the protruding out dimer tip is forming a linkage to the center region of the next dimer within the lattice row. As this BAR dimer tip tends to be "flexible" and due to the limitation of resolution no connecting density was resolved. But it could be speculated that the residues close to aa 143 of helix 2 and aa 188 of helix 3 of the protruding tip are interacting with the residues of helix 3 (close to aa 239) of the neighbouring N-BAR monomer unit (Fig. 2.28, D, bottom). Due to the inter-dimer connections by the H0 helices and the possible tip connections between the neighbouring dimers the N-BAR lattice of the main class with a tube with of 280 Å seems to be very well-connected.

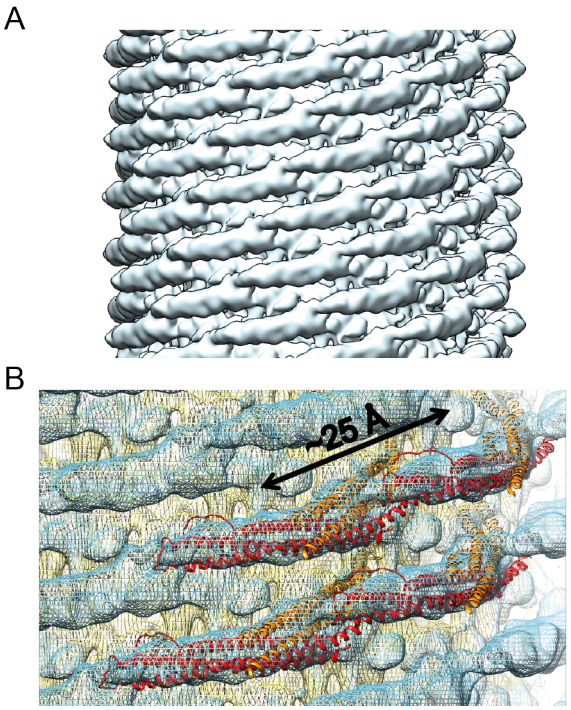

Figure 2.29 – Fitting of the *Drosophila* amphiphysin N-BAR atomic structure into the tube with a diameter of 312 Å | (A) The 3D helical reconstruction of the widest tube revealed a slightly looser arranged N-BAR assembly in contrast to the main tube with a diameter of 280 Å. (B) The fitting of the atomic structure of the crescent shaped *Drosophila* amphiphysin N-BAR (PDB code: 1URU) into the helical reconstruction was performed by rigid body fitting. In contrast to the main class with a tube width of 280 Å, the inter-dimer connections of the wider tube seem to be ~25 Å apart from each other. No additional density, which likely corresponds to the H0 helix, was visualized. Adopted from [266].

The other classes with different tube diameter showed a different BAR domain arrangement on the tube surface (Fig. 2.27). The wider tube with a diameter of 312 Å revealed that the BAR packing is slightly more loosely rearranged because 3700 Å^2 of the membrane surface are occupied by N-BAR (Fig. 2.29, A). The inter-dimer interaction points seem to be roughly 25 Å apart from each other as seen in the 280 Å tube (Fig. 2.29, B). Moreover, with this data set no additional densities of the H0 helices, which are connecting the neighbouring dimers, were visualized.
The narrower tubes with a tube width of 240 to 260 Å are tightly packed as the main class (Fig. 2.30A to C). But in contrast it rather looks like the N-BAR dimers seem to be rotated along the long axis of its crescent shape (Fig. 2.30, D to F). The inter-dimer interactions were rather changed due to the BAR rotation than by a translational movement. Here again no additional density belonging to inter-dimer connections were seen in the EM reconstructions.

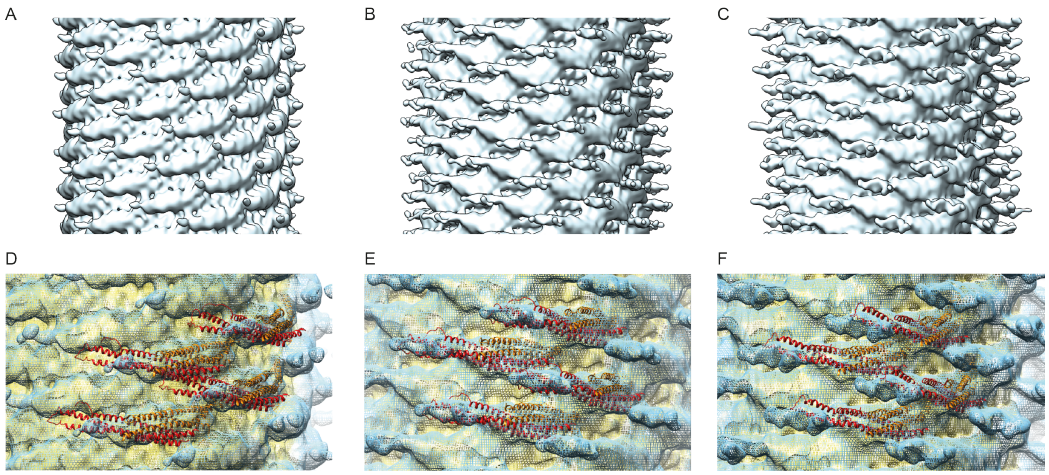

Figure 2.30 – Fitting of the *Drosophila* amphiphysin N-BAR atomic structure into the tube with a diameter of 262 Å, 250 Å and 242 Å. (A-C) The 3D helical reconstruction of the narrower tubes with a diameter of 262 Å (A), 150 Å (B) and 242 Å (C) reveal that the BAR domains seem to be rotated along the long axis of the crescent dimer. The BAR lattice was as tightly packed as the main tube with a diameter of 280 Å. (D-F) The docking of the atomic structure of the crescent shaped *Drosophila* amphiphysin N-BAR (PDB code: 1URU) into the helical reconstruction (tube width of 262 Å (D), 250 Å (E) and 242 Å (F) was done by rigid body fitting. An additional density the H0 helix was not visualized. Adopted from [266].

2.6 Amphiphysin mutant analysis

In BIN1 various mutations are interrupting the T-tubule biogenesis leading to CNM [149,166,279,280]. *Drosophila* amphiphysin is the orthologue to the mammalian muscle BIN1. To see if the BAR arrangement is disrupted by the CNM, H0 helix or tip mutations *in vitro* tubulation assays were performed by using corresponding BIN1 mutations in amphiphysin (see 2.6.1 and 2.6.2).

2.6.1 Membrane remodeling by N-BAR mutants

Several mutations in human BIN1, being involved in T-tubule formation like *Drosophila* amphiphysin, are known to be involved in the neuromuscular disorder CNM. K35N is located in H0 helix, D151N, R154Q in the BAR domain and Q434X and K346X in the SH3 domain [149,166,279,280]. As N-BAR is the smallest membrane remodeling unit. My work focused mainly on the mutations in this domain (Fig. 2.31). BIN1 K35, D151 and R154 correspond to *Drosophila* amphiphysin K30, D146 and R149, respectively. K30 is located at the intersection of the amphipathic helix H0 to the BAR domain. D146 and R149 are located in helix 2 close to the tip. It was shown by EPR studies that the tip region is immersed into the lipid membrane. The deepest insertion up to the lipid acyl chain showed the residues 144, 147 and 151 [108], which are the neighbouring residues of the disease mutations at the tip region. Based on the BIN1 mutation and the EPR studies the following mutations were used: D144R, D146R, R149E (Fig. 2.31 A

and B). Furthermore, the triple mutant KRK161EEE (K161E, R162E, K163E), which is supposed to reduce tubulation activity [43], was also analysed (Fig. 2.31, A and B). The residues were point-mutated within N-BAR by mutagenesis PCR and afterwards purified as a dimer (see Appendix A11). The membrane remodeling by the mutated N-BAR constructs was observed by negative stain EM (Fig. 2.31, C to H).

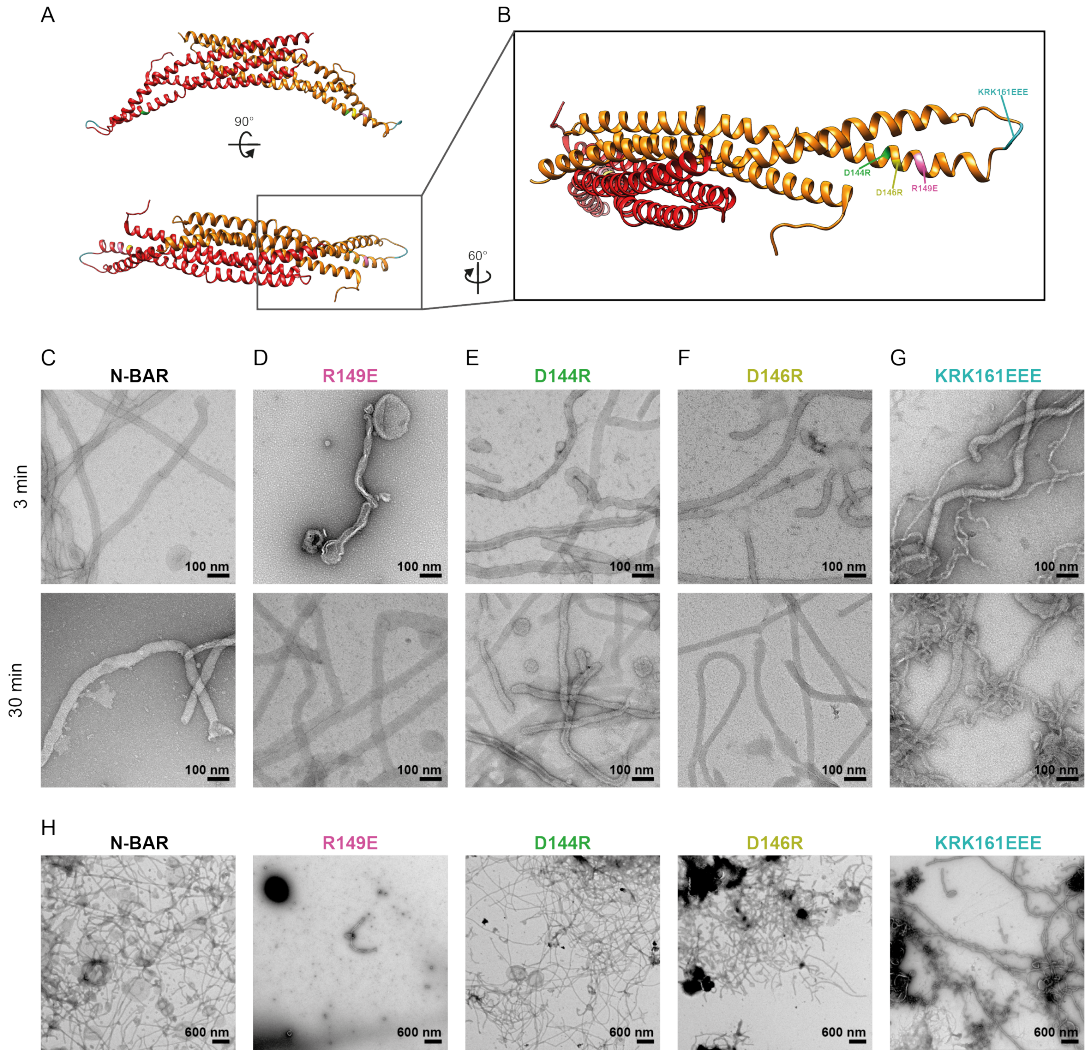

Figure 2.31 – Negative stain EM of liposome tubulation by *Drosophila* amphiphysin N-BAR mutants | (A) Atomic structure of amphiphysin N-BAR with the studied N-BAR mutations (B) of R149E (magenta). D144R (green), D146R (yellow) and KRK161EEE (blue). (C - H) Negative stain EM with higher (C - G) and lower (H) magnification showed tubulation for all N-BAR mutants of R149E (D and H, second), D144R (E and H, third), D146R (F and H, fourth) and KRK161EEE (G and H, fifth). D149E and KRK161EEE showed a changed tubulation behavior in comparison to N-BAR (C). In the mutant D149E less tubes were remodelled and they showed an altered tube morphology. KRK161EEE showed micellar and bilayer tubes. For the graphics of the modified amphiphysin N-BAR mutants (A and B) the atomic structure of *Drosophila* amphiphysin N-BAR (PDB code: 1URU) was used.

All mutants showed tube formation in the *in vitro* tubulation assay in negative stain EM (Fig. 2.31). The N-BAR mutants D144R (Fig. 2.31, E and H, D144R) and D146R (Fig. 2.31, F and H D146R) showed less membrane remodeling activity in contrast to N-BAR (Fig. 2.31, C and H, N-BAR). In addition, in the condition of D146R slightly shorter tubes were remodelled. The formed tubes of D144R and D146R were looking mostly rigid and uniform. After 30 min of incubation, D146R seemed to further remodel tubes to a narrower width. In contrast, mutant R149E (Fig. 2.31, D) and KRK161EEE (Fig. 2.31, G) had a changed tube formation behavior. Mutant R149E (Fig. 2.31, H, R149E) showed almost no tubulation and the tubes were not as rigid and uniform as N-BAR. Moreover, the tubes were shorter than N-BAR. This observation is concordant to former negative stain EM studies of the human BIN1 D154Q mutant [258]. After 30 min the tubes of R149E tended to be more rigid and uniform (Fig. 2.31, D, bottom).
Mutant KRK161EEE (Fig. 2.31, G) showed bilayer and micellar tubes. The width of the bilayer tubes seemed to be wider than those derived by N-BAR. Moreover, less tubulation was observed. After 30 min more micellar tubes were observed. In a former study the double N-BAR mutant K161E and K163E lead to less membrane binding and remodeling [43]. Mutations at the tip may facilitate fluctuation of the BAR domain on the membrane surface due to loss of an organized and connected BAR arrangement, resulting in altered remodeling behavior with thicker bilayer and micellar tube formation. In a former study they suggested that human BIN1 D151N and R154Q mutants have a lower membrane bound density on the tube surface in contrast to BIN1 N-BAR wild type [258]. This is in agreement with my observation that an organized N-BAR arrangement was not visible on the membrane surface. These results showed that some mutations at the N-BAR tip lead to a changed membrane remodeling behavior. Hence, I propose that the tip plays an important role in the membrane binding and in organizing the BAR arrangement (see 2.6.2).

2.6.2 The role of the BAR tips in an organized N-BAR arrangement

Throughout all reconstructions it was observed that one tip of N-BAR is immersed into the lipid membrane and the other tip is protruding out without membrane contact. Moreover, the mutant analysis showed that the tip plays an important role in the organized BAR arrangement. Therefore, the question was raised how important both dimer tips are for the tube formation and the N-BAR lattice arrangement.

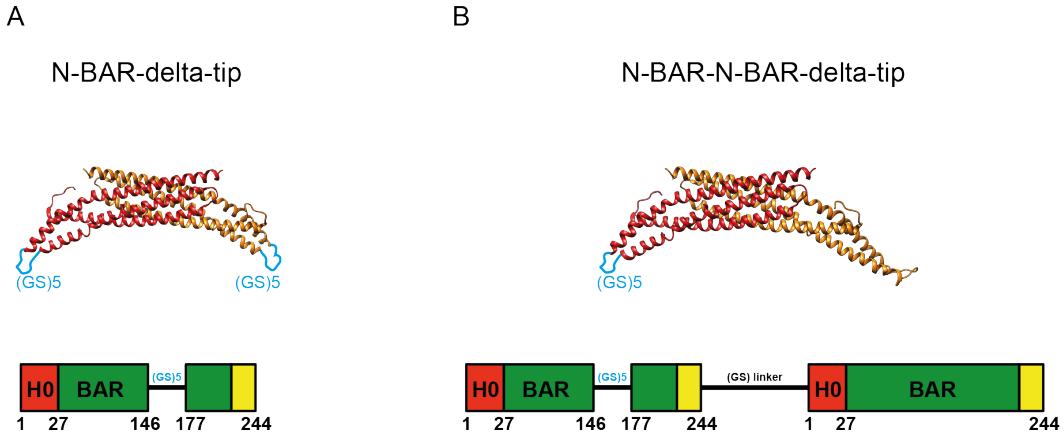

Figure 2.32 – Constructs of the N-BAR tip mutants | (A) N-BAR tip mutant N-BAR-delta-tip where both tips are exchanged by an (GS)5 linker. (B) Obligated N-BAR-N-BAR-delta-tip mutant where two BAR monomer units are linked by a (GS)-linker. In this amphiphysin "heterodimer" one monomer is like N-BAR wild type and in the other monomer unit the tip region is exchanged with an (GS)5-linker. For the graphics of the modified amphiphysin N-BAR tips (second row) the atomic structure of *Drosophila* amphiphysin N-BAR (PDB code: 1URU) was used.

Two amphiphysin N-BAR tip mutants were designed (Fig. 2.32), expressed and purified as dimer (see Appendix A12) for testing . One mutant lacked both tips by cloning an amphiphysin N-BAR fragment, in which the the residues 147 - 176 (N-BAR-delta-tip) were exchanged by a (GS)5-linker (Fig. 2.32, A). The other mutant was an obligated N-BAR fusion "heterodimer" (N-BAR-N-BAR-delta-tip), containing a linkage between one intact N-BAR monomer unit and a N-BAR domain missing residues 147 - 176, being exchanged by a (GS)5-linker (Fig. 2.32, B).

Both tip mutants were analyzed via negative stain EM, fluorescence light microscopy and critical tubulation concentration (Fig. 2.33). 6 µM of protein were mixed with 720 µM of MLVs. For fluorescence light microscopy the liposomes were labeled with 1%-Atto488-DOPE. For the critical tubulation concentration determination several protein dilutions were mixed with 720 µM liposomes.

Negative stain EM and fluorescence light microscopy observations revealed that both tip mutants are able to remodel lipsomes into tubes (Fig. 2.33, A - C). Negative stained N-BAR-N-BAR-delta-tip tubulation showed uniform rigid tubes (Fig. 2.33, + N-BAR-N-BAR-delta-tip, B). N-BAR-delta-tip remodelled tubes were less uniform and rigid in their morphology like the other tip-mutant (Fig. 2.33, + N-BAR-delta-tip, B). For both tip mutants no organized N-BAR assembly on the tube surface was visualized. Moreover, less tubes were remodelled in both cases (Fig. 2.33, A). Fluorescence microscopy of N-BAR-delta-tip showed rather thicker tubes than N-BAR-N-BAR-delta-tip or N-BAR and FL (Fig. 2.33, A).

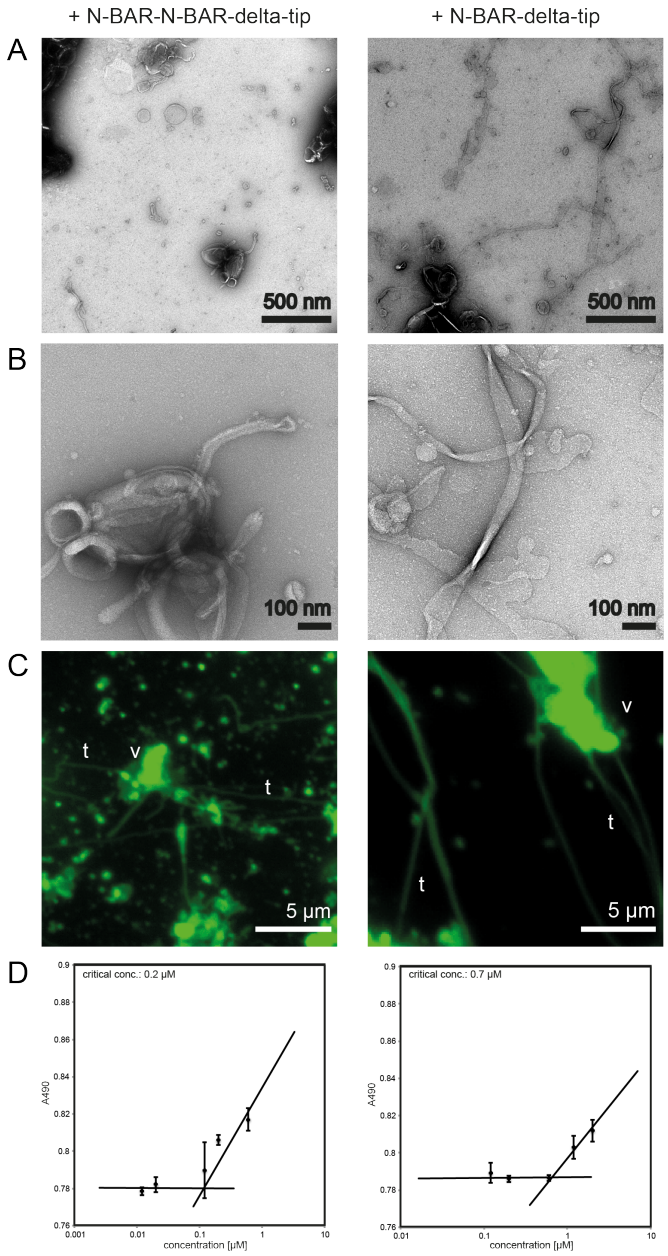

Figure 2.33 – Membrane tubulation of the N-BAR tip mutants by fluorescence light microscopy and negative stain EM | *In vitro* tubulation of N-BAR-N-BAR-delta-tip (left) and N-BAR-delta-tip (right) showed liposome remodeling for both tip mutants observed by fluorescent light microscopy (C) and negative stain EM (A and B). 6 µM of protein was mixed with 720 µM liposomes. (C) For fluorescent light microscopy experiments, the liposomes were fluorescently labeled with 1%-Atto488-DOPE. Both tip mutants (A) showed less membrane remodeling as N-BAR. N-BAR-N-BAR-delta-tip showed rigid uniform formed bilayer tubes (+N-BAR-N-BAR-delta-tip, B, left). In contrast for N-BAR-delta-tip thicker and irregular bilayer tubes were observed (+N-BAR-delta-tip, B, right). In both cases no BAR arrangement was seen on the membrane surface. (D) In addition, the critical tubulation concentration was determined for both tip mutants. No tubulation was happening anymore (guided with the flat horizontal line) for N-BAR-N-BAR-delta-tip and N-BAR-delta-tip with a protein concentration of 0.2 µM and 0.7 µM, respectively. v: examples of vesicles, t: examples of tubes. Adopted from [266].

Via light scattering a CC of 0.7 µM for N-BAR-delta-tip was determined (Fig. 2.33, + N-BAR-delta-tip, D), being higher than N-BAR and FL (0.4 µM). As the tips were missing, more proteins were needed to remodel the liposomes into tubes. The CC for N-BAR-N-BAR-delta-tip was calculated to be 0.2 µM (Fig. 2.33, + N-BAR-N-BAR-delta-tip, D), which was the lowest determined CC of all measured amphiphysin fragments. The reason for this low CC of N-BAR-N-BAR-delta-tip could result from the observed sporadic bundling of the remodelled tubes by fluorescence or electron microscopy. Likely the bundling was occurring due to some re-arrangements of the heterodimer as both monomers are connected by a linker sequence. Thus, the heterodimers may be able to form inter-dimer link,s leading to inter-tube cross-links. This resulted in an increase of the local protein concentration on the membrane surface and hence, a decrease of the critical tubulation concentration was induced.
These results show that the tips are not necessary for membrane remodeling activity. It rather seems that the both tips significantly contribute to an organized BAR assembly because no BAR domain arrangement was observed on the tube surface. Moreover, the tube morphology differed to N-BAR-mediated tubes. With one existing tip the tubes look more rigid and uniform in comparison to tubes formed by the mutant without both tips. Therefore it is likely that one tip is needed for the ability to remodel membranes whereas the other tip is necessary to organize and stabilize the helical BAR arrangement.

3 Discussion

In my thesis I present the molecular mechanism of membrane remodeling by the N-BAR domain protein *Drosophila* amphiphysin. To get insights into the membrane remodeling process on a structural basis I performed *in vitro* reconstitution assays and cryo-EM. Four amphiphysin fragments were cloned, expressed and purified and their membrane interactions were analyzed to understand role of the amphiphysin N-terminal H0 helix, BAR domain and the regulatory domains in the tube formation. Amphiphysin forms tubes out of spherical liposomes by helical polymerizing in a cooperative manner on the membrane surface. I observed that the H0 helix is not essential for membrane remodeling but it mediates a fast and rigid tube formation. The regulatory domains are not incorporated into the helical packing of the N-BAR domain and seem to be not involved in the membrane molding process. The cryo-EM image analysis of amphiphysin full-length showed that the regulatory domains are protruding out from the tube membrane. The cryo-EM 3D helical reconstruction of amphiphysin N-BAR-mediated tubes revealed a unique helical BAR domain arrangement, which is polymerizing around the tube surface. The remodelled tubes showed a tight BAR domain packing where one tip of the BAR dimer is immersed into membrane and the other one protrudes out from the tube surface. In the 3D reconstruction an additional rod-like density was visualized, connecting the BAR dimers of adjacent lattice rows. This rod-like density likely belongs to the H0 helix, which organizes and stabilizes the helical BAR arrangement. I observed that the diameter of the tube, depending on the helical arrangement of the amphiphysin N-BAR domain, is not as variable as endophilin N-BAR-remodelled tubes [100]. However, a local fluctuation of the BAR domain on the membrane surface was seen so that the rod-like density between well-connected BAR dimers was lost. Tip mutations or deletion of the tip resulted in a disorganized BAR assembly and an altered membrane remodeling activity. My study revealed that the H0 helix as well as the BAR dimer tips are required for an efficient and organized arrangement of the BAR dimers on the tube surface.

3.1 The role of the membrane lipid compositions in membrane bending by amphiphysin N-BAR

Human muscle BIN1 contains a polybasic sequence (encoded by exon 11) with the amino acid sequence RKKSKLFSRLRRKKN, which is a PI-binding motif that binds specifically to PI(4,5)P_2 [151,281]. The binding to PI(4,5)P_2 in the membrane is crucial for BIN1

to remodel T-tubules[146,173]. In the membrane unbound state the PI-binding motif is binding to the SH3 domain, resulting in an autoinhibited state of BIN1. PI(4,5)P_2 opens the autoinhibition so that the N-BAR domain with the polybasic sequence is binding to the membrane and the SH3 domain is free to bind its interaction partners such as dynamin 2[151,177]. Depletion of the exon 11 motif in muscle BIN1 leads to a lacking tubular network in myocytes[177]. Because of this auto-regulation BIN1 binds and remodels only membranes of specific subcellular regions.

Drosophila amphiphysin, being the orthologue to muscle BIN1, lacks the exon 11 spliced PI-binding motif. In a former study it was proposed that *Drosophila* amphiphysin shows only tubulation in HEK293 cells when PI(4,5)P_2 is enriched in the plasma membrane[262]. It was suggested that PI(4,5)P_2 triggers the embedding of the amphipathic helix into the membrane and the BAR domain interacts likely with PS via nonspecific electrostatic interactions. They speculated that PI(4,5)P_2 is necessary for the binding and self-association of amphiphysin N-BAR to the membrane. This is in contrast to my *in vitro* observation where I found membrane tubulation and helical self-assembly of amphiphysin N-BAR on membranes with lipid compositions without PIPs and PS. I observed that neutral charges (POPC) do not lead to membrane tubulation, but negative charges (POPG) would do. POPG is just like POPS negatively charged and therefore, should induce similar electrostatic interactions with the BAR domain. When the liposome is very strongly negatively charged, the N-BAR dimer starts to make stable micellar tubes. However, when bilayer tube formation is observed, the diameters of the tubes appear to be consistent (~200 to 350 Å) regardless of the charge composition. For a close-to-physiological condition bovine lipid brain extract (Folch Fraction I), containing several PIPs and PS, was used. In this condition amphiphysin N-BAR deforms membranes into bilayer and micellar tubes. An enrichment of negative charges within the membrane ether by an increase of POPG or PIPs leads to a stronger binding of amphiphysin N-BAR to the membrane via electrostatic interactions, resulting in micellar tube formation maybe due to a higher protein to lipid ratio as seen for endophilin N-BAR[100]. Alignment of the polybasic sequence of BIN1 with *Drosophila* amphiphysin revealed a similar but shorter consensus polybasic sequence within the region of the N-terminal amphipathic helix and concave surface of the BAR domain (helix 2 of the BAR monomers). This polybasic patches may contribute to a stronger interaction of the H0 helix and BAR domain with negatively charged lipids such as POPG or PI(4,5)P_2.

For the structural investigation of the helical arrangement of amphiphysin N-BAR on the tube surface the lipid composure with the most consistent formed tubes was chosen. Here a membrane composition with ~66% negatively charged lipids brought the best results. 2POPG:1POPE shows mostly stable remodelled bilayer tubes without micellar tube formation. As the tube diameter seems do be rather uniform and less dynamic 2POPG:1POPE was the lipid mixture of choice for further biophysical and structural analyses. It is possible that some polybasic patches within the amphiphysin N-BAR and

regulatory domains prefer the binding to $PI(4,5)P_2$ but I showed that $P(4,5)P_2$ is not necessary for the binding of the amphiphysin N-BAR domain with the membrane.

3.2 *Drosophila* amphiphysin N-BAR-mediated tubes with a unique tight BAR packing

BAR domain dimers with their banana-like shape are interacting with the membrane by electrostatic interactions and/or hydrophobic motif insertion. For membrane curvature generation BAR domain proteins use the scaffolding mechanism and intermolecular dimer-dimer connections by forming a organized helical protein assembly on the membrane surface. The 3D reconstruction of amphiphysin N-BAR remodelled tubes revealed a differently organized BAR packing in contrast to tubular membrane shaping by other BAR protein assemblies[70,88,100,103,110]. F-BAR domain proteins like CIP4/FBP17 proteins show lateral and tip-to-tip of adjacent F-BAR domain dimers within their helical lattice[88,103]. The N-BAR domain protein endophilin, having a similar N-BAR domain crystal structure like amphiphysin, stabilizes its rather loose helical assembly not by prominent lateral protein interactions but via anti-parallel and non-specific interactions between the membrane embedded amphipathic helices of neighbouring BAR dimers and possible flexible tip-to-tip interactions[70,100].
Endophilin, being involved in CME, belongs to the same BAR domain class like amphiphysin but a closer look on both helical packing revealed a different organization of the N-BAR assembly on the remodelled tube surface. Amphiphysin N-BAR-mediated tubes showed a high degree of rigidity likely due to the tightly packed BAR domain arrangement. In contrast, the assembly of endophilin is looser and more membrane surface area is exhibited. The tight amphiphysin N-BAR packing is possible because one BAR dimer tip is hidden by immersing into the membrane surface, whereas the other tip protrudes out from the tube surface. Due to this a higher protein-lipid ratio is achieved in contrast to endophilin. One amphiphysin N-BAR domain unit cell occupies ~4000 to 3000 $Å^2$, depending on the tube diameter, of the membrane surface area, while endophilin reserves for itself ~6200 to 4400 $Å^2$[100]. For the N-BAR mediated tube with an diameter of 280 Å almost one fourth of the N-BAR dimer, including the residues 130 to 190 of helix 2 to 3 with the connecting loop, has direct connection to the membrane surface. The loop region of the embedded tip seems to be deeply immersed, up to ~9 Å, into lipid bilayer so that it is enclosed by lipids. This is in accord with recent EPR measurements of the tip region where it was shown that the residues 144, 147 and 151 are immerse to the core of the membrane up to the lipid acyl chains[108]. The other tip of N-BAR is protruding out from the membrane surface, which likely facilitates the tight N-BAR arrangement and possible interaction interfaces for interacting partners in the muscle. In T-tubules several other proteins next to amphiphysin play a role in the biogenesis, stabilization and maintenance of T-tubules. It is suggested that human

muscle BIN1 is contributing to the targeting, localizing and binding of calcium channels to the T-tubules by interacting with microtubules [208,230,233]. Moreover, the BAR domain of muscle BIN1 plays an evolutionary conserved role in orchestrating the position and shape of the nucleus in muscle cells by interacting with the microtubule cytoskeleton via the MT plus-end-binding protein CLIP-170 [135,136]. In *Drosophila* the BAR domain of amphiphysin may play a similar role in the muscle cells and the protruding out tip may enable protein interactions at the T-tubule surface. So far this is only a speculation and to understand the role of the protruding out tip further experiments have to be performed. Furthermore, it has to be taken in account that under physiological condition at the T-tubules other proteins are involved in T-tubule formation and stabilization, which may change the lattice arrangement of amphiphysin N-BAR on the membrane surface.

Because amphiphysin shows this unique tight packing no tip-to-tip BAR dimer connections were observed like seen in endophilin N-BAR or CIP4/FBP17 F-BAR [70,88,100,103]. The tight N-BAR packing of amphiphysin shows well-connected BAR dimers by an additional rod-like density, which links the N-BAR dimers in adjacent rows. This connection goes from one N-BAR dimer to the junction of helix 1 and 2 (residues ~78 to 98) of one N-BAR monomer and/or helix 1 (residues ~50-62) of the other monomer within the neighbouring N-BAR dimer. This connections may play a role in the organization of the BAR assembly by specifically defining the spacing between two lattice rows. It is likely that this density linkage belongs to the amphipathic helix, which was also observed in endophilin [70]. Moreover, an additional density next to the rod-like density was weakly showing up. This density could be another candidate for a H0 helix linkage but the visualization is hampered by the immersed tip into the lipid bilayer. Due to the limited resolution of my reconstructions no precise allocation of the amphipathic helices could be done and it is rather speculative that the H0 helix belongs to the connecting rod-like density as it was not occupied by *Drosophila* amphiphysin BAR crystal structure, lacking the H0 helix.

In addition, it could be speculated that there could be tip-to-center connections between neighbouring BAR domains in one lattice row to stabilize the BAR domain lattice. This unique rigid and tight N-BAR packing of *Drosophila* amphiphysin, being an orthologue to the muscle-enriched mammalian BIN1, may point out its physiological function of forming and stabilizing the stable structure of T-tubules in muscles. In contrast, endophilin is contributing to the dynamic membrane remodeling process during endocytosis.

3.3 Rigid lattice formation due to a well-connected N-BAR assembly

Amphiphysin N-BAR organizes itself in a unique tight helical packing on the membrane surface. The rigidity of this tight N-BAR assembly is achieved because of well-connected

adjacent N-BAR domains by BAR domain inter-dimer interactions via anti-parallel amphipathic helix and likely tip-to center connection. This rigid lattice may play an important role in the stabilization of T-tubules.

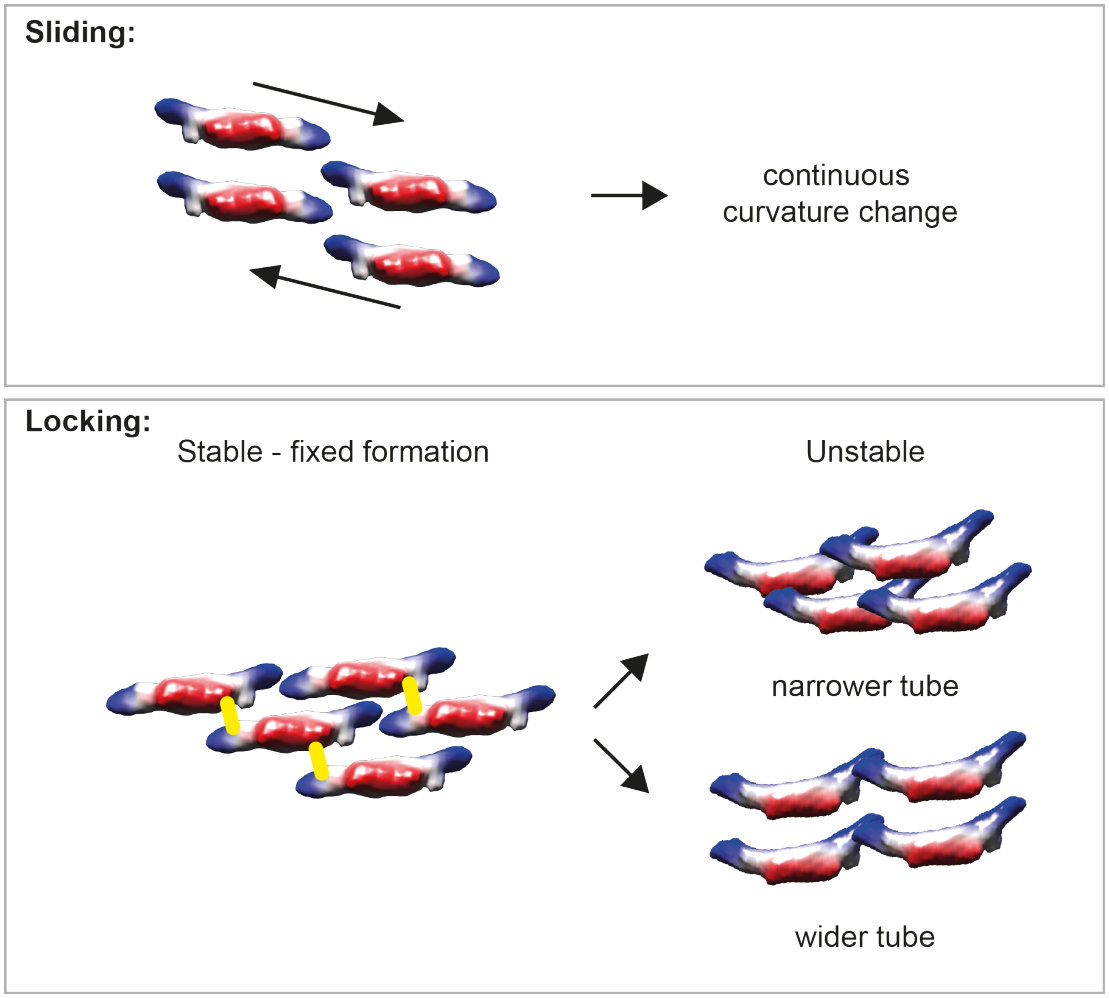

Figure 3.1 – Model of membrane remodeling by different BAR proteins | (Top) Sliding mechanism: neighbouring BAR domains seem to be weakly connected to each other, which may lead to sliding against each other on the membrane surface and subsequent to a continuously changing curvature. (Bottom) Locking mechanism: adjacent BAR domains are linked to each other by the H0 helix so that they are kind of "fixed" in their position on the membrane, leading to a rigid lattice formation. When the BAR domains rotate along their axis the connection points by the H0 helix are lost, resulting in a change of the curvature and consequential in a variation of the tube diameter. Adopted from [266].

Amphiphysin and endophilin are using the scaffolding mechanism and the amphipathic helix insertion to generate membrane curvature. After amphiphysin and endophilin N-BAR-mediated tubulation small vesicles emerge and get squeezed from the tubes. This squeezing process evolve from the inter-dimer connections. Endophilin plays a role in the dynamic membrane remodeling during CME, resulting in a variety of tube diameters along the tube axis and between remodelled tubes. Therefore in the case of endophilin,

a sliding mechanism is suggested (Fig. 3.1, top) in which the continuous curvature change is obtained likely by shallow electrostatic surface potentials of the inter-dimer interaction surfaces and rather not by specific electrostatic inter-dimer interactions [100]. Amphiphysin-mediated tubes showed less distribution in their width along the tube axis and between the formed tubes. In our analysis a small population of remodelled tubes with distinctive diameter was used, which showed in its most rigid helical tube packing (tube diameter of 280 Å) a density linking a upright inter-dimer connection between lateral arranged adjacent BAR domains. This perpendicular density, which is occurring close to the N-terminus of amphiphysin N-BAR, presumably belongs to the N-terminal H0 helix. Narrower remodelled tubes did not reveal this rod-like inter-dimer density. Instead the BAR domains appear to be rotating along their long axis, leading to tubes with a smaller diameter. For endophilin longitudinal rotation of the BAR domain also resulted in remodelled tubes with lower dynamic diameters and altered packing [100]. For endophilin it is predicted that the anti-parallel interactions of the H0 helices of N-BAR domains in neighbouring lattice rows are essential for a stable BAR assembly to generate highly curved tubes because the BAR tip-to-tip interactions alone seem to be too weak [70]. For amphiphysin BAR, lacking the N-terminal H0 helix, thicker tubes were remodelled, which would fit the observation that the H0 helix is needed for an organized and stable helical BAR assembly to induce higher membrane curvature. It seems that with strengthened support of the H0 helix amphiphysin locks inter-dimer connected neighbouring BAR domains within its helical lattice in an individual fashion so that stabilized tubes could be formed, which are necessary for the stable tubular shape of T-tubules (Fig. 3.1, bottom). Loss of locked lattice interactions lead to BAR domain rotation and hence, the proteins fluctuate on the membrane surface. After a specific time the protein fluctuation on the tube goes beyond a certain balance point and the squeezing force of the H0 helix branches off small vesicles, which emerge from the tube. An elongated N-terminal amphipathic helix changes the tubulation behavior of amphiphysin. Depending on the additional H0 helix extension the organization of parallel assembled BAR domains in adjacent lattice rows seems to be disrupted, leading to less rigid and stable remodelled tubes. In addition, the longer the H0 helix gets the stronger the squeezing force becomes so that small vesicle emergence is promoted form the tubes, which was also observed for several BAR domain proteins including rat amphiphysin 2 isoform 6 [282]. This supports the suggestion that for a stable organized BAR arrangement the H0 contributes to the locking mechanism between connected BAR dimers in the adjacent lattice row. The detected local fluctuation on the tube surface and consequently, the resulting heterogeneity in the BAR arrangement hinders a high-resolution structural analysis, which is possibly a particular characteristic of BAR protein assemblies on a flexible membrane surface. Due to the limited resolution the precise interaction interfaces of the inter-dimer connections were not identified.

3.4 The role of the H0 helix in membrane remodeling by cooperative self-assembly of N-BAR

I indicate that during the tube remodeling the amphipathic helix H0 acts like a wedge, being inserted into the membrane, and the BAR domain with its banana-like shape is responsible for the scaffolding. Amphiphysin without the N-terminal H0 helix is able to remodel membranes into tubes. For the primary tube formation the H0 helix is not necessary but the remodelled tube showed an altered tube morphology such as thicker tubes and loss of the organized helical BAR assembly on the tube surface. This implicated that the amphipathic helix is necessary for a fast, efficient and regular arrayed lattice formation of the BAR polymers. This leads to the assumption that the H0 helix is likely needed for the initiation of the membrane curvature remodeling, consequently helps to "poise" the BAR dimers to polymerize and subsequently mediates an organized BAR domain arrangement during the BAR polymerization (Fig. 3.2).

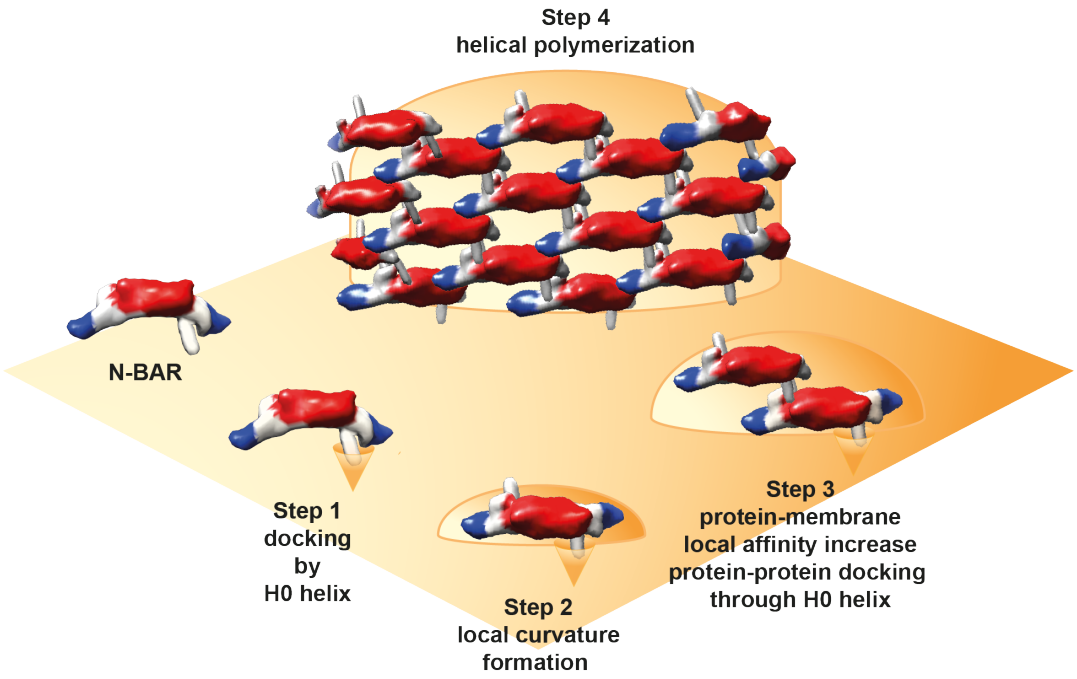

Figure 3.2 – Model of the cooperative self-assembly of the N-BAR protein amphiphysin | Amphiphysin N-BAR uses the wedging and scaffolding mechanisms by the H0 helix and BAR domain, respectively, to remodel membranes into tubular shapes. (Step 1 and 2) The docking of the first incoming N-BAR domain by its H0 helix leads to a local membrane curvature formation, being the driving force for the cooperative self-assembly of the N-BAR domain. When the local curvature fits to the crescent BAR domain shape the BAR domain itself interacts with the membrane and fixes the induces curvature by its scaffolding function. (Step 3) The next incoming BAR domain docks next to the first BAR because of the pre-fixed local curvature and the guidance of the first BAR domain, leading to an increased protein binding affinity. The adjacent BAR domains are linked to each other by the H0 helix. (Step 4) The new incoming BAR domains, being guided by the curved membrane and the membrane bound BAR domains, start to helically self-assemble on the membrane surface. Adopted from [266].

The initial membrane curvature generation from flat to curved may happen through the wedging function of the membrane inserted H0 helix of the first incoming BAR domain. When the local induced curvature by H0 helix insertion fits to the crescent shaped BAR domain the BAR domain itself can interact with and land on the membrane surface and fix the induced curvature with its scaffolding function. The next incoming BAR domain can effectively attach next to the first BAR due to the guidance of the pre-fixed local membrane curvature and the first BAR domain. The close distance of the incoming guided BAR domains to the curved membrane surface leads to an increased protein binding affinity. Hence, the arriving BAR domains, which are guided by the given membrane curvature, start to helically arrange on the membrane surface in an organized fashion and the assembled array may be stabilized by H0 helix connections between adjacent BAR domains. This is a fast and efficient way to assemble a helical packing on a membrane to induce membrane curvature and tube formation. This concept is in agreement with an earlier observation which that suggests that an increasing enrichment of amphiphysin on the membrane surface is proportional to the induced curvature due to the formation of a scaffold around the tubular shape [283]. In addition, the H0 helix may play a more important role in the initial curvature formation as the less contributing BAR tips. For the BAR domain without amphipathic helix a much higher concentration of protein is needed for membrane remodeling in contrast to BAR dimers lacking both tips (CC of 0.7 µM) and the full functional BAR domain (CC of 0.4 µM). Amphiphysin lacking the H0 may simply sense membrane curvature, which is stochastically fluctuating, and this leads to the initial membrane binding. Moreover, without the amphipathic helix the assembly of the helical BAR array seems to be slower and improperly arranged resulting in a wider range of tube diameters. The helical assembling without H0 helix is likely to slow and malfunctioning for physiological requirements. In the cell an efficient formation of T-tubules is necessary for the EC coupling, which can only be ensured when amphiphysin contains the N-terminal amphipathic helix.

3.5 The role of amphiphysin in T-tubule development

T-tubules are positively curved invaginations of the sarcolemma of muscle cells. During the biogenesis several proteins are contributing to the formation and dynamics of T-tubules. It is proposed that T-tubules are developing from CAV3 mediated caveolae, being flask-shaped plasma membrane invaginations, in the early stage of T-tubule biogenesis [146,215]. The caveolae is more deeply invaginated by human muscle BIN1 [215], being the orthologue to *Drosophila* amphiphysin. Within the formed T-tubules caveolae are often located at the sub-sarcolemma, linking T-tubules to the extracellular space [284]. Knockout mice of BIN1 or CAV3 show altered and abnormal T-tubules but they are not lacking [148,209]. This suggests that both proteins contribute to the T-tubule formation. Even though CAV3 and BIN1 are colocalizing no direct interaction is observed. Muscle BIN1 requires

$PI(4,5)P_2$ in the membrane to bind and remodel it into T-tubules [146,173,177]. From this prospect, it is possible that the enrichment of the membrane with $PI(4,5)P_2$ is already happening during caveolae formation so that amphiphysin/BIN1 is efficiently recruited for T-tubule remodeling at the caveolae.
It is reported that DYSF, which associates to the T-tubule biogenesis and T-tubule network, may play a role by the fusion of CAV3 formed caveolae with remodelled T-tubules by interacting with CAV3 and the dihydropyridine receptors [222,285]. Moreover, DYSF seems to partially colocalize with BIN1 [212]. Dysferlinopathy patients have an accumulation of vacuole-like invagination adjoining the T-tubule system [286], which supports the possible joint role of membrane fusion [212,286]. DYSF plays also a role in the maintenance of T-tubules by being involved in the repair of membrane lesions [219,224,287].
Several studies demonstrate that T-tubules are developing from already invaginated caveolae [146,193,205]. BIN1 may sense the already existing curvature, being induced by CAV3, and then cooperatively assembles around the membrane curvature to induce membrane tubulation. It could be speculated that at an later stage of myogenesis already formed T-tubules grow further by melting with adjacent caveolae. This fusion process is facilitated by the membrane repair protein DYSF.
It is known that muscle BIN1 binds to $PI(4,5)P_2$-enriched membranes by its auto-regulated PI-binding motif, which is encoded by exon 11 [112,146,173]. In the cytosol BIN1 is in its "closed" conformation whereat the SH3 domain binds to the PI-binding motif [151,177]. The conformation "opens" and the SH3 domain is released when the PI-binding motif is interacting with $PI(4,5)P_2$ in the membrane. Subsequently, in the "open" state of the auto-regulation the BAR domain and the PI-binding motif is bound to the $PI(4,5)P_2$-enriched membrane whereas the SH3 domain can recruit BIN1 downstream PI-binding proteins such as dynamin 2 [177]. It is reported that on the membrane bound BIN1 clusters $PI(4,5)P_2$ with its N-BAR domain [288]. A recent study reported that several BAR proteins are forming and then sequester PI microdomains on the membrane [289]. In contrast, the N-BAR domain of BIN1 is not occupying the clustered $PI(4,5)P_2$ so that it is available for PI-binding motifs of interaction partners such as dynamin [288]. The SH3 domain of BIN1 is binding to dynamin 2, which interacts with $PI(4,5)P_2$ in the membrane by its PI-binding PH domain [151,177,288]. The clustering of $PI(4,5)P_2$ controls the recruitment and accumulation of dynamin on the membrane surface, which may support dynamin polymerization [288]. Moreover, N-WASP is also interacting with the SH3 domain of BIN1 [290] and is activated by binding to $PI(4,5)P_2$ in the membrane [291,292]. Subtle alteration in the density of $PI(4,5)P_2$ in the membrane is regulating the activation of N-WASP and subsequently, a switch of N-WASP likely triggers N-WASP-mediated Arp2/3 and actin polymerization [293]. BIN1 recruited N-WASP is required for triad formation of the T-tubules with SR-junctions in skeletal muscles [290]. N-WASP regulates the actin cytoskeleton, which is necessary to regulate the organization and structural stability of triads. Furthermore, in cardiac muscle N-WASP forms a complex with cardiac

muscle specific BIN1 13 + 17 to remodel T-tubule folds on the T-tubule surface, which are controlling the ion influx. The T-tubule membrane and T-tubule folds are stabilized by N-WASP regulated actin polymerization[207]. This suggests that the clustering of PIPs such as PI(4,5)P_2 is contributing to the selection and recruitment of specific BIN1 downstream partners at specific T-tubule sites such as triads. Moreover, the cooperative self-assembly of amphiphysin or mammalian BIN1 on the membrane surface may also contribute to the initiation of local clustering of PI(4,5)P_2 and other PIPs and the accumulation of essential components on the membrane surface.

In vitro BIN1 is not only clustering PI(4,5)P_2 in the membrane but also other PIPs such as PI(4)P and PI(5)P[288]. Phosphoinositides phosphatase myotubularin (MTM1), which dephosphorylates PI(3)P and PI(3,5)P_2 and produces PI(5)P[294–296], forms a complex with BIN1 during T-tubule formation[150]. MTM1 contributes for normal function of skeletal muscle cells[297] and mutation of MTM1 result in X-linked CNM[298]. In a recent study it was shown that the complex of MTM1 and BIN1 locates at the triads next to the Z-line of the sarcomere[150]. Moreover, MTM1 enhances the BIN1-mediated tubulation activity likely due to its enzymatic activity and to some extent by its binding. It is assumed that the MTM1 plays a role in the formation of membrane curvature at the triads by regulation of the local PI membrane concentration or protein binding. The phosphatase activity of MTM1 is not regulated by BIN1 but only by itself. A conformational change of BIN1 is needed that MTM1 is interacting with it. It is proposed that for MTM1 binding all domains of BIN1 are needed. It seems that the PI-binding motif modulates the relative positions of the BAR and SH3 domain and thus controls the MTM1 interaction[150]. Next to the BIN1 N-BAR induced PIP clustering the local recruitment of phosphatase such as MTM1 by BIN1 may spatiotemporally regulate the PI level too, resulting in an additional regulation of BIN1 downstream interaction partners. The selection and regulation mechanisms of BIN1 downstream partner facilitate the development of T-tubules and the formation of the T-tubule network.

As *Drosophila* amphiphysin is the orthologue to muscle BIN1 it is likely that it is similarly contributing to the biogenesis and maintenance of T-tubules. Amphiphysin mutated flies show altered T-tubules and triads[49]. It is likely that *Drosophila* amphiphysin recruits similar as well as different downstream interaction partners to the T-tubules. It is known that amphiphysin cannot interact with the *Drosophila* homolog of dynamin[49,116]. The alternative downstream interaction partner of amphiphysin in *Drosophila* is not known yet. Moreover, amphiphysin is lacking the exon 11 PI-binding motif and therefore it has to be tested if the SH3 domain is also auto-regulated like seen in mammalian muscle BIN1. In my *in vitro* study I observed that amphiphysin can remodel membranes into tubes without PI(4,5)P_2 binding. It is possible that some smaller PI-binding motifs are existing in amphiphysin. Whether they play a role in membrane binding and auto-regulation has to be investigated *in vitro* and *in vivo* in the future.

3.6 The effect of CNM and delta-tip N-BAR mutants to the BAR assembly

Centronuclear myopathies are rare inherited muscle disorders leading to muscle weakness. The muscles show a high level of enlarged and centralized nuclei, fiber atrophy, a disorganized T-tubule network and abnormal triads/dyads [136,149,259,279]. Mutation in myotubularin, dynamin 2 and muscle BIN1 cause X-link, autosomal dominant and autosomal recessive and weak autosomal dominant CNM, respectively. In human BIN1 the missense mutation K35N, D151N, R154Q in the N-BAR domain [149,229], the nonsense mutations Q434X and K436X and the stop codon mutations Q573stop and K575stop in the SH3 domain [149,258,259] lead to autosomal recessive CNM. In addition an weak type of autosomal dominant CNM was found due to the following BIN1 N-BAR missense mutation R24C and and the frame shift mutation K21del (deletion of residue K21) in the H0 helix [279]. A closer look to the N-BAR mutations revealed that they are ether located at the H0 helix such as K21del, R24C and K35N (corresponding to K16, R19 and K30, respectively, in *Drosophila* amphiphysin) or at the tip of the crescent shaped BAR dimer such as D151N and R154Q (corresponding to D146 and R149, respectively). This is compatible with my observations where the H0 helix and the tip are crucial for an organized well-connected helical BAR assembly on the membrane surface. Furthermore, other studies demonstrated and discussed that the H0 helix as well as tips are playing a role in membrane remodeling by amphiphysin [108,258].

To investigate the role of the tip, I analyzed the mammalian CNM mutants D151 (D146 in *Drosophila*) and R154 (R149) and additionally, the mutant D144 and the triple mutant KRK161 in the tip region in *Drosophila*. All mutants showed a decreased remodeling activity *in vitro* but only R154 showed a significant reduction of formed tubes. In both CNM mutants shorter tubes were generated whereat the D151 mutant showed less uniform tube formation, which is consistent with a recent report [258]. The CNM mutations D151 and R154 are thought to lead to impairment or lack of tubulation *in vitro* as well es *in vivo* [149,229,258,279]. It was demonstrated that these two CNM mutants are located in or close at a residue pocket (residues ~144 to 151 in human BIN1), which deeply immerse into the lipid bilayer [108]. Possibly, this residue pocket is accounting for a specific contact of the N-BAR domain with the membrane. It is likely, that mutations at this pocket interface may lead to a disturbed membrane interaction, resulting in the reduced tubulation activity and an altered tube remodeling as seen in my observations. The mutation D144 showed only a subtle change in membrane remodeling in contrast to the CNM mutants. In N-BAR-mediated tubes the arrangement of the BAR assembly was seen by negative stain EM. The CNM and D144 mutants did not reveal an organized BAR assembly on the tube surface, which may indicate that these mutations contribute to disorganized T-tubules in myocytes. For the mutant KRK161 at the end of the BAR dimer tips, being located in the flexible loop, a decreased tubulation activity was

reported[43]. In my study I observed a slightly reduced membrane remodeling activity and the formation of thinner/thicker bilayer and micellar tubes. As I discussed before the tip is likely playing a role in the interaction of the protein with the membrane and in the assembly of a rigid BAR packing. Mutations of the tip ends seem to disturb the interaction of the BAR dimer with the membrane or adjacent dimer in the helical lattice. It could be speculated that the disturbance of the integrity of the BAR arrangement due to tip may lead to fluctuation of the BAR domain on the membrane surface leading to altered membrane remodeling.

It was reported that a residue patch, which is located around the D151, at the tip region of the BAR domain is deeply inserted into the membrane, up to the lipid acyl chain region, which is important for membrane tubulation[108]. This is consistent with my observations that the one BAR tip of the BAR dimer is immersed in to the lipid bilayer of the remodelled tube whereas the other tip is protruding out from the membrane surface. By using EPR as method it can not be detected if only one or both tips are inserted into the membrane. It can only determine that one tip is immersed into the membrane, which agrees well with my helical reconstruction of amphiphysin-mediated tubes. Interestingly, the delta-tip N-BAR mutants, lacking one or both tips of the BAR dimer unit, are able to remodel membranes to tubular shapes. In negative stain EM the formed tubes did not display any arranged BAR lattice pattern on the membrane surface, which on the contrary was seen on N-BAR-mediated tubes. This reveals that an organized helical BAR domain assembly is missing on tube surface by tip mutant formed tubes. In contrast to the BAR mutant lacking both dimer tips, generating irregular and thicker tubes, the mutant with one BAR domain tip showed rather uniform-mediated tubes. In both cases the tubulation was significantly decreased. It is likely that only one tip of the banana-shaped BAR dimer is necessary for membrane tubulation due to direct interaction with the membrane. The other BAR tip is contributing to the organization and stabilization of the helical BAR assembly by interacting with the neighbouring BAR dimer within the same lattice row. In addition, in N-BAR-deltaH0-mediated tubes, missing the H0 helix, the organization of the BAR assembly was also partly lost, possibly due to lack of the density, connecting BAR dimers in adjacent lattice rows. Moreover, the power spectrum of the 2D averaged N-BAR-deltaH0-mediated tubes revealed a shrinkage of the helical packing. The thicker remodelled tubes did not display any lattice pattern at all. This strengthened the hypothesis that an organized helical BAR assembly on the membrane surface is necessary for a rigid uniform tube formation due to well-connected adjacent BAR dimers within the lattice. Defects or deletion of the H0 helix and/or tips of the BAR dimers are showing a minor effect on the tube remodeling capability but they reveal a significant disturbance within the helical BAR arrangement. This may help to understand why CNM mutations within the amphiphysin N-BAR domain lead to a disorganized T-tubule network and abnormal triads/dyads in muscle cells. It is likely that the CNM-mediated disorganization of T-tubules and triads/dyads lead to a disturbed

excitation-contraction coupling due to defects in the calcium influx and subsequent to muscle weakness. It should be noted that I used a specific lipid composition to facilitate the structural analysis[108] but the differences may be more distinct under physiological lipid conditions.

For all types of CNM centralized nuclei are the characteristic, which is defining this muscle disorder, next to disorganized T-tubule networks and abnormal triads/dyads. In CNM the N-BAR domain as well as the SH3 domain show disease inducing mutations. Mutation in the SH3 domain such as the non-sense mutations Q434X and K436X and stop mutations Q573stop and K575stop, deleting the last 17 or 15 amino acids of the SH3 domain, respectively[149,166,258,259]. Mutations in the SH3 domain go along with the impairment of PRD binding of dynamin 2 or N-WASP[136,149,166,259,290]. Dynamin 2 and N-WASP are involved in the formation and maintenance of T-tubules and triads/dyads. Loss of interaction between dynamin 2 or N-WASP with BIN1 or mutations in one of these proteins lead to disorganized T-tubules and triads/dyads[136,177,261,290,299,300]. In addition, it was shown that BIN1 plays a role in the positioning of the nucleus within myocytes development[136,290]. Mutations in the N-BAR or SH3 domain of muscle BIN1 lead to centralized and abnormal shaped nuclei. A recent study showed that mammalian BIN1 binds nesprin at the nuclear envelope in a conformational-dependent manner, including all domains and links it to the microtubule and actin cytoskeleton[136]. During nucleus positioning mammalian BIN1 binds to nesprin and at the same time to the microtubule network via CLIP-170 by its BAR domain and to N-WASP and subsequent to the actin network by its SH3 domain. BIN1 orchestrates the positioning of the nucleus by linking nesprin to the MT plus ends, which likely pushes the nucleus[136,301], and by binding to actin, which may function as connection between NE and the actin network for the fine tuning[136]. CNM mutations in BIN1 such as D151N, R154Q or K575stop lead to an altered nuclei localization from peripheral to central within the myocytes[136,290]. The mutation of D151N in the BAR domain has a significant decreased binding to CLIP-170, leading to a loss of the pushing force of the MT to the NE[136] and the SH3 mutation K575stop impairs the binding to N-WASP, resulting in the loss of binding of the NE to the actin network[136,290]. Furthermore, the nucleus shape is affected by BIN1 CNM mutations such as D151N in the N-BAR domain or by loss of function of BIN1. It is hypothesized that the force transduction of the cytoskeleton with the NE is decreased in BIN1 CNM mutants as BIN1 is a crucial component in this process[136]. In this study they did not show if BIN1 is binding to the membrane by its BAR domain. But it is proposed that the processes of T-tubule biogenesis and maintenance and nucleus positioning by BIN1 occur independently to each other[290]. It is interesting that the mutation of D151N in the BIN1 N-BAR domain, being part of the deeply membrane immersed residue pocket, seem to impair the membrane remodeling ability *in vitro* as well as *in vivo* by BIN1 and additionally, its function in nucleus positioning due to the lack of MT binding. It seems that the residue D151 is not only involved in protein-membrane

binding but also protein-protein binding. In addition, it could be speculated that in this mutant the loss of CLIP-170 binding and subsequently, of the MT network may not only play a role in the nucleus positioning but also in the formation and stabilization of T-tubules *in vivo*. If BIN1 lacks the linkage to the MT network it can not accordingly fulfil its distinguish functions in the muscle cell. This may point out why miss-regulation of muscle BIN1 likely leads CNM.

3.7 The role of the amphiphysin regulatory domain SH3 in striated myocytes

Drosophila amphiphysin and the mammalian muscle BIN1 isoform 8 are involved in the formation and maintenance of T-tubules in skeletal muscles[49,146]. Mammalian cardiac BIN1 isoforms are contributing to the same tasks in cardiac muscles as well as the formation of specific T-tubule folds by BIN1 isoform 13 + 17[207,233]. Moreover muscle BIN1 is involved in the formation of dyads/triads[49,147,208,290], the assembly and organization of the sarcomere[175] and positioning of the peripheral nucleus[136,290]. Up till now several studies reported about the SH3 domain and its binding side for several BIN1 downstream interaction partners, contributing to the function of the excitation-contraction coupling machinery, including T-tubules, and the myocyte organization. Whereas the BAR domain mostly is involved in the deformation of membranes like in the formation of T-tubules[49,146,151,177].

In my study amphiphysin fragments with or without regulatory domains remodel membrane into tubes *in vitro*, suggesting that the regulatory domains are not necessary for the generation of membrane curvature. This indicates that the regulatory domains, containing the central region and the SH3 domain, is likely free for interactions. The cryo-EM images of amphiphysin full-length-mediated tubes revealed a similar tube formation as with N-BAR domain alone. But in the case of FL some additional needle-like densities were protruding out from the tube surface, which likely belong to the regulatory domains. Amphiphysin N-BAR and FL-remodelled tubes have a similar arranged BAR lattice on the tubes surface, which indicates that the regulatory domains are not incorporated within the helical amphiphysin assembly and rather protrude outwards. In the 2D classes no dominant sticking out density was observed as the regulatory domains could not be averaged likely due to flexibility and fluctuation of the regulatory domain on the tube surface. I suggest that the function of the N-BAR domain is mostly to scaffold and stabilize the structure of T-tubules whereas the regulatory domains may play a role as adapter for proteins being involved in T-tubule and sarcomere assembly and organization. Previous studies showed that the BIN1 BAR domain uses the scaffolding mechanism to remodel the PI(4,5)P_2 enriched sarcolemma into T-tubules[112,146,173]. After the binding of the BAR domain and the PI-biding motif of exon 11 with the PI(4,5)P_2 enriched membrane the auto-regulation of the SH3 domain is abrogated so that it can bind to

interaction partners[151,177]. This supports the suggestion that the regulatory domains, including the SH3 domain, are not involved in the BAR lattice organization, inducing membrane remodeling.
The likely protruding out SH3 domain of amphiphysin/BIN1 plays several roles within the myocytes. It was shown that the T-tubule bound BIN1 orchestrates the assembly and organization of the sarcomere by its SH3 domain, which is forming transient protein complexes with both myosin and actin and the pro-myogenic kinase Cdk5[175]. Here it is likely that the BAR domain is shaping and stabilizing the T-tubules, being located close to the myofiber sarcomere, whereas the SH3 domain is helping to assemble the myofibers by guiding and positioning sarcomeric proteins at the adequate time and place due to transient protein interactions. Moreover, during T-tubule biogenesis and maintenance the SH3 domain is binding to N-WASP, which regulates actin dynamics. It was shown that skeletal muscle BIN1 binds to N-WASP to regulate nucleus positioning and triad organization during myofiber development[290]. In cardiac muscle BIN1 13 + 17 binds and activates N-WASP to induced F-actin formation, which is necessary to form T-tubule membrane fold, being extracellular microenviroments that restrict ion diffusion. In addition, for T-tubule biogenesis and maintenance BIN1 binds to dynamin 2, which regulates membrane fission and plays a role in CNM by fragmenting T-tubules[302]. The BAR domain and the exon 11 motif binding to PI(4,5)P_2 enriched membrane leads to a clustering of PI(4,5)P_2 so that the BIN1 SH3-bound dynamin 2 can accumulate on the membrane via its PH domain, which binds to PI(4,5)P_2[288]. In relation to my results this suggest that the BAR domain and SH3 domain of amphiphysin/BIN1 have two distinct functions in myocytes. The BAR domains induce and stabilize membrane curvature by using the scaffolding mechanism. In addition, the BAR domains are able to cluster PIPs and therefore, are contributing to the binding and regulation of downstream partners, which are interacting with the regulatory domains of amphiphysin/BIN1. The SH3 domain is auto-regulated by the exon 11 encoded PI-binding motif so that it can not bind downstream interaction partners. After its release by PI(4,5)P_2-enriched membranes it is capable of interacting with downstream proteins. This agrees to my observations that the regulatory domains with the SH3 domain are not incorporated into the helical BAR packing on the membrane surface and that they are insignificant for membrane remodeling.

3.8 Outlook

Drosophila amphiphysin plays a role in T-tubule biogenesis and maintenance like its orthologue muscle BIN1 in mammals[49,146]. I showed that the BAR domain is responsible for the membrane remodeling activity of amphiphysin and that the regulatory domains, including the SH3 domain, are not incorporated into the helical BAR lattice on the tube surface. Amphiphysin N-BAR arranges itself in a cooperative manner on the membrane

surface. During this process it uses the BAR domain for the scaffolding and the H0 helix for the wedging mechanism to remodel membranes. Amphiphysin N-BAR self-assembles in a unique helical BAR arrangement where one BAR dimer tip is immersed into the membrane and the other tip protrudes outwards from the tube surface. The adjacent BAR dimers are likely well-connected to each other either by interactions of the H0 helices between the lattice rows or by dimer tip-to-center interactions. The precise interactions sites were not determined due to the middle resolution of ~11 Å. Therefore higher resolution should be achieved to visualize the H0 helices and dimer-dimer interactions sides. Due to the detected fluctuation of the BAR dimers on the tube surface with the resulting heterogeneity of the BAR arrangement it is possible that no high resolution could be gained.

Furthermore, a 3D helical reconstruction of amphiphysin full-length-mediated tubes may further help to understand the role of of the various amphiphysin regulatory domains in T-tubule development. My 2D cryo-EM observations suggest that the regulatory domains are not incorporated into the helical BAR lattice and that they are rather flexible on the membrane surface. This would make it more difficult to obtain an additional EM density, belonging to the whole regulatory domains, on the reconstructed amphiphysin-mediated tube and to achieve high resolution. Cross-linking of amphiphysin full-length, wrapping around the tube surface, may help to get structural insights of the amphiphysin BAR arrangement and orientations of regulatory domains.

In my study I used a specific lipid mixture of 2POPG:1POPE to facilitate the structural analysis. Hence, one of the next steps would be to structurally investigate the BAR domain arrangement *in vitro* with physiological membrane condition such as Folch Fraction I, containing PS, PIPs and other lipids, by using cryo-EM and 3D helical reconstruction. It would be interesting to see if a change in the helical packing would occur due to an altered protein-membrane interaction with physiological membranes, containing PIPs.

Mammalian muscle BIN1 contains an PI-binding motif (exon 11), which binds to PI(4,5)P_2 enriched membrane. This binding is necessary for T-tubule development [112,146,173]. *Drosophila* amphiphysin seems to have conserved short polybasic sequence motifs in the H0 helix and BAR domain. A previous study suggested that amphiphysin H0 helices need PI(4,5)P_2 to interact with membranes *in vivo* [262]. I found that PI(4,5)P_2 is not needed for amphiphysin binding to the membrane *in vitro*. The lipid mixture of my study was also used in an recent EPR study and tubulation was occurring [108]. It is possible that PI(4,5)P_2 is recognized by polybasic motifs in the N-BAR domain and the regulatory domain but it is not essential for membrane remodeling, as it was observed in my tubulation assay of amphiphysin N-BAR with Folch fraction I. *In vitro* pull down assays of amphiphysin with lipid vesicles, containing various PIPs, could be performed to see if amphiphysin N-BAR or full-length shows a preferred binding to specific PIPs. Moreover, several fragments of amphiphysin could be analysed if specific domains tend to

bind PI(4,5)P_2. In addition, *in vitro* pull down assays of the amphiphysin H0 helix alone with lipid vesicles of different lipid compositions containing PIPs may help to understand the membrane binding ability of the H0 helix. As the H0 helix contains only ~27 residues an additional not cleaved off C-terminal tag like sumo would help during the protein purification and in the visualization of the binding by SDS PAGE.
Moreover, a residue patch at the tip, which is deeply immersed into the membrane [108], could be mutated to see if membrane remodeling is still happening. Another way to alter the scaffolding mechanism is to mutate the muscle BIN1 PI-binding motif of exon 11. Without this polybasic sequence motif no T-tubule formation should be possible *in vivo* [146,151,177]. In *Drosophila* amphiphysin some short polybasic sequences are existing in the N-BAR domain. The role of these polybasic patches in T-tubule development is not known yet. Deletion or mutations of these sequences may result in an altered membrane remodeling ability *in vitro*, which could be analyzed by negative stain EM, cryo-EM and light scattering, as well as *in vivo*. These specific mutations in the N-BAR domain may lead to an altered protein-membrane and protein-protein interaction, resulting in a disturbed BAR scaffolding and T-tubule network formation.
I observed that amphiphysin N-BAR uses the scaffolding mechanism and hydrophobic motif insertion to remodel membranes into tubes *in vitro*. Amphiphysin is located at the T-tubules from larvae to adult flies [49] and therefore seems to be involved in the biogenesis as well as maintenance of T-tubules by acting like a rigid scaffold for T-tubules. The role of the BAR domain and its scaffold function in T-tubules could be further analyzed by changing the remodeling ability of amphiphysin.
Several mutations in the N-BAR or SH3 domain of mammalian muscle BIN1 are known to be associated with CNM [149]. It was shown that these mutations lead to a disorganized T-tubule network with abnormal triads/dyads formation [149]. Mutations in the BAR domain may lead to a disturbed packing on the tube surface and subsequently to a different T-tubule morphology. Several BAR domain mutations are known to cause CNM [149,259]. In my study I observed an altered tubulation behavior of several mutants with CNM-associated residues and mutants without N-BAR dimer tips. In my tubulation assays with the mutants I used the same specific lipid compositions as in my structural analysis of N-BAR. The usage of physiological membranes may result in a more distinct alteration of the membrane remodeling ability.
Moreover some of these mutations seem to play a role in the centralization of the nucleus such as D151N in the N-BAR domain [136]. D151 of the BAR domain seems to bind to CLIP-170 and forms a linkage to the microtubule network. Hence, the residue D151 and possible others may not only be playing a role in protein-membrane binding but also in protein-protein binding. In future studies it would be interesting to investigate if the residues, being mutated in CNM, are playing a role in only one or several functions in myocytes. Moreover, it would be interesting to see if some residues may contribute to protein-protein and/or protein-membrane binding.

Furthermore, it would be also interesting to study if *Drosophila* amphiphysin has some kind of auto-regulation such as mammalian BIN1, being regulated by PI(4,5)P_2 interactions. In muscle BIN1 the SH3 domain is auto-regulated by the PI-binding motif of exon 11. In *Drosophila* amphiphysin it is unclear if the SH3 domain is also autoinhibited. Binding assays of amphiphysin with its interaction partners, binding to the SH3 domain via their PRD domain, with and without liposomes would give a first hint if the SH3 domain is auto-regulated.

In addition, to understand the membrane remodeling abilities and dynamics of *Drosophila* amphiphysin N-BAR and mammalian muscle BIN1 in T-tubules, a comparison of amphiphysin homologous should be performed *in vitro*. Human neuronal amphiphysin I and II are involved in the neck formation of the budding vesicles in CME, which is a more dynamic process as observed with mammalian endophilin [70,100]. T-tubules are rigid formed membrane invaginations, which should not be as dynamic as the formed vesicles necks in CME. I showed that a well-connected N-BAR assembly on the tube surface is necessary to remodel rigidly shaped membrane tubes. Further studies may give insights if additional factors next to the N-BAR arrangement contribute to the maintenance of the T-tubule shape.

In the current *in vitro* study the BAR arrangement was explored in isolation but there are several other factors involved in the formation of T-tubules *in vivo*. *Drosophila* amphiphysin is not binding to dynamin in flies [49]. It has to be further investigated what binding partners are interacting with the regulatory domains of amphiphysin. Pull down experiments of amphiphysin full-length with extracted T-tubules or muscle cell extract could help to find more amphiphysin interaction partners, being involved in the T-tubule network.

The regulatory SH3 domain is the main protein-protein interaction site of amphiphysin [136,151,175,290]. But the role of the central region in T-tubule formation is unclear. [49,116,146]. T-tubules are not only formed by amphiphysin/BIN1 but also by additional scaffold proteins or transmembrane proteins [233]. In the future it would be interesting to investigate how these proteins are recruited to the T-tubules so that a T-tubule network could be developed. It was observed that mammalian muscle BIN1 is able to interact with dynamin 2 or N-WASP and the actin network by its SH3 domain [136,151,177,207,290]. The role of dynamin 2 in the T-tubule biogenesis and maintenance is not known yet. It would be interesting to structurally investigate how dynamin is helically enriched next to BIN1 on the T-tubule membrane. Binding of N-WASP with the BIN1 and the PI(4,5)P_2-enriched membrane activates actin polymerization and the formation of actin filaments, which may help to maintain the tubular T-tubule shape. *In vitro* reconstitution of this process could give insights into how the T-tubule network is stabilized within myocytes.

The observed protruding out BAR dimer tip on the tube membrane may facilitate protein interactions at the T-tubule surface next to the SH3 regulatory domain. Recently it was

reported that CLIP-170 can interact with the BAR domain to generate a linkage the microtubule network[135,136]. Cardiac muscle BIN1 localizes subunits of calcium channels to the T-tubules by linking T-tubules to the Golgi via the MT network[233]. It would be interesting to see if muscle BIN1 in skeletal muscles uses the same mechanism to locate calcium channels to the T-tubules. Moreover, *in vitro* reconstitution of membrane bound BIN1 N-BAR with MT may reveal their interaction sides. Under physiological conditions several proteins are contributing to the stabilization and maintenance of T-tubule. All these protein interactions on the membrane surface may lead to an altered lattice arrangement. Future structural studies of amphiphysin or BIN1 with interaction partners may give insights into how the BAR packing on the tube surface changes because of additional protein binding.

There are several unresolved questions in the T-tubule biogenesis and maintenance. First of all the origin of T-tubule formation is still not clear yet. There is evidence that T-tubules are expanded from CAV3 formed caveolas[146,215]. Some other studies suggested that T-tubules are formed from intracellular compartments such as the Golgi or the endosome and afterwards fuse with the sarcolemma[303–305]. It is possible that both mechanisms are existing in the cell. It is proposed that the formation of intracellular T-tubules may lead to transverse T-tubule after fusion with the the sarcolemma[304]. In addition, so far it has not been reported how the transverse and longitudinal T-tubule network is developed and how it grows. Amphiphysin N-BAR alone remodels membranes into straight tubes *in vitro*. As the function of the regulatory domain is not completely solved it has to be further investigated whether the central region and the SH3 domain are involved in the branching of T-tubules. Moreover, if T-tubules are formed from intracellular compartments[303–305] and they fuse with the sarcolemma or T-tubules, located at the sarcolemma, maybe a branched T-tubule network could develop. DYSF is known to be contributing to T-tubule biogenesis and maintenance by being involved in T-tubule membrane repair[219,221,224,287] and T-tubule fusion events[222,285]. Live cell imaging of myogenesis may give insights into the origin of T-tubules and the branching mechanism of the T-tubule network. Proteins involved in the T-tubule biogenesis could be fluorescently labeled and the developing myocytes with their compartments could be observed by light microscopy.

In my thesis I gave a structural insight into the formation of a self-assembled N-BAR domain scaffold, which remodels membrane into tubes. For future studies it would be of interest to include amphiphysin interaction partners into the membrane remodeling process. Interaction of known or new amphiphysin down-stream partners should give further knowledge about how T-tubule are formed, stabilized and maintained.

4 Materials and methods

4.1 Materials

4.1.1 Consumables and Chemicals

All used chemicals were purchased from Merck (Darmstadt, Germany), Roche Diagnostics (Mannheim, Germany), Qiagen (Venlo, The Netherlands), Serva (Heidelberg, Germany), Sigma-Aldrich (München, Germany) and Roth (Karlsruhe, Germany). Enzymes were ordered from Thermo Scientific (Epson, UK), Roche Diagnotics (Mannheim, Germany), Merck (Darmstadt, Germany) and NEB (Schwalbach, Germany). Lipids were purchased from Avanti Polar Lipids (Alabaster, USA) and Sigma Aldrich (München, Germany). Gel and DNA extraction kits were received from Qiagen (Venlo, The Netherlands). DNA oligonucleotides were synthesized by Eurofins Genomics (Ebersberg, Germany). Pre-cast gels were purchased from Bio-Rad (München, Germany). Protein concentrators were obtained from Merck Millipore (Darmstadt, Germany). Chromatography material and columns were obtained from GE Healthcare (München, Germany) and Qiagen (Venlo, The Netherlands). EM material such as forceps and grids was ordered from Plano (Wetzlar, Germany) and Quantifoil (Großlöbichau, Germany).

4.1.2 Antibiotic solutions

Antibioticum	Stock solution	Final concentration
Ampicillin	100 mg/ml	100 µg/ml
Kanamycin	50 mg/ml	50 µg/ml

Table 4.1 – Antibiotic solutions

4.1.3 Media and buffer

Medium	Compositions & system	Expression
LB	1% (w/v) Bacto Trypton, 0.5% Yeast Extract, 0.5% (w/v) NaCl, pH 7.2	*E. coli*
SOC	2% (w/v) Bacto Trypton, 0.5% Yeast Exract, 10 mM NaCl,	
	10 mM MgSO4, 2.5 mM KCl, 1 mM MgCl2, 0.4% glucose, pH 7.2	*E. coli*
ZY	1% (w/v) Bactor Trypton, 0.5% Yeast Extract, 100 mM PO4, 25 mM SO4,	
	50 mM NH4, 100 mM Na, 50 mM K, 0.5% glycerol,	*E. coli*
	0.05% glucose, 0.2% α-lactose	

Table 4.2 – Media and buffer

4.1.4 Vectors and plasmids

Name	Application	Tag	Cleavage
pEC-A-Sumo-His	Bacterial protein expression	N-terminal 6xHis-Sumo-Tag	SenP2
pEC-K-3C-His	Bacterial protein expression	N-terminal 6xHis-Tag	3C

Table 4.3 – Vectors

Constructs	Vector	Primers	Insertion site
N-BAR	pEC-K-3C-His	5JA, 6JA	LIC, 3C
N-BAR-deltaH0	pEC-A-Sumo-His	2JA, 5JA	SUMO LIC
FL	pEC-A-Sumo-His	1JA, 4JA	SUMO LIC
deltaH0	pEC-A-Sumo-His	2JA, 4JA	SUMO LIC
N-BAR-delta-tip	pEC-K-3C-His	7JA, 8JA	LIC, 3C
N-BAR-N-BAR-delta-tip	pEC-K-3C-His	insert1: 11JA, 9JA insert2: 10JA, 6JA	LIC, 3C
D144R	pEC-K-3C-His	14JA, 15JA	LIC, 3C
D146R	pEC-K-3C-His	16JA, 17JA	LIC, 3C
R149E	pEC-K-3C-His	18JA, 19JA	LIC, 3C
KRK161EEE	pEC-K-3C-His	step1: 20JA, 21JA step2: 22JA, 23JA	LIC, 3C

Table 4.4 – Plasmids

4.1.5 Oligonucleotides for cloning

Primer	Sequence (5'-3')
1JA	accaggaacaaaccggcggccgctcgatgaccgaaaataaaggcataatgctggccaaatctgttcaaaaacac
2JA	accaggaacaaaccggcggccgctcgatgaacttgggcaaagtcgatcgcactgcgg
3JA	gcaaagcaccggcctcgttatagcgtattggagccgcgctgcgattc
4JA	gcaaagcaccggcctcgttagatgggacgcgtgaagttggcggg
5JA	ccaggggcccgactcgatgaccgaaaataaaggcataat
6JA	cagaccgccaccgactgcttaggagccgcgctgcgattctg
7JA	pho-agcggcagcggcagcgaagctagacgcacctacg
8JA	pho-gccgctgccgctgccatcgtaatcaatcagctttcgg
9JA	gccggatccgccgccgctaccggagccactcccgctacccgagccagacccagaaccggagccgcgctgcgattc
10JA	ggcggcggatccggcagcggcagcggcagcggcagcggcagcggcagcggcagcatgaccgaaaataaaggcataat
11JA	taatacgactcactataggg
12JA	ccaggggcccgactcgatgacggagaacaagggtatcatgcttgcgaagagcgtgcagaagcatgcgggtatgacc gaaaataaaggcataatgctggcc
13JA	ccaggggcccgactcgatgaccgaaaacaaaggtatcatgaccgaaaataaaggcataatgctggcc
14JA	gcaaccgaaagctgattcgttacgatggccaacgac
15JA	gtcgttggccatcgtaacgaatcagctttcggttgc
16JA	ccgaaagctgattgattacagaggccaacgacactcgtttc
17JA	gaaacgagtgtcgttggcctctgtaatcaatcagctttcgg
18JA	gattgattacgatggccaagaacactcgtttcagaatctgc
19JA	gcagattctgaaacgagtgttcttggccatcgtaatcaatc
20JA	ctgcaggccaatgccaacgaggaggaagatgatgtcaaactaacc
21JA	ggttagtttgacatcatcttcctcctcgttggcattggcctgcag
22JA	ctgcaggccaatgccaacaaggaggaagatgatgtcaaactaacc
23JA	ggttagtttgacatcatcttcctccttgttggcattggcctgcag

Table 4.5 – Oligonucleotides for cloning

4.1.6 Bacterial strains

Strain	Species	Genotype
XL1 blue	*E.coli*	recA1 endA1 gyrA96 thi-1 hsdR17 supE44 relA1 lac
DH5α	*E.coli*	F^- Φ80lacZΔM15 Δ(lacZYA-argF) U169 recA1 endA1 hsdR17 (r_K^-, m_B^+) phoA supE44 λ^- thi-1 gyrA96 relA1
BL21 DE3 gold	*E.coli*	F^- dcm^+ Hte ompT hsdS(r_B^- m_B^-) gal λ(DE3) endA Tet^r

Table 4.6 – Bacterial strains

4.1.7 Buffers for Protein Purification

Buffer	Compositions	Protein	Application
Lys	20 mM Hepes, 500 mM NaCl, 1 mM DTT, pH 7.4	all constructs	Cell lysis
His1	20 mM Hepes, 500 mM NaCl, 30 mM imidazole, 1 mM DTT, pH 7.4	all constructs	Wash
His2	20 mM Hepes, 300 mM NaCl, 250 mM imidazole, 1 mM DTT, pH 7.4	all constructs	Elution
MS1	20 mM Hepes, 1 mM DTT, pH 7.4	N-BAR, N-BAR-deltaH0 N-BAR mutants, tip mutants	CEX
MS2	20 mM Hepes, 2M NaCl, 1 mM DTT, pH 7.4	N-BAR, N-BAR-deltaH0 N-BAR mutants, tip mutants	CEX
MQ1	20 mM Hepes, 1 mM DTT, pH 7.4	amphiphysin FL, deltaH0	AEX
MQ2	20 mM Hepes, 2M NaCl, 1 mM DTT, pH 7.4	amphiphysin FL, deltaH0	AEX
SEC	20 mM Hepes, 500 mM NaCl, 1 mM EDTA, 1 mM DTT, pH 7.4	all constructs	SEC

Table 4.7 – Buffers for Protein Purification

4.1.8 Lipid compositions

The following lipid compositions were used: 100% POPE, 100% POPG, 2POPG:1POPE (w/w), Folch Fraction I (bovine brains extract).

Lipid	Supplier
POPG	Avanti Polar Lipids (Alabaster, USA)
POPE	Avanti Polar Lipids (Alabaster, USA)
POPC	Avanti Polar Lipids (Alabaster, USA)
Folch Fraction I	Sigma Aldrich (MÃijnchen)

Table 4.8 – Lipid components

4.1.9 Software

Software	Supplier/Developer
BSOFT	Heymann and Belnap [269]
CTFFIND3	Mindell and Grigorieff [270]
SPIDER	Frank et al. [273]
EMAN	Ludktke et al. [271]
EMAN2	Tang et al. [306]
RELION	Scheres [267]
UCSF Chimera	Pettersen et al. [278]
Fiji/ImageJ2	Fiji and ImageJ2 developers
Pymol	Schrödinger
EM MENU4	TVIPS
SerialEM	Mastronarde [307]

Table 4.9 – Software

4.1.10 Equipment

Equipment	Supplier
Ultrasonic homogenizer	Bandelin electronic, Berlin,Germany
ÄKTA purification systems	GE Healthcare, München, Germany
NanoDrop spectrophotometer	Thermo Scientific, Epson, UK
Extruder	Avanti Polar Lipids, Alabaster, USA
Vacuum Desiccator Cabinet	Labonco Corporation, Kansas City, USA
Photometer	Bio-Rad, München, Germany
WF1 GE DelatVision Elite	GE Healthcare, München, Germany
Plasma cleaner chamber	Harrick Plasma, Ithaca, NY ,USA
Vitrobot cryo-station	FEI, Eindhoven, The Netherlands
Manual plunger	In-house workshop, Baumeister Dept.
CM200-FEG electron microscope	FEI, Eindhoven, The Netherlands
Tecnai F20 electron microscope	FEI, Eindhoven, The Netherlands
Tecnai 'Polara' G2 F30	FEI, Eindhoven, The Netherlands
TVIPS CCD camera	TVIPS, Gauting, Germany
Eeagle CCD camera	FEI, Einhocen, The Netherlands
K2 direct detector	Gatan, Pleasanton, USA

Table 4.10 – Equipment

4.2 Methods

4.2.1 Cloning of Constructs

DNA Template

The gene encoding *Drosophila* amphiphysin was shared by Ralf Langen, PhD (USC, USA).

Polymerase Chain Reaction

Polymerase chain reaction (PCR) is a method to amplify multiple copies of a specific DNA sequence from a DNA target template. The used genes were amplified from the particular template DNA and for the DNA synthesis the Phusion DNA Polymerase was used (NEB, Schwalbach, Germany). For the PCR a standard protocol was used (see Table 4.11 and 4.12) by using a Phusion Master Mix, containing the Phusion DNA polymerase, Phusion DNA polymerase buffer and dNTPs. Afterwards the PCR product was analyzed via agarose gel electrophoresis in 1% TAE buffer (40 mM Tris pH 8.0, 0.1% HOAc, 1 mM EDTA). The PCR insert was cut out of the gel and purified via gel extraction kit (Qiagen, Venlo, The Netherlands).

Components	final concentration	Amount
template	3 ng	1 µl
primer forward	10 pmol	1 µl
primer reverse	10 pmol	1 µl
Phusion master mix	2x	10 µl
H_2O	add to 20 µl	7 µl

Table 4.11 – PCR reaction

Step	Temperature	time	cycle
1	98 °C	180 sec	1
2	98 °C	10 sec	
3	64 °C	30 sec	
4	72 °C	60 sec/kb	40
5	72 °C	5 min	1
6	8 °C	hold	

Table 4.12 – PCR amplification protocol

Cloning into pEC-Vectors

The amplified genes were cloned into pEC-vectors, being generated by Jérôme Basquin and Florence Martin (MPIB), by Ligase Independent Cloining (LIC). LIC is a fast, efficient alternative cloning method in contrast to the common restriction enzyme and ligation cloning. Here the 3' –> 5'-exonuclease activity of the T4 DNA polymerase (Novagen, Merck, Darmnstadt, Germany) is used to create 12-15 base single-stranded overhangs with complementarity between the linearized target vector and the amplified PCR insert, containing the gene. By mixing the T4 DNA polymerase, DNA and only

one specific dNTP the overhangs are generated due to an equilibrium of the 3'–>5'-exonuclease and 5'–>3'-polymerase activity when the position of the specific nucleotide is reached. The annealing is taking place by mixing the DNA fragments without the help of a ligase. Here a circular construct with four nicks is formed. Due to the transformation into competent *E. coli* cells the 4 nicks will be repaired.
For the LIC cloning the pEC-vector was linearized by incubating 2 ug of vector with the particular restriction enzyme (NEB, Schwalbach, Germany) for 3h at 37 °C (see Table 4.13). Afterwards the digested vector was analyzed via 0.8% agarose gel in 1% TAE. The corresponding band of the linearized vector was cut out and the DNA was purified with a gel extraction kit (Qiagen, Venlo, The Netherlands). To get the 12-15 base overhang the linearized vector was mixed with the T4 DNA Polymerase (see Table 4.14) and incubated for 30 min at room temperature (RT). For the inactivation of the polymerase the reaction mix was incubated for 20 min at 75 °C. The final vector concentration was around 15 ng/µ/l. The PCR insert overhangs were achieved by mixing the PCR product with the T4 DNA Polymerase (see Table 4.15). The reaction mix was incubated for 30 min at RT and afterwards the polymerase was inactivated like the linearized vector. For the annealing reaction 2 µl of insert were mixed with 1 µl of vector and incubated for 10 min at RT. Afterwards 1 µl of EDTA (2m mM) was added to the annealing mix and again incubated for 10 min at RT. At last 2 µl of the mixture were transformed into (chemo- or electro-) competent *E. coli* cells. Around six colonies were picked for plasmid preparation via plasmid DNA extraction kit (Qiagen, Venlo, The Netherlands). Afterwards two plasmids were sent for DNA sequencing (Biochemistry Core Facility (MPIB) or Eurofins Genomics, Ebersberg, Germany) to confirm whether the cloning was successful.

Component	Stock concentration	Amount
vector		2 µg
NEB buffer4	10x	10 µl
SacII or ZraI (LIC, 3C)	10 U/ µl or 20 U/ µl	10 - 5 µl
H_2O		to 100 µl

Table 4.13 – Vector linearization for LIC cloning

Component	Stock concentration	Amount
linearized vector		450 ng
T4 DNA Pol. buffer (10x)	10x	3 µl
dTTP (25 mM)	25 mM	3 µl
DTT (100 mM)	100 mM	1.5 µl
T4 DNA Pol. LIC qualified (Novagen)	2.5 U/ µl	0.6 µl
H_2O		to 30 µl

Table 4.14 – LIC vector processing

Component	Stock concentration	Amount
Gel purified PCR product		600 ng
T4 DNA Pol. buffer (10x)	10x	2 µl
dATP (25 mM)	25 mM	2 µl
DTT (100 mM)	100 mM	1 µl
T4 DNA Pol. LIC qualified (Novagen)	2.5 U/ µl	0.4 µl
H_2O		to 20 µl

Table 4.15 – LIC insert processing

Cloning of mutants by site-directed mutagenesis PCR

Mutations are inserted into the gene via PCR by primers, containing the mutation. Here the forward and reverse primer are complementary to each other and they bind at the same position on the gene. The primers have around 15-20 nucleotides before and after the desired mutation. For the PCR, a standard PCR protocol was used (see Table 4.16 and 4.17).The PCR product was digested with 1 µl DpnI (NEB, Schwalbach, Germany) and incubated at 37°C for 1 hour. Afterwards the digested PCR product was transformed into XL1 blue or DH5α competent *E.coli* cells. Around six colonies were picked for plasmid preparation via plasmid DNA extraction kit (Qiagen, Venlo, The Netherlands). Afterwards two plasmids were sent for DNA sequencing (Biochemistry Core Facility (MPIB) or Eurofins Genomics, Ebersberg, Germany) to confirm whether the cloning was successful.

Components	final concentration	Amount
template	3 ng	1 µl
primer forward	10 pmol	1 µl
primer reverse	10 pmol	1 µl
Phusion master mix	2x	10 µl
H_2O	add to 20 µl	7 µl

Table 4.16 – Site-directed mutagenesis PCR reaction

Step	Temperature	time	cycle
1	98°C	180 sec	1
2	98°C	10 sec	
3	69°C	30 sec	
4	72°C	60 sec/kb	x 20
5	72°C	5 min	1
6	8°C	hold	

Table 4.17 – Site-directed mutagenesis PCR amplification protocol

Cloning of N-BAR tip mutants

For N-BAR-delta-tip the N-BAR construct was linearized by PCR amplification using the corresponding primers (5'-phosphorylated) and DNA template of N-BAR (see Table 4.18 and 4.19). Afterwards blunt end DNA ligation was performed (Rapdid DNA Ligation Kit, Roche Diagnostics, Germany) (see Table 4.19). 2 µl of the ligation reaction was transformed into 50 µl of XL1-blue *E. coli* cells. Around six colonies were picked for

plasmid preparation via plasmid DNA extraction kit (Qiagen, Venlo, The Netherlands). Afterwards two plasmids were sent for DNA sequencing (Biochemistry Core Facility (MPIB) or Eurofins Genomics, Ebersberg, Germany) to confirm whether the cloning was successful.

Components	final concentration	Amount
template	20 ng	1 µl
primer forward	10 pmol	1 µl
primer reverse	10 pmol	1 µl
Phusion master mix	2x	10 µl
H_2O	add to 20 µl	7 µl

Table 4.18 – N-BAR-delta-tip PCR reaction

Step	Temperature	time	cycle
1	98°C	180 sec	1
2	98°C	10 sec	
3	55°C	30 sec	
4	72°C	60 sec/kb	x 18
5	72°C	5 min	1
6	8°C	hold	

Table 4.19 – N-BAR-delta-tip PCR amplification protocol

Components	final concentration	Amount
DNA template		< 200 ng
DNA dilution buffer (5x)	5x	4 µl
T4 DNA ligase buffer (2x)	2x	10 µl
T4 DNA ligase	5 U/µl	1 µl
H_2O		add to 20 µl

Table 4.20 – N-BAR-delta-tip DNA ligation protocol

For the heterodimer N-BAR-N-BAR-delta-tip, insert 1 and insert 2 were amplified by PCR using the corresponding primer and DNA template of N-BAR (see Table 4.21, 4.22 and 4.23). Then 20 µl of PCR insert 1 (1 µg) was digested with 1 µl of NdeI (NEB, Schwalbach, Germany) and 1 µl BamHI (NEB, Schwalbach, Germany) and incubated at 37°C for 1 hour. 10 µl of PCR insert 2 (1 µg) was digested with 0.8 µl BamHI (NEB, Schwalbach, Germany) and 1.6 µl HindIII (NEB, Schwalbach, Germany), 3 µl cutsmart buffer (NEB, Schwalbach, Germany) and 14.6 H_2O and incubated at 37°C for 1 hour. Afterwards DNA ligation of DNA insert 1 and insert 2 was performed (Rapdid DNA Ligation Kit, Roche Diagnostics, Germany) (see Table 4.24). 2 µl of the ligation reaction and 1 µl of linearized pEC-K-3C-His vector (NdeI and HindII digest) was transformed into 50 µl of XL1-blue *E. coli* cells. Around six colonies were picked for plasmid preparation via plasmid DNA extraction kit (Qiagen, Venlo, The Netherlands). Afterwards two plasmids were sent for DNA sequencing (Biochemistry Core Facility (MPIB) or Eurofins Genomics, Ebersberg, Germany) to confirm whether the cloning was successful.

Components	final concentration	Amount
template		3 ng
primer forward	10 pmol	2.5 µl
primer reverse	10 pmol	2.5 µl
DMSO		2.5 µl
Phusion master mix	2x	25 µl
H_2O		add to 50 µl

Table 4.21 – N-BAR-N-BAR-delta-tip PCR reaction

Step	Temperature	time	cycle
1	98°C	180 sec	1
2	98°C	10 sec	
3	50°C	30 sec	
4	72°C	60 sec/kb	x 30
5	72°C	5 min	1
6	8°C	hold	

Table 4.22 – N-BAR-N-BAR-delta-tip PCR amplification protocol - insert 1

Step	Temperature	time	cycle
1	98°C	180 sec	1
2	98°C	10 sec	
3	53°C	30 sec	
4	72°C	60 sec/kb	x 30
5	72°C	5 min	1
6	8°C	hold	

Table 4.23 – N-BAR-N-BAR-delta-tip PCR amplification protocol - insert 2

Components	final concentration	Amount
DNA template insert 1 and 2		$<$ 200 ng
DNA dilution buffer (5x)	5x	4 µl
T4 DNA ligase buffer (2x)	2x	10 µl
T4 DNA ligase	5 U/µl	1 µl
H_2O		add to 20 µl

Table 4.24 – N-BAR-N-BAR-delta-tip DNA ligation protocol

Transformation in competent cells

Competent cells were prepared as described in the Qiagen E.coli Handbook and stored at -80°C. For the transformation in chemical-competent cells, the cells were thawed on ice and 100 ng of plasmid was added to 50 µl *E.coli* competent cells. The plasmid cell mix was incubated for 30 min on ice. Then the transformation was performed at 42°C for 45 sec and chilled for 2 min on ice. Afterwards 500 µl of SOC medium were added to the cells and they were incubated and shaken at 37°C for 30-60 min at 800 rpm. The bacteria cells were plated on LB agar with the corresponding appropriate antibiotic and incubated over night at 37°C.

For the transformation in electro-competent cells, the cells were thawed on ice and 100 ng

of plasmid were added to 50 µl *E.coli* competent cells and incubated for 5 min. Afterwards the plasmid cell mix was transferred into a cuvette and immediately the transformation was performed by using the electroporation process. Within 5 min 500 µl of SOC medium were added and the cells were incubated and shaken at 37°C for 30-60 min at 800 rpm. The bacteria cells were plated on LB agar with the corresponding appropriate antibiotic and incubated over night at 37°C.

4.2.2 Protein Expression in *E. coli*

The proteins were expressed in BL21 DE3 gold *E. coli* strain by using 4 l of autoinduction Zy medium[308,309], being supplemented with appropriate antibiotics. The main culture was inoculated either by an LB pre-culture (1/100) or directly with the colonies from the LB plate. The culture was incubated at 37°C for around 4 hours to and OD_{600} of 2 under constant shaking of 120 to 150 rpm. When the OD_{600} was reached the cell culture was cooled down to 18°C and incubated overnight with constant shaking of 120 to 150 rpm. The bacterial cells were harvested by centrifugation (8000 g for 15 min) and afterwards either directly used or stored at -80°C till usage.

4.2.3 Protein Purification

All steps of the protein purification were carried out on ice or at 4 °C. All used buffers are shown in Table 4.7 and the declaration is used like Lys, His1 etc. The ion exchange and size exclusion chromatography steps were carried out on ÄKTA purification systems (GE Healthcare). After the harvesting the *E. coli* cells with the recombinant amphiphysin fragments were lysed in Lys supplemented with 1 mM Pepstatin A, 1 mM AEBSF and 1 mM leupeptin through sonification (Bandelin Sonoplus, tip VS70T, pulse ON/OFF 0.5/0.5, 40% amplitude, 15 min (Bandelin electronic, Berlin, Germany)). To separate the soluble fraction the lysed cells were centrifuged (25000 x g, 45 min). The soluble fraction was loaded on an His-Trap or Ni-NTA column (GE Healthcare), which afterwards was washed with His1. The proteins were eluted from the column with His2-buffer. For the constructs with His-tag the tag was not removed. The His-sumo-tag was cleaved by SenP2 protease over night at 4°C. For all constructs except FL and deltaH0 a cation exchange chromatography (GE Healthcare) was done with buffer MS1 and MS2. An anion exchange chromatography (GE Healthcare) with buffer MQ1 and MQ2 was carried out for FL and deltaH0. Next the size exclusion chromatography (SEC) followed for all proteins by using an Superdex 200 10/30 or HiLoad Superdex 200 16/60 (GE Healthcare). The purified proteins were stored at -80°C until further usage

4.2.4 Protein biochemistry

Determination of the protein concentration and purity

The protein concentrations were determined by an absorbance measurement at 280 nm using the Nano-Drop spectrophotometer (Thermo Scientific, Epson, Uk). For the determination of the protein concentration the extinction coefficients at 280 nm of each protein were calculated using the protein amino acid sequence.
The purity of the protein was estimated by detecting the absorbance at 280 nm and 260 nm during ion exchange chromatography and SEC, determining the 260/280 nm ratio and SDS-PAGE.

Polyacrylamid gel electrophoresis
Proteins were analyzed by sodium dodecyl sulphate-polyacrylamid gel electrophoresis (Sigma-Aldrich-PAGE), using 10 - 12% SDS-gels as described by Laemmli [310] or commercially available pre-cast SDS-gels (4 - 20%, Bio-Rad, Germany. Afterwards the SDS-gels were stained with Coomassie brilliant blue R-250.

4.2.5 Interaction of proteins with liposomes

For tubulation experiments either large uni-lamellar vesicles (LUVs) or multi-lamellar vesicles (MLVs) were prepared. For the structural analysis of N-BAR only LUVs were used.

Liposome preparation and *in vitro* tubulation assay
The various lipid compositions, being in chloroform, were mixed together and the lipid mix was dried by a stream of nitrogen. To remove all the remaining chloroform, the lipid mixture was incubated under high vacuum over night. The dried lipid mixture was hydrated and solved in 20 mM Hepes (pH 7.4) to get MLVs. 90% of LUVs were achieved by extrusion with a 200 nm filter membrane (extruder and filter membranes from Avanti Polar lipids). The prepared lipids were either used directly or stored at 4 °C.
Various amphiphysin fragments (20 µM, 15 µM or 6 µM) were incubated with 180 µM of liposomes for tubulation kinetics assays at RT. The tubulation was either observed by absorbance spectrometry at 400 nm for 120 min or negative-stain EM at several time points up to 45 min.

Tube length and diameter determination
For the tube length determination, 20 or 0.2 µM of N-BAR was mixed with 720 µM 200 nm-extruded LUVs and incubated for 10 min at RT. Afterwards the mixture with tubes was embedded on a carbon coated grid, stained with 1% (w/v) uranyl-acetate staining dye and observed by CM200 (FEI) operating at 160 kV with a CCD camera and a magnification of 50,000x (pixel size: 2.16 Å /pixel). The tube length was measured in bshow (bsoft package) [269] with the "filament" option. The measured values were analyzed by a histogram.
To determine and calculate the tube diameter, the 2D class averages of the cryo-EM data

set or the 3D reconstruction reprojections were plotted. Afterwards the distributions of the measured diameter values were evaluated by a histogram.

Critical tubulation concentration determination

The critical tubulation concentration of various amphiphysin fragments was obtained by light scattering measurement and fluorescence light microscopy. To observe the tubulation various dilutions (6, 0.6, 0.06, 0.006 µM) of N-BAR, N-BAR-deltaH0, FL, deltaH0, N-BAR-delta-tip, N-BAR-N-BAR-delta-tip were mixed with 720 µM of liposomes (w/w 2POPG:1POPE), containing 1% Atto488-DOPE. Afterwards the degree of tubulation was recorded with a GE Deltavision Elite with a 60x/oil or 100x/oil objective and an excitation 475 nm / emission 525 nm bandpass filter. In addition, light scattering of the tube formation was measured to obtain the critical tubulation concentration. Various concentrations of the amphiphysin fragments N-BAR, N-BAR-deltaH0, FL, deltaH0, N-BAR-delta-tip, N-BAR-N-BAR-delta-tip were added to 720 µM 2POPG:1POPE (w/w) and afterwards the absorbance change at 490 nm was monitored and graphically visualized. At 400 nm wavelength the signal was saturated and therefore the measurements were done at 490 nm.

Mass per length determination via STEM

The samples were prepared in the standard procedure of the Brookhaven STEM facility for the STEM dark-field measurements. The N-BAR tubes were measured in 20 mM Hepes, pH 7.4. 20 µM N-BAR was freshly mixed with 720 µM 2POPG:1POPE (w/w) liposomes and incubated for 1 min. Afterwards the 3-5 µl of the mixture was added on glow discharged carbon grids. In the next step the specimen was washed for a couple of times and then plunged into liquid nitrogen for fast freezing. At the end the specimen grid was freeze-dried overnight before it was transferred into the STEM under vacuum to obtain dark-field digital micrographs. For the mass per length (MpL) analysis micrographs with a pixel size of 1 to 2 nm/pixel were analyzed by PCMass32 (available form the Brookhaven STEM resource, ftp.stem.bnl.gov). Tobacco mosaic virus (TMV) (13.1 kDa/Å) was used as mass per length reference and was added to all samples. By boxing the N-BAR and TMV the mass per length values were determined and afterwards analyzed with the help of a histogram.

4.2.6 EM structural analysis

EM grid preparation and image acquisition for negative stain EM

The EM grid preparation was done at RT. Various amphiphysin fragments were mixed with liposomes and afterwards around 10 µl of the mixture were added on glow-discharged (45 sec) carbon grids. After a short incubation of 10 to 40 sec the sample was removed by a filter paper (Whatman No. 1). Before the staining, the grid was either washed once to three times with water or was not washed at all. Finally, the specimen on the grid

was stained with 1% (w/v) uranyl-acetate staining dye. The negative staining samples were screened by CM200 (FEI, Eindhoven, Netherlands), operating at 160 kV, and with an CCD camera. A nominal magnification of 50,000x was used for recording, which corresponds to 2.16 Å /pixel.

Helical computational symmetrization

The analyzed images were recorded by negative stain EM. The amphiphysin N-BAR-mediated tubes were segmented with a box size 256 pixel of and a pixel size of 2.37 Å/pixel and the 2D class averages were determined. The diffraction pattern was calculated from the averaged 2D class. The model lattice with corresponding helical parameters was obtained with help of the power spectrum. An artificial Gaussian noise filtered cylinder with the same diameter was computationally created and used. The atomic structure of amphiphysin N-BAR (pdb code: 1URU) [43] was trimmed by low pass filtering to 8 Å and 20 Å. The low passed atomic structure was fitted to the artificial cylinder, which was accordingly to the calculated helical lattice. The helical computational symmetrization was carried out with the fitted atomic structure of N-BAR by using the helical parameters and the bsoft software bhelix [269]. Subsequently the simulated helical assembly was added on the artificial tube surface. The 2D projection and power spectrum of the computed amphiphysin N-BAR tube was determined and compared with the negative stain EM 2D class average and its power spectrum.

Grid preparation for cryo-EM

3 µl of the amphiphysin fragment with liposome mixture was applied on glow-discharged (90 to 120 sec) Quantifoil grids (Cu, R 2/1) and incubated for 10 sec at RT. Then the specimen grids were blotted for 10 sec with filter paper (Whatman No. 1) and immediately vitrified with liquid ethane by a manual plunger. The cryo-EM specimen were stored in liquid nitrogen till usage. Various microscopes were used for the cryo-EM data collection.

Image acquisition for cryo-EM

The cryo-EM micrographs were taken with a Tecnai F20 microscope (FEI, Eindhoven, Netherlands) operating at 120 kV and 200 kV. The magnification was either 62,000 x (pixel size of 1.78 Å/pixel) or 80,000 x (pixel size of 1.34 Å/pixel). The micrographs were recorded by an CCD camera (FEI, Eagle) by using SerialEM [307] software. For the defocus a range of 1 to 3 µm was used. Furthermore, for some amphiphysin fragments, an additional cryo-EM data set was taken with a Polara G2 F30 microscope (FEI), which is operating at 300 kV and a magnification of 62,000x (pixel size of 1.82 Å/pixel) was used. The data set was recorded by an Gatan K2 summit direct detector (3838x3710 pixel) and a GIF 2000 energy filter by using the serialEM [307] software. Only one position in every grid hole was used for imaging with a total exposure of 5 sec and a frame time of

0.1 sec. The frames 10 to 40 were used for the image processing which corresponds to a total electron dose of 30 electrons per Å 2. For the data set a defocus range of -0.5 to -3.2 µ m was used.

Image processing of the cryo-EM Tecnai F20 data set

For the image processing of the Tecnai F20 with a CCD camera cryo-EM data the defocus and astigmatism of the micrographs were determined by ctffind3 [270] and then the contrast transfer function was corrected by phase flipping by bctf from BSOFT software package [269]. The tubes were segmented, having an overlap of 90% and a box size of 400 pixel (pixel size of 1.34 Å/pixel) and 256 pixel (pixel size of 1.78 Å/pixel), by bshow with the filament option of the BSOFT software package [269] and afterwards reference-free aligned by refine2D by EMAN [271]. These aligned references were used for multiple statistical analysis (MSA) and 2D classification by hierarchical ascendant classification (HAC), which is implemented into SPIDER software package [273,274] to get 2D class averages. Bad particles were removed either by manually removing bad segments or by particle discarding during classification iterations. After the classification particle with similar 2D class averages and tube diameter were combined and used for further structural image analysis by iterative helical real space reconstruction (IHRSR) [311] being implemented into SPIDER software package [273,274]. As initial model an artificial Gaussian noise filtered cylinder with the same diameter was used as starting model for the reconstruction. The helical reconstructions with a pixel size of 1.34 Å/pixel were low-pass filtered to 9 Å and in addition, the atomic structure of *Drosophila* amphiphysin BAR (PDB code 1URU) [43] was fitted into the BAR density of the helical reconstructions.

Image processing of the cryo-EM Polara G2 F30 data set

For the Polara G2 F30 with a Gatan K2 summit direct detector a different way of image processing was used. First the frames were aligned and the frame drifting was corrected. Here the tubes were segmented into 26754 segments by e2helixboxer of EMAN2 [306] with a box size of 300 pixel and an overlap of 90%. The defocus and astigmatism were determined by ctffind3 [270] and then the contrast transfer function was corrected by phase flipping by bctf from BSOFT software package [269]. All segmented particles were 2D classified by Relion [267] and 19423 segments with bad quality were removed during this process. For the amphiphysin N-BAR structure analysis 5 classes with various diameter were chosen. The diameter were 280, 312, 262, 250, 242 Å . with 1948, 1392, 692, 1173, 1372 segmented particles, respectively. The particular helical reconstruction of each 2D class were done by IHRSR [311], being implemented into the SPIDER software package [273,274], with an artificial Gaussian noise filtered cylinder with similar diameter.

Iterative helical real space reconstruction (IHRSR)

The first reconstructions were done with 2x binned segmented particles with an azimuthal increment of 4 degrees and without the search of the out-of-plane tilt for a faster processing. Afterwards for the refinement the azimuthal increment was put to 1 degree and the out-of-plane tilt to 1 degree increment up to +/- 10 degree, which leads to 7200 reprojection images. These reprojections were used for the projection matching. In addition, the "hsearch" option in the IHRSR software package[311] was set to get a local conversing point. This function could be also used to initially determine the helical parameter, which was not the case here. The helical parameters of each class was calculated from the 2D class averages and the corresponding Fourier Transformation. Due to the possibility of some heterogeneity different helical parameter were calculated and used for helical 3D reconstructions. Afterwards the 3D helical reconstructions were evaluated by looking at the density map and by comparing the resulting reprojections with the 2D class averages and the corresponding power spectra.
The resolution was calculated by the Fourier shell correlation (FSC) of the half data sets with a cut off 0.5. Before the resolution determination some cycles of IHRSR were run with each half data set to get two independent reconstructions. The 3D reconstructions of the Polara G2 F30 data set were used as the final reconstructions for the structural study of amphiphysin N-BAR. The amplitudes of the final density maps of the reconstructions were corrected by using bampweigh of the bsoft software package[269] and the final helical reconstructions were low-pass filtered to 11 to 12 Å (see Amphiphysin BAR crystal structure fitting, 4.2.6).

Amphiphysin BAR crystal structure fitting

The crystal structure of *Drosophila* amphiphysin BAR (PDB code 1URU) is already known and was fitted into the reconstruction density of BAR dimer by hand. For additional refinement of the helical reconstruction an amplitude correction was done. For this the fitted atomic model of the BAR dimer was transformed into a density map by the Chimera software and afterwards the helical symmetry of reconstruction was used to get the helical BAR dimer polymer by bhelix of BSOFT software package[269]. The simulated symmetrized BAR map was taken as a reference to correct the amplitude of the reconstruction by bampweigh (BSOFT package)[269]. At the end the final maps were low-pass filtered to 11-12 Å. In addition, to get a hint of the BAR dimer interactions, around two to four *Drosophila* amphiphysin BAR crystal structures were fitted into the reconstruction with the help of the simulated symmetrized BAR map. The BAR dimer interactions were analyzed via the Chimera software.

Acknowledgments

Firstly, I would like to express my sincerest gratitude to my supervisor, Naoko Mizuno, for her expertise, enthusiasm and motivation. Her guidance supported me through all the time of my PhD project and writing of my publication and this thesis. Thanks a lot for offering me the chance to perform my research in your group.
Furthermore, I would like to particularly thank my doctoral thesis supervisor, Elena Conti, for giving me the opportunity to perform my research in her department at the Max Planck Institute of Biochemistry in Martinsried, for her support during my thesis, for her knowledge and for providing an excellent research atmosphere.
My sincere thanks also goes to Wolfgang Baumeister for treating me like a member of his department at the Max Planck Institute of Biochemistry in Martinsried and for giving me the possibility to use the electron microscope resources of his department. Without it I would not have gained my experience and widened my expertise in the field of cryo-EM. Besides, I would like to thank my Thesis Advisory Committee, including Petra Wendler, for their informative, helpful comments and encouragement.
I want to thank Joseph Wall and Beth Lin from the Brookhaven National Laboratory for the STEM measurements and Ulrich Braxa for the instruction about the analysis of the STEM data. I also want to acknowledge Ralf Langen (University of South California) for sharing the initial *Drosophila* amphiphysin plasmid.
Moreover, I have benefited from the resources and the infrastructure at the Max Planck Institute of Biochemistry. I want to thank the people in the Biochemistry Core Facility of the MPIB for offering a broad range of methods and reliable analyses. Then I would like to thank the Image Facility of the MPIB for resources. Additionally, I would like to acknowledge all people from the Conti and Baumeister department for their support and hands-on assistance. Their help, comments and suggestions opened up a new perspective on my research. In addition, a special thanks goes to Jürgen Plitzko and Günter Pfeifer for their electron microscope user support and help, Ulrike Laugks and Nikolas Schrod for their instruction on handling the Polara, Ruben Fernandez Busnadiego for his instruction about the Gatan K2 direct detector, Michael Taschner, Sebastian Falk and Eva Kowalinski for sharing their expertise in cloning, Rajan Prabu and Christian Biertümpfel for their help with the software environment, Peter Reichelt for his help with the columns and purification systems, Christian Benda and Walter Erhardt for IT and technical support and Petra Lee and Ulrike Goldschmitt for their help with organizational issues.
I would like to thank the Conti group, Baumeister department, Esben Lorentzen, Christian

Biertümpfel and their lab members for kindly sharing their equipment with me.
A special thanks goes to Christian Biertümpfel and his lab members for suggestions, discussions, their support and sharing their knowledge during my PhD time.
My sincere thanks goes to my group members for their help, technical support and for the great atmosphere in our group. Here I want to especially thank Nirakar Basent for his support and contribution to my publication. Additionally, I want to thank Dirk Dedden and Nirakar Basnet for our discussions about EM. I would also like to thank my bachelor student Matthias Beuerle for his help.
I want to acknowledge the Max Planck Society and the Deutsche Forschungsgemeinschaft (DFG) for supporting through grants within GRK1721 and MI 1745/1 and financing my PhD research. I want to thank the GRK1721 Graduiertenkollegg for their support and discussions.
Thanks a lot to Eva Kowalinski, Carina Vraschek and Angelo for the proofreading of my thesis.
I want to thank the second floor for the great working atmosphere.
Dear Carina, we started our PhD on the same day and from the start we became very good friends. I want to thank you for your help and support.
Dear Mela and Krissy, you were already in the middle of your PhD when I started. Thanks a lot for your warm welcome, all your support and help when I started. Over the years we developed a close friendship.
Dear Carina, it all started at the retreat in Nürnberg.
Dear Ulrike, thanks a lot for your help in the Baumeister department in the beginning and for your friendship.
Dear Eva, thanks a lot for your help, support and friendship.
Außerdem möchte ich mich auch noch bei meinem Partner bedanken. Vielen Dank fuür deine liebevolle Unterstützung während dem letzten Jahr meiner Doktorarbeit.
Zum Schluss möchte ich meiner Familie und meinen Freunden für ihre Unterstützung während meiner Doktorarbeit danken.

Abbreviations

$\Delta\phi$	Azimuthal rotation per subunit
Δz	Helical rise per subunit
2D	Two-dimensional
3D	Three-dimensional
aa	Amino acid
AD	Alzheimer's disease
AEBSF	4-(2-Aminoethyl) benzenesulfonyl fluoride hydrochloride
AEX	Anion-exchange chromatography
ATP	Adenosine triphosphate
BAR	Bin/Amphiphysin/Rvs
BIN1	Bridging integrator 1
CAV3	Caveolin-3
CCD	Charge-coupled device
CCP	Clathrin-coated pit
CEX	Cation-exchange chromatography
CLAP	Clathrin and AP-2 binding domain
CLIP-170	Cytoplasmic linker protein 170
CME	Clathrin-mediated endocytosis
CNM	Centronuclear myopathie
COP	Coat protein complex
CTF	Contrast transfer function
D	Aspartate
DM	Myotonic dystrophy
dNTP	Deoxynucleotide triphosphate
DPHR	Dihydropyridine receptor
Drosophila	Drosophila melanogaster
DTT	Dithiothreitol
DYSF	Dysferlin
E	Glutamate
EDTA	Ethylenediaminetetraacetic acid
EM	Electron microscopy
ENTH	Epsin N-terminal homology
ER	Endoplasmic reticulum

FL	Full-length
g	Gravity
GTP	Guanosine triphosphate
H0 helix	N-terminal amphipathic helix
HAC	Hierarchical ascendant classification
Hepes	2-[4-(2-hydroxyethyl)piperazin-1-yl]ethanesulfonic acid
IEX	Ion-exchange chromatography
IFM	Indirect flight muscle
IHRSR	Iterative helical real space reconstruction
j-SR	Junctional sarcoplasmic reticulum
JPH1/2	Junctophilin-1/2
K	Lysine
LOAD	Late onset Alzeiheimer's disease
LTCC	L-type calcium channels
LUVs	Large unilamellar vesicles
MBL1	Muscleblind-like-1
MLVs	Multi-lamellar vesicles
MPIB	Max Planck Institute of Biochemistry
MPL	Mass per Length
MS	Mass spectrometry
MSA	Multiple statistical analysis
MT	Microtubule
MTM1	Myotubularin 1
N-WASP	Neuronal WiskottâĂŞAldrich Syndrome protein
NaCl	Sodium chloride
NCBI	National center for biotechnology information
NE	Nuclear envelope
NLS	Nuclear localization signal
NMJ	Neuromuscular junction
nt	Nucleotide
on	overnight
PA	Phosphatic acid
PAGE	Polyacrylamide gel electrophoresis
PARP1	Poly-(ADP-ribose) polymerase 1
PC	Phosphatidylcholine
PCR	Polymerase chain reaction
PG	Phosphatidylglycerole
PH	Pleckstrin homology
PI	Phosphatidylinositol
PI(3)P	Phosphatidylinositol-3-phosphate

$PI(3,4)P_2$	Phosphatidylinositol-3,4-bisphosphate
$PI(3,5)P_2$	Phosphatidylinositol-3,4-bisphosphate
$PI(4,5)P_2$	phosphatidylinositol-3,4-bisphosphate
PI(5)P	Phosphatidylinositol-5-phosphate
PIP	Phosphatidylinositol phosphate
PM	Plasma membrane
POPC	1-Palmitoyl-2-oleoyl-sn-glycero-3-phosphocholine
POPE	1-Palmitoyl-2-oleoyl-sn-glycero-3-phosphoethanolamine
POPG	1-Palmitoyl-2-oleoyl-sn-glycero-3-phosphoglycerol
POPS	1-Palmitoyl-2-oleoyl-sn-glycero-3-phosphoserin
PRD	Prolin-rich domain
PS	Phosphatidylserine
R	Arginine
rpm	Revolutions per minute
RT	Room temperature
RyR	Ryanodine receptors
SDS	Sodium dodecyl sulfate
SEC	Size exclusion chromatography
SH3	SRC Homology 3
SR	Sarcoplasmic reticulum
STEM	Scanning transmission electron microscopy
TAE	Tris-acetate-EDTA
T-SR	T-tubule and sarcoplasmic reticulum system
T-tubule	Transverse tubule

Appendix

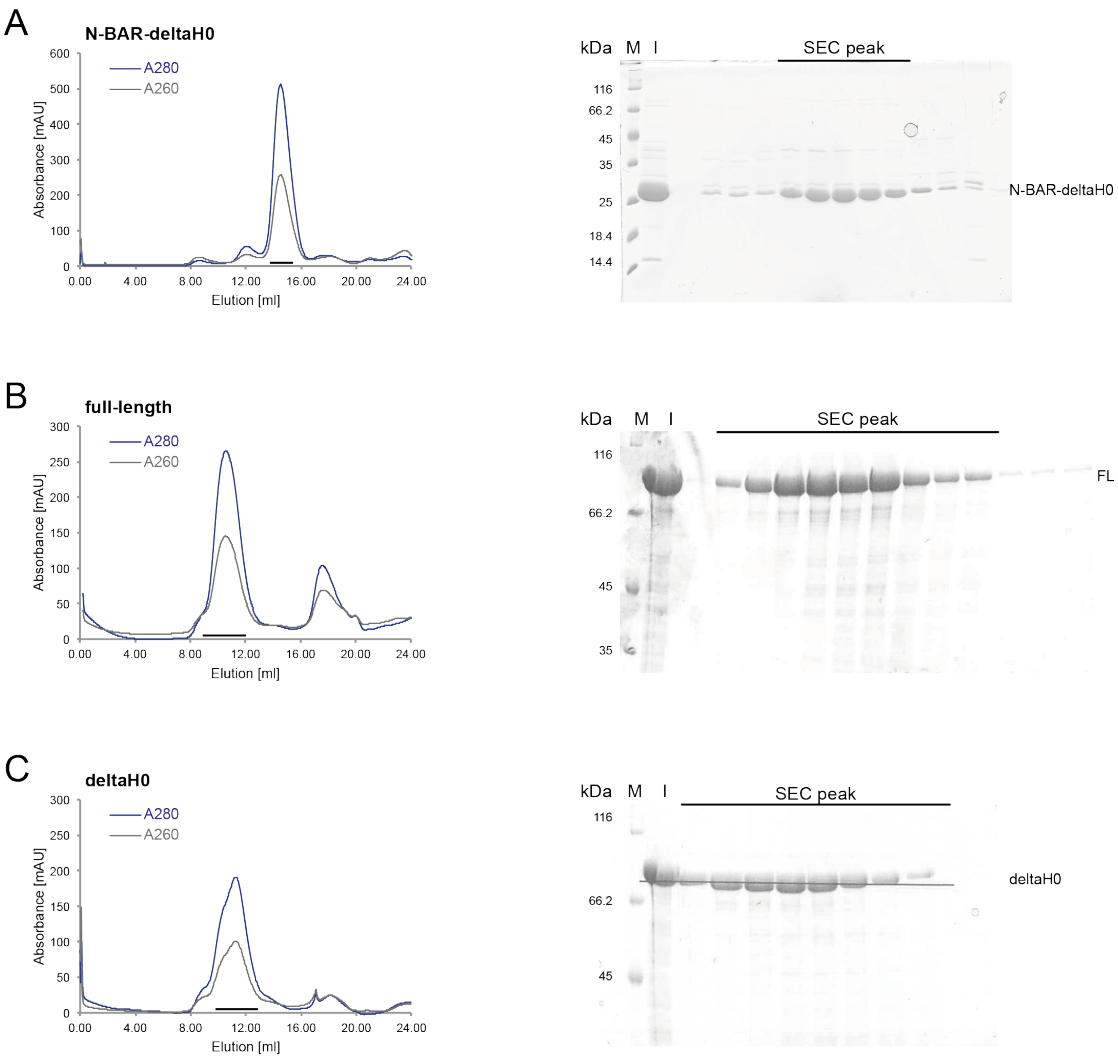

Figure A1 – SEC analysis of amphiphysin fragments using a Superdex 200 10/30 column | (Left) Size exclusion chromatogram of purified (A) N-BAR-deltaH0 (25.9 kDa), (B) full-length (66.1 kDa) and (C) deltaH0 (63.4 kDa) showed a peak at ~15 ml (corresponding to ~52 kDa), 11 ml (~135 kDa) and 11.5 ml (~125 kDa), respectively, by UV absorbance at 280 nm (blue) and 260 nm (grey). All amphiphysin fragments formed a dimer. (Right) SDS-PAGE shows the peak fractions of the particular amphiphysin fragment, which is marked by a line. M = protein marker in kDa, I = injected protein sample, SEC = Size exclusion chromatography

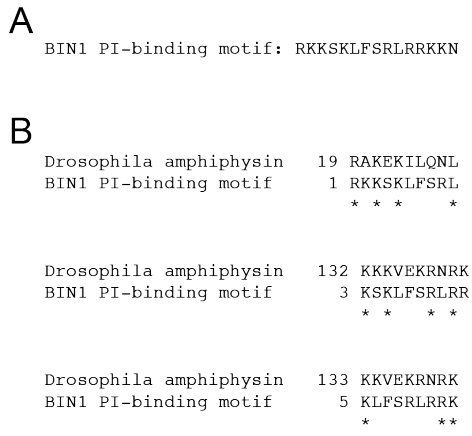

Figure A2 – Alignment of the muscle BIN1 PI-binding motif with *Drosophila* amphiphysin) | (A) PI-binding motif of human muscle BIN1 (isoform 8). (B) Alignment of the PI-binding motif with *Drosophila* amphiphysin. Alignment by the SIM alignment Tool for protein sequences. * = aa similarity

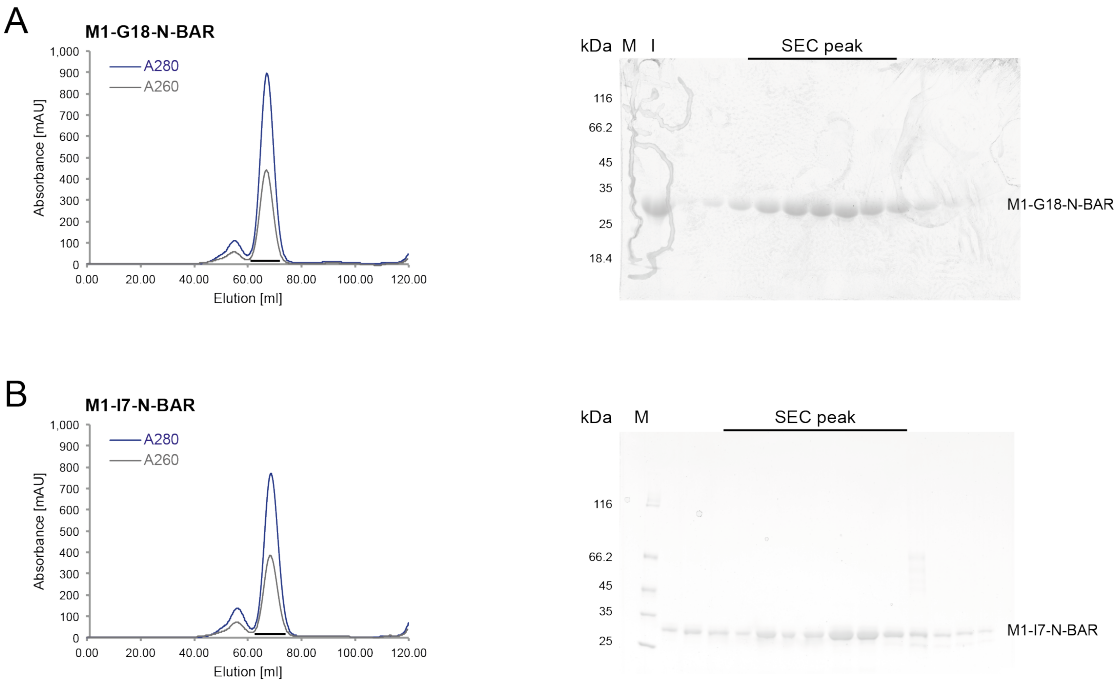

Figure A3 – SEC analysis of amphiphysin constructs with extended H0 helix using a Superdex 200 16/60 column | (Left) Size exclusion chromatogram of purified (A) M1-G18-N-BAR (32.4 kDa) and (B) M1-I7-N-BAR (31.2 kDa) showed a peak at ~70 ml (corresponding to ~64 kDa) and ~72 mL (~60 kDa), respectively, by UV absorbance at 280 nm (blue) and 260 nm (grey). Both constructs formed a dimer. (Right) SDS-PAGE shows the peak fractions of the respective amphiphysin constructs with extended H0 helix, which is marked by a line. M = protein marker in kDa, I = injected protein sample, SEC = Size exclusion chromatography

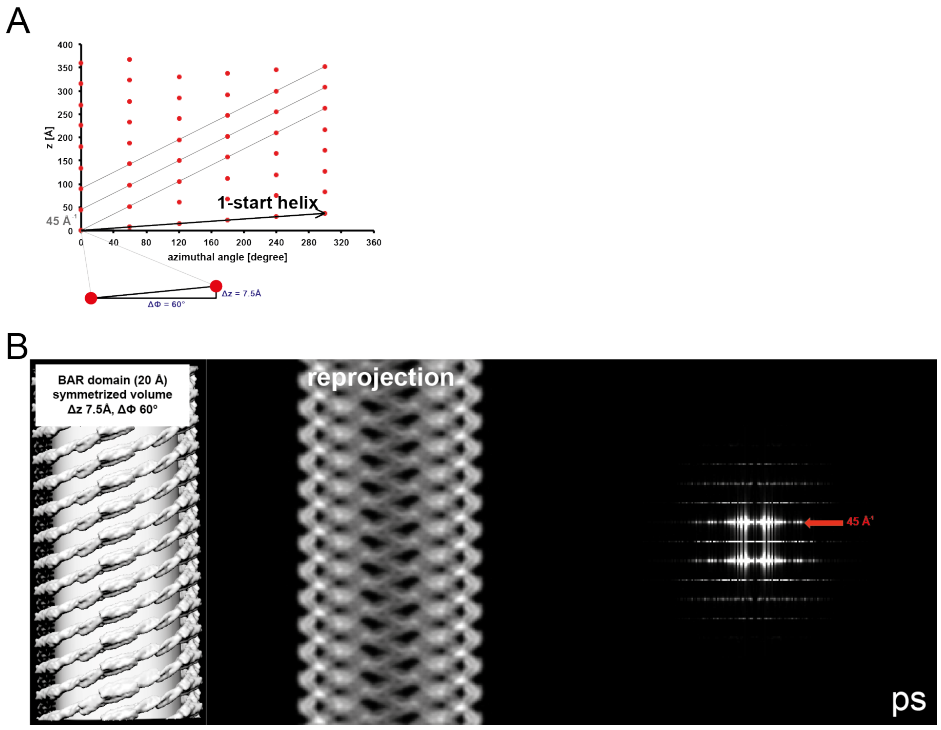

Figure A4 – Helical symmetrization of the BAR domain with the helical parameters of of Δz 7.5 Å and Δϕ 60° | (A) The 2D helical lattice of the symmetrized BAR domain showed six BAR domains in one helical turn of 360°. (B, left) The BAR domain was helically symmetrized with the helical parameters of Δz 7.5 Å and Δϕ 60°. (B, middle) The BAR domain arrangement of the helical symmetrized BAR volume visualized by its reprojection, which was not fitting to the negative stain EM 2D average of the N-BAR-mediated tube. (B, right) A diffraction signal of 45 $Å^{-1}$ is determined in the power spectrum, belonging to the periodical pattern of the BAR arrangement. ps = power spectrum

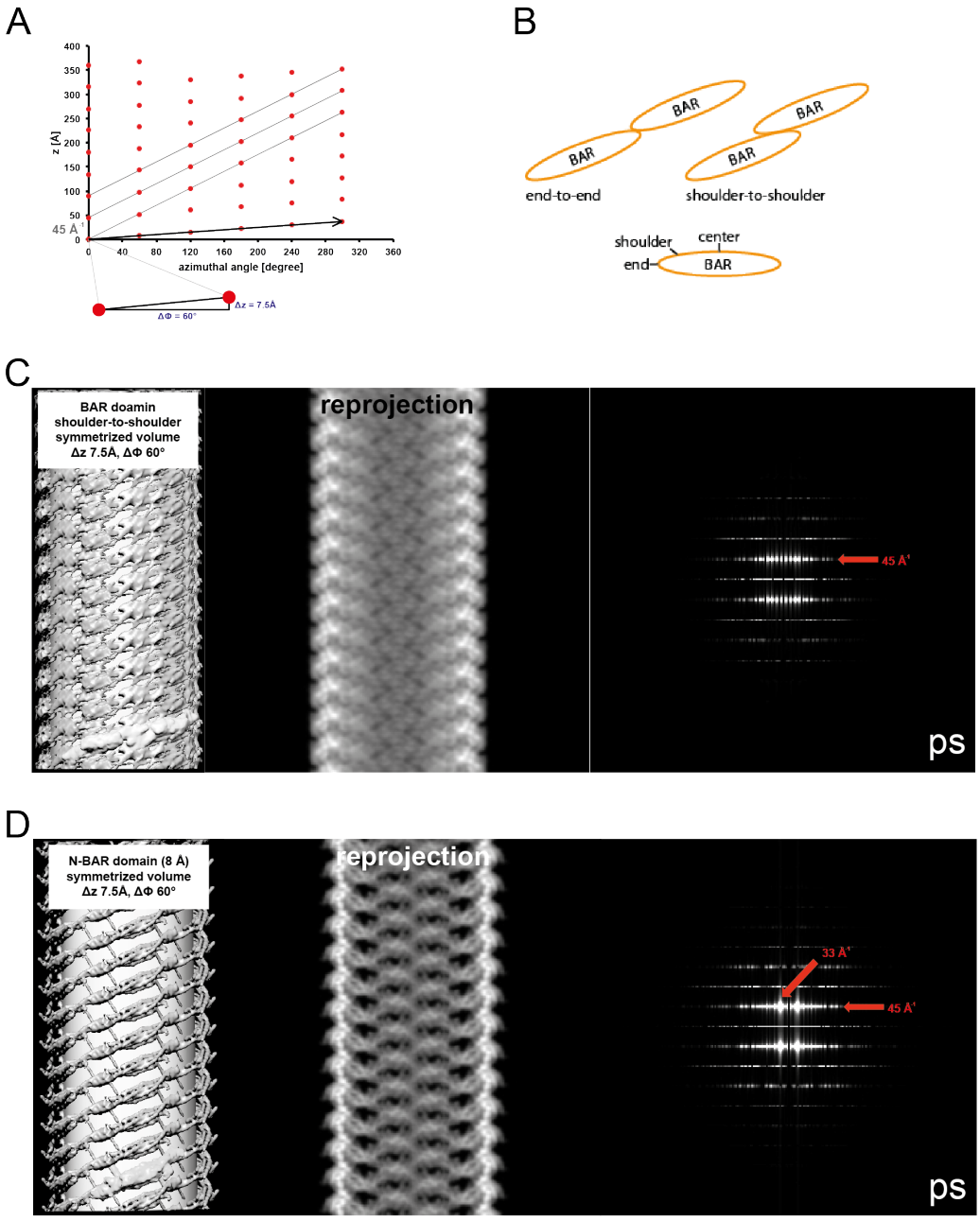

Figure A5 – Determination of the 33 Å^{-1} diffraction signal | (A) The 2D helical lattice of the symmetrized BAR domain showed six BAR domains in one helical turn of 360° . A 1-start helix with the helical parameters of Δz 7.5 Å and Δϕ 60° was determined. (B) Adjacent BAR domains in one lattice row could possibly be arranged either tip-to-tip (end-to-end) or shoulder-to shoulder. (C) Helical symmetrization of the BAR arrangement shoulder-to-shoulder with helical volume (left), reprojection (middle) and power spectrum with a periodicity of 45 Å in real space showed no resemblance to the negative stain EM image so that the 33 Å did not come from the protein-to-protein interaction.(D, left) The modified N-BAR domain with H0 helix and BAR was helically symmetrized with the helical parameters of Δz 7.5 Å and Δϕ 60°. Then it was reprojected (middle) and the power spectrum (right) revealed two diffraction signals at 45 Å^{-1} and 33 Å^{-1}, corresponding to the BAR domain and the H0 helix, respectively. ps = power spectrum

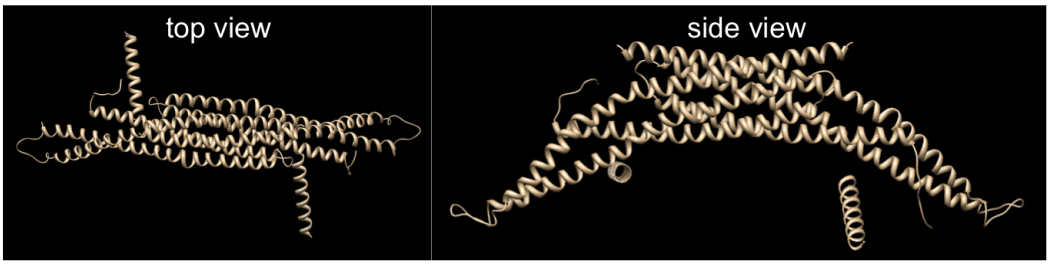

Figure A6 – Modified atomic structure of amphiphysin N-BAR | The modified atomic structure with the H0 helix and BAR domain (pdb code: 1URU [43] was provided from Ralf Langen, PhD (USC, USA). Top (left) and side (right) view of the modified pdb showed a possible orientation of the H0 helix.

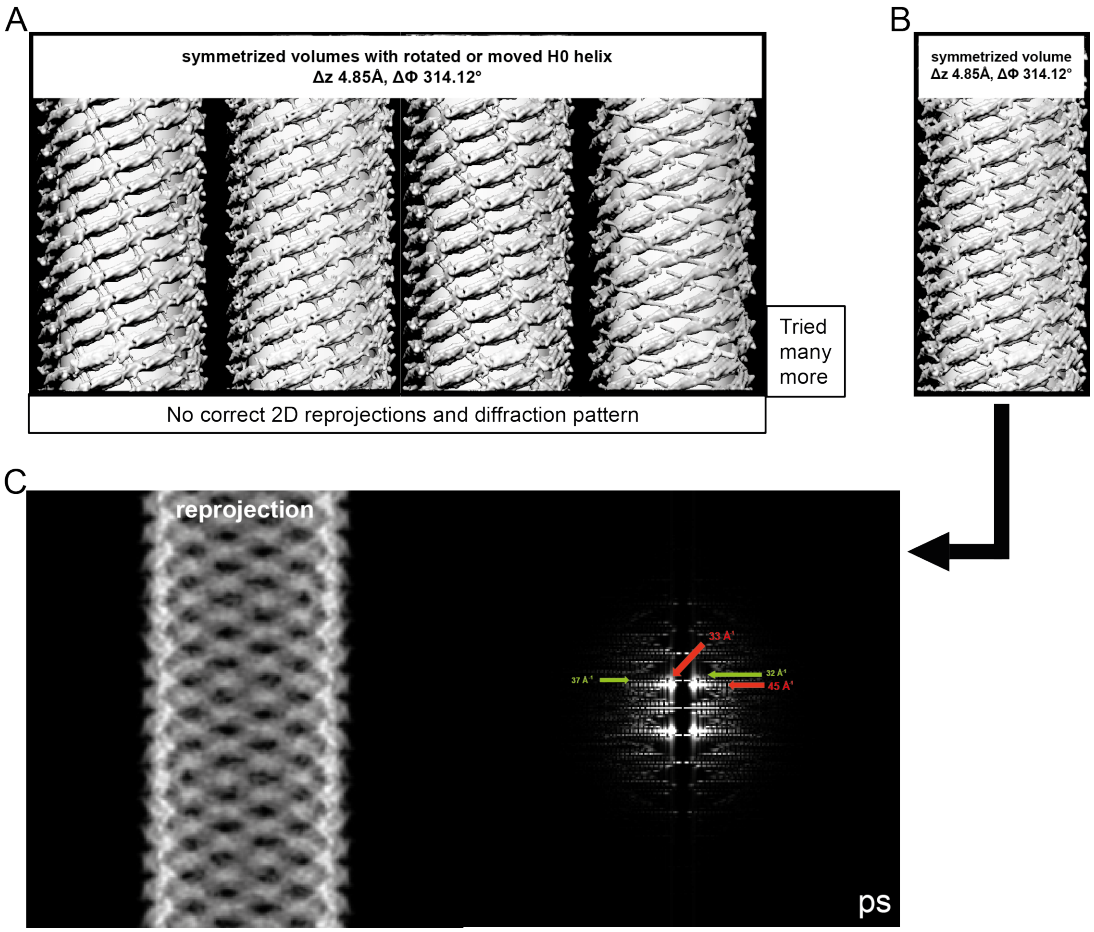

Figure A7 – Symmetrized N-BAR volumes with rotated and/or moved H0 helix | (A) Several trials of helical simulation with the helical parameters of Δz 4.85 Å and Δϕ 314.12° were performed to find the correct position of the H0 helix. In most of the trials the 2D projections and power spectra were not fitting to the negative stain EM 2D class average. (B and C) In one case (B) the projection (C, left) and power spectrum (C, right) was fitting to the negative stain 2D class average with corresponding diffraction pattern. It was determined that the spacing of 45 $Å^{-1}$ belongs to the BAR domain arrangement and the spacing of 33 $Å^{-1}$ seems to correspond to the N-terminal amphipathic helix H0. Two additional diffraction signals of 37 $Å^{-1}$ 32 $Å^{-1}$ were calculated, which origin was not clear. ps = power spectrum

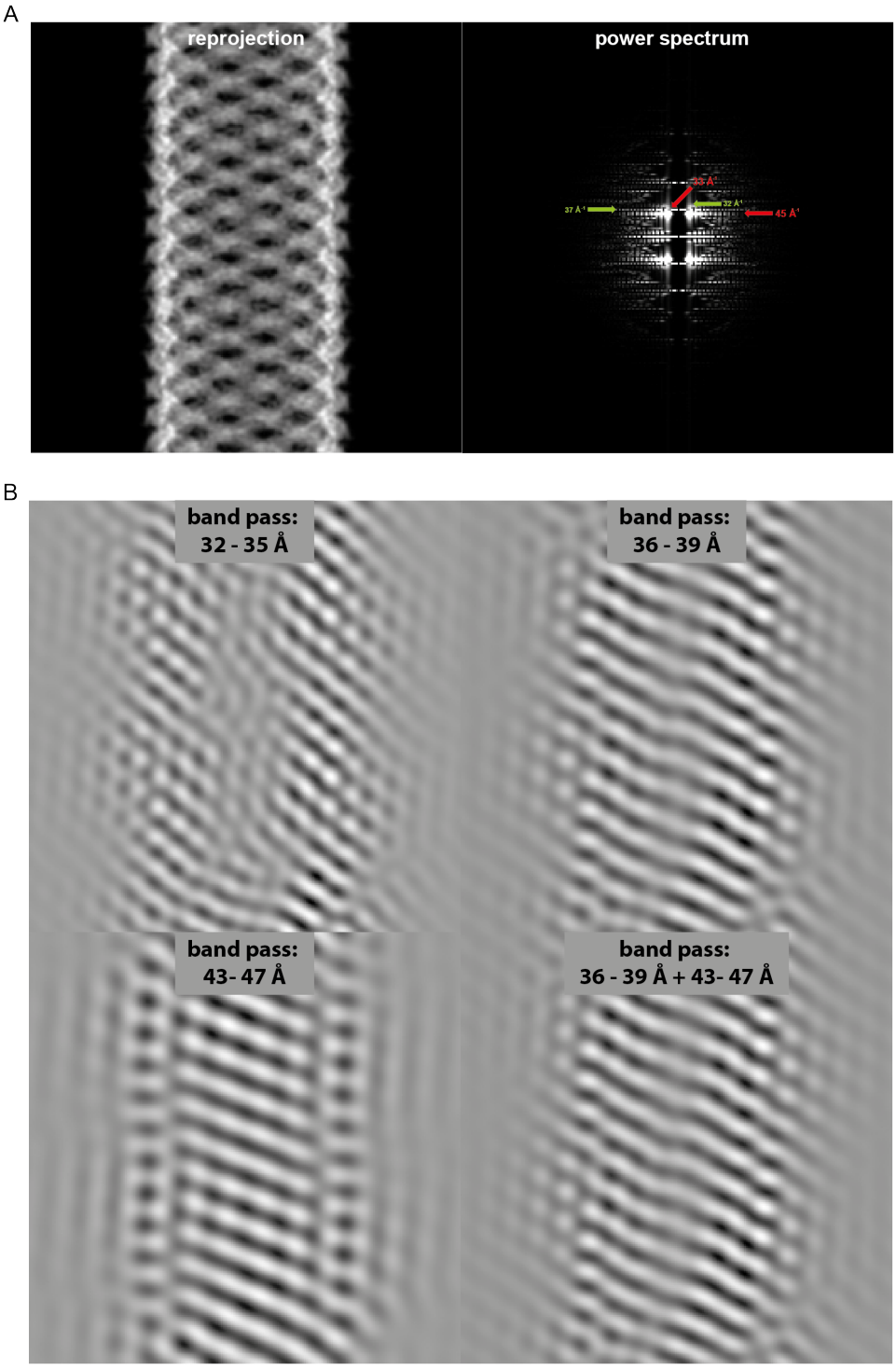

Figure A8 – Helical symmetrization of BAR with applied band pass filter | (A) Four periodical pattern of 45 Å, 37 Å, 33 Å and 32 Å were determined the reprojection of the helical symmetrization of the BAR domain (left) and the corresponding power spectrum (right). Several band pass filter revealed that the diffraction signal of 45 $Å^{-1}$ and 37 $Å^{-1}$ belonged to the BAR domain. The 33 $Å^{-1}$ and 32 $Å^{-1}$ diffraction signal showed a different periodical pattern and therefore seems not to be form the BAR arrangement.

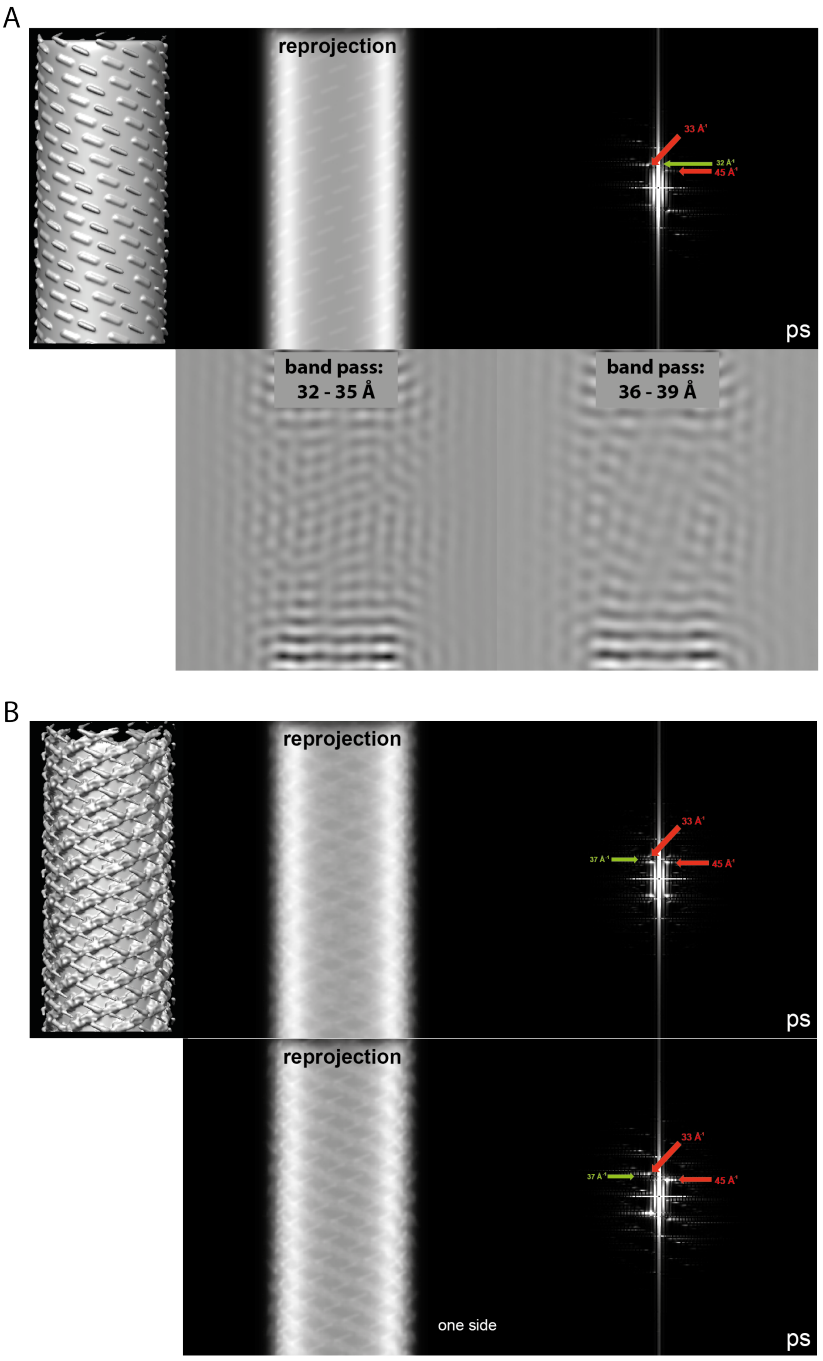

Figure A9 – Helically symmetrized volume of H0 helix and N-BAR with additional artificial tube | (A, top) Helically symmetrized volume of the H0 helix with additional artificial tube and corresponding reprojection showed three periodical pattern of 45 Å, 33 Å and 32 Å in the power spectrum. (A, bottom) Two band pass filter revealed that the diffraction signal of 33 $Å^{-1}$ and 32 $Å^{-1}$ belonged to the H0 helix. The 45 $Å^{-1}$ diffraction signal showed a different periodical pattern and therefore seems not to be form the H0 helix arrangement. (B, top) Helically symmetrized volume of the N-BAR domain with additional artificial tube and corresponding reprojection showed three periodical pattern of 45 Å, 37 Å and 33 Å in the power spectrum. (B, bottom) The reprojection of one side of the symmetrized N-BAR volume had a much weaker diffraction signal at 37 $Å^{-1}$ in contrast to the stronger 45 $Å^{-1}$ and 33 $Å^{-1}$ signal. Helical parameters of Δz 4.85 Å and $\Delta\phi$ 314.12°, ps = power spectrum

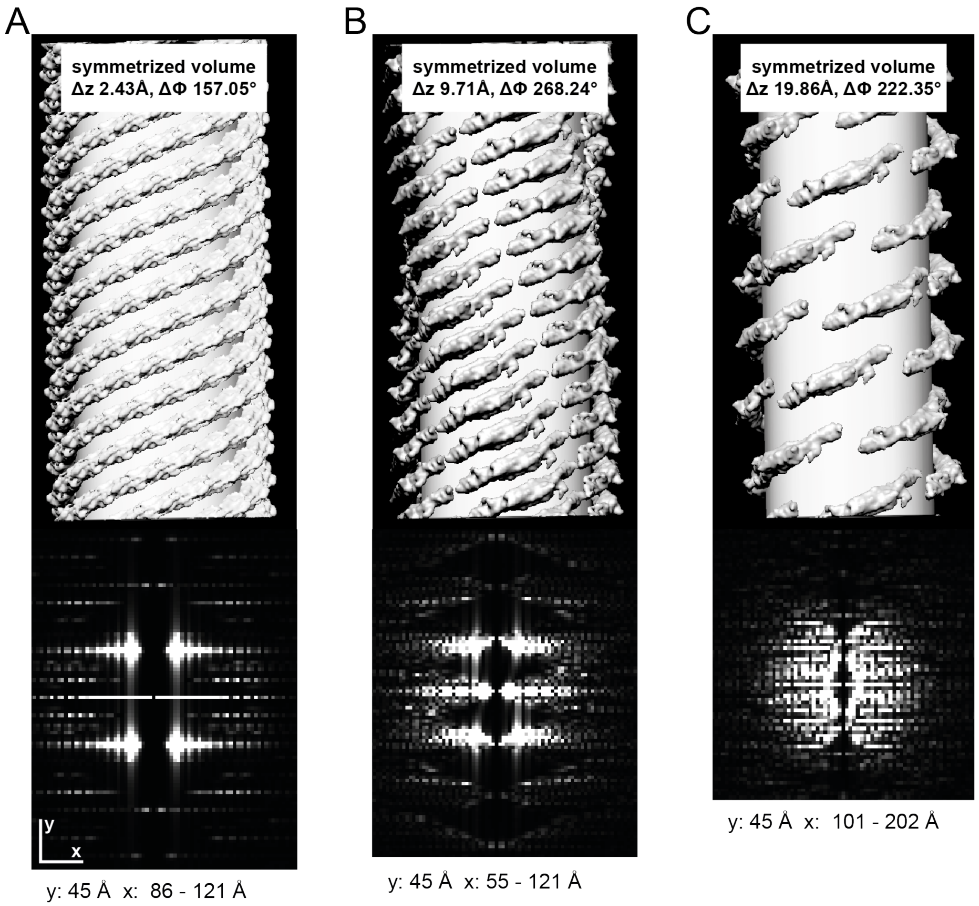

Figure A10 – Distance between adjacent BAR domains influences the helical 2D lattice | Helical symmetrized volumes (top) with corresponding power spectrum (bottom) showed a change in the periodical pattern when the distance between adjacent BAR domains became larger. The N-BAR domain was symmetrized with the following helical parameters (A) Δz 2.43 Å and $\Delta\phi$ 157.05°, (B) Δz 9.71 Å and $\Delta\phi$ 268.24° and (C) Δz 19.86 Å and $\Delta\phi$ 222.35°. Diffraction signal displacement in y and x direction.

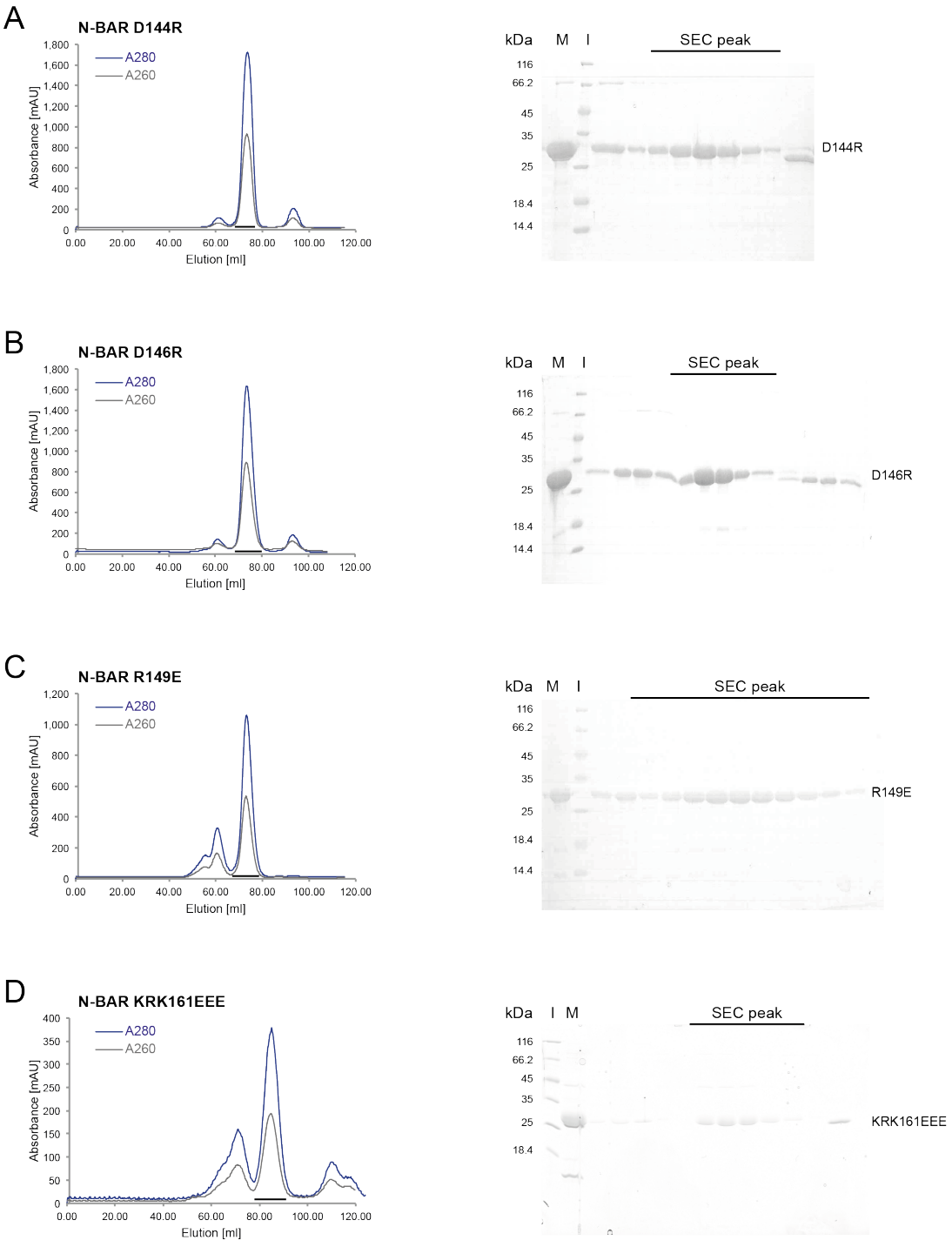

Figure A11 – SEC analysis of amphiphysin N-BAR mutants using a Superdex 200 16/60 column | (Left) Size exclusion chromatogram of purified (A) N-BAR D144R (30.5 kDa) and (B) N-BAR D146R (30.5 kDa), (C) N-BAR R149E (30.4 kDa) and (D) N-BAR KRK161EEE (30.4 kDa) showed a peak at ~75 ml (~58 kDa), ~75 ml (~58 kDa), ~75 ml (~58 kDa) and ~82 ml (~52 kDa), respectively, by UV absorbance at 280 nm (blue) and 260 nm (grey). All N-BAR mutants formed a dimer. (Right) SDS-PAGE shows the peak fractions of the respective amphiphysin constructs with extended H0 helix, which is marked by a line. M = protein marker in kDa, I = injected protein sample, SEC = Size exclusion chromatography

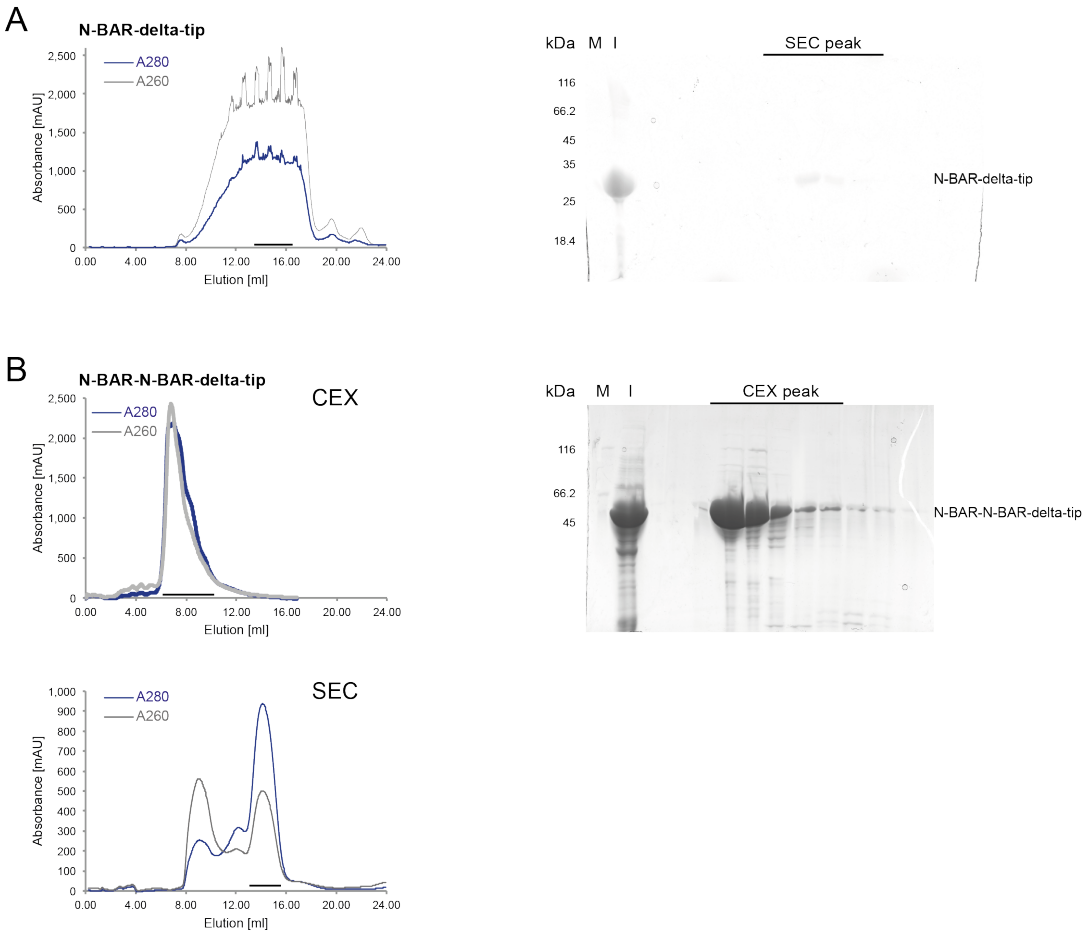

Figure A12 – SEC analysis of amphiphysin N-BAR-delta-tip mutants using a Superdex 200 10/30 column | (A, left) Size exclusion chromatogram of purified N-BAR-delta-tip (27.7 kDa) showed a broad peak at ~15 ml (~55 kDa) by UV absorbance at 280 nm (blue) and 260 nm (grey). N-BAR-delta-tip formed a dimer (A, Right) SDS-PAGE shows the peak fractions, which is marked by a line. (B, left, top) Cation exchange chromatography of purified heterodimer N-BAR-N-BAR-delta-tip (57.8 kDa) with linker sequence showed a main peak at ~300 - 350 mM NaCl by UV absorbance at 280 nm (blue) and 260 nm (grey). (B, Right) SDS-PAGE shows the peak fractions, which is marked by a line. (B, left, bottom) Size exclusion chromatogram of purified heterodimer N-BAR-N-BAR-delta-tip with linker showed a main peak at ~14.5 ml (~60 kDa) by UV absorbance at 280 nm (blue) and 260 nm (grey). The heterodimer seems to form oligomers. M = protein marker in kDa, I = injected protein sample, SEC = Size exclusion chromatography

List of Figures

List of Tables

Bibliography

[1] Tanford, C. *The hydrophobic effect : formation of micelles and biological membranes* (Wiley, New York ; Chichester, 1980), 2nd ed. edn.

[2] Gennis, R. B. *Biomembranes : molecular structure and function* (Springer-Verlag, New York, 1989).

[3] Chernomordik, L. V. & Kozlov, M. M. Protein-lipid interplay in fusion and fission of biological membranes. *Annual review of biochemistry* **72**, 175–207 (2003).

[4] Zimmerberg, J. & Kozlov, M. M. How proteins produce cellular membrane curvature. *Nature reviews. Molecular cell biology* **7**, 9–19 (2006).

[5] Vanni, S., Hirose, H., Barelli, H., Antonny, B. & Gautier, R. A sub-nanometre view of how membrane curvature and composition modulate lipid packing and protein recruitment. *Nature communications* **5**, 4916 (2014).

[6] Devaux, P. F. Is lipid translocation involved during endo- and exocytosis? *Biochimie* **82**, 497–509 (2000).

[7] Daleke, D. L. Phospholipid flippases. *The Journal of biological chemistry* **282**, 821–5 (2007).

[8] Devaux, P. F., Herrmann, A., Ohlwein, N. & Kozlov, M. M. How lipid flippases can modulate membrane structure. *Biochimica et biophysica acta* **1778**, 1591–600 (2008).

[9] Ruaud, A. F. *et al.* The c. elegans p4-atpase tat-1 regulates lysosome biogenesis and endocytosis. *Traffic* **10**, 88–100 (2009).

[10] McLaughlin, S. & Murray, D. Plasma membrane phosphoinositide organization by protein electrostatics. *Nature* **438**, 605–11 (2005).

[11] Heo, W. D. *et al.* Pi(3,4,5)p3 and pi(4,5)p2 lipids target proteins with polybasic clusters to the plasma membrane. *Science* **314**, 1458–61 (2006).

[12] Lemmon, M. A. Membrane recognition by phospholipid-binding domains. *Nature reviews. Molecular cell biology* **9**, 99–111 (2008).

[13] Takenawa, T. & Itoh, T. Membrane targeting and remodeling through phosphoinositide-binding domains. *IUBMB Life* **58**, 296–303 (2006).

[14] Aimon, S. *et al.* Membrane shape modulates transmembrane protein distribution. *Dev Cell* **28**, 212–8 (2014).

[15] Copic, A., Latham, C. F., Horlbeck, M. A., D'Arcangelo, J. G. & Miller, E. A. Er cargo properties specify a requirement for copii coat rigidity mediated by sec13p. *Science* **335**, 1359–62 (2012).

[16] MacKinnon, R., Heginbotham, L. & Abramson, T. Mapping the receptor site for charybdotoxin, a pore-blocking potassium channel inhibitor. *Neuron* **5**, 767–71 (1990).

[17] Fertuck, H. C. & Salpeter, M. M. Localization of acetylcholine receptor by 125i-labeled alpha-bungarotoxin binding at mouse motor endplates. *Proc Natl Acad Sci U S A* **71**, 1376–8 (1974).

[18] McMahon, H. T. & Gallop, J. L. Membrane curvature and mechanisms of dynamic cell membrane remodelling. *Nature* **438**, 590–6 (2005).

[19] Eckler, S. A., Kuehn, R. & Gautam, M. Deletion of n-terminal rapsyn domains disrupts clustering and has dominant negative effects on clustering of full-length rapsyn. *Neuroscience* **131**, 661–70 (2005).

[20] Boudin, H. *et al.* Presynaptic clustering of mglur7a requires the pick1 pdz domain binding site. *Neuron* **28**, 485–97 (2000).

[21] Ehrlich, M. *et al.* Endocytosis by random initiation and stabilization of clathrin-coated pits. *Cell* **118**, 591–605 (2004).

[22] Campelo, F., McMahon, H. T. & Kozlov, M. M. The hydrophobic insertion mechanism of membrane curvature generation by proteins. *Biophysical journal* **95**, 2325–39 (2008).

[23] Drin, G. *et al.* A general amphipathic alpha-helical motif for sensing membrane curvature. *Nature structural & molecular biology* **14**, 138–46 (2007).

[24] White, S. H. & Wimley, W. C. Hydrophobic interactions of peptides with membrane interfaces. *Biochimica et biophysica acta* **1376**, 339–52 (1998).

[25] Hristova, K. *et al.* An amphipathic alpha-helix at a membrane interface: a structural study using a novel x-ray diffraction method. *Journal of molecular biology* **290**, 99–117 (1999).

[26] Gallop, J. L. *et al.* Mechanism of endophilin n-bar domain-mediated membrane curvature. *The EMBO journal* **25**, 2898–910 (2006).

[27] Drin, G. & Antonny, B. Amphipathic helices and membrane curvature. *FEBS letters* **584**, 1840–7 (2010).

[28] Cornell, R. B. & Taneva, S. G. Amphipathic helices as mediators of the membrane interaction of amphitropic proteins, and as modulators of bilayer physical properties. *Current protein & peptide science* **7**, 539–52 (2006).

[29] Antonny, B. Mechanisms of membrane curvature sensing. *Annual review of biochemistry* **80**, 101–23 (2011).

[30] Segrest, J. P., De Loof, H., Dohlman, J. G., Brouillette, C. G. & Anantharamaiah, G. M. Amphipathic helix motif: classes and properties. *Proteins* **8**, 103–17 (1990).

[31] Shibata, Y., Hu, J., Kozlov, M. M. & Rapoport, T. A. Mechanisms shaping the membranes of cellular organelles. *Annu Rev Cell Dev Biol* **25**, 329–54 (2009).

[32] Hu, F. X., Wang, T. H. & Tan, Z. [role of caveolin-1 on membrane estrogen receptor mediated proliferation of endothelial progenitor cells]. *Zhonghua Xin Xue Guan Bing Za Zhi* **39**, 1044–7 (2011).

[33] Groffen, A. J. *et al.* Doc2b is a high-affinity ca2+ sensor for spontaneous neurotransmitter release. *Science* **327**, 1614–8 (2010).

[34] Hui, E., Johnson, C. P., Yao, J., Dunning, F. M. & Chapman, E. R. Synaptotagmin-mediated bending of the target membrane is a critical step in ca(2+)-regulated fusion. *Cell* **138**, 709–21 (2009).

[35] Martens, S., Kozlov, M. M. & McMahon, H. T. How synaptotagmin promotes membrane fusion. *Science* **316**, 1205–8 (2007).

[36] Martens, S. & McMahon, H. T. Mechanisms of membrane fusion: disparate players and common principles. *Nature reviews. Molecular cell biology* **9**, 543–56 (2008).

[37] Schmid, S. L. Clathrin-coated vesicle formation and protein sorting: an integrated process. *Annual review of biochemistry* **66**, 511–48 (1997).

[38] Brodsky, F. M., Chen, C. Y., Knuehl, C., Towler, M. C. & Wakeham, D. E. Biological basket weaving: formation and function of clathrin-coated vesicles. *Annual review of cell and developmental biology* **17**, 517–68 (2001).

[39] Scales, S. J., Pepperkok, R. & Kreis, T. E. Visualization of er-to-golgi transport in living cells reveals a sequential mode of action for copii and copi. *Cell* **90**, 1137–48 (1997).

[40] Brandizzi, F. & Barlowe, C. Organization of the er-golgi interface for membrane traffic control. *Nat Rev Mol Cell Biol* **14**, 382–92 (2013).

[41] Qualmann, B., Koch, D. & Kessels, M. M. Let's go bananas: revisiting the endocytic bar code. *The EMBO journal* **30**, 3501–15 (2011).

[42] Rao, Y. & Haucke, V. Membrane shaping by the bin/amphiphysin/rvs (bar) domain protein superfamily. *Cellular and molecular life sciences : CMLS* **68**, 3983–93 (2011).

[43] Peter, B. J. *et al.* Bar domains as sensors of membrane curvature: the amphiphysin bar structure. *Science* **303**, 495–9 (2004).

[44] Mim, C. & Unger, V. M. Membrane curvature and its generation by bar proteins. *Trends in biochemical sciences* **37**, 526–33 (2012).

[45] Frost, A., Unger, V. M. & De Camilli, P. The bar domain superfamily: membrane-molding macromolecules. *Cell* **137**, 191–6 (2009).

[46] Bhatia, V. K. *et al.* Amphipathic motifs in bar domains are essential for membrane curvature sensing. *The EMBO journal* **28**, 3303–14 (2009).

[47] Takei, K., Slepnev, V. I., Haucke, V. & De Camilli, P. Functional partnership between amphiphysin and dynamin in clathrin-mediated endocytosis. *Nature cell biology* **1**, 33–9 (1999).

[48] Richnau, N., Fransson, A., Farsad, K. & Aspenstrom, P. Rich-1 has a bin/amphiphysin/rvsp domain responsible for binding to membrane lipids and tubulation of liposomes. *Biochemical and biophysical research communications* **320**, 1034–42 (2004).

[49] Razzaq, A. *et al.* Amphiphysin is necessary for organization of the excitation-contraction coupling machinery of muscles, but not for synaptic vesicle endocytosis in drosophila. *Genes & development* **15**, 2967–79 (2001).

[50] Sheetz, M. P. Cell control by membrane-cytoskeleton adhesion. *Nature reviews. Molecular cell biology* **2**, 392–6 (2001).

[51] Dai, J., Ting-Beall, H. P. & Sheetz, M. P. The secretion-coupled endocytosis correlates with membrane tension changes in rbl 2h3 cells. *The Journal of general physiology* **110**, 1–10 (1997).

[52] Raucher, D. & Sheetz, M. P. Cell spreading and lamellipodial extension rate is regulated by membrane tension. *The Journal of cell biology* **148**, 127–36 (2000).

[53] Bettache, N. *et al.* Mechanical constraint imposed on plasma membrane through transverse phospholipid imbalance induces reversible actin polymerization via phosphoinositide 3-kinase activation. *Journal of cell science* **116**, 2277–84 (2003).

[54] Buss, F., Luzio, J. P. & Kendrick-Jones, J. Myosin vi, an actin motor for membrane traffic and cell migration. *Traffic* **3**, 851–8 (2002).

[55] Allan, V. & Vale, R. Movement of membrane tubules along microtubules in vitro: evidence for specialised sites of motor attachment. *Journal of cell science* **107 (Pt 7)**, 1885–97 (1994).

[56] Merrifield, C. J. Seeing is believing: imaging actin dynamics at single sites of endocytosis. *Trends in cell biology* **14**, 352–8 (2004).

[57] Itoh, T. *et al.* Dynamin and the actin cytoskeleton cooperatively regulate plasma membrane invagination by bar and f-bar proteins. *Dev Cell* **9**, 791–804 (2005).

[58] Haucke, V., Neher, E. & Sigrist, S. J. Protein scaffolds in the coupling of synaptic exocytosis and endocytosis. *Nat Rev Neurosci* **12**, 127–38 (2011).

[59] Polishchuk, R. S. *et al.* Correlative light-electron microscopy reveals the tubular-saccular ultrastructure of carriers operating between golgi apparatus and plasma membrane. *J Cell Biol* **148**, 45–58 (2000).

[60] Klumperman, J. Architecture of the mammalian golgi. *Cold Spring Harb Perspect Biol* **3** (2011).

[61] Voeltz, G. K., Prinz, W. A., Shibata, Y., Rist, J. M. & Rapoport, T. A. A class of membrane proteins shaping the tubular endoplasmic reticulum. *Cell* **124**, 573–86 (2006).

[62] Rothman, J. E. & Wieland, F. T. Protein sorting by transport vesicles. *Science* **272**, 227–34 (1996).

[63] Bonifacino, J. S. & Lippincott-Schwartz, J. Coat proteins: shaping membrane transport. *Nat Rev Mol Cell Biol* **4**, 409–14 (2003).

[64] Jensen, D. & Schekman, R. Copii-mediated vesicle formation at a glance. *J Cell Sci* **124**, 1–4 (2011).

[65] Chen, H. *et al.* Epsin is an eh-domain-binding protein implicated in clathrin-mediated endocytosis. *Nature* **394**, 793–7 (1998).

[66] Wendland, B., Steece, K. E. & Emr, S. D. Yeast epsins contain an essential n-terminal enth domain, bind clathrin and are required for endocytosis. *The EMBO journal* **18**, 4383–93 (1999).

[67] Itoh, T. *et al.* Role of the enth domain in phosphatidylinositol-4,5-bisphosphate binding and endocytosis. *Science* **291**, 1047–51 (2001).

[68] Drake, M. T., Downs, M. A. & Traub, L. M. Epsin binds to clathrin by associating directly with the clathrin-terminal domain. evidence for cooperative binding through two discrete sites. *The Journal of biological chemistry* **275**, 6479–89 (2000).

[69] Ford, M. G. *et al.* Curvature of clathrin-coated pits driven by epsin. *Nature* **419**, 361–6 (2002).

[70] Mim, C. *et al.* Structural basis of membrane bending by the n-bar protein endophilin. *Cell* **149**, 137–45 (2012).

[71] Barlowe, C., d'Enfert, C. & Schekman, R. Purification and characterization of sar1p, a small gtp-binding protein required for transport vesicle formation from the endoplasmic reticulum. *J Biol Chem* **268**, 873–9 (1993).

[72] Pucadyil, T. J. & Schmid, S. L. Conserved functions of membrane active gtpases in coated vesicle formation. *Science* **325**, 1217–20 (2009).

[73] D'Souza-Schorey, C. & Chavrier, P. Arf proteins: roles in membrane traffic and beyond. *Nat Rev Mol Cell Biol* **7**, 347–58 (2006).

[74] Krauss, M. *et al.* Arf1-gtp-induced tubule formation suggests a function of arf family proteins in curvature acquisition at sites of vesicle budding. *J Biol Chem* **283**, 27717–23 (2008).

[75] Bielli, A. *et al.* Regulation of sar1 nh2 terminus by gtp binding and hydrolysis promotes membrane deformation to control copii vesicle fission. *J Cell Biol* **171**, 919–24 (2005).

[76] Lee, M. C. *et al.* Sar1p n-terminal helix initiates membrane curvature and completes the fission of a copii vesicle. *Cell* **122**, 605–17 (2005).

[77] Yorimitsu, T., Sato, K. & Takeuchi, M. Molecular mechanisms of sar/arf gtpases in vesicular trafficking in yeast and plants. *Front Plant Sci* **5**, 411 (2014).

[78] Bi, X., Corpina, R. A. & Goldberg, J. Structure of the sec23/24-sar1 pre-budding complex of the copii vesicle coat. *Nature* **419**, 271–7 (2002).

[79] Fath, S., Mancias, J. D., Bi, X. & Goldberg, J. Structure and organization of coat proteins in the copii cage. *Cell* **129**, 1325–36 (2007).

[80] Zanetti, G. *et al.* The structure of the copii transport-vesicle coat assembled on membranes. *Elife* **2**, e00951 (2013).

[81] Adolf, F. *et al.* Scission of copi and copii vesicles is independent of gtp hydrolysis. *Traffic* **14**, 922–32 (2013).

[82] Kozlov, M. M., McMahon, H. T. & Chernomordik, L. V. Protein-driven membrane stresses in fusion and fission. *Trends Biochem Sci* **35**, 699–706 (2010).

[83] Drin, G., Morello, V., Casella, J. F., Gounon, P. & Antonny, B. Asymmetric tethering of flat and curved lipid membranes by a golgin. *Science* **320**, 670–3 (2008).

[84] Jahn, R. & Scheller, R. H. Snares–engines for membrane fusion. *Nat Rev Mol Cell Biol* **7**, 631–43 (2006).

[85] McMahon, H. T., Kozlov, M. M. & Martens, S. Membrane curvature in synaptic vesicle fusion and beyond. *Cell* **140**, 601–5 (2010).

[86] de Groot, J. C. *et al.* Structural basis for complex formation between human irsp53 and the translocated intimin receptor tir of enterohemorrhagic e. coli. *Structure* **19**, 1294–306 (2011).

[87] Pylypenko, O., Lundmark, R., Rasmuson, E., Carlsson, S. R. & Rak, A. The px-bar membrane-remodeling unit of sorting nexin 9. *The EMBO journal* **26**, 4788–800 (2007).

[88] Shimada, A. *et al.* Curved efc/f-bar-domain dimers are joined end to end into a filament for membrane invagination in endocytosis. *Cell* **129**, 761–72 (2007).

[89] Henne, W. M. *et al.* Structure and analysis of fcho2 f-bar domain: a dimerizing and membrane recruitment module that effects membrane curvature. *Structure* **15**, 839–52 (2007).

[90] Casal, E. *et al.* The crystal structure of the bar domain from human bin1/amphiphysin ii and its implications for molecular recognition. *Biochemistry* **45**, 12917–28 (2006).

[91] Suetsugu, S., Kurisu, S. & Takenawa, T. Dynamic shaping of cellular membranes by phospholipids and membrane-deforming proteins. *Physiol Rev* **94**, 1219–48 (2014).

[92] Nakamura, K. *et al.* Structural basis for membrane binding specificity of the bin/amphiphysin/rvs (bar) domain of arfaptin-2 determined by arl1 gtpase. *J Biol Chem* **287**, 25478–89 (2012).

[93] de Kreuk, B. J. & Hordijk, P. L. Control of rho gtpase function by bar-domains. *Small GTPases* **3**, 45–52 (2012).

[94] Roberts-Galbraith, R. H. & Gould, K. L. Setting the f-bar: functions and regulation of the f-bar protein family. *Cell Cycle* **9**, 4091–7 (2010).

[95] Heath, R. J. & Insall, R. H. F-bar domains: multifunctional regulators of membrane curvature. *J Cell Sci* **121**, 1951–4 (2008).

[96] Zhao, H., Pykalainen, A. & Lappalainen, P. I-bar domain proteins: linking actin and plasma membrane dynamics. *Curr Opin Cell Biol* **23**, 14–21 (2011).

[97] Millard, T. H. *et al.* Structural basis of filopodia formation induced by the irsp53/mim homology domain of human irsp53. *EMBO J* **24**, 240–50 (2005).

[98] PykÃdlÃdinen, A. *et al.* Pinkbar is an epithelial-specific bar domain protein that generates planar membrane structures. *Nat Struct Mol Biol* **18**, 902–907 (2011).

[99] Ayton, G. S., Blood, P. D. & Voth, G. A. Membrane remodeling from n-bar domain interactions: insights from multi-scale simulation. *Biophys J* **92**, 3595–602 (2007).

[100] Mizuno, N., Jao, C. C., Langen, R. & Steven, A. C. Multiple modes of endophilin-mediated conversion of lipid vesicles into coated tubes: implications for synaptic endocytosis. *The Journal of biological chemistry* **285**, 23351–8 (2010).

[101] Kessels, M. M. & Qualmann, B. Syndapin oligomers interconnect the machineries for endocytic vesicle formation and actin polymerization. *J Biol Chem* **281**, 13285–99 (2006).

[102] Shin, N. *et al.* Sorting nexin 9 interacts with dynamin 1 and n-wasp and coordinates synaptic vesicle endocytosis. *J Biol Chem* **282**, 28939–50 (2007).

[103] Frost, A. *et al.* Structural basis of membrane invagination by f-bar domains. *Cell* **132**, 807–17 (2008).

[104] Chial, H. J. *et al.* Membrane targeting by appl1 and appl2: dynamic scaffolds that oligomerize and bind phosphoinositides. *Traffic* **9**, 215–29 (2008).

[105] Wang, Q. *et al.* Molecular mechanism of membrane constriction and tubulation mediated by the f-bar protein pacsin/syndapin. *Proc Natl Acad Sci U S A* **106**, 12700–5 (2009).

[106] Varkey, J. *et al.* Membrane curvature induction and tubulation are common features of synucleins and apolipoproteins. *J Biol Chem* **285**, 32486–93 (2010).

[107] Jao, C. C. *et al.* Roles of amphipathic helices and the bin/amphiphysin/rvs (bar) domain of endophilin in membrane curvature generation. *The Journal of biological chemistry* **285**, 20164–70 (2010).

[108] Isas, J. M., Ambroso, M. R., Hegde, P. B., Langen, J. & Langen, R. Tubulation by amphiphysin requires concentration-dependent switching from wedging to scaffolding. *Structure* **23**, 873–81 (2015).

[109] Farsad, K. *et al.* Generation of high curvature membranes mediated by direct endophilin bilayer interactions. *The Journal of cell biology* **155**, 193–200 (2001).

[110] Pang, X. *et al.* A ph domain in acap1 possesses key features of the bar domain in promoting membrane curvature. *Dev Cell* **31**, 73–86 (2014).

[111] Yamamoto, R., Li, X., Francke, U. & Kilimann, M. W. Genetic mapping of the human amphiphysin gene (amph) at 7p14-p13 excludes its involvement in retinitis pigmentosa 9 or dominant cystoid macular dystrophy. *Am J Hum Genet* **57**, 970–2 (1995).

[112] Butler, M. H. *et al.* Amphiphysin ii (sh3p9; bin1), a member of the amphiphysin/rvs family, is concentrated in the cortical cytomatrix of axon initial segments and nodes of ranvier in brain and around t tubules in skeletal muscle. *The Journal of cell biology* **137**, 1355–67 (1997).

[113] Wechsler-Reya, R., Sakamuro, D., Zhang, J., Duhadaway, J. & Prendergast, G. C. Structural analysis of the human bin1 gene. evidence for tissue-specific transcriptional regulation and alternate rna splicing. *J Biol Chem* **272**, 31453–8 (1997).

[114] McMahon, H. T., Wigge, P. & Smith, C. Clathrin interacts specifically with amphiphysin and is displaced by dynamin. *FEBS Lett* **413**, 319–22 (1997).

[115] Leventis, P. A. *et al.* Drosophila amphiphysin is a post-synaptic protein required for normal locomotion but not endocytosis. *Traffic* **2**, 839–50 (2001).

[116] Zelhof, A. C. *et al.* Drosophila amphiphysin is implicated in protein localization and membrane morphogenesis but not in synaptic vesicle endocytosis. *Development* **128**, 5005–15 (2001).

[117] Lichte, B., Veh, R. W., Meyer, H. E. & Kilimann, M. W. Amphiphysin, a novel protein associated with synaptic vesicles. *The EMBO journal* **11**, 2521–30 (1992).

[118] De Camilli, P. *et al.* The synaptic vesicle-associated protein amphiphysin is the 128-kd autoantigen of stiff-man syndrome with breast cancer. *J Exp Med* **178**, 2219–23 (1993).

[119] David, C., Solimena, M. & De Camilli, P. Autoimmunity in stiff-man syndrome with breast cancer is targeted to the c-terminal region of human amphiphysin, a protein similar to the yeast proteins, rvs167 and rvs161. *FEBS Lett* **351**, 73–9 (1994).

[120] David, C., McPherson, P. S., Mundigl, O. & de Camilli, P. A role of amphiphysin in synaptic vesicle endocytosis suggested by its binding to dynamin in nerve terminals. *Proc Natl Acad Sci U S A* **93**, 331–5 (1996).

[121] Ramjaun, A. R., Micheva, K. D., Bouchelet, I. & McPherson, P. S. Identification and characterization of a nerve terminal-enriched amphiphysin isoform. *J Biol Chem* **272**, 16700–6 (1997).

[122] Wigge, P. *et al.* Amphiphysin heterodimers: potential role in clathrin-mediated endocytosis. *Molecular biology of the cell* **8**, 2003–15 (1997).

[123] Floyd, S. *et al.* Expression of amphiphysin i, an autoantigen of paraneoplastic neurological syndromes, in breast cancer. *Mol Med* **4**, 29–39 (1998).

[124] Terada, Y. *et al.* Novel splice variants of amphiphysin i are expressed in retina. *FEBS Lett* **519**, 185–90 (2002).

[125] Cestra, G. *et al.* The sh3 domains of endophilin and amphiphysin bind to the proline-rich region of synaptojanin 1 at distinct sites that display an unconventional binding specificity. *J Biol Chem* **274**, 32001–7 (1999).

[126] Yamada, H. *et al.* Dynamic interaction of amphiphysin with n-wasp regulates actin assembly. *The Journal of biological chemistry* **284**, 34244–56 (2009).

[127] Micheva, K. D., Kay, B. K. & McPherson, P. S. Synaptojanin forms two separate complexes in the nerve terminal. interactions with endophilin and amphiphysin. *J Biol Chem* **272**, 27239–45 (1997).

[128] Slepnev, V. I., Ochoa, G. C., Butler, M. H. & De Camilli, P. Tandem arrangement of the clathrin and ap-2 binding domains in amphiphysin 1 and disruption of clathrin coat function by amphiphysin fragments comprising these sites. *J Biol Chem* **275**, 17583–9 (2000).

[129] Micheva, K. D., Ramjaun, A. R., Kay, B. K. & McPherson, P. S. Sh3 domain-dependent interactions of endophilin with amphiphysin. *FEBS Lett* **414**, 308–12 (1997).

[130] Sundborger, A. *et al.* An endophilin-dynamin complex promotes budding of clathrin-coated vesicles during synaptic vesicle recycling. *J Cell Sci* **124**, 133–43 (2011).

[131] Shupliakov, O. *et al.* Synaptic vesicle endocytosis impaired by disruption of dynamin-sh3 domain interactions. *Science* **276**, 259–63 (1997).

[132] Zhang, B. & Zelhof, A. C. Amphiphysins: raising the bar for synaptic vesicle recycling and membrane dynamics. bin-amphiphysin-rvsp. *Traffic* **3**, 452–60 (2002).

[133] Taylor, M. J., Perrais, D. & Merrifield, C. J. A high precision survey of the molecular dynamics of mammalian clathrin-mediated endocytosis. *PLoS biology* **9**, e1000604 (2011).

[134] Yamada, H. *et al.* Amphiphysin 1 is important for actin polymerization during phagocytosis. *Mol Biol Cell* **18**, 4669–80 (2007).

[135] Meunier, B., Quaranta, M., Daviet, L., Hatzoglou, A. & Leprince, C. The membrane-tubulating potential of amphiphysin 2/bin1 is dependent on the microtubule-binding cytoplasmic linker protein 170 (clip-170). *Eur J Cell Biol* **88**, 91–102 (2009).

[136] D'Alessandro, M. *et al.* Amphiphysin 2 orchestrates nucleus positioning and shape by linking the nuclear envelope to the actin and microtubule cytoskeleton. *Dev Cell* **35**, 186–98 (2015).

[137] Sakamuro, D., Elliott, K. J., Wechsler-Reya, R. & Prendergast, G. C. Bin1 is a novel myc-interacting protein with features of a tumour suppressor. *Nat Genet* **14**, 69–77 (1996).

[138] Elliott, K. *et al.* Bin1 functionally interacts with myc and inhibits cell proliferation via multiple mechanisms. *Oncogene* **18**, 3564–73 (1999).

[139] Prendergast, G. C. Mechanisms of apoptosis by c-myc. *Oncogene* **18**, 2967–87 (1999).

[140] Ren, G., Vajjhala, P., Lee, J. S., Winsor, B. & Munn, A. L. The bar domain proteins: molding membranes in fission, fusion, and phagy. *Microbiol Mol Biol Rev* **70**, 37–120 (2006).

[141] Leprince, C. *et al.* Sorting nexin 4 and amphiphysin 2, a new partnership between endocytosis and intracellular trafficking. *J Cell Sci* **116**, 1937–48 (2003).

[142] Tsutsui, K., Maeda, Y., Tsutsui, K., Seki, S. & Tokunaga, A. cdna cloning of a novel amphiphysin isoform and tissue-specific expression of its multiple splice variants. *Biochem Biophys Res Commun* **236**, 178–83 (1997).

[143] Wechsler-Reya, R. J., Elliott, K. J. & Prendergast, G. C. A role for the putative tumor suppressor bin1 in muscle cell differentiation. *Mol Cell Biol* **18**, 566–75 (1998).

[144] Ramjaun, A. R., Philie, J., de Heuvel, E. & McPherson, P. S. The n terminus of amphiphysin ii mediates dimerization and plasma membrane targeting. *The Journal of biological chemistry* **274**, 19785–91 (1999).

[145] Di Paolo, G. *et al.* Decreased synaptic vesicle recycling efficiency and cognitive deficits in amphiphysin 1 knockout mice. *Neuron* **33**, 789–804 (2002).

[146] Lee, E. *et al.* Amphiphysin 2 (bin1) and t-tubule biogenesis in muscle. *Science* **297**, 1193–6 (2002).

[147] Al-Qusairi, L. & Laporte, J. T-tubule biogenesis and triad formation in skeletal muscle and implication in human diseases. *Skeletal muscle* **1**, 26 (2011).

[148] Muller, A. J. *et al.* Targeted disruption of the murine bin1/amphiphysin ii gene does not disable endocytosis but results in embryonic cardiomyopathy with aberrant myofibril formation. *Mol Cell Biol* **23**, 4295–306 (2003).

[149] Nicot, A. S. *et al.* Mutations in amphiphysin 2 (bin1) disrupt interaction with dynamin 2 and cause autosomal recessive centronuclear myopathy. *Nature genetics* **39**, 1134–9 (2007).

[150] Royer, B. *et al.* The myotubularin-amphiphysin 2 complex in membrane tubulation and centronuclear myopathies. *EMBO Rep* **14**, 907–15 (2013).

[151] Wu, T. & Baumgart, T. Bin1 membrane curvature sensing and generation show autoinhibition regulated by downstream ligands and pi(4,5)p2. *Biochemistry* **53**, 7297–309 (2014).

[152] Romero, N. B. Centronuclear myopathies: a widening concept. *Neuromuscul Disord* **20**, 223–8 (2010).

[153] Fugier, C. *et al.* Misregulated alternative splicing of bin1 is associated with t tubule alterations and muscle weakness in myotonic dystrophy. *Nat Med* **17**, 720–5 (2011).

[154] Ge, K. *et al.* Mechanism for elimination of a tumor suppressor: aberrant splicing of a brain-specific exon causes loss of function of bin1 in melanoma. *Proc Natl Acad Sci U S A* **96**, 9689–94 (1999).

[155] Prendergast, G. C., Muller, A. J., Ramalingam, A. & Chang, M. Y. Bar the door: cancer suppression by amphiphysin-like genes. *Biochim Biophys Acta* **1795**, 25–36 (2009).

[156] Elliott, K., Ge, K., Du, W. & Prendergast, G. C. The c-myc-interacting adaptor protein bin1 activates a caspase-independent cell death program. *Oncogene* **19**, 4669–84 (2000).

[157] DuHadaway, J. B., Sakamuro, D., Ewert, D. L. & Prendergast, G. C. Bin1 mediates apoptosis by c-myc in transformed primary cells. *Cancer Res* **61**, 3151–6 (2001).

[158] Ge, K. *et al.* Losses of the tumor suppressor bin1 in breast carcinoma are frequent and reflect deficits in programmed cell death capacity. *Int J Cancer* **85**, 376–83 (2000).

[159] Ge, K. *et al.* Loss of heterozygosity and tumor suppressor activity of bin1 in prostate carcinoma. *Int J Cancer* **86**, 155–61 (2000).

[160] Pyndiah, S. *et al.* c-myc suppresses bin1 to release poly(adp-ribose) polymerase 1: a mechanism by which cancer cells acquire cisplatin resistance. *Sci Signal* **4**, ra19 (2011).

[161] Meyer-Ficca, M. L., Meyer, R. G., Jacobson, E. L. & Jacobson, M. K. Poly(adp-ribose) polymerases: managing genome stability. *Int J Biochem Cell Biol* **37**, 920–6 (2005).

[162] Prokic, I., Cowling, B. S. & Laporte, J. Amphiphysin 2 (bin1) in physiology and diseases. *Journal of molecular medicine* **92**, 453–63 (2014).

[163] Fu, Y. & Hong, T. Bin1 regulates dynamic t-tubule membrane. *Biochimica et biophysica acta* (2015).

[164] Koh, T. W., Verstreken, P. & Bellen, H. J. Dap160/intersectin acts as a stabilizing scaffold required for synaptic development and vesicle endocytosis. *Neuron* **43**, 193–205 (2004).

[165] Mathew, D., Popescu, A. & Budnik, V. Drosophila amphiphysin functions during synaptic fasciclin ii membrane cycling. *J Neurosci* **23**, 10710–6 (2003).

[166] Cowling, B. S. *et al.* Increased expression of wild-type or a centronuclear myopathy mutant of dynamin 2 in skeletal muscle of adult mice leads to structural defects and muscle weakness. *Am J Pathol* **178**, 2224–35 (2011).

[167] Su, J., Chow, B., Boulianne, G. L. & Wilde, A. The bar domain of amphiphysin is required for cleavage furrow tip-tubule formation during cellularization in drosophila embryos. *Molecular biology of the cell* **24**, 1444–53 (2013).

[168] Mazumdar, A. & Mazumdar, M. How one becomes many: blastoderm cellularization in drosophila melanogaster. *Bioessays* **24**, 1012–22 (2002).

[169] Sokac, A. M. & Wieschaus, E. Zygotically controlled f-actin establishes cortical compartments to stabilize furrows during drosophila cellularization. *J Cell Sci* **121**, 1815–24 (2008).

[170] Leprince, C. *et al.* A new member of the amphiphysin family connecting endocytosis and signal transduction pathways. *J Biol Chem* **272**, 15101–5 (1997).

[171] Owen, D. J. *et al.* Crystal structure of the amphiphysin-2 sh3 domain and its role in the prevention of dynamin ring formation. *EMBO J* **17**, 5273–85 (1998).

[172] Ellis, J. D. *et al.* Tissue-specific alternative splicing remodels protein-protein interaction networks. *Mol Cell* **46**, 884–92 (2012).

[173] Ramjaun, A. R. & McPherson, P. S. Multiple amphiphysin ii splice variants display differential clathrin binding: identification of two distinct clathrin-binding sites. *J Neurochem* **70**, 2369–76 (1998).

[174] Yu, H. *et al.* Structural basis for the binding of proline-rich peptides to sh3 domains. *Cell* **76**, 933–45 (1994).

[175] Fernando, P. *et al.* Bin1 src homology 3 domain acts as a scaffold for myofiber sarcomere assembly. *J Biol Chem* **284**, 27674–86 (2009).

[176] Bohm, J. *et al.* Altered splicing of the bin1 muscle-specific exon in humans and dogs with highly progressive centronuclear myopathy. *PLoS Genet* **9**, e1003430 (2013).

[177] Kojima, C. *et al.* Regulation of bin1 sh3 domain binding by phosphoinositides. *The EMBO journal* **23**, 4413–22 (2004).

[178] Tomizawa, K. *et al.* Cophosphorylation of amphiphysin i and dynamin i by cdk5 regulates clathrin-mediated endocytosis of synaptic vesicles. *J Cell Biol* **163**, 813–24 (2003).

[179] Liang, S. *et al.* Major cdk5-dependent phosphorylation sites of amphiphysin 1 are implicated in the regulation of the membrane binding and endocytosis. *J Neurochem* **102**, 1466–76 (2007).

[180] Shang, W. H. *et al.* Regulation of amphiphysin1 by mitogen-activated protein kinase: its significance in nerve growth factor receptor-mediated endocytosis. *J Biol Chem* **279**, 40890–6 (2004).

[181] Doring, M., Loos, A., Schrader, N., Pfander, B. & Bauerfeind, R. Nerve growth factor-induced phosphorylation of amphiphysin-1 by casein kinase 2 regulates clathrin-amphiphysin interactions. *J Neurochem* **98**, 2013–22 (2006).

[182] Razzaq, A. *et al.* Characterisation of the gene for drosophila amphiphysin. *Gene* **241**, 167–74 (2000).

[183] Floyd, S. R. *et al.* Amphiphysin 1 binds the cyclin-dependent kinase (cdk) 5 regulatory subunit p35 and is phosphorylated by cdk5 and cdc2. *J Biol Chem* **276**, 8104–10 (2001).

[184] Wu, Y., Matsui, H. & Tomizawa, K. Amphiphysin i and regulation of synaptic vesicle endocytosis. *Acta medica Okayama* **63**, 305–23 (2009).

[185] Bers, D. M. Cardiac excitation-contraction coupling. *Nature* **415**, 198–205 (2002).

[186] Inui, M., Saito, A. & Fleischer, S. Isolation of the ryanodine receptor from cardiac sarcoplasmic reticulum and identity with the feet structures. *J Biol Chem* **262**, 15637–42 (1987).

[187] Lee, E. H. *et al.* Conformational coupling of dhpr and ryr1 in skeletal myotubes is influenced by long-range allosterism: evidence for a negative regulatory module. *Am J Physiol Cell Physiol* **286**, C179–89 (2004).

[188] Pinali, C., Bennett, H., Davenport, J. B., Trafford, A. W. & Kitmitto, A. Three-dimensional reconstruction of cardiac sarcoplasmic reticulum reveals a continuous network linking transverse-tubules: this organization is perturbed in heart failure. *Circ Res* **113**, 1219–30 (2013).

[189] Song, X. *et al.* In situ visualizing t-tubule/sr junction reveals the ultra-structures of calcium storage and release machinery. *Int J Biol Macromol* **82**, 7–12 (2016).

[190] Szent-Gyorgyi, A. G. Calcium regulation of muscle contraction. *Biophys J* **15**, 707–23 (1975).

[191] Herzberg, O., Moult, J. & James, M. N. Calcium binding to skeletal muscle troponin c and the regulation of muscle contraction. *Ciba Found Symp* **122**, 120–44 (1986).

[192] Farah, C. S. & Reinach, F. C. The troponin complex and regulation of muscle contraction. *FASEB J* **9**, 755–67 (1995).

[193] Flucher, B. E., Takekura, H. & Franzini-Armstrong, C. Development of the excitation-contraction coupling apparatus in skeletal muscle: association of sarcoplasmic reticulum and transverse tubules with myofibrils. *Dev Biol* **160**, 135–47 (1993).

[194] Soeller, C. & Cannell, M. B. Examination of the transverse tubular system in living cardiac rat myocytes by 2-photon microscopy and digital image-processing techniques. *Circ Res* **84**, 266–75 (1999).

[195] Curtis, B. M. & Catterall, W. A. Purification of the calcium antagonist receptor of the voltage-sensitive calcium channel from skeletal muscle transverse tubules. *Biochemistry* **23**, 2113–8 (1984).

[196] Brette, F. & Orchard, C. T-tubule function in mammalian cardiac myocytes. *Circ Res* **92**, 1182–92 (2003).

[197] Forbes, M. S., Hawkey, L. A. & Sperelakis, N. The transverse-axial tubular system (tats) of mouse myocardium: its morphology in the developing and adult animal. *Am J Anat* **170**, 143–62 (1984).

[198] Ogata, T. & Yamasaki, Y. High-resolution scanning electron microscopic studies on the three-dimensional structure of the transverse-axial tubular system, sarcoplasmic reticulum and intercalated disc of the rat myocardium. *Anat Rec* **228**, 277–87 (1990).

[199] Page, E. Quantitative ultrastructural analysis in cardiac membrane physiology. *Am J Physiol* **235**, C147–58 (1978).

[200] Page, E. & Surdyk-Droske, M. Distribution, surface density, and membrane area of diadic junctional contacts between plasma membrane and terminal cisterns in mammalian ventricle. *Circ Res* **45**, 260–7 (1979).

[201] Franzini-Armstrong, C., Landmesser, L. & Pilar, G. Size and shape of transverse tubule openings in frog twitch muscle fibers. *J Cell Biol* **64**, 493–7 (1975).

[202] Sandow, A. Excitation-contraction coupling in skeletal muscle. *Pharmacol Rev* **17**, 265–320 (1965).

[203] Franzini-Armstrong, C. Morphologic approaches to the study of skeletal muscle. *Anat Rec Suppl* **1**, 67–84 (1983).

[204] Flucher, B. E. *et al.* Triad formation: organization and function of the sarcoplasmic reticulum calcium release channel and triadin in normal and dysgenic muscle in vitro. *J Cell Biol* **123**, 1161–74 (1993).

[205] Takekura, H., Flucher, B. E. & Franzini-Armstrong, C. Sequential docking, molecular differentiation, and positioning of t-tubule/sr junctions in developing mouse skeletal muscle. *Dev Biol* **239**, 204–14 (2001).

[206] Kieval, R. S., Bloch, R. J., Lindenmayer, G. E., Ambesi, A. & Lederer, W. J. Immunofluorescence localization of the na-ca exchanger in heart cells. *Am J Physiol* **263**, C545–50 (1992).

[207] Hong, T. *et al.* Cardiac bin1 folds t-tubule membrane, controlling ion flux and limiting arrhythmia. *Nature medicine* **20**, 624–32 (2014).

[208] Caldwell, J. L. *et al.* Dependence of cardiac transverse tubules on the bar domain protein amphiphysin ii (bin-1). *Circulation research* **115**, 986–96 (2014).

[209] Galbiati, F. *et al.* Caveolin-3 null mice show a loss of caveolae, changes in the microdomain distribution of the dystrophin-glycoprotein complex, and t-tubule abnormalities. *J Biol Chem* **276**, 21425–33 (2001).

[210] Beavers, D. L., Landstrom, A. P., Chiang, D. Y. & Wehrens, X. H. Emerging roles of junctophilin-2 in the heart and implications for cardiac diseases. *Cardiovasc Res* **103**, 198–205 (2014).

[211] Liu, J. *et al.* Dysferlin, a novel skeletal muscle gene, is mutated in miyoshi myopathy and limb girdle muscular dystrophy. *Nat Genet* **20**, 31–6 (1998).

[212] Klinge, L. *et al.* From t-tubule to sarcolemma: damage-induced dysferlin translocation in early myogenesis. *FASEB J* **21**, 1768–76 (2007).

[213] Tang, Z. *et al.* Molecular cloning of caveolin-3, a novel member of the caveolin gene family expressed predominantly in muscle. *J Biol Chem* **271**, 2255–61 (1996).

[214] Song, K. S. *et al.* Co-purification and direct interaction of ras with caveolin, an integral membrane protein of caveolae microdomains. detergent-free purification of caveolae microdomains. *J Biol Chem* **271**, 9690–7 (1996).

[215] Parton, R. G., Way, M., Zorzi, N. & Stang, E. Caveolin-3 associates with developing t-tubules during muscle differentiation. *J Cell Biol* **136**, 137–54 (1997).

[216] Ishikawa, H. Formation of elaborate networks of t-system tubules in cultured skeletal muscle with special reference to the t-system formation. *J Cell Biol* **38**, 51–66 (1968).

[217] Franzini-Armstrong, C. Simultaneous maturation of transverse tubules and sarcoplasmic reticulum during muscle differentiation in the mouse. *Dev Biol* **146**, 353–63 (1991).

[218] Klinge, L. *et al.* Dysferlin associates with the developing t-tubule system in rodent and human skeletal muscle. *Muscle Nerve* **41**, 166–73 (2010).

[219] Lek, A., Evesson, F. J., Sutton, R. B., North, K. N. & Cooper, S. T. Ferlins: regulators of vesicle fusion for auditory neurotransmission, receptor trafficking and membrane repair. *Traffic* **13**, 185–94 (2012).

[220] Kerr, J. P. *et al.* Dysferlin stabilizes stress-induced ca2+ signaling in the transverse tubule membrane. *Proc Natl Acad Sci U S A* **110**, 20831–6 (2013).

[221] Kerr, J. P., Ward, C. W. & Bloch, R. J. Dysferlin at transverse tubules regulates ca(2+) homeostasis in skeletal muscle. *Front Physiol* **5**, 89 (2014).

[222] Ampong, B. N., Imamura, M., Matsumiya, T., Yoshida, M. & Takeda, S. Intracellular localization of dysferlin and its association with the dihydropyridine receptor. *Acta Myol* **24**, 134–44 (2005).

[223] Demonbreun, A. R. *et al.* Dysferlin and myoferlin regulate transverse tubule formation and glycerol sensitivity. *Am J Pathol* **184**, 248–59 (2014).

[224] Waddell, L. B. *et al.* Dysferlin, annexin a1, and mitsugumin 53 are upregulated in muscular dystrophy and localize to longitudinal tubules of the t-system with stretch. *J Neuropathol Exp Neurol* **70**, 302–13 (2011).

[225] Nishi, M., Mizushima, A., Nakagawara, K. & Takeshima, H. Characterization of human junctophilin subtype genes. *Biochem Biophys Res Commun* **273**, 920–7 (2000).

[226] Ito, K. *et al.* Deficiency of triad junction and contraction in mutant skeletal muscle lacking junctophilin type 1. *J Cell Biol* **154**, 1059–67 (2001).

[227] Komazaki, S., Ito, K., Takeshima, H. & Nakamura, H. Deficiency of triad formation in developing skeletal muscle cells lacking junctophilin type 1. *FEBS Lett* **524**, 225–9 (2002).

[228] Wei, S. *et al.* T-tubule remodeling during transition from hypertrophy to heart failure. *Circ Res* **107**, 520–31 (2010).

[229] Claeys, K. G. *et al.* Phenotype of a patient with recessive centronuclear myopathy and a novel bin1 mutation. *Neurology* **74**, 519–21 (2010).

[230] Hong, T. T. *et al.* Bin1 is reduced and cav1.2 trafficking is impaired in human failing cardiomyocytes. *Heart Rhythm* **9**, 812–20 (2012).

[231] Asimaki, A. Bin1: a new biomarker to track arvc? *Heart Rhythm* **9**, 968–9 (2012).

[232] Lyon, A. R. *et al.* Plasticity of surface structures and beta(2)-adrenergic receptor localization in failing ventricular cardiomyocytes during recovery from heart failure. *Circ Heart Fail* **5**, 357–65 (2012).

[233] Hong, T. T. *et al.* Bin1 localizes the l-type calcium channel to cardiac t-tubules. *PLoS Biol* **8**, e1000312 (2010).

[234] Lederer, W. J., Niggli, E. & Hadley, R. W. Sodium-calcium exchange in excitable cells: fuzzy space. *Science* **248**, 283 (1990).

[235] Shepherd, N. & McDonough, H. B. Ionic diffusion in transverse tubules of cardiac ventricular myocytes. *Am J Physiol* **275**, H852–60 (1998).

[236] Pasek, M., Simurda, J. & Christe, G. The functional role of cardiac t-tubules explored in a model of rat ventricular myocytes. *Philos Trans A Math Phys Eng Sci* **364**, 1187–206 (2006).

[237] Swift, F., Stromme, T. A., Amundsen, B., Sejersted, O. M. & Sjaastad, I. Slow diffusion of k+ in the t tubules of rat cardiomyocytes. *J Appl Physiol (1985)* **101**, 1170–6 (2006).

[238] Forssmann, W. G. & Girardier, L. A study of the t system in rat heart. *J Cell Biol* **44**, 1–19 (1970).

[239] Lavorato, M. *et al.* Dyad content is reduced in cardiac myocytes of mice with impaired calmodulin regulation of ryr2. *J Muscle Res Cell Motil* **36**, 205–14 (2015).

[240] Smith, L. L., Gupta, V. A. & Beggs, A. H. Bridging integrator 1 (bin1) deficiency in zebrafish results in centronuclear myopathy. *Hum Mol Genet* **23**, 3566–78 (2014).

[241] Tuvia, S., Buhusi, M., Davis, L., Reedy, M. & Bennett, V. Ankyrin-b is required for intracellular sorting of structurally diverse ca2+ homeostasis proteins. *J Cell Biol* **147**, 995–1008 (1999).

[242] Scriven, D. R., Dan, P. & Moore, E. D. Distribution of proteins implicated in excitation-contraction coupling in rat ventricular myocytes. *Biophys J* **79**, 2682–91 (2000).

[243] Ghaneie, A. *et al.* Bin1 attenuation in breast cancer is correlated to nodal metastasis and reduced survival. *Cancer Biol Ther* **6**, 192–4 (2007).

[244] Chang, M. Y. *et al.* Bin1 ablation increases susceptibility to cancer during aging, particularly lung cancer. *Cancer Res* **67**, 7605–12 (2007).

[245] Zhong, X. *et al.* Bin1 is linked to metastatic potential and chemosensitivity in neuroblastoma. *Pediatr Blood Cancer* **53**, 332–7 (2009).

[246] Pan, K. *et al.* Characterization of bridging integrator 1 (bin1) as a potential tumor suppressor and prognostic marker in hepatocellular carcinoma. *Mol Med* **18**, 507–18 (2012).

[247] Kennah, E. *et al.* Identification of tyrosine kinase, hck, and tumor suppressor, bin1, as potential mediators of ahi-1 oncogene in primary and transformed ctcl cells. *Blood* **113**, 4646–55 (2009).

[248] Hogarty, M. D. *et al.* Bin1 inhibits colony formation and induces apoptosis in neuroblastoma cell lines with mycn amplification. *Med Pediatr Oncol* **35**, 559–62 (2000).

[249] Matsunaga, T. *et al.* Enhanced expression of n-myc messenger rna in neuroblastomas found by mass screening. *Clin Cancer Res* **6**, 3199–204 (2000).

[250] Seeger, R. C. *et al.* Association of multiple copies of the n-myc oncogene with rapid progression of neuroblastomas. *N Engl J Med* **313**, 1111–6 (1985).

[251] Brodeur, G. M., Seeger, R. C., Schwab, M., Varmus, H. E. & Bishop, J. M. Amplification of n-myc in untreated human neuroblastomas correlates with advanced disease stage. *Science* **224**, 1121–4 (1984).

[252] Tajiri, T. *et al.* Expression of a mycn-interacting isoform of the tumor suppressor bin1 is reduced in neuroblastomas with unfavorable biological features. *Clin Cancer Res* **9**, 3345–55 (2003).

[253] Raj, T. *et al.* Alzheimer disease susceptibility loci: evidence for a protein network under natural selection. *Am J Hum Genet* **90**, 720–6 (2012).

[254] Tan, M. S., Yu, J. T. & Tan, L. Bridging integrator 1 (bin1): form, function, and alzheimer's disease. *Trends in molecular medicine* **19**, 594–603 (2013).

[255] Chapuis, J. *et al.* Increased expression of bin1 mediates alzheimer genetic risk by modulating tau pathology. *Mol Psychiatry* **18**, 1225–34 (2013).

[256] Braak, H., Thal, D. R., Ghebremedhin, E. & Del Tredici, K. Stages of the pathologic process in alzheimer disease: age categories from 1 to 100 years. *J Neuropathol Exp Neurol* **70**, 960–9 (2011).

[257] Nakamura, K. *et al.* Proline isomer-specific antibodies reveal the early pathogenic tau conformation in alzheimer's disease. *Cell* **149**, 232–44 (2012).

[258] Wu, T., Shi, Z. & Baumgart, T. Mutations in bin1 associated with centronuclear myopathy disrupt membrane remodeling by affecting protein density and oligomerization. *PLoS One* **9**, e93060 (2014).

[259] Bohm, J. *et al.* Case report of intrafamilial variability in autosomal recessive centronuclear myopathy associated to a novel bin1 stop mutation. *Orphanet journal of rare diseases* **5**, 35 (2010).

[260] Romero, N. B. & Bitoun, M. Centronuclear myopathies. *Semin Pediatr Neurol* **18**, 250–6 (2011).

[261] Bitoun, M. *et al.* Mutations in dynamin 2 cause dominant centronuclear myopathy. *Nat Genet* **37**, 1207–9 (2005).

[262] Yoon, Y., Zhang, X. & Cho, W. Phosphatidylinositol 4,5-bisphosphate (ptdins(4,5)p2) specifically induces membrane penetration and deformation by bin/amphiphysin/rvs (bar) domains. *The Journal of biological chemistry* **287**, 34078–90 (2012).

[263] Ohi, M., Li, Y., Cheng, Y. & Walz, T. Negative staining and image classification - powerful tools in modern electron microscopy. *Biol Proced Online* **6**, 23–34 (2004).

[264] Adrian, M., Dubochet, J., Lepault, J. & McDowall, A. W. Cryo-electron microscopy of viruses. *Nature* **308**, 32–6 (1984).

[265] Itoh, T. & Takenawa, T. Mechanisms of membrane deformation by lipid-binding domains. *Progress in lipid research* **48**, 298–305 (2009).

[266] Adam, J., Basnet, N. & Mizuno, N. Structural insights into the cooperative remodeling of membranes by amphiphysin/bin1. *Scientific reports* **5**, 15452 (2015).

[267] Scheres, S. H. Relion: implementation of a bayesian approach to cryo-em structure determination. *J Struct Biol* **180**, 519–30 (2012).

[268] Diaz, R., Rice, W. J. & Stokes, D. L. Fourier-bessel reconstruction of helical assemblies. *Methods Enzymol* **482**, 131–65 (2010).

[269] Heymann, J. B. & Belnap, D. M. Bsoft: image processing and molecular modeling for electron microscopy. *Journal of structural biology* **157**, 3–18 (2007).

[270] Mindell, J. A. & Grigorieff, N. Accurate determination of local defocus and specimen tilt in electron microscopy. *J Struct Biol* **142**, 334–47 (2003).

[271] Ludtke, S. J., Baldwin, P. R. & Chiu, W. Eman: semiautomated software for high-resolution single-particle reconstructions. *J Struct Biol* **128**, 82–97 (1999).

[272] Ruprecht, J. & Nield, J. Determining the structure of biological macromolecules by transmission electron microscopy, single particle analysis and 3d reconstruction. *Progress in biophysics and molecular biology* **75**, 121–64 (2001).

[273] Frank, J. *et al.* Spider and web: processing and visualization of images in 3d electron microscopy and related fields. *J Struct Biol* **116**, 190–9 (1996).

[274] Shaikh, T. R. *et al.* Spider image processing for single-particle reconstruction of biological macromolecules from electron micrographs. *Nat Protoc* **3**, 1941–74 (2008).

[275] Egelman, E. H. Reconstruction of helical filaments and tubes. *Methods Enzymol* **482**, 167–83 (2010).

[276] Egelman, E. H. A robust algorithm for the reconstruction of helical filaments using single-particle methods. *Ultramicroscopy* **85**, 225–34 (2000).

[277] Jiang, W. & Ludtke, S. J. Electron cryomicroscopy of single particles at subnanometer resolution. *Curr Opin Struct Biol* **15**, 571–7 (2005).

[278] Pettersen, E. F. *et al.* Ucsf chimera–a visualization system for exploratory research and analysis. *Journal of computational chemistry* **25**, 1605–12 (2004).

[279] Bohm, J. *et al.* Adult-onset autosomal dominant centronuclear myopathy due to bin1 mutations. *Brain* **137**, 3160–70 (2014).

[280] Mejaddam, A. Y., Nennesmo, I. & Sejersen, T. Severe phenotype of a patient with autosomal recessive centronuclear myopathy due to a bin1 mutation. *Acta Myol* **28**, 91–3 (2009).

[281] Lee, M. C. & Schekman, R. Cell biology. bar domains go on a bender. *Science* **303**, 479–80 (2004).

[282] Boucrot, E. *et al.* Membrane fission is promoted by insertion of amphipathic helices and is restricted by crescent bar domains. *Cell* **149**, 124–36 (2012).

[283] Sorre, B. *et al.* Nature of curvature coupling of amphiphysin with membranes depends on its bound density. *Proc Natl Acad Sci U S A* **109**, 173–8 (2012).

[284] Zampighi, G., Vergara, J. & Ramon, F. On the connection between the transverse tubules and the plasma membrane in frog semitendinosus skeletal muscle. are caveolae the mouths of the transverse tubule system? *J Cell Biol* **64**, 734–40 (1975).

[285] Hernandez-Deviez, D. J. *et al.* Aberrant dysferlin trafficking in cells lacking caveolin or expressing dystrophy mutants of caveolin-3. *Hum Mol Genet* **15**, 129–42 (2006).

[286] Selcen, D., Stilling, G. & Engel, A. G. The earliest pathologic alterations in dysferlinopathy. *Neurology* **56**, 1472–81 (2001).

[287] Bansal, D. *et al.* Defective membrane repair in dysferlin-deficient muscular dystrophy. *Nature* **423**, 168–72 (2003).

[288] Picas, L. *et al.* Bin1/m-amphiphysin2 induces clustering of phosphoinositides to recruit its downstream partner dynamin. *Nat Commun* **5**, 5647 (2014).

[289] Zhao, H. *et al.* Membrane-sculpting bar domains generate stable lipid microdomains. *Cell Rep* **4**, 1213–23 (2013).

[290] Falcone, S. *et al.* N-wasp is required for amphiphysin-2/bin1-dependent nuclear positioning and triad organization in skeletal muscle and is involved in the pathophysiology of centronuclear myopathy. *EMBO Mol Med* **6**, 1455–75 (2014).

[291] Rohatgi, R., Ho, H. Y. & Kirschner, M. W. Mechanism of n-wasp activation by cdc42 and phosphatidylinositol 4, 5-bisphosphate. *J Cell Biol* **150**, 1299–310 (2000).

[292] Miki, H., Miura, K. & Takenawa, T. N-wasp, a novel actin-depolymerizing protein, regulates the cortical cytoskeletal rearrangement in a pip2-dependent manner downstream of tyrosine kinases. *EMBO J* **15**, 5326–35 (1996).

[293] Papayannopoulos, V. *et al.* A polybasic motif allows n-wasp to act as a sensor of pip(2) density. *Mol Cell* **17**, 181–91 (2005).

[294] Blondeau, F. *et al.* Myotubularin, a phosphatase deficient in myotubular myopathy, acts on phosphatidylinositol 3-kinase and phosphatidylinositol 3-phosphate pathway. *Hum Mol Genet* **9**, 2223–9 (2000).

[295] Taylor, G. S., Maehama, T. & Dixon, J. E. Myotubularin, a protein tyrosine phosphatase mutated in myotubular myopathy, dephosphorylates the lipid second messenger, phosphatidylinositol 3-phosphate. *Proc Natl Acad Sci U S A* **97**, 8910–5 (2000).

[296] Tronchere, H. *et al.* Production of phosphatidylinositol 5-phosphate by the phosphoinositide 3-phosphatase myotubularin in mammalian cells. *J Biol Chem* **279**, 7304–12 (2004).

[297] Amoasii, L. *et al.* Phosphatase-dead myotubularin ameliorates x-linked centronuclear myopathy phenotypes in mice. *PLoS Genet* **8**, e1002965 (2012).

[298] Laporte, J. *et al.* A gene mutated in x-linked myotubular myopathy defines a new putative tyrosine phosphatase family conserved in yeast. *Nat Genet* **13**, 175–82 (1996).

[299] Cowling, B. S. *et al.* Increased expression of wild-type or a centronuclear myopathy mutant of dynamin 2 in skeletal muscle of adult mice leads to structural defects and muscle weakness. *Am J Pathol* **178**, 2224–35 (2011).

[300] Durieux, A. C., Prudhon, B., Guicheney, P. & Bitoun, M. Dynamin 2 and human diseases. *J Mol Med (Berl)* **88**, 339–50 (2010).

[301] Zhao, T., Graham, O. S., Raposo, A. & St Johnston, D. Growing microtubules push the oocyte nucleus to polarize the drosophila dorsal-ventral axis. *Science* **336**, 999–1003 (2012).

[302] Chin, Y. H. *et al.* Dynamin-2 mutations associated with centronuclear myopathy are hypermorphic and lead to t-tubule fragmentation. *Hum Mol Genet* **24**, 5542–54 (2015).

[303] Schiaffino, S., Cantini, M. & Sartore, S. T-system formation in cultured rat skeletal tissue. *Tissue Cell* **9**, 437–46 (1977).

[304] Flucher, B. E., Phillips, J. L., Powell, J. A., Andrews, S. B. & Daniels, M. P. Coordinated development of myofibrils, sarcoplasmic reticulum and transverse tubules in normal and dysgenic mouse skeletal muscle, in vivo and in vitro. *Dev Biol* **150**, 266–80 (1992).

[305] Carozzi, A. J., Ikonen, E., Lindsay, M. R. & Parton, R. G. Role of cholesterol in developing t-tubules: analogous mechanisms for t-tubule and caveolae biogenesis. *Traffic* **1**, 326–41 (2000).

[306] Tang, G. *et al.* Eman2: an extensible image processing suite for electron microscopy. *J Struct Biol* **157**, 38–46 (2007).

[307] Mastronarde, D. N. Automated electron microscope tomography using robust prediction of specimen movements. *Journal of structural biology* **152**, 36–51 (2005).

[308] Studier, F. W. Protein production by auto-induction in high density shaking cultures. *Protein Expr Purif* **41**, 207–34 (2005).

[309] Studier, F. W. Stable expression clones and auto-induction for protein production in e. coli. *Methods Mol Biol* **1091**, 17–32 (2014).

[310] Laemmli, U. K. Cleavage of structural proteins during the assembly of the head of bacteriophage t4. *Nature* **227**, 680–5 (1970).

[311] Egelman, E. H. The iterative helical real space reconstruction method: surmounting the problems posed by real polymers. *J Struct Biol* **157**, 83–94 (2007).